



Università di Napoli Federico II

Dipartimento di Ingegneria Industriale

Doctorate Thesis

**TRANSPORT PHENOMENA IN POROUS MEDIA:
FROM OPEN-CELL FOAMS
TO BIOLOGICAL SYSTEMS**

Marcello Iasiello

Advisor

Prof. Nicola Bianco



Università degli Studi di Napoli Federico II

School of Doctorate in Industrial Engineering

Research Doctorate Program in Mechanical Systems Engineering

XXVIII Cycle

Doctorate Thesis

**TRANSPORT PHENOMENA IN POROUS MEDIA: FROM OPEN-CELL
FOAMS TO BIOLOGICAL SYSTEMS**

School of Doctorate Coordinator

Prof. Antonio Moccia

Doctorate Program Coordinator

Prof. Fabio Bozza

Advisor

Prof. Nicola Bianco

Candidate

Marcello Iasiello

To my parents

ACKNOWLEDGMENTS

I want to thank:

- The Dipartimento di Ingegneria Industriale (DII) of the Università degli Studi di Napoli Federico II,
- the UniNA and Compagnia di San Paolo, that financially supported, in the frame of Programme STAR, my stay at the University of California, Riverside (UCR),
- Prof. Kambiz Vafai of the University of California, Riverside (UCR) to have had the opportunity and the honor to work with him at UCR,
- Prof. Wilson K. S. Chiu of the University of Connecticut (UConn) for letting me work with him also after my master thesis,
- Prof. Assunta Andreozzi for her contribution on transport phenomena in biological systems,
- Dr. Salvatore Cunsolo for its contribution on experimental and numerical pore-scale studies on open-cell foams,
- Drs. Giuseppe Ambrosio, Paolino Ambrosino and Alberto Milella for their contribution in developing results on heat transfer in open-cell foams.

Finally, a special thanks to Prof. Nicola Bianco and Prof. Vincenzo Naso that gave me the opportunity to develop my doctorate project in these three years.

ABSTRACT

The complex geometry of a porous medium makes challenging the study of transport phenomena through it. Investigations are carried out treating the whole macroscopic porous medium as an equivalent homogeneous medium, whose governing equations are averaged over a Representative Elementary Volume (REV). Governing equations are coupled with the microscopic problem scales by means of the so-called closing coefficients.

Results of the study of transport phenomena in two classes of porous media: open-cell foams and biological systems, also with reference to human arteries are presented in this thesis.

For open-cell foams, analysis of microscales pressure drop and convective heat transfer were carried out with both experimental and numerical techniques. Experiments were carried out for various open-cell aluminum foam samples with different porosities and PPI in order to study pressure drop. Local convection heat transfer in one foam sample, for different inlet velocities of the fluid, was analyzed. Numerical predictions were obtained by using a finite element scheme. The geometry for the numerical models was reconstructed by means of two techniques. In the first, tomographic scans on three open-cell aluminum foam samples with different porosities were carried out to obtain a real foam; in the second the geometry was computationally reconstructed with reference to Kelvin's foam model, obtaining an ideal foam. The ideal foam geometry was further modified in order to analyze thermally developing effects and strut shape effects on pressure drop and convection heat transfer. Nusselt number was correlated to process parameters, for thermally developed flow, and it was shown that the accuracy of the ideal model improves when the strut shape is well-modeled.

By using the macroscopic porous medium approach, two industrial applications of open-cell foams were studied with a numerical approach. The first application is a volumetric solar receiver, where an open-cell ceramic foam is employed as the porous absorber; the second one was an aluminum foam-based heat sink. In both cases, results are presented for different foam morphologies and thermo-fluid-dynamic conditions.

Low density lipoprotein (LDL) deposition through the walls of human arteries was studied by using a macroscopic porous medium approach. Different arteries were analyzed: a straight artery, a stenosed artery and the aorta-iliac bifurcation. Governing equations, with the appropriate boundary conditions, were solved by using both a numerical approach and an analytical approach.

Abstract

For the straight artery, Numerical modeling allowed to analyze the non-Newtonian fluid effects on the prediction of LDL deposition in different size straight artery. The above effects were studied by comparing various non-Newtonian fluid models and showed that a Newtonian fluid assumption can be used without introducing remarkable differences. An analytical approach was used to investigate LDL deposition in an arterial wall under hyperthermia and hypertension, obtaining a simplified analytical solution. Energy and species equations were coupled by means of the Ludwig-Soret effect. LDL accumulation under hyperthermia in a stenosed artery modeled with a cosinusoidal function was numerically analyzed. In all cases, hyperthermia and hypertension increase LDL accumulation. For the aorta-iliac bifurcation, a numerical 2-D study of non-Newtonian effects on LDL mass transport showed that the Newtonian fluid assumption is weak in presence of recirculation zones.

ACKNOWLEDGMENTS**ABSTRACT****SUMMARY****NOMENCLATURE**

1. INTRODUCTION	1
1.1. Open-cell foams: a key to enhance heat transfer	3
1.2. The role of the porous media theory in biological systems	6
1.3. Present thesis	8
2. TRANSPORT PHENOMENA IN POROUS MEDIA	11
2.1. Basic conservation equations	12
2.2. Porous media governing equations: the Volume Averaging Technique (VAT)	16
<i>2.2.1. Basic definitions and theorems</i>	16
<i>2.2.2. Mass and momentum equations</i>	18
<i>2.2.3. Energy equations</i>	20
<i>2.2.4. Species equations</i>	23
2.3. The closure problem in the volume-averaged governing equations	24
3. FLUID FLOW AND HEAT TRANSFER IN OPEN-CELL FOAMS	27
3.1. Basic definitions	28
3.2. Manufacturing techniques	28
3.3. Morphology of an open-cell foam	30
<i>3.3.1. Real foams</i>	32
<i>3.3.2. Ideal foams</i>	33
3.4. State-of-art	36
<i>3.4.1. Pressure drop</i>	36
<i>3.4.2. Convection heat transfer</i>	40
3.5. An experimental approach to the closing coefficients	44
<i>3.5.1. Description of the experimental apparatus</i>	44
<i>3.5.2. Experimental determination of the closing coefficients</i>	46
<i>3.5.3. Results</i>	48

Summary

3.5.3.1. <u>Pressure drop</u>	48
3.5.3.2. <u>Convection heat transfer</u>	50
3.6. Predictive models for the closing coefficients	52
3.6.1. <i>Foam geometry reconstruction</i>	52
3.6.1.1. <u>Real model: the RVE theory</u>	52
3.6.1.2. <u>Ideal model: generating the foam</u>	57
3.6.2. <i>Mathematical model</i>	59
3.6.3. <i>Results</i>	63
3.6.3.1. <u>Data reduction</u>	63
3.6.3.2. <u>Results for the real model</u>	65
3.6.3.3. <u>Results for the ideal model: thermally developing effects</u>	67
3.6.3.4. <u>Results for the ideal model: strut shape effects</u>	74
3.7. Engineering applications of open-cell foams	77
3.7.1. <i>Concentrated Solar Power (CSP)</i>	77
3.7.1.1. <u>Description of the technology: the volumetric solar receiver</u>	77
3.7.1.2. <u>Mathematical model</u>	79
3.7.1.3. <u>Results</u>	81
3.7.2. <i>Heat sinks</i>	83
3.7.2.1. <u>Metal-foam based heat sinks for electronic cooling</u>	83
3.7.2.2. <u>Mathematical model</u>	85
3.7.2.3. <u>Results</u>	87
4. BIOLOGICAL SYSTEMS: A POROUS-MEDIA BASED APPROACH	91
4.1. The cardiovascular system	92
4.1.1. <i>General description</i>	92
4.1.2. <i>Anatomy of an artery</i>	95
4.1.3. <i>Atherosclerotic plaque growth process</i>	97
4.2. Modeling Low-Density Lipoprotein (LDL) transport: state-of-art	100
4.2.1. <i>Wall-free and monolayer models</i>	100
4.2.2. <i>Multilayer models</i>	102
4.3. Straight artery	104
4.3.1. <i>Mathematical model</i>	104
4.3.2. <i>Numerical approaches</i>	111

<u>4.3.2.1. Non-Newtonian effects</u>	111
4.3.3. <i>Analytical approaches</i>	116
<u>4.3.3.1. Deriving a simplified analytical solution</u>	116
<u>4.3.3.2. Hypertension and hyperthermia effects</u>	127
4.4. Stenosed artery	129
4.4.1. <i>Mathematical model</i>	130
4.4.2. <i>Hyperthermia effects</i>	132
4.5. Aorta-iliac bifurcation	134
4.5.1. <i>Mathematical model</i>	134
4.5.2. <i>Non-Newtonian effects</i>	135
CONCLUSIONS	141
REFERENCES	145

NOMENCLATURE

Symbol	Name	Units
Latin letters		
A	cross-section area	m^2
A	fitting coefficient (Eq. (48))	$Pa\ s/m^2$
A	particular solution polynomial (Eq. (78))	
B	fitting coefficient (Eq. (48))	$Pa\ s^2/m^3$
\mathbf{B}	coefficients matrix	
c	concentration	mol/m^3
c_1, c_2	constant coefficients	
C	Forchheimer coefficient	$1/m$
C_D	discharge coefficient	
C_p	heat capacity at constant pressure	$J/kg\ K$
d	size	m
D	diffusivity	m^2/s
D	duct diameter	m
Da	Darcy number	
\mathbf{e}	known terms vector	
f	inertial coefficient	
\mathbf{g}	unknowns vector	
h	enthalpy	J/kg
h_c	heat transfer coefficient (Eq. (17))	$W/m^2\ K$
h_v	volumetric heat transfer coefficient (Eq. (17))	$W/m^3\ K$
H	curvature (Eq. (2))	$1/m$
H	heat sink height (Fig. 63)	m
I	radiative intensity (Eq. (19))	W/m^2
\mathbf{j}	mass flux	$mol/m^2\ s$
k	thermal conductivity	$W/m\ K$
k	first-order reaction rate (Eq. (26))	$1/s$
k'	moles reacted per unit volume (Eq. (8))	$mol/m^3\ s$
k_T	thermodiffusion coefficient	
K	permeability	m^2
\mathbf{K}	permeability tensor	m^2
K^*	power-law permeability (Eq. (66))	m^2
L	length	m
Le	Lewis number	
m	mass fraction (Eq. (6a))	

Nomenclature

M	molecular weight (Eq. (7))	g/mol
\mathbf{n}	normal vector	
N	number of elements (Eq. (51a))	
n	power-law index	
Nu	Nusselt number	
Nu_v	volumetric Nusselt number	
p	pressure	Pa
p	order of accuracy (Eq. (51b))	
Pe	Peclet number	
Pr	Prandtl number	
q	isoperimetric coefficient (Fig. 14)	
q	Carreau-Yasuda coefficient	
\mathbf{q}	heat flux	W/m ²
Q	heat rate	W
r	radius	m
Re	Reynolds number	
R	grid refinement coefficient (Eq. (51a))	
R	universal gas constant (Eq. (6a))	J/mol K
s	fin spacing (Fig. 63)	m
s_2	two-point correlation function (Eq. (32))	
S	surface area	m
S/V	specific surface area	1/m
t	time	s
t	tapering factor (Fig. 27)	
t	fin thickness (Fig. 63)	m
T	temperature	K
\mathbf{T}	stress tensor	N/m ²
u, v	velocity vector components	m/s
u_c	combined standard uncertainty (Eq. (47))	
\mathbf{u}	velocity vector	m/s
v	filtration velocity	m/s
V	volume	m ³
W	heat sink side	m
x	molar fraction (Eq. (6a))	
x, y, z	cartesian coordinates	m
Greek letters		
α	thermal diffusivity	m ² /s
β	extinction coefficient	1/m

β	foam shape factor (Fig. 27)	
β_λ	spectral extinction coefficient	1/m
γ	surface tension (Eq. (2))	N/m
$\dot{\gamma}$	shear rate	1/s
δ	stenosis severity	
ε	porosity	
ε	gas expansibility factor (Eq. (48))	
ε	emissivity (Fig. 55)	
θ	angle	
κ_λ	spectral absorption coefficient (Eq. (19))	1/m
λ	wavelength	m
λ	relaxation time	s
$\lambda_{1,2}$	eigenvalues	
μ	viscosity	kg/m s
μ	mean (Fig. 30)	
μ^*	fluid consistency index	Pa s ⁿ
π	osmotic pressure	Pa
ρ	density	kg/m ³
σ	Stefan-Boltzmann constant (Fig. 55)	W/m ² K ⁴
σ	standard deviation (Fig. 30)	
σ_0	osmosis selective permeability	
σ_s	Staverman reflection coefficient	
σ_λ	spectral scattering coefficient (Eq. (19))	1/m
τ	shear stress	Pa
τ	tortuosity	
ϕ	generic variable	
ψ_λ	scattering phase function (Eq. (19))	
Subscripts		
∞	infinite shear rate	
0	ambient/reference	
b	black body	
c	cell	
C	cold	
<i>circ</i>	circle (Fig. 27)	
<i>dom</i>	computational domain	
<i>eff</i>	effective	

Nomenclature

<i>f</i>	fluid
<i>h</i>	hydraulic
<i>H</i>	hot
<i>i, j</i>	indexes
<i>in</i>	inlet
<i>j</i>	junction
<i>lumen</i>	lumen
<i>M</i>	mean
<i>out</i>	outlet
<i>p</i>	fin (Fig. 63)
<i>p</i>	pore
<i>r</i>	radiative
<i>REF</i>	reference
<i>REV</i>	Representative Elementary Volume
<i>RVE</i>	Representative Volume Element
<i>s</i>	solid
<i>s</i>	strut (Eq. (34))
<i>st</i>	stenosis
<i>T</i>	thermally developed
<i>w</i>	wall
<i>z</i>	zero shear rate
Superscripts	
*	dimensionless
-	spatial deviation
<i>a</i>	advective (Eq. (60))
<i>D</i>	diffusive (Eq. (60))
<i>end</i>	endothelium
<i>f</i>	fluid
<i>i</i>	index
<i>IEL</i>	Internal Elastic Lamina
<i>int</i>	intima
<i>med</i>	media
<i>s</i>	solid
<i>T</i>	transpose (Eq. (4b))
<i>T</i>	thermal
Other	
<>	average

Frequent acronyms

<i>CV</i>	Coefficient of Variation	
<i>LDL</i>	Low-Density Lipoprotein	
<i>LTE</i>	Local Thermal Equilibrium	
<i>LTNE</i>	Local Thermal Non-Equilibrium	
<i>PPI</i>	Pores Per Inch	1/in
<i>RE</i>	Richardson Extrapolation	
<i>REV</i>	Representative Elementary Volume	
<i>RVE</i>	Representative Volume Element	
<i>WSS</i>	Wall Shear Stresses	Pa
<i>xCT</i>	x-ray Computed Tomography	

1.

INTRODUCTION

1. INTRODUCTION

The word “pore” derives from the ancient greek “πόρος”, that means “passage”. This word is also similar to “πείρω”, that means “passing through”. This gives the sense of what is meant as porous. A porous material is a material that is not perfectly compact, with many voids. [1]. It is possible to find porous materials everywhere: ground, sand, rocks are porous (Fig. 1). Porous materials are two-phase media, made up by a solid matrix and a fluid that fills the pores.

Various length scales for a porous medium can be identified (Fig. 2). Starting from the Brinkman screening distance \sqrt{K} , where K is the permeability, it is possible to define a pore size, d_p , a Representative Elementary Volume (REV) size, L_{REV} , and a linear dimension of the system, L , [2]:

$$\sqrt{K} \ll d_p < L_{REV} \ll L \quad (1)$$

The Representative Elementary Volume is defined as the smallest volume characterized by the local average properties, with a particular reference to the porosity [2]. This volume must be large enough, in order to avoid microscale effects on averaged properties, and small enough, to appreciate their spatial dependence. The above constraints are satisfied by small enough REV's for the majority of porous media of practical importance [3].

Due to its complex geometry, analyzing transport phenomena in a porous medium at every scale is challenging. For macroscopic porous media, the most used technique treats the whole porous medium as an equivalent homogeneous medium. However, this approach needs experiments or pore-scale analysis to close governing equations of the equivalent medium. Due to the increasing computational capacity, more detailed pore-scale analyses have been performed worldwide only recently [2].



Fig. 1. Examples of porous materials.

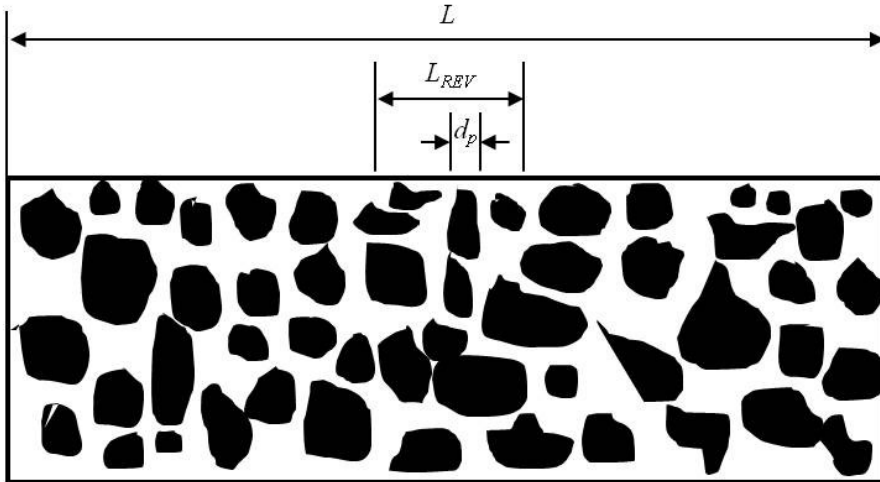


Fig. 2. Various length scales of a porous medium.

Transport in porous media has received a growing attention by the scientific community in the last years. Various books have been written on this subject, among which *Principles of Heat Transfer in Porous Media* [4], *Convection in Porous Media* [5], *Handbook of Porous Media* [6], *Dynamics of Fluid in Porous Media* [7]. Very recently, the book *Porous Media: Applications in Biological Systems and Biotechnology* [8] deals on current and potential applications of porous media theory in modeling biological systems. Besides, the great interest of the scientific community in this topic is testified by three peer-reviewed journals entirely devoted to it: *Transport in Porous Media*, *Journal of Porous Media and Special Topics*, *Reviews in Porous Media*.

1.1. Open-cell foams: a key to enhance heat transfer

An example of a man-made porous material is an open-cell foam. It is characterized by a relatively high ratio of the volume of the voids to the total volume of the porous material. Open-cell foams differ from closed-cell foams because the voids communicate each other. Though they are a man-made material, respecting some defined laws, foams are so named since they resemble foams available in nature. Such laws are Plateau's laws, which had been derived by the Belgian scientist Joseph Plateau in 1873 [9]. For an ideal foam, a necessary and sufficient condition that ensures mechanical equilibrium is that foams have to verify three laws, for faces, edges and vertices, respectively [10].

For the faces, the soap films have a constant average curvature, and they are smooth. Their curvature is ruled by Young-Laplace law:

Introduction

$$\Delta p_{i,j} = 2 \gamma \langle H_{i,j} \rangle = 2 \gamma (1/r_{1,i,j} + 1/r_{2,i,j}) \quad (2)$$

where $\Delta p_{i,j}$ is the pressure difference between two bubbles i and j , γ is the surface tension, $\langle H_{i,j} \rangle$ the mean curvature of the film that separates bubbles i and j , and $r_{1,i,j}$ and $r_{2,i,j}$ are the two principal radii of curvature of the film, respectively.

For the edges equilibrium, angles of $\arccos(-1/2) = 120^\circ$ are formed between the soap films, that meet in threes along edges (or Plateau borders).

For the equilibrium of vertices, angles of $\arccos(-1/3) \approx 109.5^\circ$ are formed between four edges, that meet at vertices [10]. If these laws are not respected by means of an infinitesimal perturbation, then all the films will rearrange in order to respect these laws. It is also important to observe that such laws are strictly valid for a dry foam, that is a foam with edges. Man-made foams are usually wet foams, in which the edges are thickened by the solid material. Plateau's laws for wet foams should remain valid, at least approximately [10]. A SEM image of an open-cell foam, with a sketch of Plateau's laws, is reported in Fig.3.

Foams can be also classified with reference to the solid matrix material. The most diffused solid matrix is polyurethane. Polyurethane was invented by Bayer [11], while he was working for IG Farbenindustrie AG, from the condensation

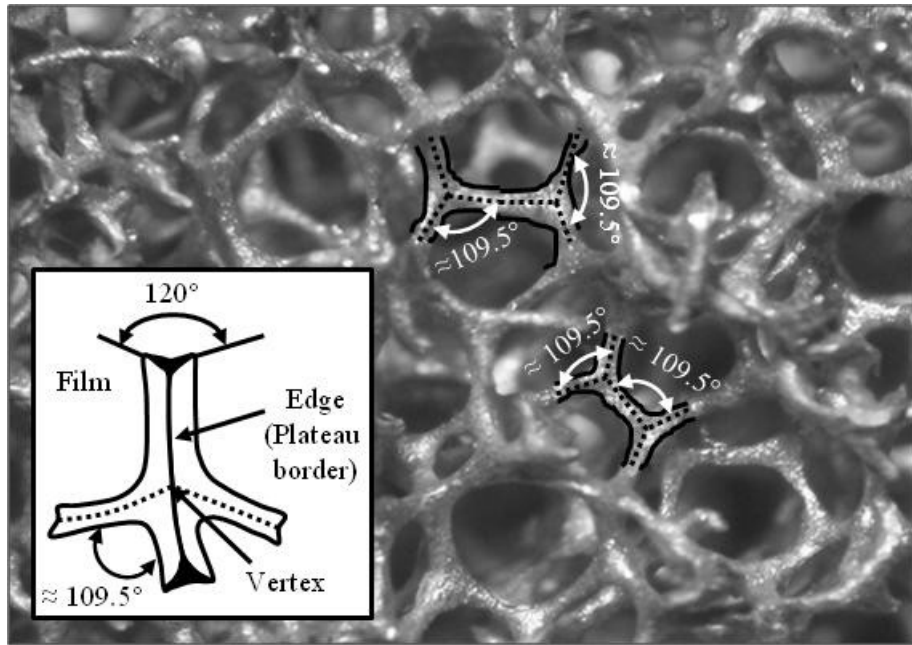


Fig. 3. SEM of an open-cell foam (wet foam) with a sketch of Plateau's laws.

of two monomers, difunctional hexane diisocyanate and 1,4-butanediol [12]. When there is a trace of water in the reactants, carbon dioxide gas is produced from the chemical reaction. This CO₂ forms many small empty areas in the final product, obtaining a polyurethane foam [12]. A very important contribution to the polyurethane foams development was given by Volz [13], while he was working at Scott Paper Company. He patented a route to manufacture a reticulated foam, that was a pretty regular low-density foam with open pores. Other solid matrixes can be used, for example a metallic matrix made with aluminum, copper or other metals. As reported by Banhart [14], the first mention of metal foaming was made by De Meller [15]. A development of this process was patented by Elliott [16]. Many foaming techniques were proposed during the years, and research is still carried out, not only to improve foam properties but also to reduce its costs [14]. Ashby reported that the price of a metal foam can vary from 7 to 12,000 \$/kg [17].

Foams can also be made up by a ceramic material as the solid matrix, for example the silicon carbide SiC. Binner [18] reported that the first patent had been issued by Schwartzwalder and Somers [19]. Nowadays, several manufacturing routes are available. An innovative technique has been developed by Ortona et al. [20]. They proposed the indirect production of a ceramic foam starting from a combination of 3D printing of polymer inks with replication. Open-cell metal and ceramic foams are represented in Fig. 4. Glass and cement have also been proposed [21].

Both closed-cell and open-cell foams have lots of applications. Depending on their solid matrix, the advantages are low density, acoustic and vibration damping, relatively high or low thermal and electrical conductivities, resistance to corrosion and oxidation, stability at high temperatures, thermal and electromagnetic shielding [22]. Focusing only on metal or ceramic open-cell foams, some applications [22, 23] are reported in the following. Metal foams can be used in the automotive sector in the crash element or as diesel particulate filters. In the aerospace sector, they can be used as tailbooms of helicopters, as CO₂ scrubbers, as bearing structures or as thermal, electromagnetic and microsatellite shields. In the biomedical sector, due to their geometry, metal foams can be used for orthopedic or dental implants. In buildings, they can be used for sound absorption, or for the protection from fire and electromagnetic fields. Fuel cells can also be equipped with a metal foam.

Apart from the various fields of applications, particular attention needs to be paid to open-cell foams when heat transfer needs to be enhanced. In this case, the advantages are the complex internal geometry that favors flow mixing, the

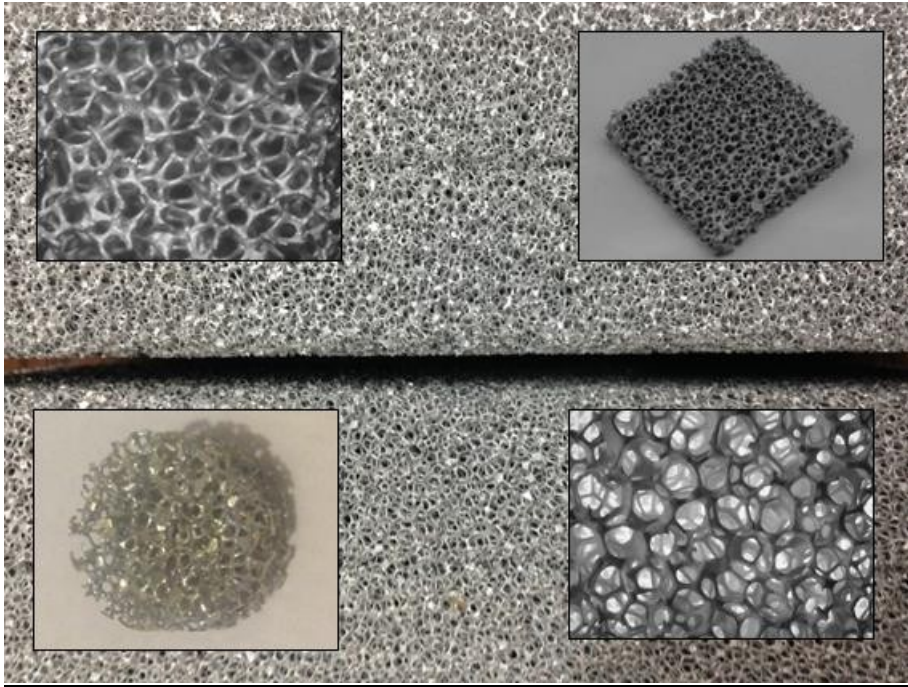


Fig. 4. Background, upper left and lower left: metal open-cell foams;
Upper right and lower right: ceramic foams.

high heat transfer surface to total volume ratio and the relatively high thermal conductivity. Metal foams can be employed as heat exchangers, heat sinks, burners, Phase Change Materials (PCM), heat pipes or volumetric receivers for Concentrated Solar Power (CSP) or hydrogen production. Due to their high performances at high temperatures, ceramic foams can be used for high temperature filters and heat exchangers, burners, or for volumetric receivers for hydrogen production or for CSP. Some applications are reported in Fig. 5.

1.2. The role of the porous media theory for biological systems

From the above mentioned definition of a porous medium, it is possible to conclude that porous media can be found more easily than one can imagine. One of the most straightforward examples is a biological system. Indeed, many of these can be considered as porous materials. For example, porous media theories can be applied to marine biological modeling, like the nutrient that are released into seawater from sinking marine aggregates, the tortuosity of marine sediments, or the transport activities caused by burrowing macrozoobenthos species [25]. Other examples are the biofilms, that are complex aggregation of

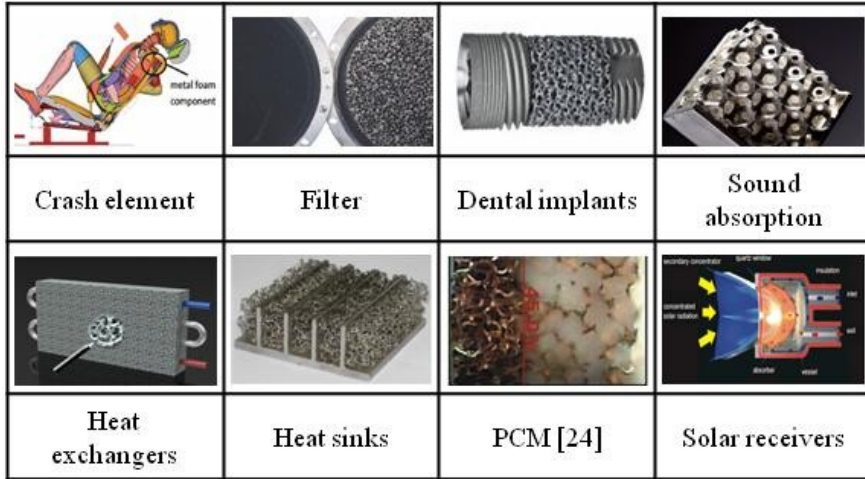


Fig. 5. Examples of open-cell foams.

microorganisms growing on a solid substrate [8]. They can be helpful in bioremediation, and damaging in other cases, such as water pipes.

For the human body, some applications can be here mentioned. Many human tissues and organs can be treated as porous media [8]. Some phenomena that can be studied with a porous media approach are diffusion in brain tissues, Magnetic Resonance Imaging (MRI) to characterize tissue properties, blood flow in tumors, drug delivery [26, 27]. In tissue engineering, porous scaffolds can be used as the template for the growth of the cells, leading to the formation of an artificial tissue. Heat transfer in the human body can also be modeled by means of a porous media approach. This is very important for hyperthermia in treating tumors, laser eye surgery, venous diseases or other applications. In hyperthermia, necrosis in the tissues is induced by a thermal dose. It is widely used in liver cancers, and also for esophagus or lung cancers. Various techniques are used [28]. In the radiofrequency thermal ablation, a needle is put on the tumor lesion. Electromagnetic radiations are generated at a frequency of about 500 kHz. An alternate current passes through the tissue, close to the needle, causing heating due to ions agitation. The best necrosis can be induced when the temperature of the tissue ranges between 70 °C and 95 °C, for 4-6 minutes [28]. A technique that seems to be more advantageous is the microwave thermal ablation. Differently from the radiofrequency-based technique, it is based on very high frequency electromagnetic waves (about 2450 MHz). With such frequencies, the electrode starts to act like an antenna, causing the agitation of water molecules, heating the tissue. The advantage is that there is no current

Introduction

passage through the patient body. Other techniques are used, like the laser thermoablation. However, the first two mentioned are the less invasive. Because local temperatures have a main role, the accurate knowledge of temperature fields is very important, in order to apply the thermal dose that damages as less as possible healthy tissues. Nakayama and Kuwahara [29] were the first that recently developed a model of bioheat transfer based on the theory of porous media. They identified the two phases of the porous media as the tissue and the blood vessels.

The part of the human body that has been modeled most recently with a porous-media based approach is the arterial wall. It is divided into various porous layers and predictions on macromolecule transport through it are carried out. This way, transport of macromolecules, such as High-Density Lipoprotein (HDL) or Low-Density Lipoprotein (LDL) is studied, in order to investigate with a good accuracy how deposition occurs on an arterial wall. A resume of porous media applications in biological systems is depicted in Fig. 6.

1.3. Present thesis

Open-cell foams and biological systems, in particular the arterial wall, are studied in the present thesis.

Governing equations for transport in porous media are introduced in Chapter 2. Mass, momentum, energy and species equations are obtained by means of the Volume Averaging Technique (VAT), with which the macroscopic porous media is treated as a homogeneous equivalent medium. The closure problem in the volume-averaged governing equations is discussed.

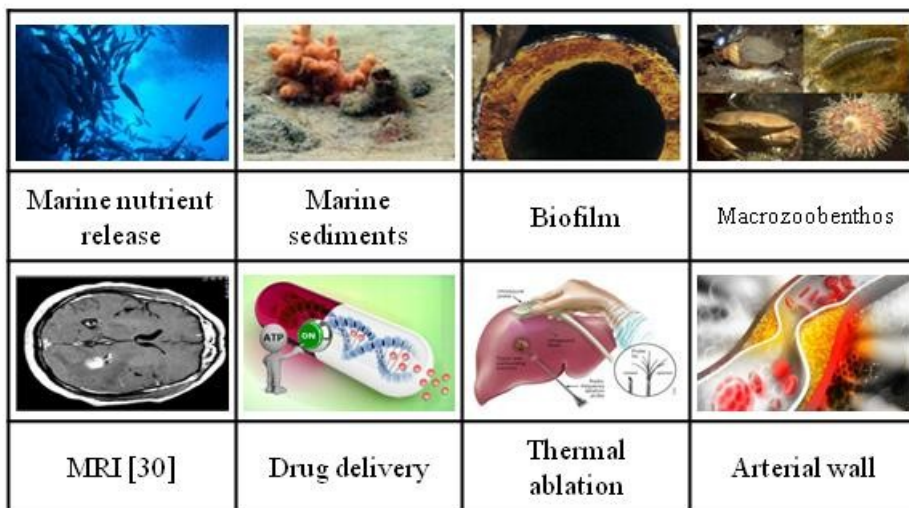


Fig. 6. Applications of porous media to biological systems.

Fluid flow and heat transfer in open-cell foams are analyzed in Chapter 3. Production techniques, microstructure, and geometrical reconstruction techniques of open-cell foams are first presented. The chapter is subdivided into two parts: pressure drop and convection heat transfer are first studied, in order to obtain closing coefficients; then, open-cell foams in some industrial applications are modeled with a macroscopic porous media approach. In the first part, the literature on forced convection and pressure drop is reviewed and experimental and numerical results for the determination of closing coefficients are presented. In the second part, some examples of open-cell foams industrial applications, such as CSP and heat sinks.

Porous media concepts are applied to a biological system, in particular to an artery, in Chapter 4. Anatomy of the artery and the atherosclerotic plaque growth process are introduced. LDL transport in an artery is predicted, using a multi-layer porous model for the wall. Analytical and numerical solutions are developed for a straight artery, accounting for hypertension, hyperthermia and non-Newtonian rheology effects on mass transport. Different artery geometries are also numerically analyzed. For a stenosed artery, hyperthermia effects are also included in the model, while, for the aorta-iliac bifurcation, non-Newtonian effects on mass transport are analyzed.

The aim of the work described in this thesis is to provide useful information on porous media transport. For the open-cell foams, closing coefficients can be used in various thermal applications, in order to improve predictive ability of macroscopic models. Macroscopic models have been derived and reported in the following with their advantages compared to conventional technologies. For the biological systems, the studies on LDL mass transport in an artery through the wall will provide important information in understanding the atherosclerosis process. Topics investigated in the present thesis are resumed in Fig. 7.

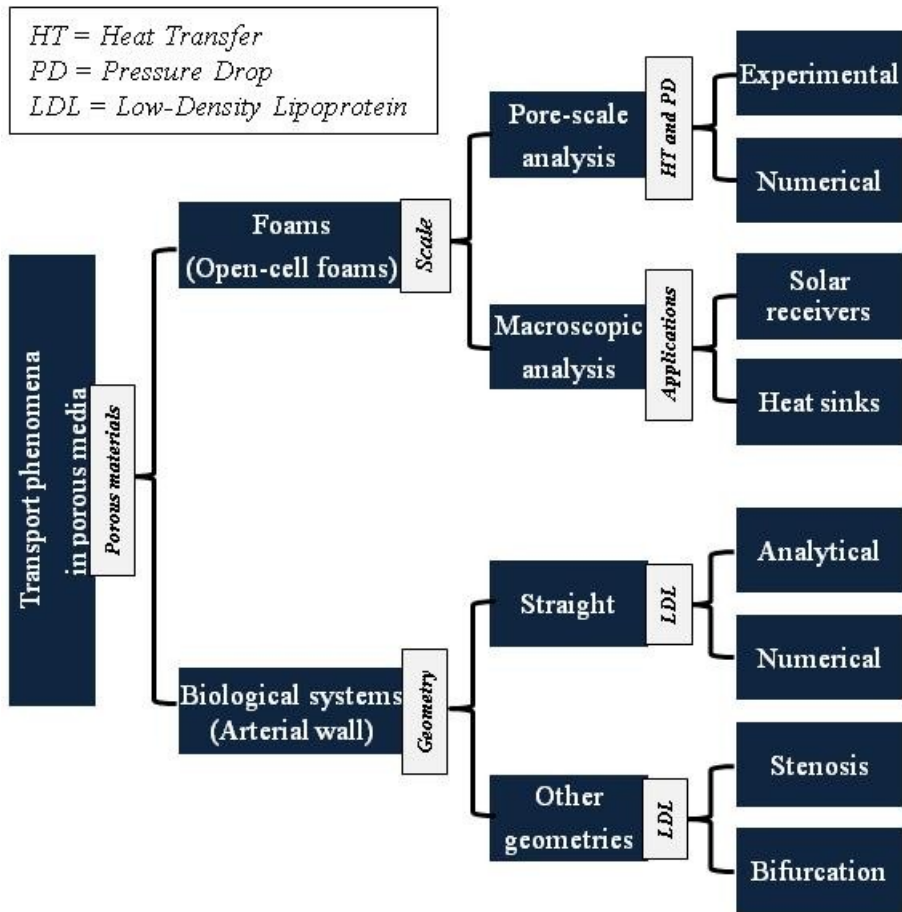


Fig. 7. Topics investigated in the present thesis

2.

**TRANSPORT PHENOMENA
IN POROUS MEDIA**

2. TRANSPORT PHENOMENA IN POROUS MEDIA

Modeling of transport phenomena in porous media is presented in this chapter. Single-phase conservation equations for mass, momentum, energy and species are presented. It will be shown how the Volume Averaging Technique (VAT) can be used to write such equations for an equivalent single-phase porous media. Finally, the closure problem for these equations is introduced with some examples.

2.1. Basic conservation equations

Mass, momentum, energy and species equations for a fluid are presented in a differential form. Energy equation will be also presented for a solid and for a fixed control volume, V .

The mass conservation law is

$$\frac{\partial \rho}{\partial t} + \nabla \cdot \rho \mathbf{u} = 0 \quad (3a)$$

where ρ is the fluid density, t the time and \mathbf{u} the fluid velocity vector. The two terms in the equation are the transient and the advective term, When the flow is stationary compressible, Eq.3a becomes

$$\nabla \cdot (\rho \mathbf{u}) = 0 \quad (3b)$$

When the flow is stationary incompressible, it becomes

$$\nabla \cdot \mathbf{u} = 0 \quad (3c)$$

The momentum equation, derived from the application of Newton's second law on a fluid element, is:

$$\rho \left(\frac{\partial \mathbf{u}}{\partial t} + \mathbf{u} \cdot \nabla \mathbf{u} \right) = -\nabla p + \nabla \cdot \mathbf{T} + \mathbf{f} \quad (4a)$$

where p is the pressure, \mathbf{T} is the stress tensor, \mathbf{f} is a body force per unit volume and μ is the dynamic viscosity. The two terms on the left side are the transient and the advective term, that represent the inertial terms. The first two terms on the right side account for the stresses effects in the fluid; the third term represents body forces, for example the gravity force.

When the flow is Newtonian compressible, with $\mathbf{f} = 0$, Eq.(4a) becomes:

$$\rho \left(\frac{\partial \mathbf{u}}{\partial t} + \mathbf{u} \cdot \nabla \mathbf{u} \right) = -\nabla p + \nabla \cdot \left(\mu \left(\nabla \mathbf{u} + (\nabla \mathbf{u})^T \right) \right) - \nabla \left(\frac{2}{3} \mu \nabla \cdot \mathbf{u} \right) \quad (4b)$$

where the superscript T stands for transpose.

When the flow is Newtonian incompressible, Eq.(4b) becomes

$$\rho \left(\frac{\partial \mathbf{u}}{\partial t} + \mathbf{u} \cdot \nabla \mathbf{u} \right) = -\nabla p + \mu \nabla^2 \mathbf{u} \quad (4c)$$

When the flow is Newtonian stationary incompressible, Eq. (4c) becomes

$$\rho \mathbf{u} \cdot \nabla \mathbf{u} = -\nabla p + \mu \nabla^2 \mathbf{u} \quad (4d)$$

The pressure and velocity flow fields can be determined when the above mass and momentum equations are coupled with the appropriate boundary conditions.

The temperature field is obtained introducing the energy equation. It is derived from the first law of thermodynamics, applied on an elementary fluid element. For a pure substance, neglecting the viscous dissipation effects, we can write:

$$\rho \left(\frac{\partial h}{\partial t} + \mathbf{u} \cdot \nabla h \right) = \nabla \cdot (k \nabla T) + \left(\frac{\partial p}{\partial t} + \mathbf{u} \cdot \nabla p \right) + \frac{Q}{V} \quad (5a)$$

where h is the specific enthalpy, k is the thermal conductivity, Q is the heat power, and C_p is the heat capacity at constant pressure of the fluid. Equation (5a) balances the enthalpy variation, the heat transferred, the energy increase due to the compression and the internal energy generation.

Equation (5a) reduces to Eq. (5b) when there is no internal energy generation and pressure gradients effects on temperature can be neglected.

$$\rho C_p \left(\frac{\partial T}{\partial t} + \mathbf{u} \cdot \nabla T \right) = \nabla \cdot (k \nabla T) \quad (5b)$$

In steady-state conditions Eq. (5b) reduces to:

$$\rho C_p \mathbf{u} \cdot \nabla T = \nabla \cdot (k \nabla T) \quad (5c)$$

Finally, for a steady-state solid or retained fluid Eq. (5c) becomes:

$$\nabla^2 T = 0 \quad (5d)$$

A particular case of the energy equation is reported in the following. Dufour [31] found out that concentration gradients can induce heat transfer in a multicomponent mixture, then named Dufour effect. Even if it is often negligible [32], it can play a role in areas such as hydrology, petrology and geosciences [33]. The Dufour effect can be described by using the nonequilibrium thermodynamics [34]. A comprehensive description of the Dufour effect was given by Bird et al. [35]. The heat flux \mathbf{q} for a binary mixture can be expressed as:

$$\mathbf{q} = -k \nabla T + \sum_{i=1}^N h_i \mathbf{j}_i + \sum_{i=1}^N \sum_{\substack{j=1 \\ j \neq i}}^N \frac{c R T x_i x_j}{\rho_i} \frac{k_T \rho_i D_{ij} m_i m_j}{x_i x_j D_{ij}} \left(\frac{\mathbf{j}_i}{\rho_i} - \frac{\mathbf{j}_j}{\rho_j} \right) \quad (6a)$$

where \mathbf{j}_i is the mass flux referred to the i -species, provided by Fick's law of diffusion

$$\mathbf{j}_i = -\rho D_{ij} \nabla m_i = \rho_i (\mathbf{u}_i - \mathbf{u}_{REF}) \quad (6b)$$

c is the concentration of the mixture; R is the universal gas constant; x_i and m_i are the molar and the mass fraction of the i -component, respectively; k_T is the thermo-diffusion coefficient; D_{ij} is the mass diffusivity of the species i through j ; \mathbf{u}_i is the velocity of the species i ; \mathbf{u}_{REF} is a reference velocity, that often is the mass average velocity. It is worth noticing that in Eq. (6a) the Maxwell-Stefan diffusivities are correlated to Fick mass diffusivities D_{ij} via the term $x_i x_j / m_i m_j$. In Eq. (6a), the first term is the heat conduction term, the second is the heat diffusion term, that accounts for the heat transport each diffusing species, the third term is the Dufour term, that depends on the mass fluxes. Besides, the term in parenthesis can be also expressed as $(\mathbf{u}_i - \mathbf{u}_j)$, that is the relative velocity of diffusion between the two species.

Equation (6a) can be further modified. Let's consider a solid-liquid binary mixture at almost constant pressure. The enthalpy can be expressed as $h = f(T, p)$; if the pressure is taken constant, $dh = C_p dT$, that becomes $\Delta h = C_p \Delta T$ for finite differences. Making reference to a zero-enthalpy state, the second term on the right side of Eq. (6a), combined with Eq. (6b), can be written as $-\rho_i C_p \mathbf{u}_i (T_i - T_{REF})$, with T_{REF} the reference temperature of the zero-enthalpy state and \mathbf{u}_i the net velocity of the species i . The third term on the right side of the equation can

be modified by using Eq. (6b) and some basics relationships of mass transfer. Finally Eq. (6a) can be rewritten as:

$$\mathbf{q} = -k \nabla T - \rho_i C_p \mathbf{u}_i (T_i - T_{REF}) - \frac{R T k_T \rho_i}{M} \frac{D_{ij}}{c_i} \nabla c_i \quad (7)$$

where M is the molecular weight of the mixture.

In a mixture, the mass transfer is due to the movement of particles of a given species through it, driven by the concentration gradient of the species. It is ruled by Fick's law of diffusion (Eq. (6b)), that has a strong analogy with Fourier's law for heat conduction. For each component, it is possible to write a species-conservation equation, that reminds of energy equation (Eq. (6b)):

$$\frac{\partial c_i}{\partial t} + \nabla \cdot (c_i \mathbf{u}) = D_{ij} \nabla^2 c_i + k' \quad (8)$$

where k' refers to the rate of production or destruction of moles of i per unit volume. This equation is valid if the Fick diffusivity D_{ij} is homogeneous and isotropic. It is important to observe that the velocity term refers to the molar average velocity [35]. Indeed, different chemical species move at different velocities through a mixture, thus a molar average velocity is needed.

In the species equation, the counterpart for the Dufour effect is the Ludwig-Soret effect. This effect was first observed by Carl Ludwig for liquids [36] and was named only later by Soret [37]. The experiment performed by Soret consisted in a tube of salt water, where the two extremities were at different temperatures. He observed that the salt tends to migrate from the hot end to the cold one, meaning that temperature has an effect on mass species transport. Like for the Dufour effect, if the Ludwig-Soret effect is taken into account, the mass flux \mathbf{j}_i of a mixture can be written by means non-equilibrium thermodynamics theories. If gradients of electrical potential and pressure effects on the mass flux are neglected, the following correlation can be written for a binary mixture:

$$\mathbf{j}_i = -D_{ij} \nabla c_i - \frac{\rho D_{ij} k_T \nabla \ln T}{M} = -D_{ij} \nabla c_i - \frac{\rho D_{ij} k_T}{M T} \nabla T \quad (9)$$

However, depending on the sign of the thermo-diffusion coefficient k_T , the species could tend to move either to the hot region or to the cold one [35], for example in some gaseous binary mixtures when temperature is lowered [38]. The thermo-diffusion coefficient k_T physically represents the importance of the mass flux due to the thermal diffusion compared to that due to molecular

diffusion. A typical value of k_T is 0.01 [38, 39]. Two comprehensive reviews of the Ludwig-Soret effect were carried out by Platten [40] and Rahman and Saghir [41].

2.2. Porous media governing equations: the Volume Averaging Technique (VAT)

Because of the complex geometry of porous media, it is very convenient to solve flow, temperature and chemical species fields making reference to the averaged form of transport governing equations. This is accomplished through the Volume Averaging Technique (VAT), that was introduced by many authors simultaneously [42 – 45]. It allows to go through averaged transport equations, that are valid for an equivalent single-phase porous medium.

In the following basic definitions of VAT technique are first introduced; then governing equations presented in Subsection 2.2 will be introduced for a porous medium, highlighting the closure problem.

2.2.1. Basic definitions and theorems

Let us consider a flow through a porous medium, with a velocity modulus $|\mathbf{u}|$. The scale that is represented for a Representative Elementary Volume (REV) is larger than the pore scale, but far smaller than the whole macroscopic porous medium scale ($d < L_{REV} \ll L$), as reported in Eq. (1) and sketched in Fig.8.

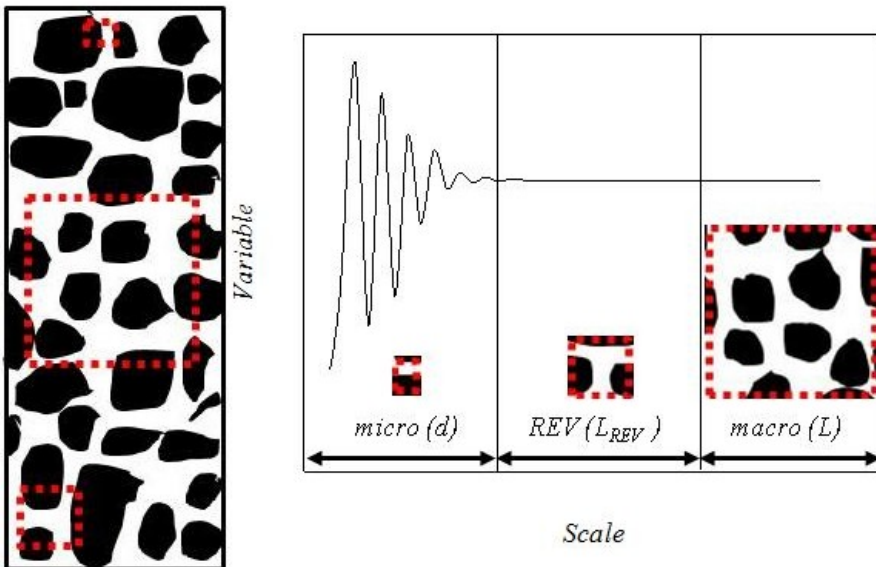


Fig. 8. Porous media scales: from micro (d) to macro (L).

Velocity and pressure fields can be solved simultaneously with appropriate boundary conditions. However, the complex geometry makes the problem difficult to be solved analytically. Moreover, a numerical solution would be also rather difficult, due to the large number of elements required. This is schematically resumed in Fig. 9.

A way to solve the problem is to average the governing equations on the REV. By doing this for all REV in a macroscopic porous medium, it is easy to evaluate the flow and temperature fields. Due to the increasing computational capacity, pore-scale methods are recently playing a more important role in transport through porous media [2].

The first step in the volume-averaging process is the definition of a local volume average and its intrinsic volume average. The porosity, ε , of a porous medium, made up by voids and solid, is defined as the ratio of the volume of the voids, V_f , to the total volume of the porous medium, $V = V_f + V_s$, with V_s the volume of the solid; thus: $\varepsilon = V_f/V$. The local volume average of a generic variable ϕ and its intrinsic volume average, $\langle \phi \rangle^f$, averaged over V_f , are so correlated:

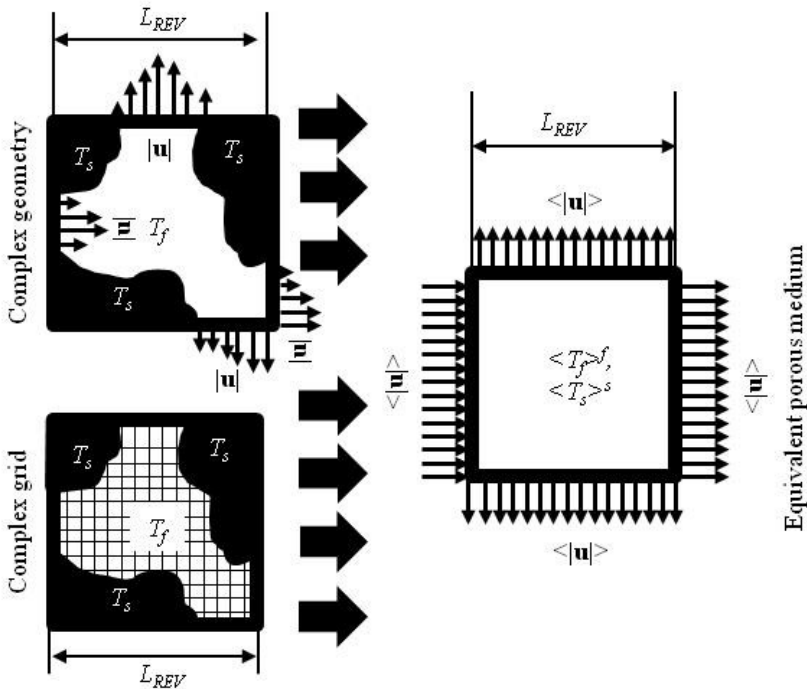


Fig. 9. Velocity distribution in a Representative Elementary Volume of the porous medium.

$$\langle \phi \rangle = \frac{1}{V} \int_{V_f} \phi \, dV = \varepsilon \langle \phi \rangle^f \quad (10)$$

The same process is performed for the solid phase, averaging variables over V_s and replacing ε by $1 - \varepsilon$. The volume averaging of transport equations requires the use of volume-averaged operators. Three theorems are presented: the volume averaged form of the transport theorem (Eq. 11a), the theorem for the volume average of a gradient (Eq. 11b), the theorem for the volume average of a divergence (Eq. 11c) [46, 47]:

$$\left\langle \frac{\partial \phi}{\partial t} \right\rangle = \frac{\partial \langle \phi \rangle}{\partial t} - \frac{1}{V} \int_S \phi \, \mathbf{u} \cdot \mathbf{n} \, dS \quad (11a)$$

$$\langle \nabla \phi \rangle = \nabla \langle \phi \rangle + \frac{1}{V} \int_S \phi \, \mathbf{n} \, dS \quad (11b)$$

$$\langle \nabla \cdot \mathbf{b} \rangle = \nabla \cdot \langle \mathbf{b} \rangle + \frac{1}{V} \int_S \mathbf{b} \cdot \mathbf{n} \, dS \quad (11c)$$

where \mathbf{b} is a generic vector. Another often made assumption is the decomposition of a variable into its intrinsic average and its spatial deviation [48], with which $\phi = \langle \phi \rangle^f + \bar{\phi}$ for a scalar and $\mathbf{b} = \langle \mathbf{b} \rangle^f + \bar{\mathbf{b}}$ for a vector. This assumption is very helpful in the averaging process, and it is often used by many authors [3, 49 – 51].

With this premise, the volume averaged form of mass, momentum, energy and species equations are derived in the following subsections.

2.2.2. Mass and momentum equations

The volume averaged general form of the continuity equation for a porous media is obtained by substituting Eqs. (11a) and (11c) in Eq. (3a):

$$\frac{\partial \langle \rho \rangle}{\partial t} + \nabla \cdot \langle \rho \mathbf{u} \rangle = 0 \quad (12a)$$

For a stationary compressible flow Eq.(12a) becomes:

$$\nabla \cdot \langle \rho \mathbf{u} \rangle = 0 \quad (12b)$$

and for a stationary incompressible flow Eq. (12b) becomes:

$$\nabla \cdot \langle \mathbf{u} \rangle = 0 \quad (12c)$$

The momentum equation, accounting for the microscopic effects of the solid matrix, can be derived either by the volume averaging of the momentum equation for a free fluid [3, 50] or with the homogenization technique [2] or with a semi-heuristic method [2, 52]. Among the above mentioned methods the volume averaging process is the most robust approach from a theoretical point of view. After using Eqs. (11a – 11c), the volume averaged form of the momentum equation (Eq. (4a)) becomes:

$$\rho \left(\frac{\partial \langle \mathbf{u} \rangle}{\partial t} + \langle \mathbf{u} \cdot \nabla \mathbf{u} \rangle \right) = -\nabla \langle p \rangle + \nabla \cdot \langle \mathbf{T} \rangle + \langle \mathbf{f} \rangle + \frac{1}{V} \int_S \mathbf{T} \cdot \mathbf{n} \, dA \quad (13)$$

where \mathbf{n} is a normal vector oriented from the solid to the fluid phase. Equation (13) allows the evaluation of the integral on the right side, that represents the microscopic effects of the solid matrix on the fluid. The theoretical derivation was performed by Whitaker [50]. From the well-established results from literature, considering also the case of a Newtonian fluid, it is possible to write the momentum equation [52, 53]:

$$\frac{\rho}{\varepsilon} \left(\frac{\partial \langle \mathbf{u} \rangle}{\partial t} + \nabla \cdot \frac{\langle \mathbf{u} \rangle \cdot \langle \mathbf{u} \rangle}{\varepsilon} \right) = -\nabla \langle p \rangle + \frac{\mu}{\varepsilon} \nabla^2 \langle \mathbf{u} \rangle + \langle \mathbf{f} \rangle - \frac{\mu}{\mathbf{K}} \langle \mathbf{u} \rangle - \frac{\rho f}{\sqrt{\mathbf{K}}} |\langle \mathbf{u} \rangle| \langle \mathbf{u} \rangle \quad (14a)$$

that, for incompressible flows, reduces to [52]:

$$\frac{\rho}{\varepsilon} \left(\frac{\partial \langle \mathbf{u} \rangle}{\partial t} + \frac{\langle \mathbf{u} \rangle}{\varepsilon} \cdot \nabla \langle \mathbf{u} \rangle \right) = -\nabla \langle p \rangle + \frac{\mu}{\varepsilon} \nabla^2 \langle \mathbf{u} \rangle + \langle \mathbf{f} \rangle - \frac{\mu}{\mathbf{K}} \langle \mathbf{u} \rangle - \frac{\rho f}{\sqrt{\mathbf{K}}} |\langle \mathbf{u} \rangle| \langle \mathbf{u} \rangle \quad (14b)$$

with \mathbf{K} the permeability, a third-order tensor, and f the inertial coefficient, that typically ranges between $10^{-2} \div 10^{-1}$ for open cell foams. In both equations, the left side represents the macroscopic inertial force, made up by a transient and an advective term, while, terms on the right side represent the pressure, the Brinkman macroscopic viscous shear stress [54], the Darcy microscopic viscous shear stress [55], and the Forchheimer microscopic inertial force [56]). The microscopic inertial force term is sometimes expressed in different forms [22]. It is important to remark that both macroscopical inertial force and viscous shear stress terms in Eqs. (14a) and (14b) are often negligible [50]. Besides, it is

worth noticing that Eq. (14b) can be applied to compressible fluids as long as Knudsen numbers are small enough [57].

The momentum equation for a porous medium reminds of Staverman-Kedem-Katchalsky equations for a membrane [58], that account also for osmosis. The osmotic pressure is defined as the minimum pressure of a solution that doesn't allow the solvent to pass through a semi-permeable membrane. The osmotic pressure, π , was defined by Van't Hoff as $\pi = R T c_i$. If reference is made to the selective permeability of the membrane to some solutes, σ_0 , [59], the osmosis can be taken into account by modifying Eq. (14b) into:

$$\begin{aligned} \frac{\rho}{\varepsilon} \left(\frac{\partial \langle \mathbf{u} \rangle}{\partial t} + \frac{\langle \mathbf{u} \rangle}{\varepsilon} \cdot \nabla \langle \mathbf{u} \rangle \right) &= -\nabla \langle p \rangle + \frac{\mu}{\varepsilon} \nabla^2 \langle \mathbf{u} \rangle + \langle \mathbf{f} \rangle - \frac{\mu}{\mathbf{K}} \langle \mathbf{u} \rangle - \\ &- \frac{\rho f}{\sqrt{\mathbf{K}}} |\langle \mathbf{u} \rangle| \langle \mathbf{u} \rangle + \sigma_o R T \nabla \langle c_i \rangle \end{aligned} \quad (15)$$

2.2.3. Energy equations

Energy equations for both solid and fluid phases are here presented. Two models for the energy equations can be used. The Local Thermal Equilibrium (LTE) model assumes the two phases to be in local thermal equilibrium. The Local Thermal Non-Equilibrium (LTNE) model accounts for a local convection heat transfer between the two phases. In the former case, only one energy equation is needed for both phases, while in the latter case two energy equations are needed, coupled by a convection heat transfer term. LTNE model equations are first presented in the following.

Volume averaging theorems reported in Eqs. (11a – 11c), with spatial decompositions, applied to Eq. (5b), allow to obtain, for both liquid and solid phases, respectively:

$$\begin{aligned} (\rho C_p)_f \left(\varepsilon \frac{\partial \langle T_f \rangle^f}{\partial t} + \langle \mathbf{u} \rangle \cdot \nabla \langle T_f \rangle^f \right) &= \nabla \cdot \left(k_{eff,f} \nabla \langle T_f \rangle^f \right) + \\ + \frac{1}{V} \int_S (k_f \nabla T_f) \cdot \mathbf{n} \, dS &+ \frac{1}{V} \int_S k_f T_f \cdot \mathbf{n} \, dS - \\ - \nabla \cdot \left(\varepsilon (\rho C_p)_f \langle \bar{\mathbf{u}} \rangle^f \langle T_f \rangle^f \right) & \end{aligned} \quad (16a)$$

$$\begin{aligned}
 (1-\varepsilon)(\rho C_p)_s \left(\frac{\partial \langle T_s \rangle^s}{\partial t} \right) &= \nabla \cdot (k_{eff,s} \nabla \langle T_s \rangle^s) + \frac{1}{V} \int_S (k_s \nabla T_s) \cdot \mathbf{n} \, dS - \\
 - \frac{1}{V} \int_S k_s T_s \cdot \mathbf{n} \, dS + \nabla \cdot \mathbf{q}_r
 \end{aligned} \tag{16b}$$

where the effective fluid thermal conductivity is $k_{eff,f} = \varepsilon k_f$ and the effective solid thermal conductivity can be expressed as $k_{eff,s} = (1 - \varepsilon)k_s/3$ for a foam [60] and as $k_{eff,s} = (1 - \varepsilon)k_s$ for a porous medium; the subscripts f and s refer to the fluid and solid phases, respectively.

Equation (16a) for the fluid phase has the transient and an advective term on the left side, while on the right there are the conduction, the interfacial convection, the thermal tortuosity and the thermal dispersion terms. On the left side of Eq. (16b) for the solid phase there is the transient term and on the right side there are the conduction, the interfacial convection, the thermal tortuosity and the divergence of the radiation flux $\nabla \cdot \mathbf{q}_r$ terms. The interfacial convection term recalls Newton's correlation:

$$\frac{1}{V} \int_S (k_f \nabla T_f) \cdot \mathbf{n} \, dS = h_c \frac{S}{V} (\langle T_s \rangle^s - \langle T_f \rangle^f) = h_v (\langle T_s \rangle^s - \langle T_f \rangle^f) \tag{17}$$

A volumetric heat transfer coefficient, $h_v = h_c (S/V)$, can, thus, be defined, with h_c the convection heat transfer coefficient and S/V the specific surface area. The thermal tortuosity and dispersion terms are often negligible; however, they can be modeled with a gradient diffusion assumption and included into the solid effective thermal conductivity term.

With such assumptions, energy equations for the stationary flow in the fluid and solid phases are, respectively:

$$(\rho C_p)_f \langle \mathbf{u} \rangle \cdot \nabla \langle T_f \rangle^f = \nabla \cdot (k_{eff,f} \nabla \langle T_f \rangle^f) + h_v (\langle T_s \rangle^s - \langle T_f \rangle^f) \tag{18a}$$

$$0 = \nabla \cdot (k_{eff,s} \nabla \langle T_s \rangle^s) - h_v (\langle T_s \rangle^s - \langle T_f \rangle^f) + \nabla \cdot \mathbf{q}_r \tag{18b}$$

Radiation effects in a porous medium can be investigated with a very simple approach, the Rosseland diffusive approximation [61], that assumes the medium to be optically thick. With this approximation, the equivalent radiative thermal conductivity k_r is included in the solid effective thermal conductivity $k_{eff,s}$.

A more accurate approach models the porous medium as a participating-medium, characterizing the radiation through a porous medium, starting from a balance of photons with wavelength, λ , direction, θ , intensity, $I(\lambda, x, \theta)$, in an elementary volume dx long. The intensity can vary in the elementary volume because of interactions between photons and material, that imply absorption, emission in the θ direction, outscattering in directions different from θ , and inscattering, that refers to the photons coming from other directions and reflected in θ direction. The balance, sketched in Fig. 10, is reported in the expression, known as Radiative Transfer Equation (RTE) equation:

$$\frac{\partial I(\lambda, x, \theta)}{\partial x} = -\langle \kappa_\lambda \rangle I(\lambda, x, \theta) + \langle \kappa_\lambda \rangle I_b(\lambda, x, \theta) [T(x)] - \langle \sigma_\lambda \rangle I(\lambda, x, \theta) + \frac{\langle \sigma_\lambda \rangle}{2} \int_{-1}^1 I(\lambda, x, \theta) \langle \psi_\lambda \rangle (\theta_i \rightarrow \theta) d\theta \quad (19)$$

where κ_λ is the spectral absorption coefficient, σ_λ is the spectral scattering coefficient, the subscript b stands for black body, and $\langle \psi_\lambda \rangle (\theta_i \rightarrow \theta)$ is the scattering phase function, that accounts for the angular distribution of the scattered energy. Equation (19) allows to evaluate the function $I(\lambda, x, \theta)$, that is correlated with the energy equation by defining a radiative heat flux \mathbf{q}_r . The expression of $\nabla \cdot \mathbf{q}_r$, for all wavelengths and a gray medium [61] is:

$$\nabla \cdot \mathbf{q}_r = \kappa (4\sigma T^4 - \int_{4\pi} I d\theta) \quad (20)$$

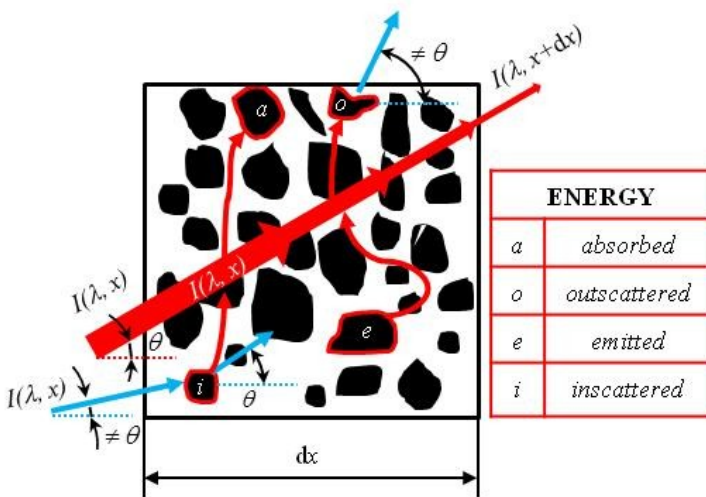


Fig. 10. Radiative energy balance for a dx long elementary volume.

A simplified form for the RTE can be derived when the radiation is assumed to be collimated. A collimated radiation occurs when the radiation that hits the participating medium make this with all light waves parallel among each other. In such case, for which Eq. (19) is written without considering inscattering from other directions and emission, it is possible to write:

$$\frac{\partial I(\lambda, x)}{\partial x} = -\langle \beta_\lambda \rangle I(\lambda, x) \quad (21)$$

with β_λ the coefficient of extinction, that is equal to $\langle \beta_\lambda \rangle = \langle \kappa_\lambda \rangle + \langle \sigma_\lambda \rangle$. Eq. (21) provides Beer-Lambert-Bouguer law:

$$I(\lambda, x) = I_0(\lambda) e^{-\langle \beta_\lambda \rangle x} \quad (22)$$

that describes the exponential decay behavior of collimated radiation through a semitransparent media. In order to correlate Eq. (22) with the radiative heat flux divergence, $\nabla \cdot \mathbf{q}_r$, it is possible to write the following correlation, since direction and space coordinates are independent of each other:

$$\nabla \cdot \mathbf{q}_r = \mathbf{n} \cdot \nabla I = \frac{dI(x)}{dx} = -\langle \beta \rangle I_0 e^{-\langle \beta \rangle x} \quad (23)$$

where \mathbf{n} is the unit vector describing the direction of the radiative intensity field. Equation (23) is valid for all wavelengths and directions.

When reference is made to the LTE model, only one temperature is defined, $\langle T_f \rangle^f = \langle T_s \rangle^s = \langle T \rangle$, and one energy equation is be written, that also accounts for the Dufour effect:

$$\begin{aligned} & \left[(1-\varepsilon)(\rho C_p)_s + \varepsilon(\rho C_p)_f \right] \frac{\partial \langle T \rangle}{\partial t} + (\rho C_p)_f \langle \mathbf{u} \rangle \cdot \nabla \langle T \rangle = \\ & = \nabla \cdot (k_{eff} \nabla \langle T \rangle) + \nabla \cdot \mathbf{q}_r + \frac{R \langle T \rangle k_T \rho_i}{M} \frac{D_{ij}}{\langle c_i \rangle} \nabla^2 \langle c_i \rangle \end{aligned} \quad (24)$$

with $k_{eff} = k_{eff, f} + k_{eff, s}$.

2.3.4. Species equations

The volume averaged form of the species equation (Eq. (8)) is:

$$\frac{\partial \langle c \rangle}{\partial t} + \langle \mathbf{u} \rangle \cdot \nabla \langle c \rangle = D_{eff} \nabla^2 \langle c \rangle + \langle k' \rangle \quad (25)$$

with D_{eff} the effective diffusivity, that is commonly expressed as $D_{eff} = \tau \varepsilon D_i$, where τ is the tortuosity. The tortuosity is the ratio of the curved path length between two points of a porous material to the length of the straight line connecting them. When a chemical reaction term needs to be modeled, the term $\langle k' \rangle$ becomes $k \langle c \rangle$, where k is an effective volumetric first-order reaction rate.

As it was observed for the volume-averaged momentum equation (Eq. 15), also the species equation reminds of the Staverman-Kedem-Katchalsky equations for transport across membranes [58]. The selective rejection of the membrane to certain solutes can be modeled by including the Staverman reflection coefficient, σ_s , that varies in the $0 \div 1$ range, and in some cases is equal to the osmosis reflection coefficient [62]. By considering the selective rejection of solutes and the chemical reaction term depicted above, the volume-averaged species equation can be written:

$$\frac{\partial \langle c \rangle}{\partial t} + (1 - \sigma_s) \langle \mathbf{u} \rangle \cdot \nabla \langle c \rangle = D_{eff} \nabla^2 \langle c \rangle + k \langle c \rangle \quad (26)$$

Finally, the volume-averaged species equation for a porous media with Ludwig-Soret effect is:

$$\frac{\partial \langle c \rangle}{\partial t} + (1 - \sigma_s) \langle \mathbf{u} \rangle \cdot \nabla \langle c \rangle = D_{eff} \nabla^2 \langle c \rangle + k \langle c \rangle + \frac{\rho D_{eff}}{M} \frac{k_T}{\langle T \rangle} \nabla^2 \langle T \rangle \quad (27)$$

2.4. The closure problem in the volume-averaged governing equations

The above presented volume-averaged equations, coupled with the appropriate boundary conditions, can solve the flow, temperature and species fields of a macroscopic porous medium. However, because of the volume averaging process, the governing equations contain some unknown quantities, called closing coefficients, that must be known in advance for solving the transport fields. They are resumed in Table 1.

The accuracy of closing coefficients strongly affects the macroscopic solution accuracy. They can be obtained either with experiments or pore-scale simulation or simplified models or very simplified analytical solutions. Their evaluation is still challenging. Only recently the increased computational resources improved the method based on pore-scale simulations. One of the challenges of this method is the representation of the pore-scale geometry, for

Table 1. Closing coefficients for volume-averaged mass, momentum, energy and species equations.

Equation	Phase	Coefficient	Symbol	Unit
Momentum	Fluid	Permeability	K	m^2
Momentum	Fluid	Inertial coefficient	f	1/m
Energy	Fluid	Effective thermal conductivity	$k_{eff,f}$	W/m K
Energy	Solid	Effective thermal conductivity	$k_{eff,s}$	W/m K
Energy	Solid	Scattering	σ_λ	1/m
Energy	Solid	Absorption	κ_λ	1/m
Energy	Solid	Phase function	ψ	-
Energy	Solid	Volumetric interfacial heat	h_v	W/m ³ K
	Fluid	transfer coefficient		
Species	Fluid	Tortuosity	τ	-
Species	Fluid	Effective diffusivity	D_{eff}	m^2/s

which advanced techniques, like the x-ray Computed Tomography (xCT), can be very helpful. Some of the most used correlations for closing coefficients are reported in the following as examples. More details for open-cell foams are reported in the next chapter.

In the momentum equations, the permeability, K , was introduced by Darcy [55]. Typical values of the permeability are 10^{-16} m^2 for sandstone, 10^{-11} m^2 for fiberglass, 10^{-9} m^2 for a cigarette and 10^{-7} m^2 for an open cell foam. The Forchheimer extension was introduced in [56]. A review of models used for permeability is presented in [2]. One of the most common correlations for permeability is the Carman-Kozeny equation [2, 63]:

$$K = \frac{\varepsilon^3}{180(1-\varepsilon)^2} d^2 \quad (28)$$

Another correlation, accounting also for inertial effects, was developed by Ergun [64]. An extension of it for fluidized beds was presented in [65]:

$$K = \frac{\varepsilon^3}{150(1-\varepsilon)^2} d^2 \quad (29)$$

$$f = \frac{1.75}{d\sqrt{K}} \frac{(1-\varepsilon)}{\varepsilon^3} \quad (30)$$

For the energy equation, the effective thermal conductivity is usually modeled by using a weighted average form. Foams are an exception since the actual effective thermal conductivity differs from the weighted average one [66]. As it has already mentioned, the thermal dispersion can be modeled with a gradient diffusion hypothesis, and the radiative heat transfer too. The participating media approach for radiation allows to determine the closing coefficients κ_λ and σ_λ as well as their sum, $\beta_\lambda = \kappa_\lambda + \sigma_\lambda$. For large values of the size parameter, using geometric optics the porous material is represented as a monodisperse assembly of independently scattering voids [67]:

$$\beta = \frac{3}{d}(1 - \varepsilon) \quad (31)$$

The interest of the scientific community in the interfacial volumetric heat transfer coefficient has become important only recently, due to the growing interest on LTNE models. The most simplified approach uses the correlations for tube banks proposed in [68]. The majority of models for porous media are based on packed sphere beds. Kuwahara et al. [69] developed a model based on staggered structural units that simulate the solid part of a porous media. A correlation for turbulent flow over an array of square rods was developed by Saito and de Lemos [70]. However, the real problem of the interfacial volumetric heat transfer coefficient evaluation is the determination of the specific surface area (Eq. (17)), that is quite hard because of the complexity of the geometry. This point will be discussed in the next chapter.

Finally, the effective diffusivity of the species transport equations makes the determination of the tortuosity often difficult. Some examples are an electrical analogy [71], the pore theory [72], empirical methods [73].

In conclusion, the accuracy of a volume-averaged macroscopic porous medium strongly depends on the closing coefficients. An analysis on closing coefficients related to the momentum equation and to the LTNE model, for open-cell foams, will be presented in the next chapter.

3.

**FLUID FLOW
AND HEAT TRANSFER
IN OPEN-CELL FOAMS**

3. FLUID FLOW AND HEAT TRANSFER IN OPEN-CELL FOAMS

Fluid flow and heat transfer in open-cell foams, with an emphasis on pressure drop and convection heat transfer, with their corresponding closing coefficients, are discussed in this chapter. Basic definitions, manufacturing techniques and foam morphology are presented. Closing coefficients are determined with both experiments and numerical simulations. Simulations of heat transfer in open-cell foams engineering applications, such as volumetric solar receivers and heat sinks, are presented.

3.1. Basic definitions

Open-cell foams are a particular class of porous material. Their morphology is pretty regular, *i.e.* almost periodical. They are also defined as cellular materials. The term “cellular” is an adjective that derives from the word “cell”, that means compartment [74]. A cellular material is characterized by many cells packed together to fill a space, thus a cell is a single unit periodically repeated in such space. An example of cellular material is the honeycomb, made up by polygons that fill a plane area. A foam is characterized by polyhedral cells that fill a three-dimensional space; it is called open-cell foam when the solid material is contained only in the edges, which are named struts. The struts meet in vertices of finite dimensions, named junctions, on which, at least approximately, Plateau’s laws are valid. In an open-cell foam, the faces of the polyhedral are open, then a flow can pass through these openings, that are called pores. A resume of these basic definitions is depicted in Fig. 11.

3.2. Manufacturing techniques

Open-cell foams used to enhance heat transfer can be based on a metal solid

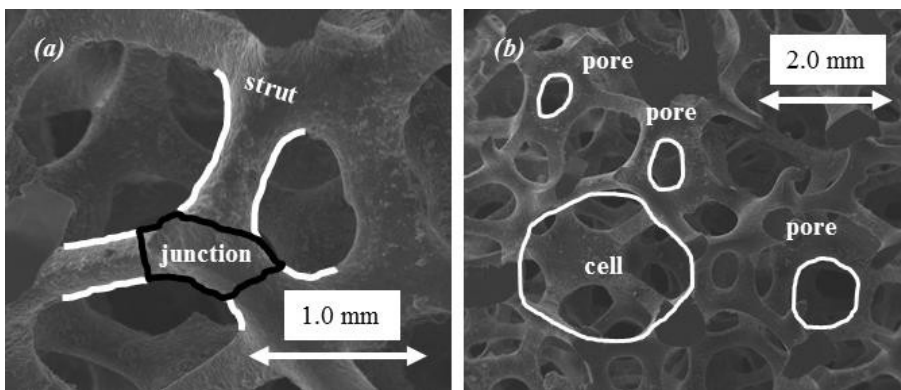


Fig. 11. Open-cell foams basic definitions.

matrix, due to the high thermal conductivity of metals, or on a ceramic material, like silicon carbide SiC. The latter solid matrix material is used when temperatures are above the melting point of metals, for example in a volumetric solar receiver. An exhaustive book on polymer foams has been written by Mills [75]. Open-cell metal foams can be manufactured with the three methods outlined below; ceramic foams can be manufactured by means of the second and third following techniques.

The first, most used, technique is the casting method [17]. An open-cell polymer foam is the template matrix. It is dried and embedded in casting sand after coating with a mold casting slurry. The casting material is hardened by baking, and the template tends to evaporate, obtaining a negative image of the foam. After inserting the molten metal, the metal foam is obtained by directional solidification and cooling, and the mold material is removed, obtaining the final product. This technique is used by ERG Aerospace [23].

Another technique, that can be used for the production of metal foams, such as nickel foams [17], is based on Chemical Vapor Deposition (CVD). Again the template is an open-cell polymer. In order to obtain the nickel-based foam, the template foam is put into a CVD reactor with nickel carbonyl $\text{Ni}(\text{CO})_4$, that splits into nickel and carbon monoxide at a temperature of about $100\text{ }^\circ\text{C}$, depositing on the template. Infrared heating can be used to burn the polymer template, and an open-cell foam with hollow struts is obtained. For applications where enhancing the heat transfer is the target, this technique is less convenient than the casting method because the hollow struts reduce the overall foam thermal conductivity.

A third method, based on casting metal over a stacked bed of soluble spheres that could be made of salt [76], is called leachable bed casting. It allows to obtain very regular foams.

Metal open-cell foams obtained with the above mentioned techniques are sketched in Fig. 12.

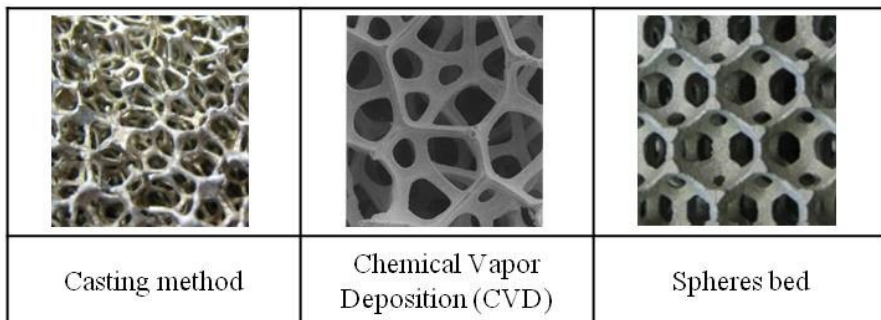


Fig. 12. Methods used for manufacturing open-cell foams.

3.3. Morphology of an open-cell foam

Because of their complex microstructure, open-cell foams morphology plays a fundamental role in transport phenomena, such as heat transfer and pressure drop. An accurate knowledge of foam microstructure is quite challenging due to the high uncertainty in measurements. Predictive models based on geometries that represent a foam can be also employed to model foam microstructure. In the following, measurements techniques and predictive models for various morphological parameters are described, after presenting definitions of foam morphological properties.

The porosity of a foam, ε , has been previously defined as the ratio of the void volume to the foam total volume. The specific surface area, S/V , is the ratio of the heat transfer surface area to the total volume of the foam. The heat transfer surface area, that is referred to the interfacial surface area between the two phases, is the sum of the struts surface area plus the junctions surface area. The high specific surface area of foams is one of their advantages in terms of heat transfer, and it is also challenging to obtain. For this purpose, various techniques can be employed. Experimental techniques are based on the Brunauer-Emmett-Teller (BET) theory, which states that the specific surface area can be indirectly evaluated from the adsorption of non-corrosive gases like nitrogen on a surface. However, for ceramic foams, this method tends to overestimate the value of the specific surface area because of the rough surface of the struts [77]. Techniques based on Magnetic Resonance Imaging (MRI) [78] and x-ray Computed Tomography (xCT) [79] construct experimentally the geometry of the foam and measurements are carried out in by computation After reconstructing the foam with one of the aforementioned methods, various techniques can be employed for the determination of the specific surface area. A statistically-based method makes use of the two-point correlation function [80, 81], that is the probability that within a porous medium two points at a distance r , are in the fluid volume at the same time. This function is a two-dimensional auto-correlation function, equal to $s_2(r) = \langle f(x) f(x+r) \rangle$, where $f(x)$ is the indicator function of the coordinate x . It can be determined with the Monte Carlo method, and it is very useful due to its properties. Indeed, the two-point correlation function is used to determine key parameters, such as porosity and specific surface area:

$$\begin{cases} s_2|_{r=0} = \varepsilon \\ s_2|_{r \rightarrow \infty} = \varepsilon^2 \\ ds_2 / dr|_{r=0} = -S / 4V \end{cases} \quad (32)$$

Another method (BoneJ) is based on the discretization of the foam solid interfacial surfaces, subdivided into many triangles [82] and the surface area is the sum of the areas of the triangles. The surface area can be also determined by measuring the length of the interface of each slice. Other techniques for the evaluation of the specific surface area are based both on computationally-generated foam geometrical models and on analytical considerations on ideal foam structures [77, 83, 84].

Linear morphological characteristics that need to be determined are the Pores Per Inch (PPI), the pore size, the cell size and the strut size (Fig. 11). For the strut, two sizes can be identified, respectively along the axial and the orthogonal directions.

The Pores per Inch give the information on how dense a foam is. The higher the PPI the more pores are counted along a fixed direction. Simplified determinations of the pore size are based on the reciprocal of the PPI. However, Howell et al. [85], after collecting many literature data, concluded that, at a given PPI value, the actual pore size is generally different from the nominal value provided by the manufacturer.

The pore size has been defined in several ways; as: the cord length distributions [86], the diameter of the circle having an area equal to that of the pore [77], the arithmetic mean of the long and short axes of an ellipse that approximates the pore [78], the diameter of the largest circle contained in the pore [79]. Petrasch et al. [87] reported a pore size distribution of a ceramic foam, where two peaks can be identified as the small longitudinal pores mean diameter and the macroscopic pore size. They defined the pore size as the diameter of the largest sphere that includes a point in the pore space, fitted completely within the pore space [88]. The standard deviation of a pore size distribution tends to increase when the pore density becomes lower.

The cell size received less attention in the years, because of the high uncertainty in measurements [78]. It has been defined similarly to the pore size. Thanks to the almost-spherical shape of a cell, Iasiello et al. [79] defined the cell size as the diameter of the largest sphere contained in a cell. Inayat [89] argued that cell size can be obtained from the void volume enclosed by the three dimensionally interconnected foam struts. Grosse et al. [78] defined the cell size as the diameter of a volume-equivalent sphere. Maire et al. [90] defined it as the average circular segment diameter divided by a factor 0.785.

The strut has variable cross sections, due to the foaming process, as sketched in Fig. 11. Inayat et al. [77] assumed the thickness of the minimum strut cross section as the strut size. The strut size has also been defined as the height of a

solid strut equilateral triangle cross-section [91]. More exhaustive models take into account also the variability of the strut section along the strut length [92].

Finally, the strut length is defined as the distance between its extremity vertices, measured center to center [93].

3.3.1. Real foams

In this paper, a real foam is referred to as a foam whose structure is obtained by means of an imaging technique, such as the Magnetic Resonance Image (MRI) or the x-ray Computed Tomography (xCT). Microstructure measurements carried out on real foams are classified as experimental, and they're often more accurate than pure experimental techniques, such as BET [77].

Even if it has less quality than tomography, MRI is used in imaging since it has an acceptable images resolution [78]. This technique is widely used in medicine, due to its accuracy and to the non-ionizing radiations. It is physically based on the Nuclear Magnetic Resonance (NMR), a technique that was first presented by Rabi et al. [94] for molecular beams. It is based on the precession of nuclear spins induced by a magnetic field. Images are obtained as a function of the time that nuclei require to reset their initial equilibrium condition. This technology is also used in engineering applications [95]. Grosse et al. [78] applied it investigating foams morphology. In order to perform measurements, the pore space was filled with a liquid suitable for ^1H -MRI measurements, since the magnetic resonance is a technique that requires elements with non-zero nuclear spin, that possess a magnetic moment.

The most used imaging technique is the x-ray Computed Tomography (xCT). The CT scanner was invented by Godfrey Hounsfield and Allan Cormack in 1972, and they won the Nobel Peace Prize for this. The invention was announced in 1972, even if Hounsfield conceived his idea in 1967. With this technique, x-rays are emitted from a source to a detector, and they are attenuated by the material through which x-rays pass, obtaining an image depending on the attenuation. Taking images from different angles, cross-section images of a rotating object hit by x-rays is computationally reconstructed in three-dimensions. This technique is widely used in medicine, with the object (the patient) settling and the x-ray source rotating around the object. The x-ray attenuation depends on the attenuation coefficient of the object, and the computational reconstruction is obtained with complex algorithms, such as the Filtered Back Projection (FBP). FBP is used when the x-ray beam hitting each detector element has parallel components [96]. Images obtained via MRI and xCT are reported in Fig. 13.

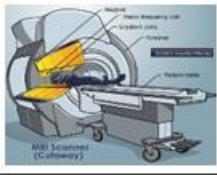
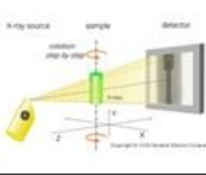
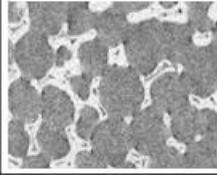
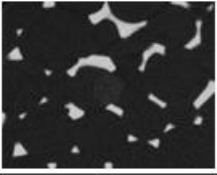
Techniques		Imaging	
MRI	xCT	MRI	xCT
			

Fig. 13. Imaging techniques for real foam.

The 3D image obtained is then postprocessed. Indeed, images are obtained in gray-scale, without indications on threshold between the two phases. Various postprocessing techniques are employed to determine the threshold between the two phases. Two techniques are the iterative selection thresholding method [97] and the Otsu method [98]. The former is an iterative procedure based on the isodata algorithm, while, in the latter, the threshold is chosen in order to minimize the intra-class variance between the two classes. Other postprocessing tools can be employed in order to improve the quality of the images.

From the scan data, it is possible to evaluate all the morphological properties that have been presented in the previous sub-section. In particular, among the various properties, the specific surface area can be determined in several ways. However, it is worth to underline that a high uncertainty can be found, because of several issues, such as the quality of the images, errors due to the used method, etc..

3.3.2. Ideal foams

How to represent a foam is an ancient problem. Since a foam tends to minimize its surface area, it is a minimal surface problem, ruled by the principle of minimum energy, that is a restatement of the second law of thermodynamics. It states that any physical configuration tends to reach the equilibrium in order to minimize its internal energy, that in the case of foams is due to the intermolecular forces. Besides, a foam must be space-filling, and has to respect Plateau's laws. It is also to take into account that foaming is not only affected by surface tension, but also by other factors, such as competitive growth or viscosity forces [21].

Since the aim is to find a minimal surface area, the isoperimetric quotient can be used here. It is defined as $q = 36 \pi V^2/S^3$, in order to have $q = 1$ for a sphere. The first ideal foam was proposed by Plateau [9]. Starting from the Face-Centered-Cubic (FCC) lattice, it is possible to obtain, with a Voronoi

tessellation, a rhombic dodecahedron, with twelve rhombic faces. It is reported in Fig. 14; its isoperimetric quotient is equal to 0.7045 [99]. This geometry was improved by Kelvin [100]. He obtained from the Body-Centered-Cubic (BCC) lattice a fourteen-sided polyhedral, named tetrakaidekahedron or truncated octahedron, with slightly curved hexagonal faces, that guarantees the minimal surface area condition. In the above referred solid eight faces are hexagonal and six are square, with $q = 0.757$ [99]. In this tetrakaidekahedron with plane faces, $q = 0.753$. It was the best space-filling ideal foam since, about a century later, Weaire and Phelan [101] identified a unit cell with even lower specific surface area than Kelvin foam model. Using Surface Evolver [102], a software for the study of surface shaped by surface tension or other energies, they obtained a unit cell starting from the Voronoi tessellation of the A15 phase, that is a series of intermetallic compounds. They found a unit cell made up by eight equal volume cells. Two of them are pyritohedra, an irregular dodecahedron with pentagonal faces, and six are truncated hexagonal trapezohedra, a tetrakaidekahedron with two hexagonal and twelve pentagonal curved faces. The surface energy, that is proportional to the surface area when the thickness is uniform, is minimized of approximately 0.3% with respect to Kelvin's model, resulting in $q = 0.764$ [99].

Some architectural structures are based on ideal foams and minimal surfaces concepts. Tensile structures, which are structures with only tension and no compression or bending, are based on this. The design of the roof of the Olympic Stadium in Munich was based on this idea. Another example is the

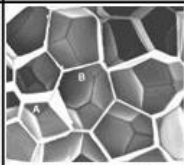
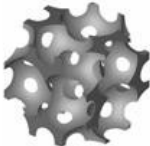
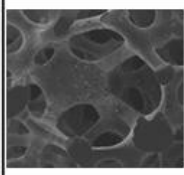
	Plateau	Kelvin	Weaire-Phelan	SEM
Dry				
q	0.7045	0.757	0.764	---
Wet				

Fig. 14. Ideal dry and wet foams, with their isoperimetric quotients, q .

Beijing National Aquatics Center, also known as Water Cube, whose design of the outer wall is based on the Weaire-Phelan structure. The photos of the above structures are reported in Fig. 15.

Modeling foam morphology by using an ideal foam is cheaper than using imaging techniques. For the specific surface area, no exhaustive correlations are available yet [77]. Richardson et al. [83] used a Lord Kelvin foam modified model with triangular struts, d_s , wide, that is the strut thickness. Starting from considerations from Gibson and Ashby [21] among the other morphological parameters, the following correlation for the specific surface area has been derived:

$$\frac{S}{V} = \frac{12.979 \left[1 - 0.971 \sqrt{1 - \varepsilon} \right]}{d_p \sqrt{1 - \varepsilon}} \quad (33)$$

with d_p the pore size, that is the diameter of a circle with an area equivalent to an hexagonal pore. Another correlation was proposed by Buciuman and Kraushaar-Czarnetzki [103]. They too used the Lord Kelvin modified model and the correlations from Gibson and Ashby [21]. The pore size was assumed as the diameter of a circle having the same area as the weighted average of all the 14 pores of a tetrakaidecahedron:

$$\frac{S}{V} = \frac{4.82}{d_p + d_s} \sqrt{1 - \varepsilon} \quad (34)$$

Inayat et al. [77], with reference to a model based on Kelvin foam, presented correlations accounting for the strut shape:

$$S/V = 4.867 \left[1 - 0.971 \sqrt{1 - \varepsilon} \right] / d_p \quad (35)$$



Fig. 15. The Water Cube in Beijing and the Olympic Stadium in Munich.

$$S/V = 6.49 \left[1 - 0.971 \sqrt{1 - \varepsilon} \right] / d_p \quad (36)$$

where Eq. (35) holds for a circular strut, that in an open-cell foam represents the lowest porosity for an open-cell foam, while Eq. (36) is valid for a triangular-concave strut, that exhibits the highest possible porosity of an open-cell foam. More recently, correlations have been derived also for computationally-generated ideal foams. Wu et al. [104] modeled an open-cell foam starting from Lord Kelvin foam model, using a Computer-Aided Design (CAD) software. The struts were circular, and the strut surfaces smoothing at junctions was designed with a face-blended structure with the curvature depending on porosity:

$$\frac{S}{V} = \frac{15.71 - 52.45 \varepsilon + 79.51 \varepsilon^2 - 41.5 \varepsilon^3}{d_c} \quad (37)$$

3.4. State-of-art

3.4.1. Pressure drop

Pressure drop in an open-cell foam represents an issue, because of concentrated pressure drops in the solid matrix of the porous domain. Even if there are advantages in terms of heat transfer, pressure drop is to be taken into account in the design of open-cell foams applications. As it was depicted in the previous section, the first correlations for open-cell foams were based on different porous materials, such as packed sphere beds. Only more recently, foams pressure drop is modeled by using either correlations or experiments based on open-cell foams.

Closing coefficients can be obtained by applying a least-squares quadratic curve fit on the pressure drop per unit length as a function of the velocity [105]:

$$\frac{\Delta p}{L} = \frac{\mu}{K} |\mathbf{u}| + \frac{\rho f}{\sqrt{K}} |\mathbf{u}|^2 = A |\mathbf{u}| + B |\mathbf{u}|^2 \quad (38)$$

where L is the length, A and B are two coefficients, $|\mathbf{u}|$ is the modulus of the superficial velocity, that is the inlet velocity of the fluid through the open-cell foam. It is defined as the ratio of the volumetric flow rate to the cross section area of the channel. Equation (38) is a finite-differential one-dimensional form of Eqs (14a) and (14b), where macroscopic inertial forces, shear stresses and body forces are neglected, and the media is assumed to be isotropic with respect to the permeability.

A least-square quadratic curve fit allows to evaluate coefficients A and B . By imposing $A = \mu/K$ and $B = \rho f/\sqrt{K}$, closing coefficients K and f are obtained. The same result is obtained with a linear fit on the linearized form of Eq. (38):

$$\frac{\Delta p}{L} \frac{1}{|\mathbf{u}|} = \frac{\mu}{K} + \frac{\rho f}{\sqrt{K}} |\mathbf{u}| = A + B |\mathbf{u}| \quad (39)$$

Bhattacharya et al. [106] suggested that differences between the two methods are negligible. The linear fit can be useful to clearly identify the transition region from Darcy to Forchheimer flow regimes, because the function is constant when Darcy's law holds, while it is linear when Forchheimer's extension is to be taken into account. Boomsma and Poulikakos [107] studied water flow through an aluminium open-cell foam. They reported that, for 10, 20 and 40 PPI foams with almost 0.92 porosity, transition from Darcy to Forchheimer regimes occurs at 0.101, 0.110 and 0.074 m/s, respectively.

Three methods are used to study pressure drop in open-cell foams. The first is based on experiments, the second on simulations carried out on real foams; the third on simulations on representative geometries or ideal foams. It is worth noticing that the second and third methods can present problems of symmetry boundary conditions in the CFD modeling [115].

Experiments for pressure drop are quite easy to carry out. A stream of air (or other fluids, such as water) passes through an open-cell foam at a certain velocity, and the pressure difference between inlet and outlet sections is measured with a pressure transducer. Recently pressure drop and heat transfer coefficients in refrigerant fluids, such as CO₂ in supercritical conditions [108] or R1234yf and R1234ze [109], were investigated experimentally. Many studies on measurements of pressure drop are available in the open literature. A resume of such results for different PPI values is reported in Fig. 16.

The method based on simulations carried out on real foams is a hybrid method because the geometry is experimentally determined, but Computational Fluid Dynamics (CFD) is also employed. After reconstructing the geometry with an imaging technique, simulations are performed on the one-phase fluid domain, and pressure difference between the flow inlet and outlet are determined from data reduction. Closing coefficients are obtained from Eqs. (38) or (39). Direct Pore Level Simulations (DPLS) were performed by Petrasch et al. [87]. They used a finite volume CFD code to solve incompressible continuity and Navier-Stokes equations with an in-house mesh generator, using a 10 PPI open-cell ceramic foam with almost 0.86 porosity. Considering the solution obtained as an exact solution within the limits of a numerical study,

Fluid flow and heat transfer in open-cell foams

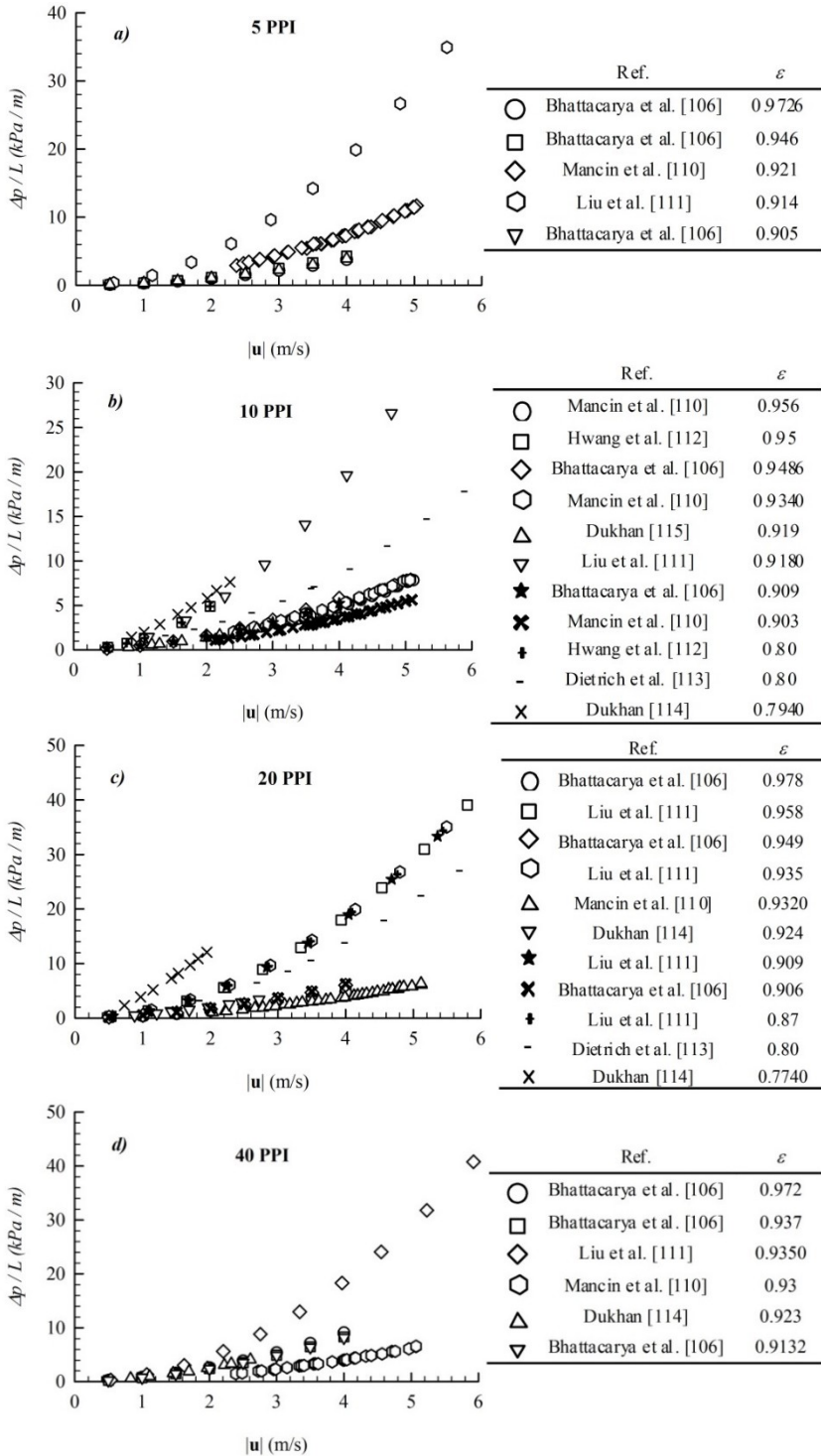


Fig. 16 Pressure drop per unit length: a) 5 PPI; b) 10 PPI; c) 20 PPI; d) 40 PPI.

they compared results in terms of permeability and Forchheimer coefficient with solutions based on simplified approaches, such as Carman-Kozeny equation (hydraulic radius model) or the two-point correlation bound. Haussner et al. [116] obtained closing coefficients, including permeability and Forchheimer coefficient, by using DPLS on a 20 PPI foam with 0.91 porosity. Both Petrasch et al. [87] and Haussner et al. [116] used a slip boundary condition at the interior walls of the computational domain, in order to simulate foam symmetry. Ranut et al. [117] analyzed PPI effects on pressure drop, concluding that at higher PPI pressure drop has an isotropic behavior compared to 20 and 10 PPI, that exhibit a slight anisotropy. A comparison between real and ideal foam models has been performed by Iasiello et al. [79], who found a better agreement with experimental data for the real model. Diani et al. [118] performed simulations for copper foams with different PPI and about 0.935 porosity, with a difference from experimental results no larger than 20%.

Ideal foams pressure drop models have been receiving a wide attention in the last years, since, compared to direct experiments or to real foam based techniques, they allow a huge safe in terms of costs and time. A geometric analytical model representing the microstructure of an open-cell foam was introduced 1988 by Du Plessis and Masliyah [119]. It consisted of three square section ducts, mutually perpendicularly-oriented. This model is called the Representative Unit Cell (RUC), and was used by Fourie et al. [120], in order to improve the predictive accuracy of the analytical model from Du Plessis and Masliyah [119] in modeling Forchheimer regime. The permeability K and the inertial coefficient f are expressed as follows:

$$K = \frac{(d_s + d_p)^2 \varepsilon^2}{36 \tau(\tau - 1)} \quad (40)$$

$$f = \frac{2.05 \tau(\tau - 1)}{\varepsilon^2 (3 - \tau)} \frac{\sqrt{K}}{(d_s + d_p)^2} \quad (41)$$

with the tortuosity, τ , is $\tau = \varepsilon (d_s + d_p)^2 / A_p$ and the pore opening, A_p , $A_p = (\pi/4) (d_p^2 - d_s^2)$. It is worth noticing that $d_s + d_p$ is equal to the microscopic characteristic length of the RUC by Fourie et al. [120]. Fourie and Du Plessis [121] ameliorated the model using the Representative Hydraulic Diameter (RHD) model, that accounts for the effects of a triangular strut.

Another analytical model, based on the analogy with bank of tubes, the cubic cell model, was proposed by Lu et al. [122]. It consists of three mutually

perpendicular equivalent cylinders, each having a diameter d_s and a length equal to the pore size, d_p . The same approach was used by Lacroix et al. [123]. A model based on a pentagonal dodecahedron was developed by Huu et al. [124]. Following Lacroix et al. [123], they started from Ergun's equation, substituting the particle diameter with an equivalent strut diameter derived from a different geometric model. It is important to observe that a pentagonal dodecahedra is not a perfectly filling-space geometry, but it can be modified in order to satisfy this condition.

Recently, the increase in computational capacities allowed to employ foam geometries in pressure drop modeling. Boomsma et al. [115] analyzed the fluid flow through an open-cell foam by using the Weaire-Phelan foam model. The comparison of pressure drop with experimental results showed differences of about 25%, that authors attributed to a lack of wall effects in the numerical model. The Weaire-Phelan foam was also used by Kopanidis et al. [91] and Cunsolo et al. [125], who concluded that the lighter Kelvin's model can be used without remarkable differences in modeling convection and pressure drop for high porosity foams. The Kelvin's model was used by many authors [79, 104, 125 – 127] since it is simpler than the Weaire-Phelan one. Correlations for permeability K and inertial coefficient f as a function of porosity ε and cell size d_c are herein reported from Wu et al. [104]:

$$K = \frac{d_c^2}{1039 - 1002 \varepsilon} \quad (42)$$

$$f = \frac{0.5138 \varepsilon^{-5.739}}{d_c} \sqrt{K} \quad (43)$$

Suleiman and Dukhan [126] performed simulations over an array of Kelvin foam cell in series, and found maximum differences of about 15% for low velocity regime pressure drop compared with experiments run on their own. However, it is reported that there is still a lack of data on exhaustive and reliable models for pressure drop modeling based on ideal foams.

3.4.2. Convection heat transfer

The local heat transfer between the two phases when they are not in thermal equilibrium (LTNE model) is referred as interfacial convection heat transfer. Sometimes, rather than to the coefficient of convection, h_c , reference is made to the volumetric heat transfer coefficient, h_v , that accounts to heat transferred in the whole porous medium, also for conduction through the solid struts. The

same three methods described for the evaluation of pressure drop can be used to evaluate the interfacial convection heat transfer coefficient and the corresponding volumetric heat transfer coefficient.

Many experimental techniques can be employed. They can be classified as stationary or transient techniques. A stationary technique was used by Fuller et al. [128]. They calculated the volumetric heat transfer coefficient in Eq. (17) by using a heating pad at the bottom of the foam sample. Data reduction was performed by making an energy balance over the foam domain. However, this technique underestimates volumetric heat transfer coefficients, since the temperature gradient in the foam reduces at decreasing Biot number. Dukhan et al. [129] investigated water convection heat transfer through an aluminum foam. A surface heater wrapped the foam sample and the surface temperature was measured at the bottom of the sample in the flow direction. The authors identified a region in the solid where the slope of the temperature profile was uniform, the temperature field being fully developed. Therefore the temperature profile in the fluid was the same as in the solid and was obtained by measuring the fluid temperature in the exit section of the foam. A similar technique was used for the thermally developing region, by using the inlet water temperature instead of the outlet one. Another experimental technique considers the foam as an extended heat transfer surface. After obtaining an overall heat transfer coefficient, the thermal resistance of the foam struts is taken into account, in order to obtain an interfacial coefficient, by defining a foam efficiency based on the concept of fin efficiency [130]. This technique was used by Mancin et al. [131]. Even if it is the most accurate steady-state technique, it still depends on the solid material of the foam. The correlation proposed by the authors, valid for $30 < Re < 200$ and $Pr = 0.7$, is:

$$h_c = 0.418 Re^{0.53} Pr^{0.33} \frac{k_f}{d_s} \quad (44)$$

with the Reynolds number $Re = |\mathbf{u}| \rho d_s / \mu_f$ and the Prandtl number $Pr = \mu_f C_{p,f} / k_f$. Fluid properties are evaluated at mean fluid temperature and pressure.

The most accurate experimental technique is the transient technique, based on an inverse method. The experimental apparatus is set up in such a way as to guarantee a local temperature difference between the two phases; thus a LTNE model can be applied. Temperature profiles of solid and fluid as a function of the time are measured. By employing Eqs. (18a) and (18b), the volumetric heat transfer coefficient, h_v , is iteratively modified in order to match simulated profiles and measured profiles within a fixed tolerance. The volumetric heat transfer coefficient is independent of the foam solid matrix and, if the specific

surface area is known, the interfacial heat transfer coefficient is obtained by means of Eq. (17). In most cases the problem is assumed to be one-dimensional. Thermocouples are located at the inlet, outlet and side boundaries of the foam. Experimental results in the literature are resumed in Fig. 17.

Convection heat transfer in real foams has been investigated numerically with the same approach as that for a single-phase fluid presented in the previous section, with the appropriate boundary conditions. The convection heat transfer coefficient is obtained as:

$$h_c = \frac{|\mathbf{q}|}{\langle T_s \rangle^s - \langle T_f \rangle^f} \quad (45)$$

where both temperatures are averaged over the computational domain, the temperature of the solid $\langle T_s \rangle^s$ is taken at the solid/fluid interface, and the temperature of the fluid $\langle T_f \rangle^f$ is the bulk temperature. The interfacial boundary condition can be either a uniform heat flux or a uniform interfacial temperature. Petrasch et al. [87] and Haussner et al. [116] used DPLS to investigate heat transfer coefficients under a constant solid temperature boundary condition.

Anisotropy effects were analyzed by Ranut et al. [117] under either uniform heat flux or uniform interfacial temperature boundary condition, observing slightly anisotropy for lower PPI. Uniform heat flux boundary condition has been also used by Iasiello et al. [79] for a 40 PPI foam with about 0.90 porosity and by Diani et al. [118]. Results are often presented in terms of heat transfer coefficients and a volumetric heat transfer coefficient is obtained by using the specific surface area calculated directly on the scanned real foam. Since this is a new technique, only few data is available in the literature.

With reference to the third technique, the first simplified geometrical models were based on Zukauskas correlations [68] for tube banks. Lu et al. [122] developed a cubic cell model using existing heat transfer data for convection crossflow through cylinder banks. More recently, geometries based on ideal foams were used to study the interfacial convection heat transfer. Differences in coefficients of convection heat transfer predicted by the Weaire-Phelan's and Kelvin's foam models were found to be negligible for high porosity foams [125]. Kelvin model is preferred because it is lighter than Weaire-Phelan one.

Pusterla et al. [137] investigated the effects of the morphology of the Kelvin's foam, in terms of junction thickness, cell inclination angle and strut tapering, that is the ratio between junction diameter and strut minimum diameter. The effects of struts shape on convection heat transfer were analyzed by

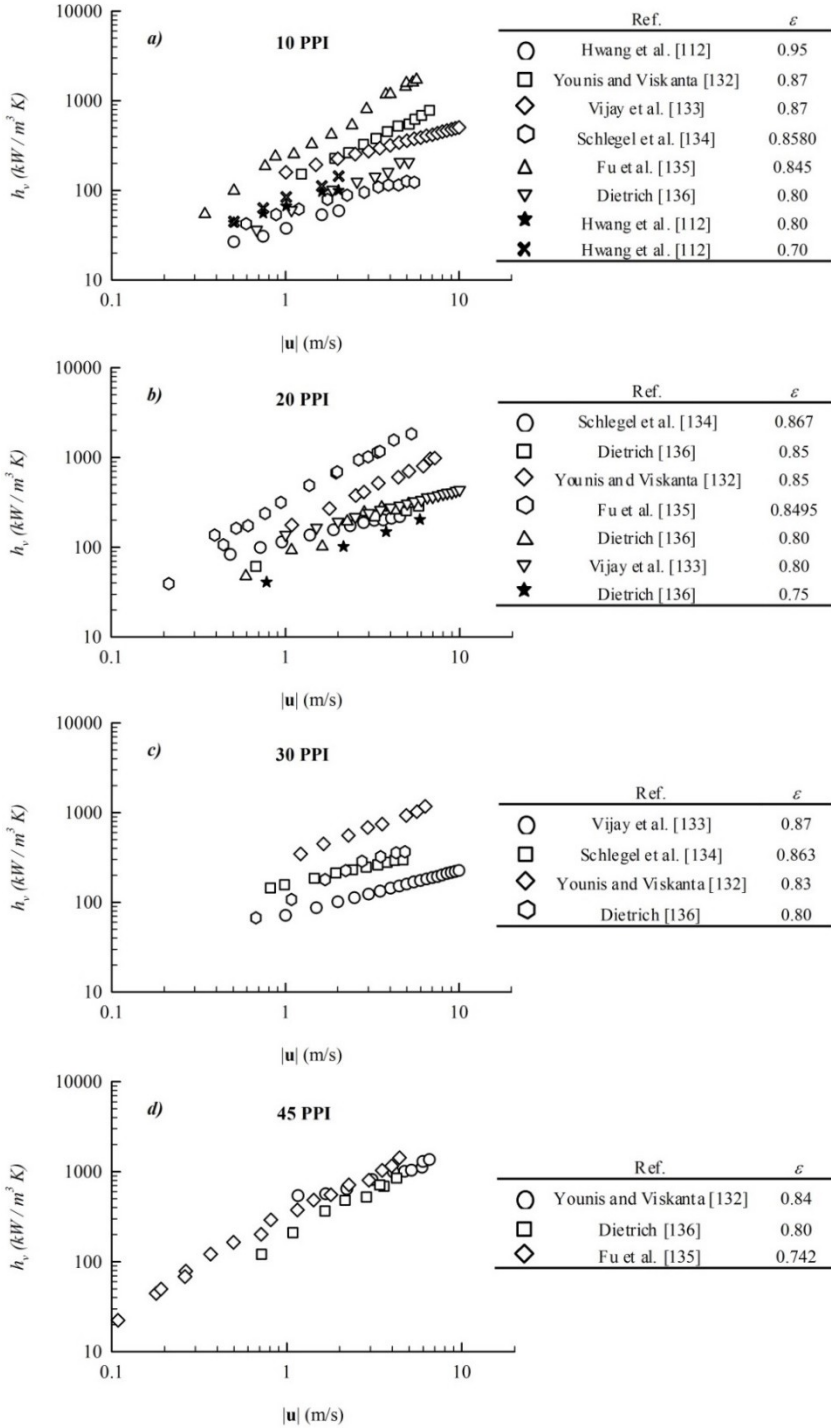


Fig. 17. Experimental volumetric heat transfer coefficient: a) 5 PPI; b) 10 PPI; c) 20 PPI; d) 40 PPI.

Ambrosio et al. [138]. Thermally developing effects were analyzed by Wu et al. [139] by simulating an array of Kelvin's foams in series. By applying a uniform surface temperature boundary condition, they identified three regions for thermally developing flow: a boundary affected region, a stable convection region and a thermal equilibrium region. They also found that the convection heat transfer is more affected by the cell size than by the porosity. They presented the following correlation [139, 140]:

$$h_v = \left(32.50 \varepsilon^{0.38} - 109.94 \varepsilon^{1.38} + 166.65 \varepsilon^{2.38} - 86.98 \varepsilon^{3.38} \right) \text{Re}_c^{0.438} \varepsilon^{0.438} \frac{k_f}{d_c^2} \quad (46)$$

that is valid in the thermally developed region, for $0.66 < \varepsilon < 0.93$ and $70 < \text{Re}_c < 800$, where $\text{Re}_c = |\mathbf{u}| d_c/\nu$. Both representative and ideal models can be developed by improving the foam geometry. For example, the correlation proposed by Wu et al. [139] is based on cylindrical struts, a simplified geometry of the struts.

3.5. An experimental approach for the closing coefficients

3.5.1. Description of the experimental apparatus

Based on a transient technique for the evaluation of the convection heat transfer, an innovative experimental apparatus has been designed and set up. The scheme of the apparatus is reported in Fig. 18. The stainless-steel AISI 316L test rig is an open-circuit, with a rectangular cross section. An Atlas Copco GA7VSD screw air compressor guarantees a variable air flow rate at a constant pressure. The volumetric flow rate varies in the 0.4 - 1.2 m³/min range.

Before exiting the compressor, the air is dehumidified by an R134a drier, water, oil and particulate are removed by a set of filters. The air stream passes through a pressure control valve, that makes the pressure close to the atmospheric pressure value. The mass flow rate is measured with a volumetric orifice flow meter (Fig. 19a), useful for stationary measurements, due to its costs and accuracy. It is equipped with a differential pressure transducer, according to EN 5167-1:2003 [141]. The air density is given by the ideal gas law $p/\rho = RT$. It has been checked that using a gas law by considering humid air provides a negligible error. The absolute pressure is determined with an Eliwell piezoelectric transducer, with a 0.5- 8.0 bar operating range between and a $\pm 1.0\%$ full-scale accuracy. The temperature is measured with a K-type thermocouple, with a ± 1.1 °C accuracy, and a Agilent 34901 cold junction compensation, with an accuracy of ± 1.0 °C. Downstream of the volumetric

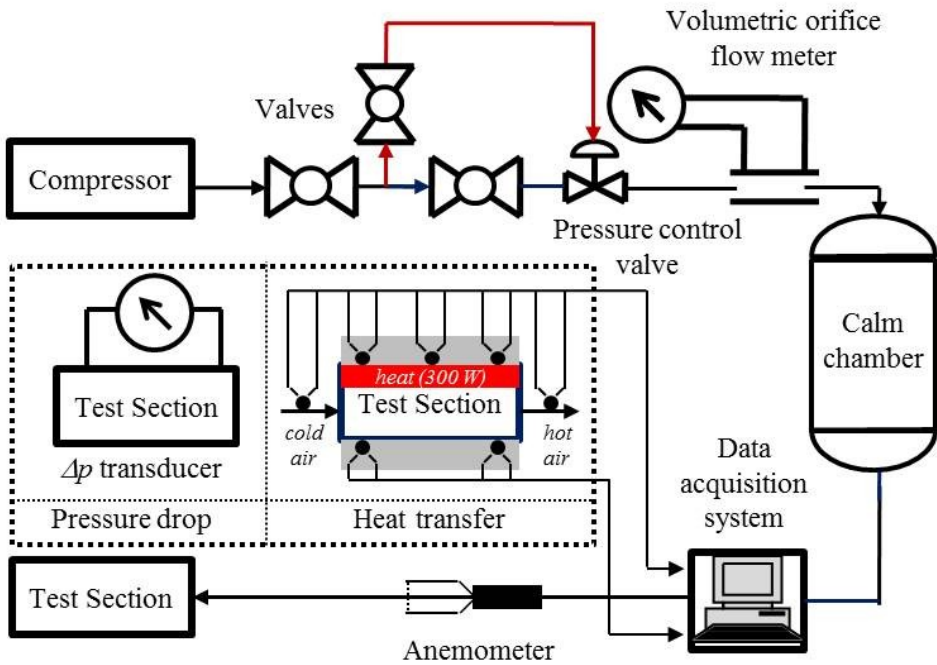


Fig. 18. Scheme of the experimental apparatus.

flow rate measurement section, a calm chamber stabilizes the flow and the circular cross section changes into a rectangular one. Since measurements are carried out in transient conditions, a DANTEC Mini CTA 54T30 temperature anemometer is used to evaluate the fluid velocity upstream of the test section.

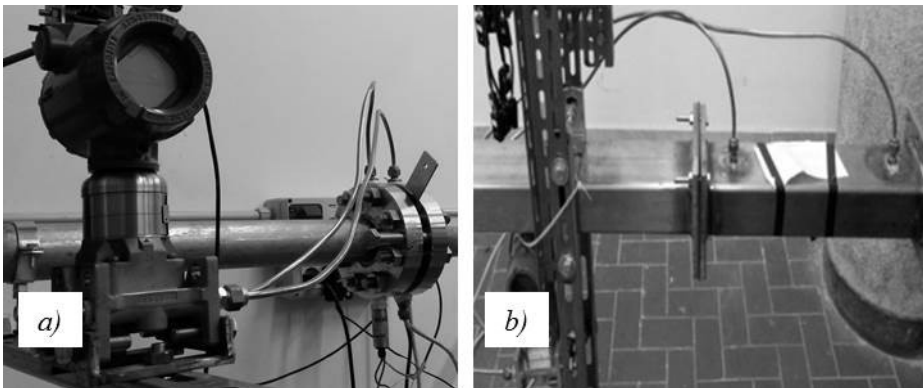


Fig. 19. a) Volumetric flow orifice flow meter; b) Test section.

The anemometer is calibrated before the tests, using the volumetric orifice flow meter. The photo of the test section is reported in Fig. 19b. The test section is long 300 mm, with a 100 x 60 mm² rectangular section. A 3051 Rosemount pressure transmitter, with a ± 1.1 Pa accuracy, is used to measure the pressure drop between the inlet and outlet section of the sample. A 300 W mica heating pad is mounted at the top of the sample. The test section is insulated with calcium-magnesium silicate sheets. Five K-type thermocouples are used to measure the solid temperature. Three are equally-spaced at the top of the sample and two are mounted at the bottom at the extremities. Inlet and outlet fluid temperatures are measured by using six T-type thermocouples, with a ± 0.5 K accuracy, three at the inlet and three at the outlet, respectively. These thermocouples are equally-spaced, mounted in order to avoid the contact with the solid sample. T-type thermocouples were chosen due to their high response in frequency. All the eleven thermocouples use the cold junction compensation from the Agilent 34901A data acquisition card. Runs have been performed on aluminum foam samples (6101-T6) provided by ERG Aerospace, whose geometrical and morphological parameters are resumed in Table 2.

3.5.2. Experimental determination of the closing coefficients

The aim of the experimental runs is to determine pressure drop and interfacial convection heat transfer in an open-cell foam. In particular, permeability, K , inertial factor, f , and volumetric heat transfer coefficient, h_v , are determined from experimental data. The Forchheimer coefficient, C , can be obtained also from $C = f/\sqrt{K}$. Procedures for both pressure drop and volumetric heat transfer coefficients are described in the following.

Pressure drops are evaluated with a differential pressure transducer. Dividing the pressure drop by the sample length we to obtain the pressure drop per unit

Table 2. Parameters of the investigated foams.

Porosity	PPI	Cross section (mm ²)	Length (mm)
0.944	5	54 x 94	194
0.945	10		194
0.943	20		194
0.940	20		185
0.902	40		194
0.970	40		175

length. By performing different runs at different superficial velocities, $|\mathbf{u}|$, shows that the dependence of pressure drop on the velocity is almost quadratic, as depicted in Eq. (38) or Eq. (39). Closing coefficients are obtained by applying either Eq. (38) or Eq. (39). In this work, reference is made to Eq. (39). Coefficients A and B can be obtained by a quadratic or linear regression of experimental data; thus K and f are obtained by $A = \mu/K$ and $B = \rho f/\sqrt{K}$. Uncertainty analysis is performed by applying propagation of uncertainties without variable correlations. Defining a functional relationship $y = f(x_1, x_2, \dots, x_N)$, the composed uncertainty, $u_c(y)$, is derived:

$$u_c(y) = \sqrt{\sum_{i=1}^N \left(\frac{\partial f}{\partial x_i} \right)^2 u^2(x_i)} \quad (47)$$

where $u^2(x_i)$ is the variance of x_i . Since the volumetric flow rate is measured with a volumetric orifice flow meter equipped with a differential pressure transducer, the velocity is determined with the following correlation[141]:

$$|\mathbf{u}| = \frac{C_D}{\sqrt{\rho [1 - (d/D)^4]}} \varepsilon (d/D)^2 \sqrt{2\Delta p} \quad (48)$$

where C_D is the discharge coefficient; d/D is the ratio of the orifice diameter to the duct diameter; ε is the fluid expansibility factor; ρ is the fluid density, measured upstream of the tapping plane; Δp is the pressure drop between the orifice upstream and downstream pressure. The discharge coefficient, given by the Reader-Harris/Gallagher equation [141], is evaluated by an iterative procedure; the fluid expansibility factor is obtained from an empirical formula [141]. Uncertainty of the velocity in Eq. (48) is determined according to EN ISO 5167-1:2003 [141].

The volumetric heat transfer coefficient is evaluated with a transient-hybrid technique, in order to point out its dependence on time. The experimental procedure is described in the following. The heating pad is switched on with stagnant air, thus the solid temperature increases, especially on the top of the heating section. Heat transferred by conduction through the struts warms up the bottom of the sample. By switching off and on the heating pad, equilibrium in temperatures is attained with a 5 K maximum temperature difference among the five thermocouples. When the equilibrium temperature is reached, the heating

pad is switched off, and air at ambient temperature starts to flow through the sample by opening a valve. Because of the heat transferred from the foam struts, the temperature of the air increases along the sample. The temperature of the air in the exit section of the foam decreases with the time, finally assuming the value of the struts temperature located in the inlet section, and air and solid temperature profiles are obtained.

The volumetric heat transfer coefficient is given by following equation:

$$h_v = h_c \frac{S}{V} = \frac{Q}{V\Delta T} = \frac{Q}{V(T_s - \langle T_f \rangle)} \quad (49)$$

where the heat rate, Q , is evaluated as the total enthalpy variation between the entrance and the exit of the foam; V is the total volume of the foam, T_s is the mean temperature of the solid measured by the five K-type thermocouples. Since thermocouples are located on the heating pad, thermal inertia lag effects may cause errors in measured temperatures. The dependence of the solid temperature on time has been evaluated by applying a transient first-law balance on a control volume that encloses only the solid part of the foam. Besides, since Biot number is small in an aluminum metal foam, a uniform temperature in each strut has been assumed. $\langle T_f \rangle$ is the mean value of fluid temperatures at the outlet and inlet flow sections of the foam, by the six T-type thermocouples located at the outlet and inlet sections, respectively.

3.5.3. Results

3.5.3.1. Pressure drop

Pressure drop measurements have been carried out by varying the inlet velocity of the air from 0.5 to 3.5 m/s.

Pressure drop per unit length as a function of the air velocity, the ratio of pressure drop per unit length to the velocity for various values of PPI and porosity, is presented in Figs.20 and 21, respectively. The dependence of pressure drop on the inlet velocity is almost quadratic, in agreement with Darcy-Forchheimer law (Eq. 38).

Figure 20a points out PPI effects, while Fig.20b emphasizes porosity effects. With references to PPI effect ($\varepsilon \approx 0.94$), we notice that the larger PPI the larger the pressure drop, because the flow faces an increasing number of obstacles along its path. A slight increase of the pressure drop with porosity is exhibited in Fig. 20b, where PPI = 40. This behaviour, also observed by Mancin et al.

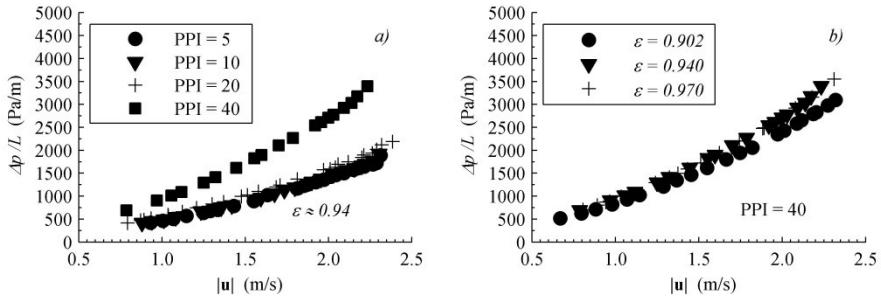


Fig. 20. Pressure drop per unit length vs. air velocity:
a) $\epsilon \approx 0.94$ and various PPI; b) PPI = 40 and various ϵ .

[110], is caused by the variation of the strut section shape with porosity in a foam. The shape changes from triangular to concave-triangular, increasing drag forces.

Figure 21 shows linear regressions, with R^2 always higher than 0.98. It allows to determine the permeability, the inertial coefficient and the Forchheimer coefficient by means of Eq. (39).

Permeability, inertial factor and Forchheimer coefficient as a function of porosity and PPI are reported in Fig.22. One can notice that in a 40 PPI foam, the permeability is almost independent of the porosity, whereas a fair increase of the inertial coefficient is exhibited. This is due to the variation of the strut section shape with porosity, thus there is an increase in drag forces. Fig.22b shows that the permeability of lower PPI foams is larger, meaning that the fluid flows more easily through the foam. On the other hand, Forchheimer coefficient increases with PPI, because of increasing inertial effects.

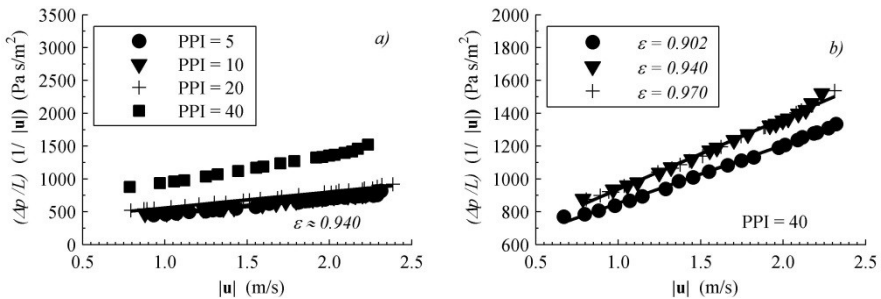


Fig. 21. Ratio of pressure drop per unit length to the velocity vs. the velocity:
a) $\epsilon \approx 0.94$ and various PPI; b) PPI = 40 and various ϵ .

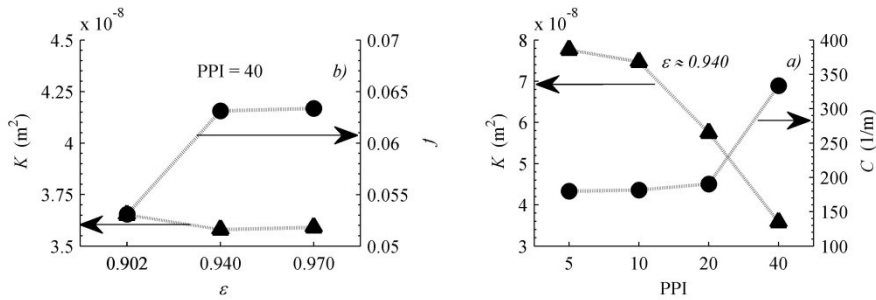


Fig. 22. a) Permeability and inertial factor vs. the porosity, at 40 PPI; b) Permeability and Forchheimer coefficient vs. PPI, for $\epsilon \approx 0.94$.

Pressure drop per unit length as a function of the air velocity, for 40 PPI and $\epsilon = 0.902$, together with data taken from the literature, is presented in Fig. 23.

Equation (47) allows to evaluate uncertainties of the closing coefficients. The uncertainty of inlet velocity was no higher than 1.30 %; the maximum uncertainties of closing coefficients were 6.97 % for K , 2.47 % for C and 2.56 % for f , for $\epsilon = 0.944$ and PPI = 5.

In conclusion, it has been shown that PPI affects pressure drop and closing coefficients more than the porosity.

3.5.3.2. Convection heat transfer

Volumetric convection heat transfer coefficients are evaluated for a foam with $\epsilon = 0.902$ and 40 PPI, inlet velocity of 1.50 m/s, 2.50 m/s and 3.50 m/s.

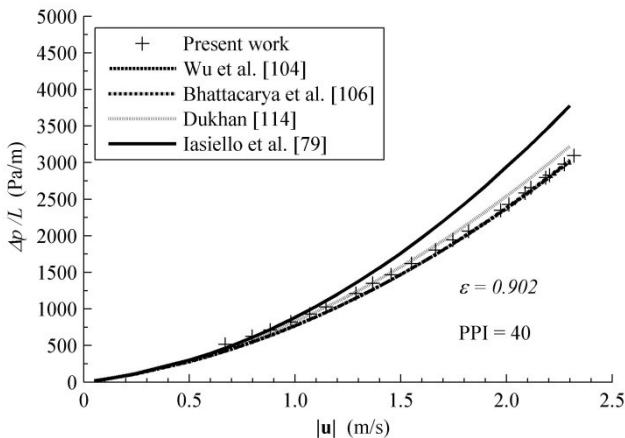


Fig. 23. Pressure drop per unit length vs. air velocity, for 40 PPI and $\epsilon = 0.902$.

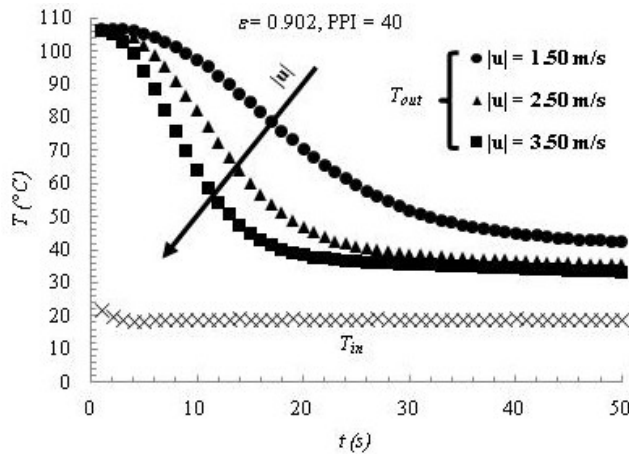


Fig. 24. Fluid temperature in the inlet and outlet sections of the foam vs. time, for $\varepsilon = 0.902$, PPI = 40 and various inlet velocities.

The fluid temperature in the inlet and outlet sections of the foam as a function of time, for $\varepsilon = 0.902$, PPI = 40 and various inlet velocities, is reported in Fig. 24. Since the heating pad is switched off during the transient, the fluid temperature in the outlet section rapidly decreases with time, tending asymptotically to the unchanging inlet fluid temperature. One can also notice that the higher the velocity, the faster the transient.

The volumetric heat transfer coefficient as a function of time, for $\varepsilon = 0.902$, PPI = 40 and various inlet velocities, is reported in Fig. 25.

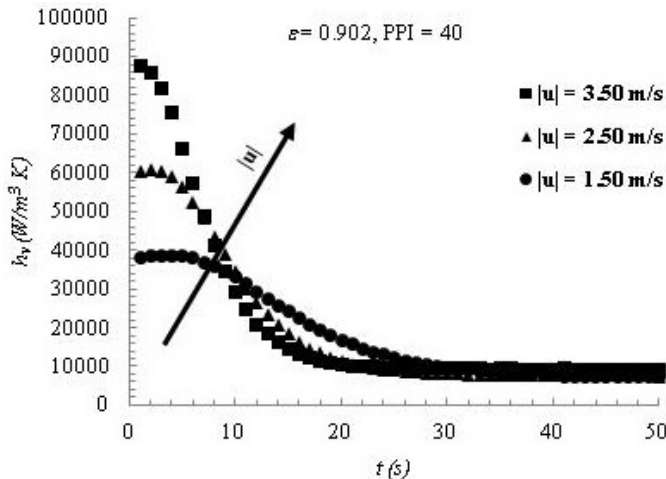


Fig. 25. Volumetric heat transfer coefficient vs. time, for $\varepsilon = 0.902$, PPI = 40 and various inlet velocities.

The figure shows that during the transient heat transfer coefficients decrease faster with increasing velocity. One can also remark an equal duration of the transient for 3.50 m/s and 2.50 m/s whereas it is longer for 1.50 m/s velocity.

3.6. Predictive models for the closing coefficients

Together with experimental approaches, numerical simulations based on real and ideal foams have been performed. Predictions of pressure drop and convection heat transfer for real and ideal foams are presented in this section.

3.6.1. Foam geometry reconstruction

The geometry of both real and ideal foams can be reconstructed in several ways. In research herein described the real foam was reconstructed by using xCT, while the ideal foam was built up with reference to Kelvin's foam model. Since differences in pressure drop and convection heat transfer between Kelvin's and Weaire-Phelan's foam models are negligible at high porosities [125], the simpler and computationally lighter Kelvin's foam model was preferred.

3.6.1.1. Real model: the RVE theory

Three real foam cylindrical samples (10 mm length and 10 mm diameter), having the same 40 PPI value, with 0.88, 0.94, 0.97 nominal porosities and 0.87, 0.94, 0.96 measured porosities, manufactured by ERG Aerospace, were scanned. Scans were performed with an Xradia MicroxCT-400 machine, that ensures a spatial resolution $< 1 \mu\text{m}$ and a pixel size down to $0.3 \mu\text{m}$. The x-ray source maximum voltage and power are 90 kV and 8 W, respectively; for a light material, such as aluminum, 20 kV and 3 W are typically used. The x-ray detector is a 4 megapixel (2048x2048) 16-bit digital CCD camera, equipped with a lens that magnifies the images. 1X and 4X magnifications were used in this research. The pixel sizes were $17.7 \mu\text{m}$, $17.8 \mu\text{m}$ and $18.9 \mu\text{m}$ for 0.88, 0.94 and 0.97 porosities, respectively, for the 1X magnification. For the same porosities, Pixel size were $4.59 \mu\text{m}$, $4.41 \mu\text{m}$ and $4.66 \mu\text{m}$, when the 4X lens was used. The spatial resolution, that is the size of the smallest object that can be detected through the sample, was about $40 \mu\text{m}$ and about $10 \mu\text{m}$ for 1X and 4X magnification, respectively. Together with the pixel size, the spatial resolutions depends on the field of view. Grey-scale images are then obtained for both magnifications, as depicted in Fig. 26, where the scans of a 0.96 for the 0.96 porosity foam are presented. It is clear that in both cases the strut shape is

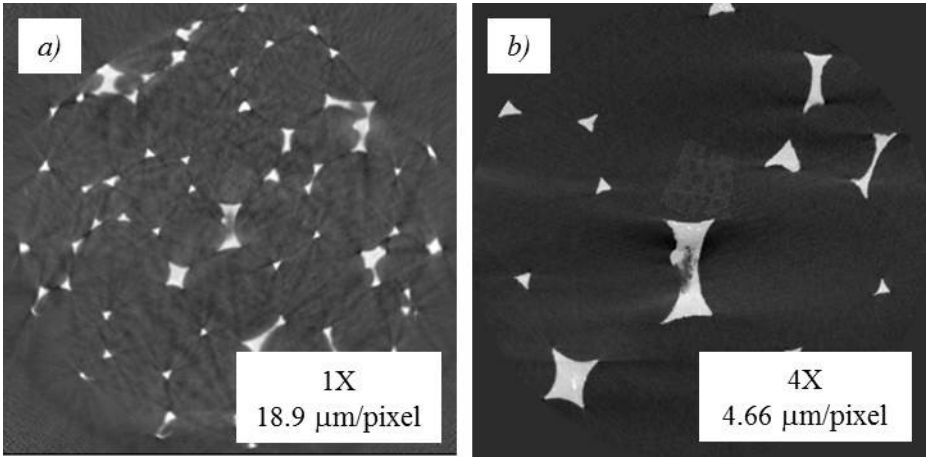


Fig. 26. CT scans for a 0.96 porosity foam: a) 1X and 18.9 μm pixel size; b) 4X and 4.66 μm pixel size.

crisp. Thus the 1X magnification guarantees an accurate enough analysis, as the subsequent morphological analysis will confirm. To obtain the binary images from the grey-scale ones, the freeware program ImageJ was used. A $7.1 \times 7.1 \times 10 \text{ mm}^3$ sub-volume was cut, in order to remove corner artifacts from the CT data. The threshold was determined with the iterative selection thresholding method [97], and it was verified that the Otsu method provides negligible differences on porosity [98].

The morphological analysis was carried out to evaluate the porosity, the specific surface area, the cell size, the pore size, the strut size, the strut length and the junction size. The strut size refers to its middle cross section, that is the minimum value along the strut length. The specific surface area was evaluated with the two-point correlation function and its properties are reported in Eq. (32). Reference has been made to two definitions of all the above mentioned sizes. The first, herein named definition #1, assumes the size as the diameter of the largest sphere inscribed into each foam morphological parameter; the second, definition (#2), assumes the size as the diameter, $\sqrt{4A/\pi}$, of an equivalent circle, with an area, A , equal to that of the cross-section of each measured morphological parameter. Two dimensionless parameters have also been used. The first is the strut tapering, $t = d_j/d_s$, [138] and the foam shape factor, $\beta = A_s/A_{circ}$, where A_s is the average area of the strut cross section and A_{circ} is the average area of the smallest circle that contains the cross section of the strut. All measurements were carried out on 2D slices of the CT data. The

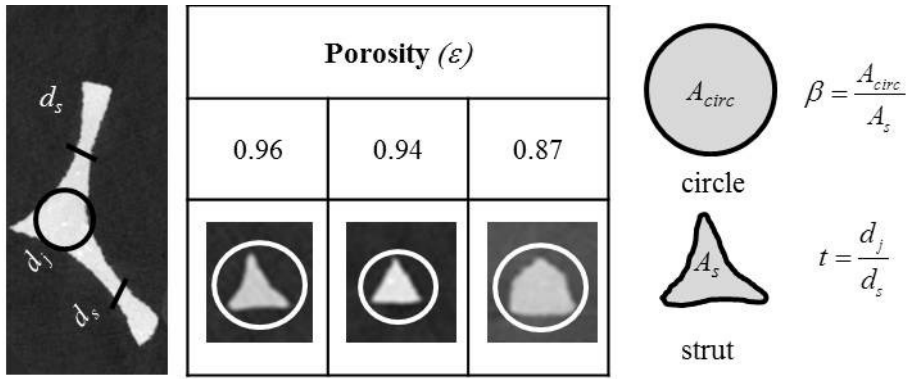


Fig. 27. Foam strut shapes as a function of the porosity.

comparison of d_c and d_p values for 1X and 4X exhibited differences less than 0.3%; thus 1X data are used in the following. The above parameters are resumed in Fig. 27.

Sizes were evaluated as the average values of 30 runs for pores, struts and junctions and 10 runs for the cells. The distribution of pore size, according to definitions #1 and #2, for various porosities is reported in Fig.28. The figure shows that distributions gather around a common value, especially when reference is made to definition #2. We also notice that the higher the porosity the lower the spread in the distributions. The average measured morphological characteristics, together with their standard deviations, are reported in Table 3.

With reference to both foam morphologies, defined as #1 and #2, Fig.27 showed that the larger the porosity the smaller the foam shape factor, with the strut shape varying from convex-triangular to concave-triangular. The strut

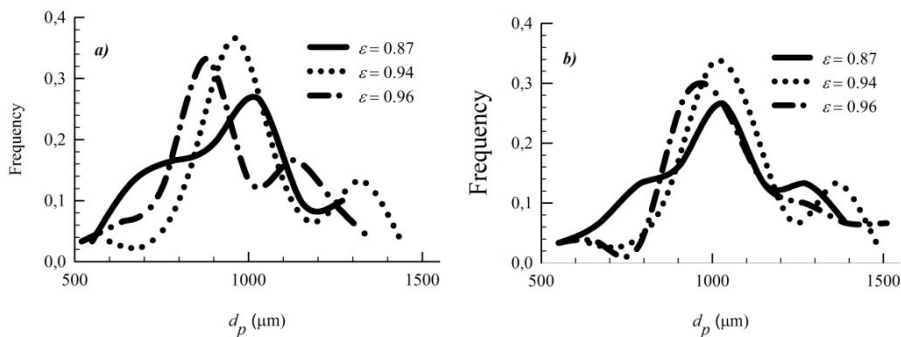


Fig. 28. Pore size distribution: a) definition #1; b) definition #2.

Table 3. Average measured morphological characteristics (standard deviation in parentheses).

ε	β	\bar{L}_s (mm)	S/V (1/m)	\bar{d}_c (mm)	\bar{d}_p (mm)	\bar{d}_s (mm)	t
Definition #1							
0.87	0.67 (0.07)	1.32 (0.15)	1408	1.72 (0.15)	0.88 (0.19)	0.29 (0.11)	2.2 (0.3)
0.94	0.59 (0.06)	1.37 (0.14)	954	1.85 (0.21)	0.95 (0.19)	0.20 (0.04)	2.1 (0.3)
0.96	0.49 (0.05)	1.45 (0.14)	922	2.03 (0.17)	0.89 (0.20)	0.16 (0.05)	1.8 (0.2)
Definition #2							
0.87	0.67 (0.07)	1.32 (0.15)	1408	1.71 (0.16)	0.99 (0.23)	0.29 (0.09)	2.1 (0.3)
0.94	0.59 (0.06)	1.37 (0.14)	954	1.84 (0.21)	1.00 (0.19)	0.18 (0.03)	2.0 (0.2)
0.96	0.49 (0.05)	1.45 (0.14)	922	1.99 (0.16)	0.96 (0.22)	0.15 (0.02)	1.5 (0.2)

length increases at increasing porosity, because the distance between its extreme cross sections increases as the percentage of solid in the foam decreases. For the same reason the specific surface area and the strut size decrease at increasing porosity. The cell size increases with porosity because convex-triangular struts occupy more room in a cell. Figure 28 showed that pore size is almost independent of porosity. Since the junction diameter increases faster than the strut diameter, the strut tapering increases at decreasing porosity.

The comparison of the sizes by definitions #1 and #2, shows that differences are less about than 1%, except for the pore sizes, for which, as usual, the difference is larger, also 10%. Reference will be made in the following to definition #1, since it is simpler to carry out.

Since the simulation of the whole CT scanned sample is computationally expensive, the Representative Volume Element (RVE) concept helps save computational power in simulations. An RVE is sketched in Fig.29. Haussner et al. [116] proposed a cubic RVE, with $L_{RVE} = 3.50 d_p$, that guarantees the invariance of porosity, extinction coefficient and thermal conductivity. Since no data are available for a cubic RVE that guarantees the invariance of pressure drop per unit length and the volumetric heat transfer coefficient, in the present

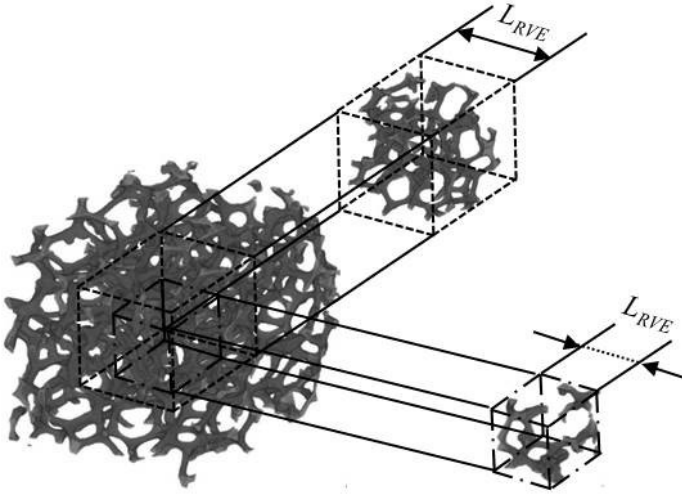


Fig. 29. The Representative Volume Element (RVE).

study only porosity and specific surface area will be treated as invariant, assuming a suitable length of the RVE. Moreover, when the RVE dimension is being chosen, the spatial invariance of the RVE in the scanned sample must be guaranteed. The CT scanned sample is first divided into cubic elements, having the same volume, L_{RVE}^3 . The Monte Carlo method is used on each element to obtain the two-point correlation function with a C++ code [79]. The porosity and the specific surface area of each cubic element is evaluated by means of the properties of the two-point correlation function in Eq. (32) and, therefore, their distribution in the scanned sample is obtained. Thus, a mean and a standard deviation can be obtained from these calculations for both ε and S/V , and a Coefficient of Variation (CV) is defined as the ratio of the standard deviation to the mean value. The same procedure is followed for different cubic elements of volume L_{RVE}^3 , obtaining CV s for the different values of L_{RVE} . The chosen RVE is that with the lowest L_{RVE} for which $CV < 0.15$, for both porosity and specific surface area. It is worth remarking that this methodology makes the RVE independent of its position in the scanned sample; therefore, it is also defined as the Statistical Representative Volume Element (SRVE). Mean values of the porosity and the specific surface area as well as the coefficient of variation as a function of the length of the Representative Volume Element scaled with the cell size, for $\varepsilon = 0.94$, are reported in Fig.30. The grey region in the figure denotes the values of the abscissa that can be assumed as representative of the

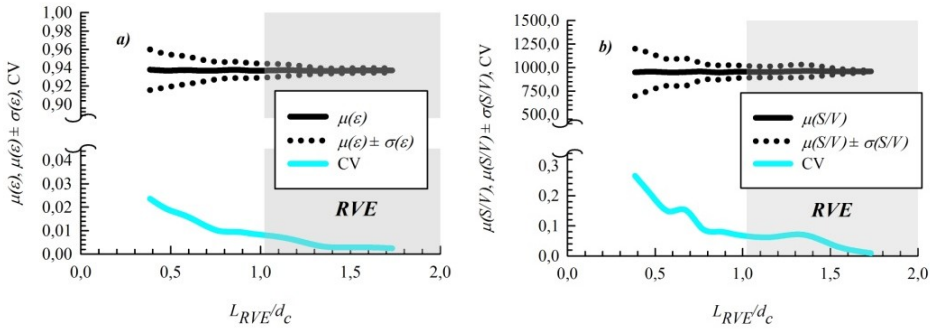


Fig. 30. Mean values of the porosity (a)) and the specific surface area (b)), vs. the length of the Representative Volume Element scaled with the cell size.

scanned sample.

The characteristics of the chosen RVEs are reported in Table 4.

3.6.1.2. Ideal model: generating the foam

The ideal foam model is generated according with Kelvin's foam model, by using the free-to-use software Surface Evolver [102], as described in the following.

First of all, three vectors are described, in such a way to form a cubic lattice in R^3 space and to use periodic conditions. Vertices of a surface can move through the domain. Due to periodic conditions, only 12 vertices coordinates are necessary to characterize the 24 vertices that form the Kelvin's foam. Vertices are linked by edges (36 in the Kelvin's foam). Only 24 edges are associated in the code, and the r 8 edges are determined by indicating if an edge is oriented in a certain direction in the R^3 space, starting from one of the 24 edges. Finally, the edges linked by the 14 faces (6 squares and 8 hexagons) are indicated, and two Kelvin's foams with equal volume are obtained.

Table 4. Morphological characteristics of the Representative Volume Elements.

L_{RVE} (mm)	ϵ	$CV \cdot 10^2$	S/V (1/m)	$CV \cdot 10^2$
1.88	0.87	2.47	1408	13.79
1.89	0.94	0.86	954	7.10
1.91	0.96	0.39	922	3.37

The slightly curved configuration that enhances the isoperimetric quotient q (Fig. 14) is obtained refining the foam geometry and the surface energy is reduced by using a gradient-descent method. The wet foam is built up by using the command `wetfoam2.cmd`, that substitutes the edges with nearly-equilateral triangular section edges of a chosen width, which characterizes the foam porosity. Again, the geometry is refined and the surface energy is reduced with a gradient-descent method, obtaining a wet (open-cell) foam with a concave-triangular strut shape. The generation of a wet foam is sketched in Fig. 31. It is worth remarking that the foam is obtained as a simplicial complex; thus refining the geometry is very important to improve the quality of its boundaries.

The foam so obtained is saved as a IGES file and exported into COMSOL Multiphysics, that scales and replicates it along every direction. Because thermally developing effects are also analyzed in the present study, a single Kelvin's cell is replicated twenty times along the flow direction. Besides, from a single cell, it is possible to calculate the specific surface area S/V for different porosities and cell sizes. Indeed, only two parameters are necessary to univocally define the morphology of a foam. By generating foams with different porosities and scaling them for different cell sizes, the following correlation is derived by means of a multiple regression:

$$\frac{S}{V} = 2.121 \frac{\varepsilon^{-3.513}}{d_c} \quad (50)$$

with a coefficient of determination $R^2 = 0.9954$. Eq. (50) is valid for $0.85 < \varepsilon < 0.95$ and $0.5 \text{ mm} < d_c < 2.0 \text{ mm}$.

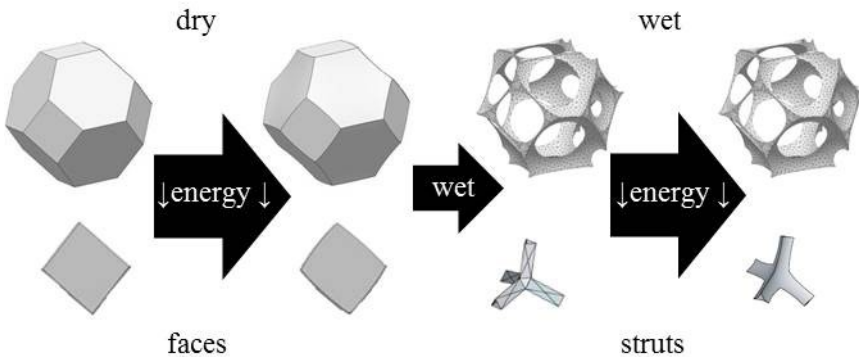


Fig. 31. Wet foam generation with Surface Evolver [142].

Foams generated with this technique have a concave-triangular shape due to the minimization of surface energy process. It is known that foams generated with a casting process exhibit a strut shape dependent on the porosity, varying from circular to concave-triangular, as it was sketched in Fig. 27. In order to generate foams with different strut-shapes, foams developed with Surface Evolver must undergo some modifications. An in-house MATLAB code is used to generate Kelvin's foams with different struts shapes, with a preset porosity. Making references to the three scanned foams, with 0.87, 0.94 and 0.96 porosity, the ideal foam strut shape has been adjusted in order to obtain different strut shapes and, time by time, the shape that matches the real foam shape. The code is developed in such way as to make negligible the dependence of porosity and cell size on the struts shape. It is worth remarking that modifications make difficult to carry out simulations for array of cells.

Different strut shapes of ideal and real foams are sketched in Fig.32, where the images within black frames indicate the shape of ideal struts that reproduces the corresponding real one.

The specific surface areas obtained are measured with MATLAB as the sum of the areas of the interfacial triangles divided by the foam volume. They are resumed in Table 5.

3.6.2. Mathematical model

Three-dimensional single-phase fluid mass, momentum and energy governing equations are employed in the evaluation of heat transfer and pressure drop. The flow is assumed to be stationary and incompressible, with uniform thermophysical properties of the air in the entire computational domain. The flow can be assumed as laminar, if the Reynolds number based on

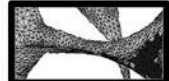
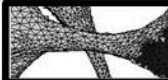
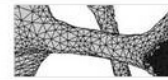
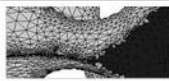
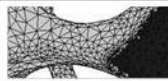
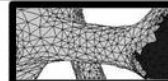
Model Shape	Ideal			Real Real
	Concave	Triangular	Convex	
$\varepsilon = 0.97$				
$\varepsilon = 0.94$				
$\varepsilon = 0.88$				

Fig. 32. Different strut shapes of ideal and real foams.

Table 5. Specific surface area of the investigated 40 PPI foams.

ε	S/V (1/m)			
	Ideal			Real
	Concave	Triangular	Convex	
0.96	1142	945	779	922
0.94	1509	1223	1166	954
0.87	2053	1801	1675	1408

the pore size, Re_p , is less only than 200. Dybbs and Edwards [142] showed that in the 150 – 300 range of the pore Reynolds number flow in a porous medium is laminar unsteady. Hall and Hyatt [143] showed that the transition to a fully turbulent flow occurs for Re_p about 150 and Della Torre et al. [144] showed that at $Re_p = 200$ there are some instabilities in the flow, denoting that transition from laminar to turbulent is starting. However, they concluded that pressure drop are fairly dependent on flow regimes, and Wu et al. [139] reported that differences between laminar and turbulence simulations are negligible. Comparisons of results from the present work with numerical and experimental data from the open literature confirm the feasibility of the present model.

Governing equations (3c), (4d) and (5c) are employed in the following. Boundary conditions for the real foam model are presented in Fig. 33. Boundary conditions for the ideal foam model are the same, and, in order to save computational power, simulations of thermally developing flow in the ideal foam made reference to a quarter of the structure, accounting for symmetry boundary conditions. Inlet and outlet fictitious sections are used to make computations easier. A plug flow inlet condition is assumed, for different superficial velocities $|\mathbf{u}|$, and a temperature $T_0 = 293.15$ K is set. At the outlet section, the ambient pressure $p_0 = 101$ kPa is set, with no viscous stresses. The lateral boundaries of the computational domain are assumed as symmetrical, with a slip condition, with no shear stresses for the flow field and an adiabatic boundary condition for the energy equation. At the solid/fluid interface, the fluid is set as no slip and a Neumann boundary condition is employed in the energy equation, setting a $|\mathbf{q}| = 1000$ W/m² heat flux entering the fluid from the solid phase.

The aforementioned governing equations coupled with boundary conditions are solved with a finite-element scheme based on the Galerkin method by using

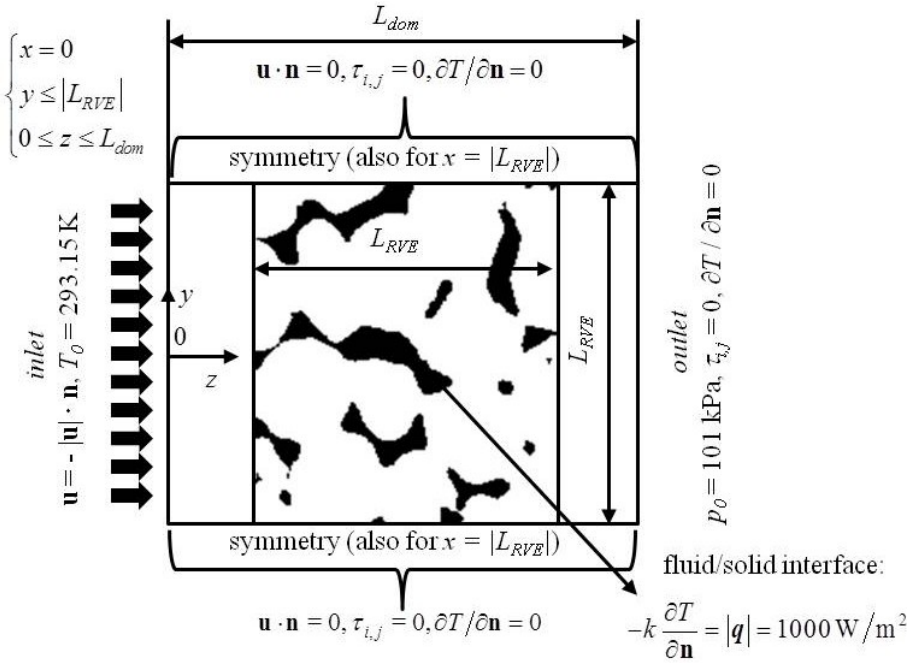


Fig. 33. Boundary conditions for the real foam model.

the commercial code COMSOL Multiphysics. Streamline and crosswind stabilization are used, and quadratic shape functions are employed. A non-linear solver is used to solve simultaneously governing equations, with a Lower Upper (LU) factorization method using the PARDISO sparse solver. Convergence criterion of 10^{-4} for velocity, pressure and temperature is verified, while mass and energy conservation are always checked with an error always less than 1%.

A tetrahedral mesh with a higher resolution near the boundaries is chosen for the numerical analysis. The meshes for the real foam and for the ideal foam with different struts shape are generated with iso2mesh (MATLAB), while the mesh for the ideal foams obtained directly from Surface Evolver is generated with the meshing tool of COMSOL Multiphysics. The grid independence has always been checked with the Richardson Extrapolation (RE). This statistical technique is a sequence acceleration method used to improve the rate of convergence of a sequence. The grid independence is verified for both real and ideal cases, on the most restrictive case, that with which the maximum pore velocity, $u_p = |\mathbf{u}|/\varepsilon$. The above test is performed on the differences of a variable, $\Delta\phi$, that could be either the average phases temperature difference $\Delta T = \langle T_s \rangle^s -$

$\langle T_f \rangle^f$, that is proportional to the heat transfer coefficient, or the pressure drop, Δp , between inlet and outlet sections.

Three meshes are defined, with N_i elements ($i = 1, 2, 3$), for which three variables, $\Delta\phi_b$, ($i = 1, 2, 3$) are obtained from simulations. The refinement grid coefficient, R , is defined as $R = N_{i+1}/N_i = \text{const}$. The Richardson Extrapolation of the variable difference, $\Delta\phi_{RE}$, is an estimation of $\Delta\phi$ when $N \rightarrow \infty$, and it is defined with the order of accuracy, p , as:

$$\Delta\phi_{RE} = \Delta\phi_{N_1} + \frac{\Delta\phi_{N_1} - \Delta\phi_{N_2}}{R^p - 1} \quad (51a)$$

$$p = \frac{\ln\left(\frac{\Delta\phi_{N_3} - \Delta\phi_{N_2}}{\Delta\phi_{N_2} - \Delta\phi_{N_1}}\right)}{\ln(R)} \quad (51b)$$

The Richardson Extrapolation of the variable difference, that is either ΔT or Δp , for the real foam, is reported in Fig. 34. By considering a 3% tolerance from the RE for both ΔT and Δp , it is possible to conclude that a mesh with 600,000 elements simulates real foams with a satisfactory accuracy.

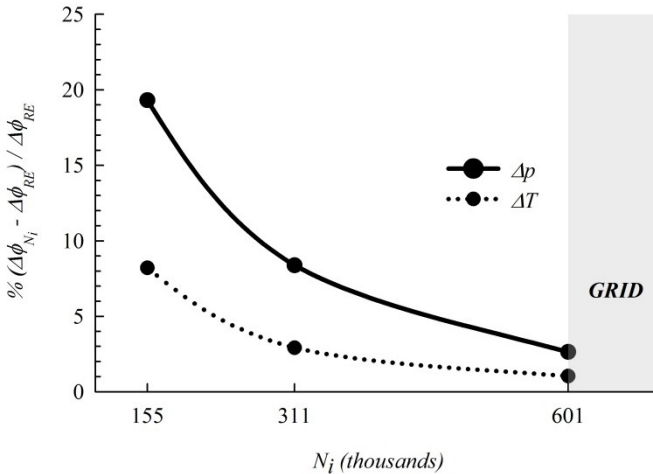


Fig. 34. Richardson Extrapolation of ΔT and Δp , for a real foam.

3.6.3. Results

Velocity, pressure and temperature fields are evaluated by solving the mathematical model previously described. Velocity and temperature fields, for $\varepsilon = 0.87$ and $|\mathbf{u}| = 1.5$ m/s, are presented in Figs. 35 and 36, respectively. Figure 35a shows that velocity profiles are modified by the porous matrix, while Fig.35 b points out that the entering heat flux increases temperature along the flow direction due to the entering heat flux.

3.6.3.1. Data reduction

Pressure drop, heat transfer coefficients and volumetric heat transfer coefficients are obtained from data reduction. Pressure drop are obtained either as $\Delta p = \langle p_{in} \rangle - \langle p_{out} \rangle$, when the pressure is taken as a surface average in the inlet and outlet sections, or as $p - p_{out}$, when different cross sections along the flow direction are considered. With reference to Eq. (17), volumetric transfer coefficient, h_v , and heat transfer coefficient, h_c , are given by:

$$h_v = h_c \frac{S}{V} = \frac{|\mathbf{q}|}{\langle T_s \rangle^s - \langle T_f \rangle^f} \frac{S}{V} \quad (52)$$

When thermally developing effects are analyzed, local effects are taken into account. Thus, a local $\langle T_s \rangle^s - \langle T_f \rangle^f$ is required. The physical scale for an open-cell foam is the cell scale. Therefore, an average temperature difference is evaluated for each cell, obtaining a value of heat transfer coefficients for each cell.

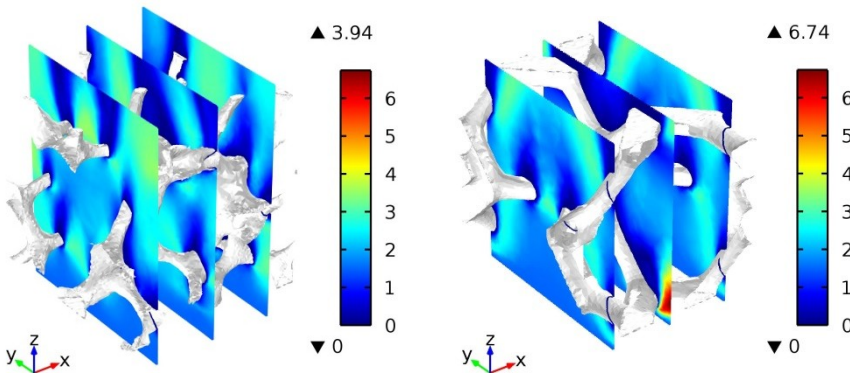


Fig. 35. Velocity modulus (m/s), for $\varepsilon = 0.87$ and $|\mathbf{u}| = 1.5$ m/s: real foam (left); ideal foam (right).

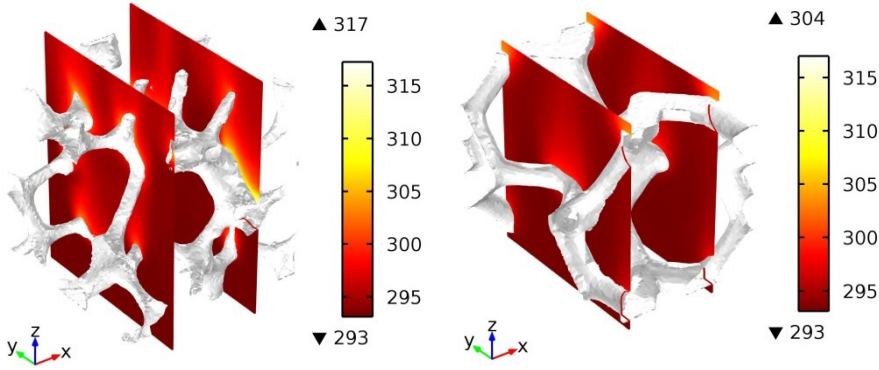


Fig. 36. Temperature fields (K), for $\varepsilon = 0.87$ and $|\mathbf{u}| = 1.5$ m/s: real foam (left); ideal foam (right).

A Nusselt number, Nu , and a volumetric Nusselt number, Nu_v , are defined as:

$$Nu_v = Nu \frac{S}{V} L = \frac{h_c L S}{k_f V} L = \frac{h_v L^2}{k_f} \quad (53)$$

where L is a characteristic length, that has to be defined. It should represent the typical scale of the problem, giving a physical sense to the dimensionless number. Similar considerations can be made on the Reynolds number, $Re = |\mathbf{u}| L/\nu$. Various characteristic lengths for the convection problem in porous media have been proposed. Examples are the square root of permeability, \sqrt{K} [2], that is the Brinkman screening distance; the product $K \cdot C$ [146]; the strut size, d_s [131]; the cell size d_c [139]; the pore size, d_p [132]; the reciprocal of the specific surface area, V/S [147]. Among these, the cell size seems to be the best choice because it is representative of the physical problem, it doesn't vary a lot in a foam sample, and it is easy to determine. The hydraulic diameter, d_h , was also proposed as a characteristic length by Schlegel et al. [134]:

$$d_h = 4 \frac{A_f}{L_f} = 4 \frac{\int_0^L A_f(L) dL}{\int_0^L L_f(L) dL} = 4 \frac{V_f V}{S V} = 4 \frac{\varepsilon}{S/V} \quad (54)$$

where A_f is the cross section available for flow, L_f is the wetted perimeter, and L is the length of the foam. From Eq. (54), it is possible to see that $d_h = f(\varepsilon, S/V)$. It is important to observe that the morphology of a foam can be uniquely

characterized if two morphological parameters are known, making d_h a very interesting characteristic length parameter. Besides, the cell size can be scaled with the porosity, thus obtaining a characteristic length, d_c/ε , that contains two morphological parameters for the characterization of a foam. In conclusion, it is possible to argue that d_h and d_c/ε are the best characteristic lengths.

3.6.3.2. Results for the real model

Volumetric and superficial convection heat transfer as a function of the superficial velocity $|\mathbf{u}|$, for different foam porosities, are reported in Fig. 37. The figure shows that both coefficients increase with superficial velocity. The convection heat transfer slightly decreases with increasing porosity because of the decrease of pore velocity $u_p = |\mathbf{u}|/\varepsilon$, while the decrease with porosity in the volumetric heat transfer coefficient is larger because of the dependence of the specific surface area on the porosity, previously reported in Table 3.

Pressure drop per unit length as a function of the superficial velocity, for different foam porosities, is reported in Fig. 38. The figure exhibits an almost quadratic dependence of the pressure drop on the velocity and a slight increase in the pressure drop at decreasing porosity. Experiments carried out on real foams showed a fairly agreement between experimental and numerical results.

Indeed, modeling pressure drop allows to account for wall effects, that highly affect the numerical solution [115]. However, the comparison with experimental data, reported in the following, will show that the real model can

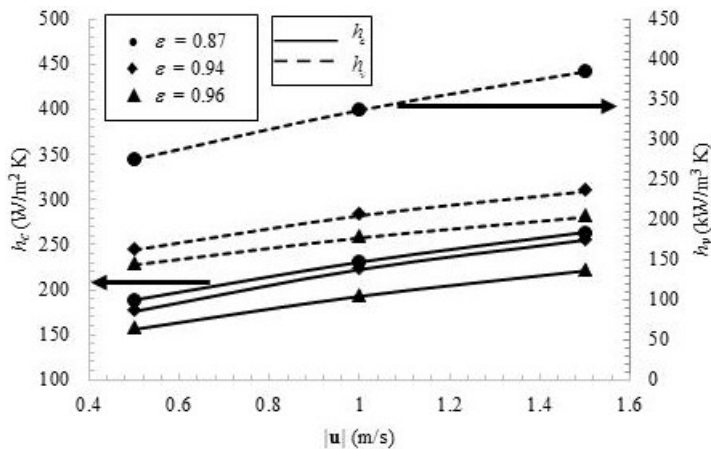


Fig. 37. Heat transfer coefficient and volumetric heat transfer coefficient vs. superficial velocity, for different porosities.

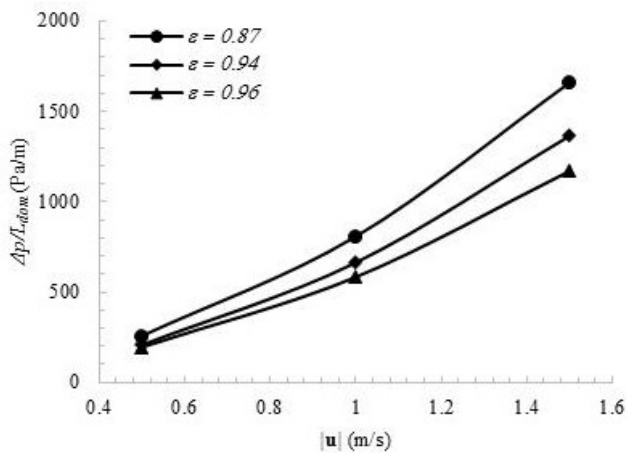


Fig. 38. Pressure drop per unit length vs. superficial velocity, for different porosities.

still provide acceptable results.

The convection heat transfer coefficient and the ratio of the pressure drop per unit length to the superficial velocity, for PPI = 40 and $\varepsilon = 0.94$, predicted by the real model are reported in Fig. 39. For the sake of comparison, data taken from the literature are also reported in the figure. Predicted convection heat transfer and pressure drop can be compared with Eq. (44) [131] and with numerical results, for $\varepsilon = 0.936$, from Diani et al. [118]; predicted pressure drops can also be compared with experimental data from Bhattacharya et al. [106], for $\varepsilon = 0.937$, and from Dukhan [114], for $\varepsilon = 0.923$. A very good

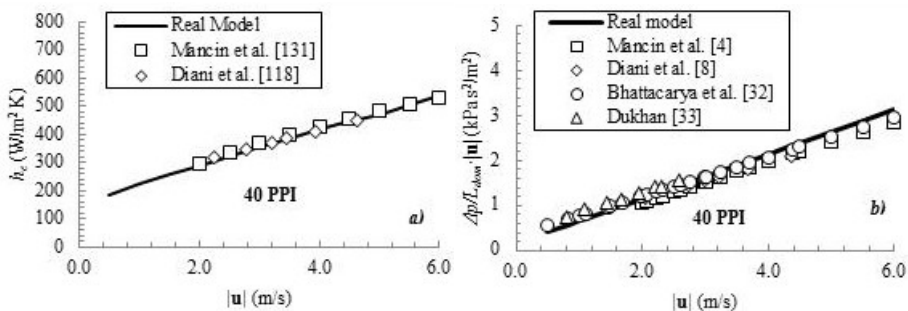


Fig. 39. Predictions of the real model vs. superficial velocity, for $\varepsilon = 0.94$ and PPI = 40: a) heat transfer coefficient; b) ratio of the pressure drop per unit length to the superficial velocity.

agreement is exhibited for both convection heat transfer coefficient and pressure drop.

3.6.3.3. Results for the ideal model: thermally developing effects

Results of simulations carried out on a Kelvin's foam model built up only by using Surface Evolver are presented in the following. In order to analyze thermally developing effects, reference as been made to a foam made up by twenty elementary cells aligned along the flow direction. The convection heat transfer coefficient is scaled using d_c/ε as the characteristic length. Therefore, the cell Nusselt number is defined as $Nu_c = h_c d_c/k_f \varepsilon$ and the cell Reynolds number is defined as $Re_c = \rho |\mathbf{u}| d_c/\mu \varepsilon$.

Simulations have been carried out for $\varepsilon = 0.87, 0.91$ and 0.94 , and for $67 < Re_c < 434$.

Nusselt number as a function of the ratio of the axial coordinate to the cell size, for various Reynolds numbers and $\varepsilon = 0.87, 0.94$, is reported in Fig. 40.

Nusselt number as a function of the ratio of the axial coordinate to the cell size, for various Reynolds numbers and porosities, is reported in Fig. 41.

Both figures show that Nusselt number increases along the flow direction reaching a maximum, then it decreases, reaching an asymptotic value after a certain cells number. Thus, three regions can be identified. The first is called the impingement region, the second is the thermally developing flow, and the third is the thermally developed region. In the impinging region, Nusselt number increases along the flow direction due to impinging effects in the inlet section, which affect downstream cells. For lower Reynolds numbers, this region

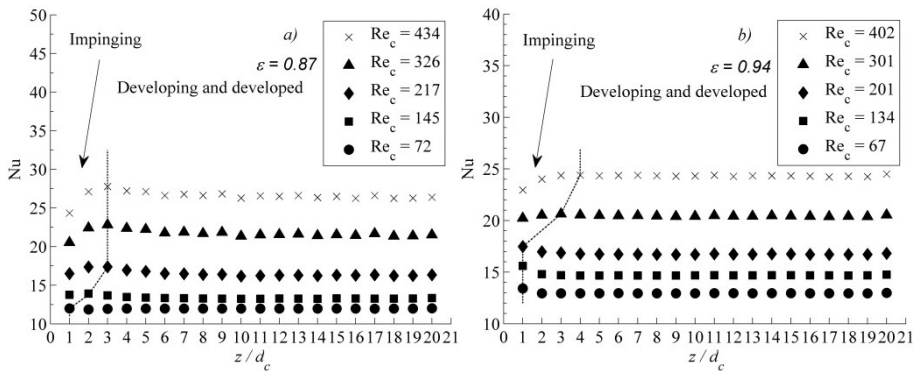


Fig. 40. Nusselt number vs. the ratio of the axial coordinate to the cell size, for various Reynolds numbers: a) $\varepsilon = 0.87$; b) $\varepsilon = 0.94$.

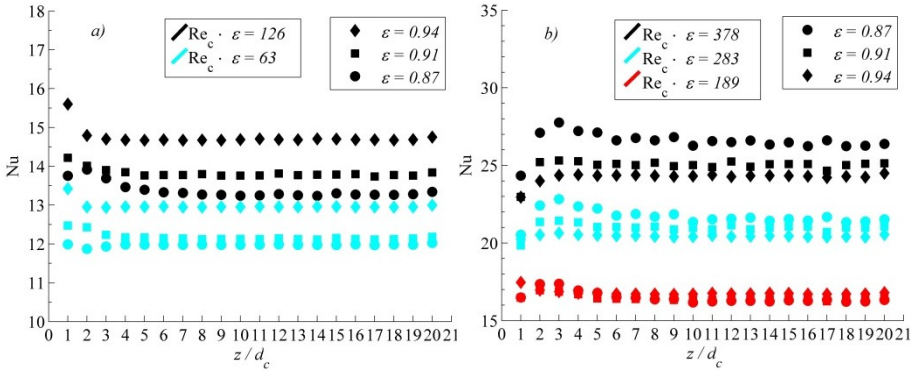


Fig. 41. Nusselt number vs. the ratio of the axial coordinate to the cell size, for various cell Reynolds numbers and porosities.

becomes practically negligible, and, on the other hand, this region is wider when Reynolds number increases, because of inertial effects in the fluid. Besides, since porosity is included in the Reynolds number, a decrease in porosity increases the Reynolds number and enlarges the impinging region. We state that the impinging flow effects must be taken into account when $Re_c \cdot \epsilon \geq 284$. The thermally developing region begins when Nusselt number reaches its maximum value. Afterwards, the Nusselt number reaches an asymptotic value, and a thermally developed region can be identified.

Figure 41 shows that Nusselt number increases with porosity at lower Reynolds numbers, while the opposite occurs at higher Reynolds numbers. This point will be clarified later with a pore-scale analysis.

The thermally developed Nusselt number, Nu_T , is defined as the Nusselt number of the i cell for which differences with the Nusselt number of the $i-1$ cell becomes lower than 1%. The thermal entrance length, z_T , is the axial coordinate at which the flow becomes thermally developed. Its ratio to the cell size, L_T/d_c , as a function of the porosity, for various Reynolds numbers, is reported in Fig. 42. One can notice that the larger the porosity the shorter the entrance length, since a larger quantity of solid material requires a larger length for the flow development. The entrance length increases at increasing $Re_c \cdot \epsilon$, as it occurs in a duct.

Volumetric Nusselt number as a function of the ratio of the axial coordinate to the cell size, for various Reynolds numbers and porosities, is reported in Fig. 43. By performing a multiple least-square, the following correlation is obtained:

$$Nu_{v,T} = 2.897 Re_c^{0.4827} \epsilon^{-4.271} \quad (55)$$

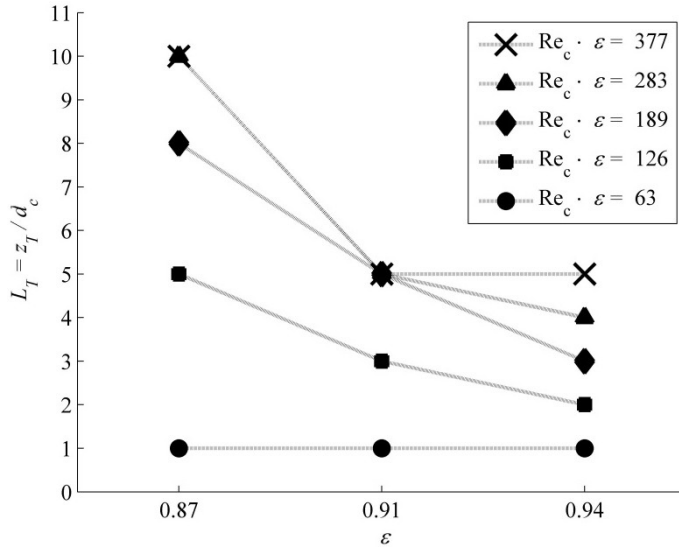


Fig. 42. Dimensionless thermal entrance length vs. the porosity, for various Reynolds numbers.

with $R^2 = 0.957$, that is valid for $0.87 < \varepsilon < 0.94$ and $67 < Re_c < 434$.

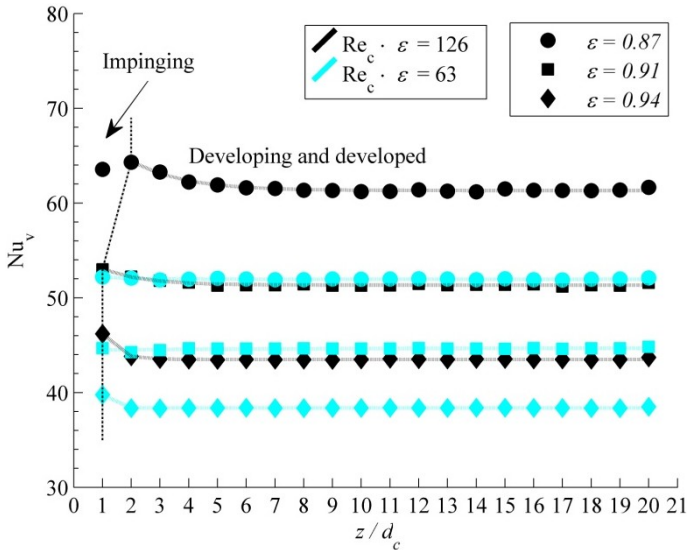


Fig. 43. Volumetric Nusselt number vs. the ratio of the axial coordinate to the cell size, for different Reynolds numbers and porosities.

Predictions by the ideal model are now compared with both experimental results from Younis and Viskanta [132] and with Eq. (46) [139, 140]. In order to compare Eq. (55) with experimental data, the cell size is to be correlated with the pore size. Using correlations among strut length, L_s , strut thickness, d_s , porosity, ε , and pore size, d_p , from [21, 83], and defining the cell size, with reference to the tetrakaidecahedron, by means of the correlation $V = 11.31 L_s^3 = 4/3 \pi (d_c/2)^3$, we obtain:

$$d_p = d_c \frac{1 - 0.971\sqrt{1 - \varepsilon}}{1.5312} \quad (56)$$

Comparisons with data from Wu et al. [139, 140] are made by means of Eqs. (46) and (55). The volumetric heat transfer coefficient as a function of the velocity, for different values of PPI, cells size and porosity, is reported in Fig.44. The comparison with experimental data show differences less than about 30 %; predictions are more accurate for low than for high velocities. The comparison with numerical data from Wu et al. [139, 140] shows a very good agreement. It is worth reminding that Wu et al. [139, 140] assumed a uniform temperature condition in a CAD-generated foam with circular struts.

A pore-scale analysis of the thermally developed region has also been carried out. For the sake of comparison, 10 values of Nusselt number were obtained for a single cell, thus the temperature difference in Eq. (52) was evaluated considering 1/10 of a single cell. A normalized Nusselt number, Nu^* ,

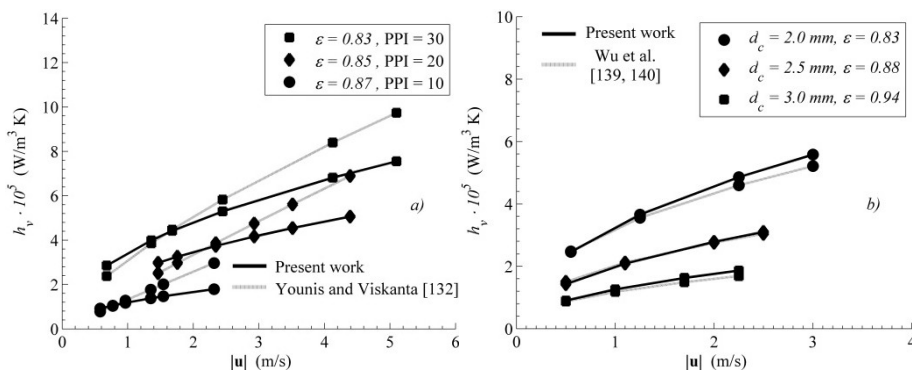


Fig. 44. Volumetric heat transfer coefficient vs. the velocity, for different values of PPI, cells size and porosity: a) experimental literature data; b) numerical literature data.

is defined as the ratio of the local Nusselt number to the thermally developed Nusselt number, Nu_T .

The normalized Nusselt number in two adjacent cells as a function of the dimensionless thermal entrance length, for $\varepsilon = 0.94$ and $Re_c = 201$, is reported in Fig. 45. Streamlines are in gray-scale, with lighter gray meaning faster pathlines. One can notice that the flow separation at the rear of foam struts, and a periodic behavior of the normalized Nusselt number through a developed cell; Nu^* minimum value is attained in regions of the aforementioned separation.

Due to flow mixing in the back of a strut at high velocities, Nusselt number increases. Downstream of a cell, from $z_T/d_c = 0.6$ to 1.0, the Nusselt number increases faster than upstream, due to the different orientation of the struts.

Figure 46, for a triangular foam strut with $Re_c = 72$, shows that the separation region can be quite large.

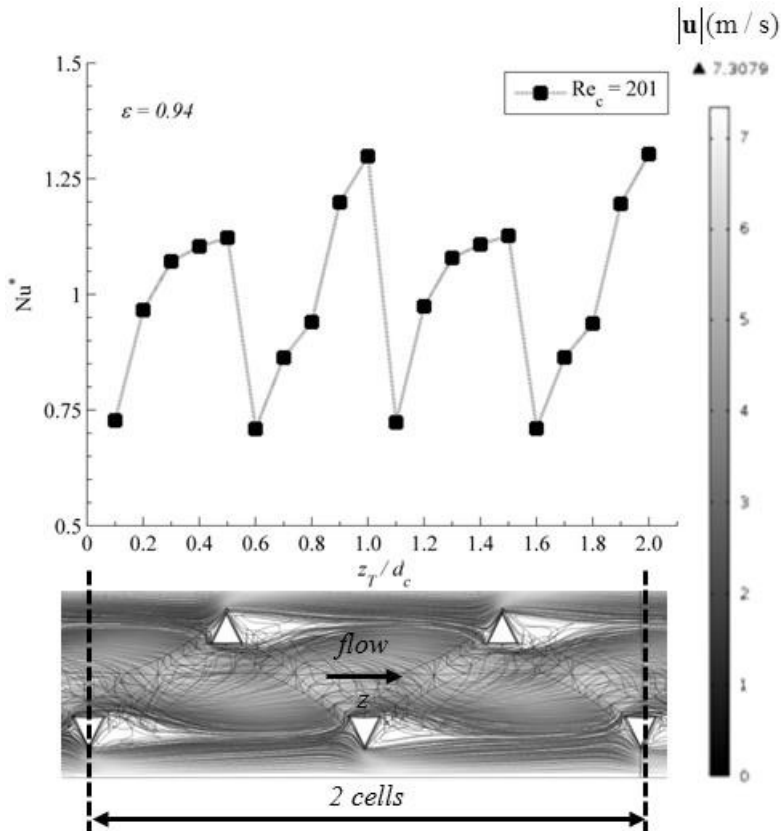


Fig. 45. Normalized Nusselt number in two adjacent cells vs. the dimensionless thermal entrance length, for $\varepsilon = 0.94$ and $Re_c = 201$.

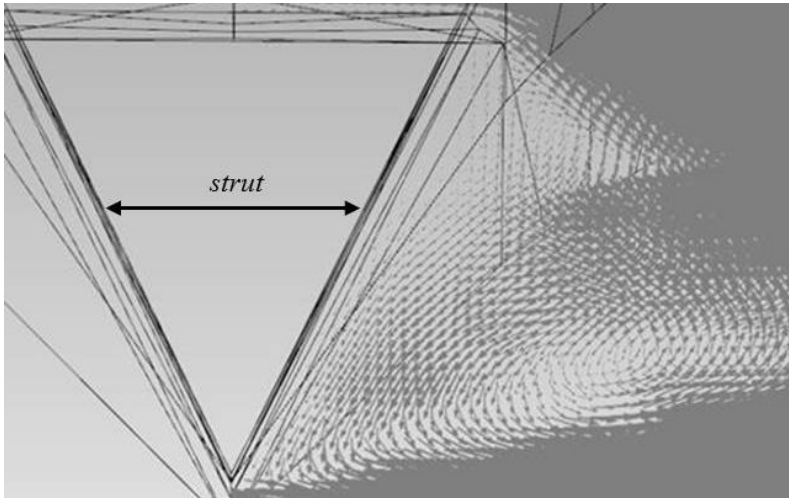


Fig.46. The separation region downstream of a triangular foam strut, with $Re_c = 72$.

In connection with Fig. 41, the above observed separation helps understand the reason why Nusselt number increases with porosity at lower Reynolds numbers, whereas the opposite occurs at higher Reynolds numbers. Two competitive effects are observed at pore scales: first, the velocity increase with decreasing porosity enhances the convection heat transfer; second, the separation increase with decreasing porosity reduces the convection heat transfer. At higher Reynolds numbers the first effect likely prevails on the second and increases Nusselt number at increasing porosity, whereas, at lower Reynolds numbers, the second effect prevails on the second and reduces convection heat transfer.

The heat transfer coefficient as a function of the dimensionless thermal entrance length in two adjacent cells, for thermally developed flow, various Reynolds numbers and $\varepsilon = 0.87$ and 0.94 , is reported in Fig.47.

The heat transfer coefficient as a function of the dimensionless thermal entrance length in two adjacent cells, for thermally developed flow, $\varepsilon = 0.87, 0.91, 0.94$ and various Reynolds numbers, is reported in Fig.48.

Figures 47a and 47b show a downstream shift of the axial coordinate at which the heat transfer coefficient attains the maximum value. The shift is inversely proportional to the Reynolds number. It is also worth noticing that, at both porosities, the larger the Reynolds number the larger the variation of the heat transfer coefficient with the axial coordinate within a cell.

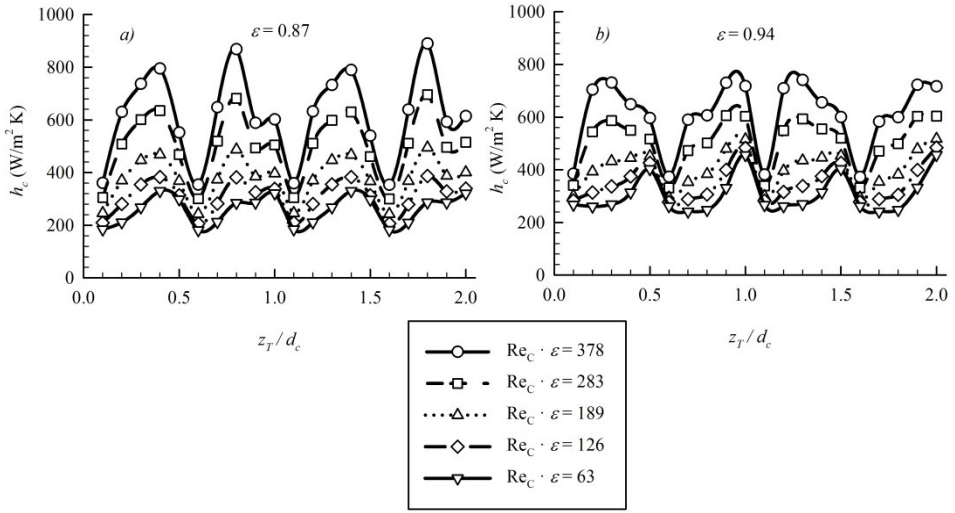


Fig. 47. Heat transfer coefficient vs. the axial coordinate in two adjacent cells, for thermally developed flow and various Reynolds numbers: a) $\varepsilon = 0.87$; b) $\varepsilon = 0.94$.

Figure 48a shows that at the lower Reynolds number the heat transfer coefficient increases at increasing porosity, whereas Fig.48b shows that does not occur at the higher Reynolds number. The figure exhibits also higher values

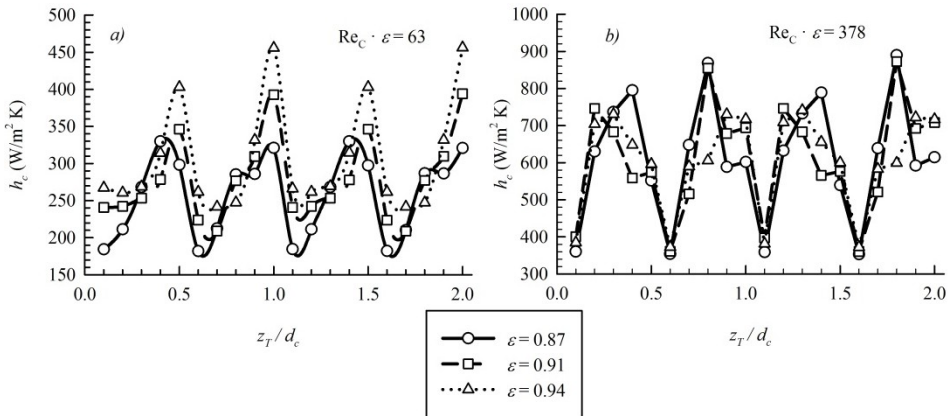


Fig. 48. Heat transfer coefficient vs. the axial coordinate in two adjacent cells, for thermally developed flow and $\varepsilon = 0.87, 0.91, 0.94$: a) $Re_c \cdot \varepsilon = 63$; b) $Re_c \cdot \varepsilon = 378$.

of the heat transfer coefficient for lower porosities than for higher porosities. As it was already discussed, the lowest value of the heat transfer coefficient in a cell occurs on the rear surface of the struts, because of the flow recirculation. Fig.48a exhibits remarkable differences between the lower values of the heat transfer coefficient at different porosities, whereas at the larger Reynolds number (Fig. 48b), the above mentioned differences are rather small.

3.6.3.4. Results for the ideal model: struts shape effects

The numerical model that allows to characterize the thermally developing flow in open-cell foams herein presented can be improved, taking into account some aspects of the foam morphology. By observing Fig.30, we see that the strut shape of a foam manufactured with the casting method depends on porosity. Since struts of foams generated by Surface Evolver have a concave-triangular shape, because of the minimizing energy process, some modifications with MATLAB are needed on the geometries in order to simulate the real strut shape. The process by which the above mentioned modifications are accomplished is described in this section.

Due to computational reasons, only one cell has been investigated. However predictions can be considered accurate enough, since Figs. 42 and 43 exhibited small differences among Nusselt numbers in the developing and fully developed regions. In the following the hydraulic diameter defined in (Eq. 54) is used as the characteristic length in Nusselt number, Nu_h , and Reynolds number, Re_h . Nusselt number as a function of Reynolds number, for different strut shapes and $\varepsilon = 0.87, 0.94, 0.96$ is reported in Fig.49. The figure shows that Nusselt numbers predicted by the ideal models are closer to those predicted by the real models when the shape of the ideal struts shape better approximates the shape of the real struts. In particular, among the ideal models the convex-triangular struts shape, with the highest foam shape factor ($\beta = 0.67$), maximizes the convection heat transfer. This occurs because the smoother strut geometry reduces local flow separation effects, that have a negative impact on convection.

Pressure drop as a function of the axial coordinate, for different strut shapes, $\varepsilon = 0.87, 0.94, 0.96$ and $|\mathbf{u}| = 0.5 \text{ m/s}, 1.0 \text{ m/s}, 1.5 \text{ m/s}$, is reported in Figs. 50, 51, 52, respectively. The pressure drop has been analyzed neglecting inlet effects, that are higher in an ideal foam than in a real foam, because of the the different strut arrangement. Indeed, the ideal foam is a geometrically-ordered foam, while the real foam is taken with the RVE approach, for which the strut orientation effects are not taken into account.

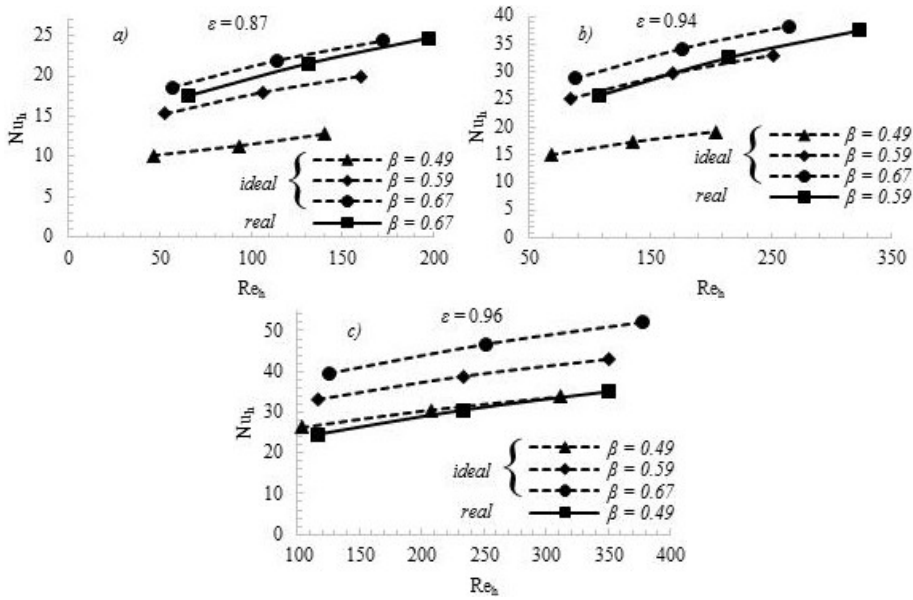


Fig. 49. Nusselt number vs. Reynolds number for different strut shapes: a) $\varepsilon = 0.87$; b) $\varepsilon = 0.94$; c) $\varepsilon = 0.96$.

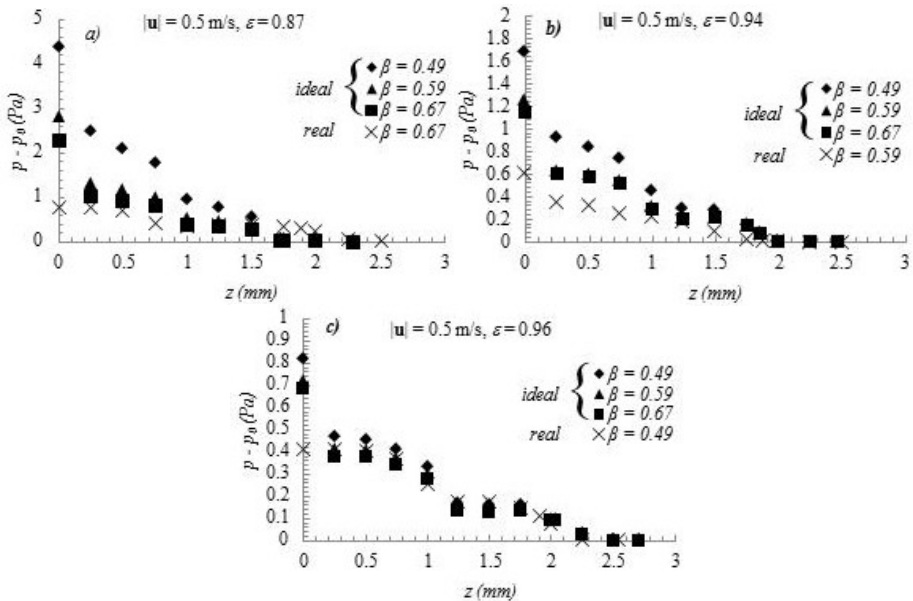


Fig. 50. Pressure drop vs. the axial coordinate, for different strut shapes and $|u| = 0.5$ m/s: a) $\varepsilon = 0.87$; b) $\varepsilon = 0.94$; c) $\varepsilon = 0.96$.

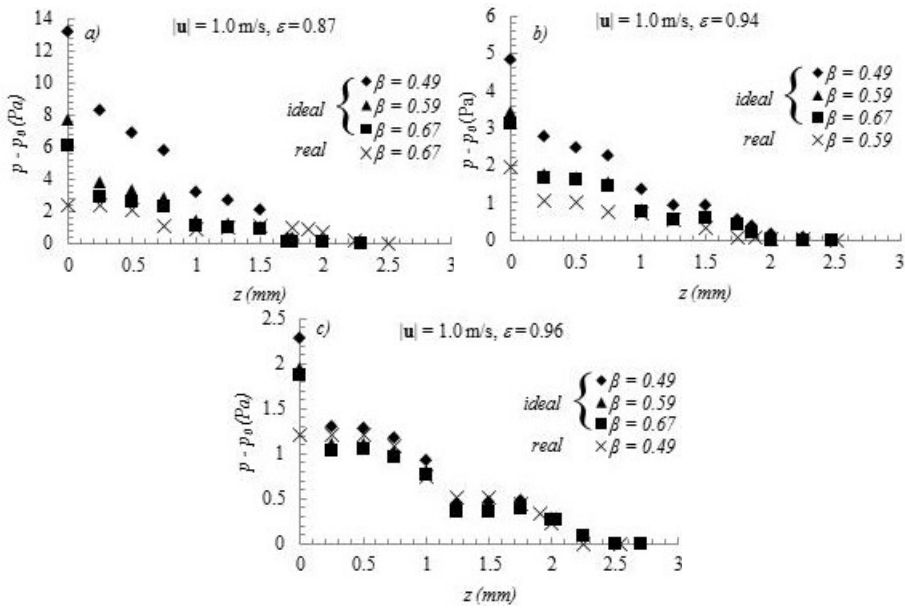


Fig. 51. Pressure drop vs. the axial coordinate, for different strut shapes and $|u| = 1.0$ m/s: a) $\epsilon = 0.87$; b) $\epsilon = 0.94$; c) $\epsilon = 0.96$.

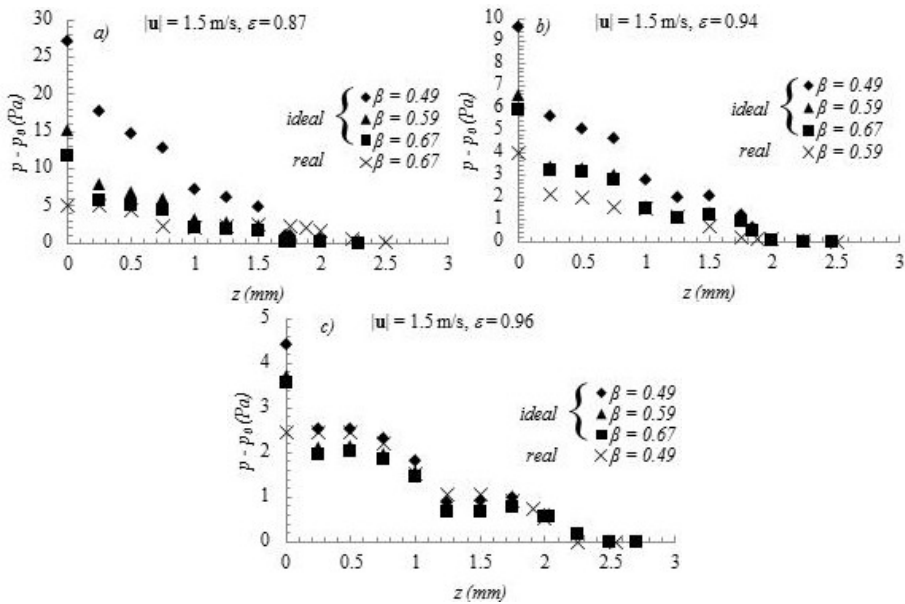


Fig. 52. Pressure drop vs. the axial coordinate, for different strut shapes and $|u| = 1.5$ m/s: a) $\epsilon = 0.87$; b) $\epsilon = 0.94$; c) $\epsilon = 0.96$.

Figures 50 – 52 confirm that, immediately downstream of the inlet section, the minimum difference between pressure drop predicted by ideal and real models occurs when the foam shape factor is the same. As a matter of fact, large differences between real and ideal models predictions are exhibited in the inlet section of the foam, since the arrangement of struts in ideal models causes a higher pressure drop. If reference is made only to the ideal models, figures show that the maximum pressure drop occurs for $\beta = 0.49$, because the concave-triangular strut shape enhances drag forces.

In conclusion, we can state that:

- Real foam models predict highly accurate convection heat transfer coefficients, whereas the accuracy of predicted pressure drop is affected by factors, such as the RVE choice that is limited by computational resources;
- There are both impinging and thermally developing effects in open-cell foams less than 10 cells long; the investigated cases downstream of the tenth cell the flow was thermally developed;
- Since the struts shape affects both heat transfer and pressure drop, the accuracy of predictions by the ideal model improves when the strut shape is the same as that of the real foam. The convex-triangular struts shape with the maximum foam shape factor maximizes the Nusselt number and minimizes pressure drop.

3.7. Engineering applications of open-cell foams

Macroscopic analyses of engineering applications where open-cell foams enhance heat transfer are presented in the following.

3.7.1. Concentrated Solar Power (CSP)

3.7.1.1. Description of the technology: the volumetric solar receiver

The use of mirrors to concentrate solar rays in a point in order to warm surfaces is a very ancient issue. In 212 a.C., during the Siege of Siracusa (Italy), Archimedes used it to deflect sun rays onto the ships of the Roman fleet, causing fires (Fig. 53).

Nowadays, this principle can be used to obtain thermal or electrical energy. There are two types of receivers, that is the point where mirrors focus the solar radiation: the tubular receiver and the volumetric receiver (Fig. 54). In the first receiver sunlight is focused on a tube, where a fluid flows through; in the second receiver sunlight irradiates a porous material, that absorbs radiation and



Fig. 53. Giulio Parigi, *Greek mathematician Archimedes' mirror burning Roman military ships*, 1599-1600. Fresco. Stanzino delle matematiche, Galleria degli Uffizi, Firenze, Italy.

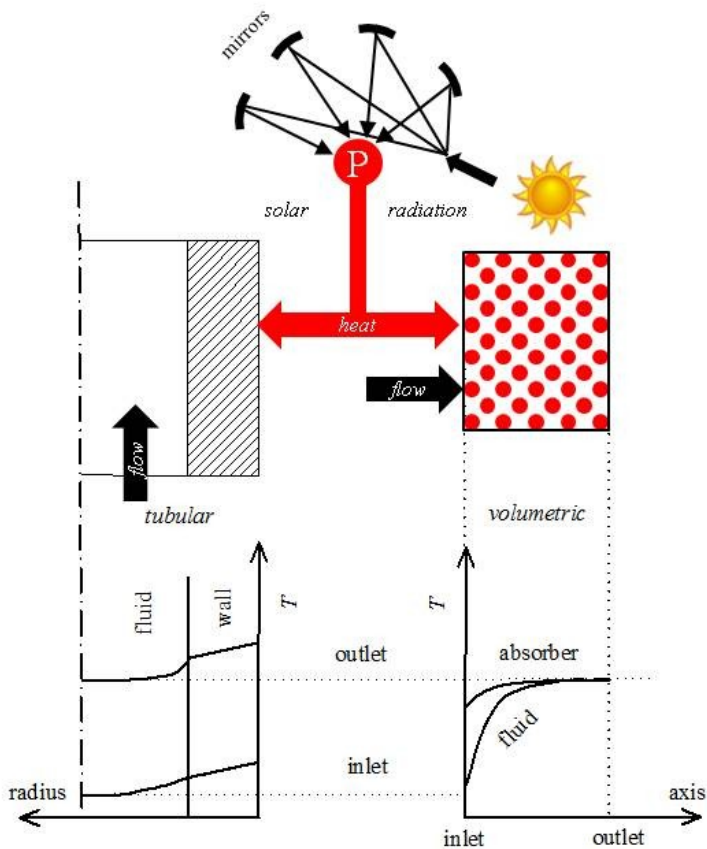


Fig. 54. Tubular and volumetric solar receivers.

transfers energy to a fluid that flows through. In the second receiver the volumetric effect reduces radiative losses, increasing the thermal efficiency.

Two Concentrated Solar Power CSP configurations can be distinguished for volumetric solar receiver applications [148]: in an open-loop receiver a stream of air, after being heated by the receiver, transfers heat to a steam generator, that moves a steam turbine; in a closed-loop receiver the air is directly expanded in a gas turbine of a Combined Cycle system (CC).

A first example of volumetric absorber was proposed by Fricker [149] in the 1983. Many prototypes and projects have then been presented. In the SOLGATE project [150], three modules in series, with different working temperatures, were the receiver. The first, at the lowest temperature, was a metal tube; the second, at intermediate temperature, was a metal wire mesh; the third, at the highest temperature, was a ceramic foam. The only operative volumetric solar receiver in the world is the 60 meters-high solar tower CSP located in Julich, in North Rhine-Westphalia (Germany), that uses a 1.5 MW steam turbine. The absorber module is made from SiSiC, consisting in an extruded parallel channel structure inserted into a cup [151].

3.7.1.2. Mathematical model

A parametric analysis of the thermal performance of a volumetric solar air receiver based on a ceramic foam will be carried out by using a macroscopic porous media approach.

The volumetric solar receiver is a high porosity ceramic foam cylinder, with a length of 50 mm and a diameter of 100 mm. The concentrated solar heat flux irradiating the inlet section is equal to 600 kW/m^2 . Air at ambient temperature enters the porous material and, flowing through it, is warmed up. Because of the irradiation at the inlet section, a LTNE model is employed.

The computational domain, with boundary conditions, is sketched in Fig. 55. Volume-averaged governing equations are Eq. (12b) for the mass, Eq. (14a) for the momentum, and Eqs. (18a) and (18b) for the fluid and solid energy. The radiative term $\nabla \cdot \mathbf{q}_r$ is modeled according to Beer-Lambert-Bouguer law (Eq. (22)), thus Eq. (23) is used. The coefficients needed to close such equations are the permeability, K , the inertial factor, f , the volumetric heat transfer coefficient, h_{cv} , the effective thermal conductivity for the solid phase, $k_{eff,s}$, the extinction coefficient, β . The first two mentioned closed coefficients are modeled by using Eqs. (42) and (43), the volumetric heat transfer coefficient is determined by using Eq. (55), the effective thermal conductivity for the solid phase is assumed

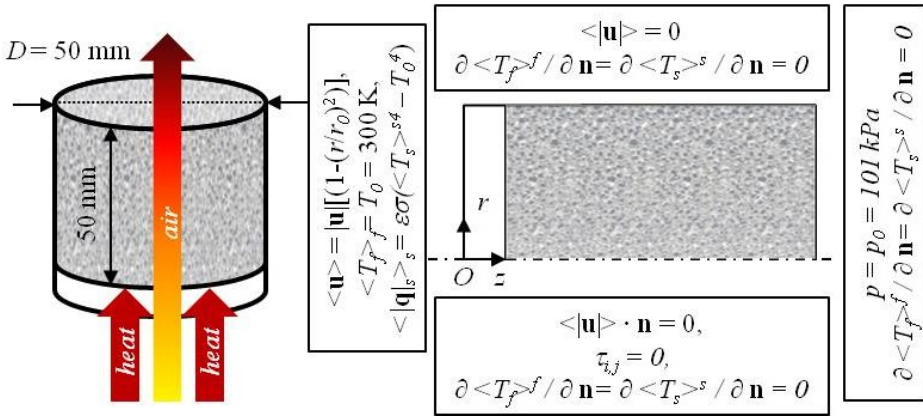


Fig. 55. The computational domain and boundary conditions of the volumetric solar receiver.

to be $k_{eff,s} = (1 - \varepsilon) k_s/3$ [54], and the extinction coefficient is evaluated from Eq. (31). The dependence of thermophysical properties on temperature is taken into account by using COMSOL Multiphysics material libraries.

Boundary conditions for the momentum equation are a laminar inflow condition in the inlet section, thus the flow is assumed to be fully developed at the entrance section by using a fictitious air inlet domain, a no-slip condition at the wall, a symmetry slip condition on the symmetry axis, and an atmospheric pressure condition at the outlet. As to the fluid phase energy equation, air at ambient temperature, $T_0 = 300 \text{ K}$ is assumed to enter the receiver; side walls and symmetry axis are adiabatic; an outflow condition is used in the outlet section. In the solid phase energy equation, radiation losses at the inlet section are taken into account by assuming a heat flux $|\mathbf{q}| = \varepsilon \sigma (\langle T_s \rangle_s^4 - T_0^4)$, where ε is the apparent emissivity of the ceramic foam at ambient temperature ($\varepsilon = 0.95$), σ is the Stefan-Boltzmann constant, T_s is the solid temperature at the inlet section. Zero-gradient temperature boundary conditions are employed at the symmetry axis, side wall and outlet section. The aforementioned governing equations, with closing coefficients and boundary conditions, are solved numerically with COMSOL Multiphysics. A 2D mesh with both triangles and quadrilaterals of about 15,000 elements has been used, with a convergence criterion of 10^{-4} . Both grid independence and relative tolerance have been checked. It is interesting to notice that computational times are far much smaller than for discrete simulations performed before.

3.7.1.3. Results

Simulations are performed for different values of inlet velocity, $|\mathbf{u}|$, cell size, d_c , and porosity, ε . The fluid and solid volume average temperatures as a function of the axial coordinate, predicted in the present study, for different values of the inlet velocity, the cell size, the porosity, together with numerical predictions by Wu et al. [140], are presented in Fig.56.

Wu et al. [140] modeled the radiation using the RTE with a P-1 model, that requires one more equation for the model. The model of the present study is simpler. It overestimates temperatures, since emitted and outscattered radiations are not accounted for. The figure shows that differences between temperatures predicted by the present model and by the Wu et al.'s model are less than 5%.

Radiation intensity vs. axial coordinate in a cell predicted in this study, for various cell sizes and porosities, is reported in Fig. 57. Figure 57a points out that the larger the cell size the higher the radiation intensity, because of the easier propagation of the radiation. In Fig.57b we can remark that the radiation intensity increases at increasing porosity, since again the propagation of radiation is made easier by the decreasing fraction of the solid volume.

The fluid and solid volume average temperatures as a function of the axial coordinate, predicted in the present study, for $|\mathbf{u}| = 1.30$ m/s and different values the cell size and the porosity, are reported in Fig.58. The figure shows that, whichever the cell size and the porosity, a same common value of the fluid and solid temperatures, called the equilibrium temperature, is attained. In a well performing volumetric receiver the so-called volumetric effect occurs, this meaning that the temperature of the irradiated side of the absorber is lower than the temperature of the fluid leaving the absorber. From a physical point of view,

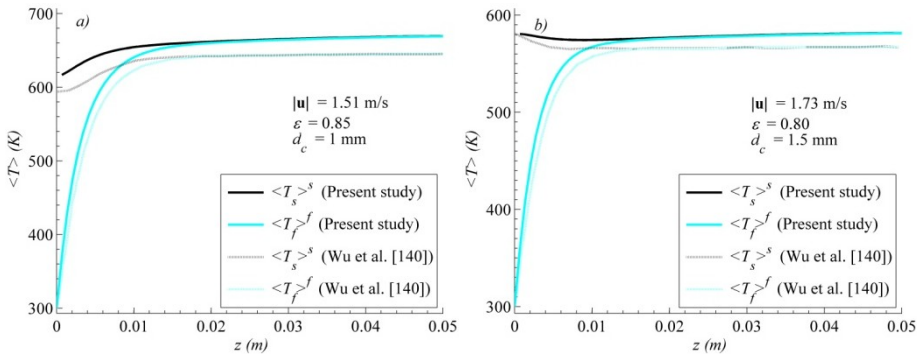


Fig. 56. Fluid and solid volume average temperatures vs. axial coordinate: a) $|\mathbf{u}| = 1.51$ m/s, $\varepsilon = 0.85$, $d_c = 1.0$ mm; b) $|\mathbf{u}| = 1.73$ m/s, $\varepsilon = 0.80$, $d_c = 1.5$ mm.

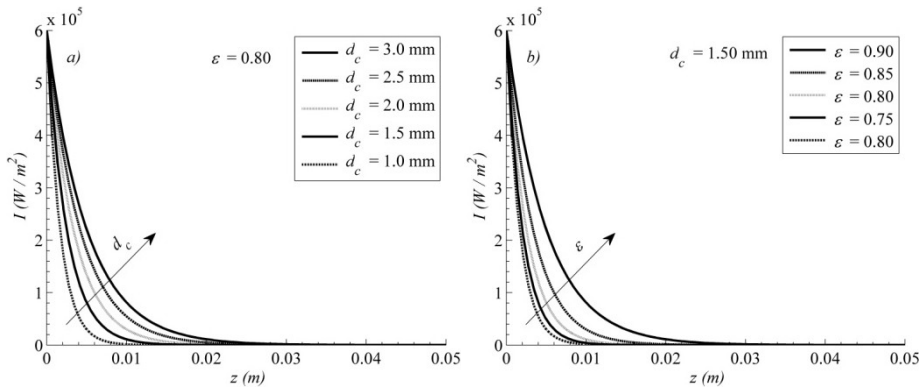


Fig. 57. Radiation intensity vs. axial coordinate; a) $\epsilon = 0.80$ and various cell sizes; b) $d_c = 1.5$ mm and various porosities.

the volumetric effect is characterized by a competition between radiation and interfacial convection. The radiation being the same, an increase in convection heat transfer increases the volumetric effect because heat is transferred more efficiently by the solid to the fluid.

The best volumetric receivers are that for $d_c = 1$ mm and that for $\epsilon = 0.90$ among those reported in Figs.58a and 58b, respectively.

The fluid and solid volume average temperatures and pressure drop as a function of the axial coordinate in a cell, for $\epsilon = 0.80$, $d_c = 1.50$ mm and various velocities, are reported in Fig.59. Figure 59a shows that the lower the velocity and, consequently, the lower the mass flow rate, the higher the equilibrium

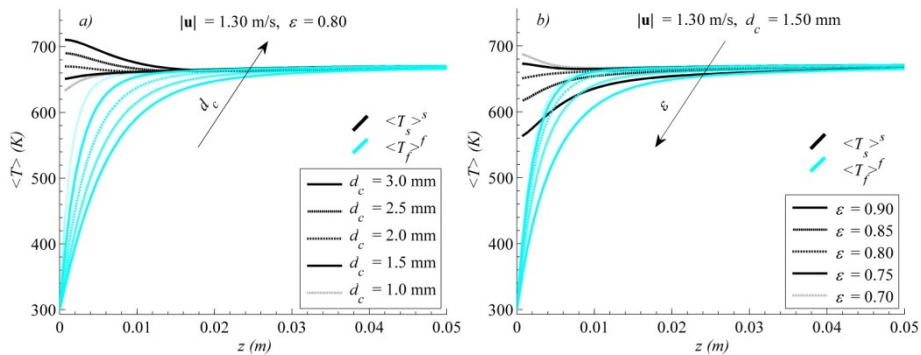


Fig. 58. Fluid and solid volume average temperatures vs. the axial coordinate, for $|u| = 1.30$ m/s: a) $\epsilon = 0.80$ and various cell sizes; b) $d_c = 1.50$ mm and various porosities.

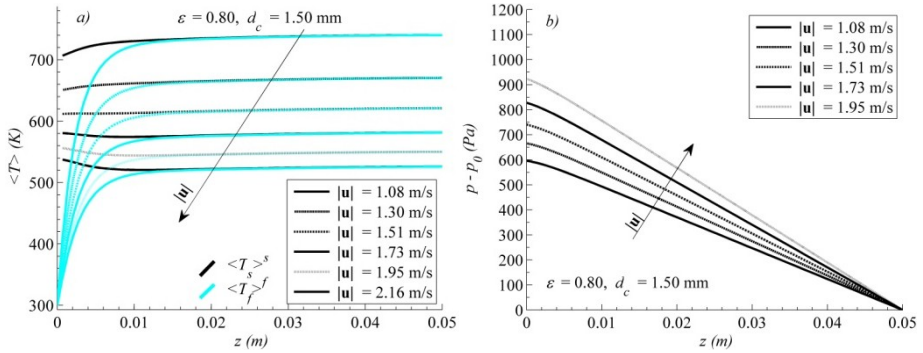


Fig. 59. Fluid and solid volume average temperatures and pressure drop vs. the axial coordinate, for $\varepsilon = 0.80$, $d_c = 1.50$ mm and various velocities.

temperature. We can also notice that radiation heat losses are higher at the inlet section.

Finally, the fluid and solid volume average temperatures and pressure drop as a function of the axial coordinate in a cell, for $\varepsilon = 0.90$, $d_c = 1.50$ mm, $|u| = 1.30$ m/s, air and helium, are reported in Fig.60. The comparison between air and helium shows the better performance of helium, that exhibits equal radiation heat losses and higher equilibrium temperatures. This was to be expected, because of the higher thermal conductivity of helium than air. Differences between pressure drop in air and helium are almost negligible.

3.7.2. Heat sinks

3.7.2.1. Metal-foam based heat sinks for electronic cooling

Nowadays, the progress of microchips technology is growing up very fast.

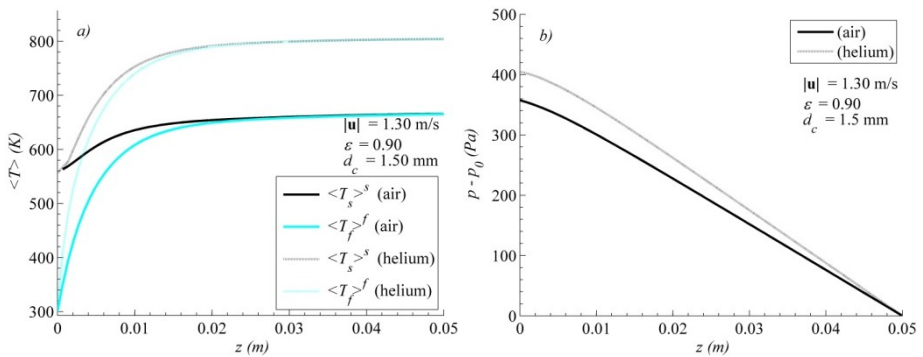


Fig. 60. Comparisons between air and helium volumetric receiver: a) temperature profiles and b) pressure drop.

The number of transistors in a dense integrated circuit doubles approximately every two years, according to the Moore's law (Fig. 61). A transistor is a semiconductor device with at least three terminals connected to an external circuit. It can be used to amplify or to switch an electronic signal. By applying a current or a tension to two of the terminals, it is possible to vary the current flow or other electrical quantities with the help of the third terminal. Thus, heat rate proportional to the square of the current is generated by means of Joule effect. In the coming years, due to the miniaturization of components, power density of about than 100 W/cm^2 are expected to be reached, as shown in Fig. 62. In fan-cooled heat sinks, where heat is removed from a surface by using a finned heat sink combined with a fan, fins are used to extend the heat transfer surface. However, with growing power density, new technologies are needed.

Metal foams are promising because they have a high specific surface area and a tortuous morphology that promote flow mixing, thus enhancing convection heat transfer. A finned metal foam geometry made up by inserts of aluminum foam between fins was proposed by Bhattacharya and Mahajan [152]. They concluded that this geometry enhances six times the heat transfer

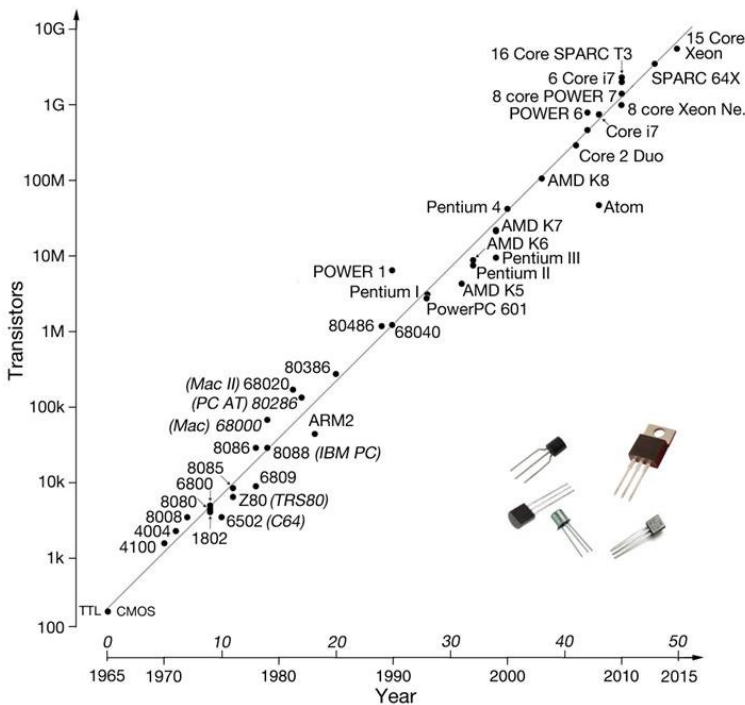


Fig. 61. Moore's law.

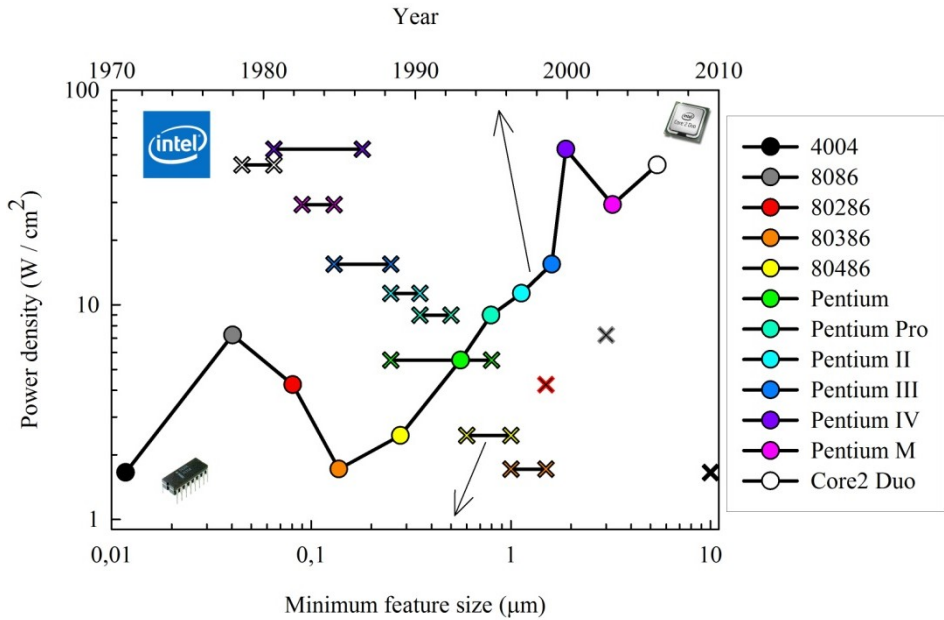


Fig. 62. Intel microprocessors power density vs. minimum feature size and year of introduction.

coefficient in conventional longitudinal finned heat sinks. However, if the comparison is made at the same value of pressure drop, the enhance in heat transfer reduces to 1.5 – 2 times. Hsieh et al. [153] proposed a heat sink made up by a aluminium foam under an impinging flow with a restricted flow outlet, that further enhances heat transfer. An experimental and numerical study of a finned aluminum-foam based heat sink, with a 0.963 porosity and 8 PPI, employing a circular impinging air jet cooling flow was carried out by Feng et al. [154]. They, analyzing metal foam heat sinks with and without fins, concluded that the finned configuration enhances of 1.5-2.8 times the heat transfer once the flow rate or the pumping power is fixed.

3.7.2.2 Mathematical model

An aluminium Finned Metal Foam (FMF) heat sink, together with the boundary conditions, is reported in Fig. 63. Boundary conditions hold also for the Metal Foam (MF) based heat sink, that has the same configuration without fins. The heated plate is a 68 x 68 mm² square. The ratio of the impinging flow section diameter, D , to the heated plate side, W , varied from 0.25 to 1. The height of the computational domain, H , varied between 10 mm and 40 mm. The

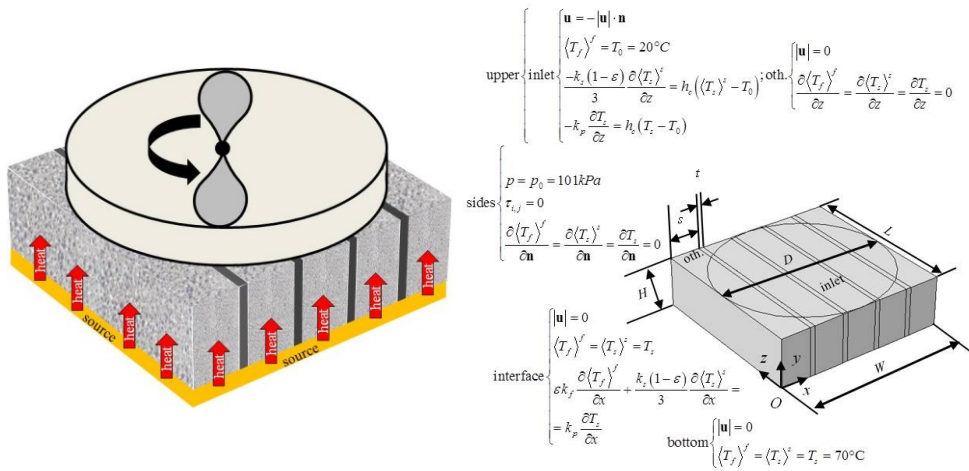


Fig. 63. Sketch of a metal foam based heat sink (FMF) and boundary conditions for the mathematical model.

fin thickness, t , is either 2 mm or 4mm. A 2 mm and 4 mm fins pitch was assumed. The number of fins used in the computations was 1, 2, 4, 6, 8 and 10. The porosity and the PPI of the aluminium foam varied from 0.88 to 0.97 and from 5 to 40, respectively. The thermal analysis was carried out applying a 50 °C temperature difference between the two extremities, with the heated plate at 70 °C, an acceptable temperature for a microchip. Due to the physics of the problem, an LTNE model is employed. Governing mass, momentum and energy equations for the porous domain are Eqs. (12c), (14b), (18a) and (18b), respectively, with $\nabla \cdot \mathbf{q}_r = 0$. The aluminium fins were modeled by using Eq. (5d). The volume-averaged momentum equation closing coefficients were Eqs. (42) and (43), taken from correlations from Wu et al. [104], while Eq. (55) was used for the volumetric heat transfer coefficient. The solid effective thermal conductivity was set as $k_{eff, s} = (1 - \varepsilon) k_s / 3$ [54]. Thermophysical properties were assumed to be independent of the temperature. Boundary conditions for the fluid flow are a plug flow at the inlet section, a no slip boundary condition on the upper part of the fins facing the plug flow, on the space between the upper square and the impinging section, on the foam-finned boundaries, and on the heated plate, due to the impinging flow. A zero relative pressure boundary condition with no shear stresses is imposed at the sides of the computational domain. In the energy equations, temperature is set as equal to 20 °C in the inlet section, except for the part of the fins that are in contact with the impinging flow, and to 70 °C on the heated plate. Outflow conditions are used on the

confining wall and in the outlet section. Robin boundary conditions are employed both on internal interfaces between fins and foam and on the upper part of fins. In both cases, the correlations for the heat transfer coefficients used by Feng et al. [154] are employed. Governing equations with boundary conditions are solved with COMSOL Multiphysics by using a 48,000 tetraedral mesh for the finned metal foam heat sink, while a 35,000 mesh was used for the foam heat sink. The above values were checked by verifying the number of elements that made the discretization error negligible. Like for the volumetric solar receiver model, computational times were very short.

3.7.2.3 Results

Dissipated heat rate as a function of the velocity, for the FMF and MF heat sinks, together with data by Feng et al. [154], is reported in Fig.64. The figure exhibits differences between predictions by the present model and Feng et al.'s model less than 8% for the FM model and less than 18% for the FMF model.

Let the convection heat transfer, h_c , be defined as:

$$h_c = |\mathbf{q}|/\Delta T \quad (57)$$

where the heat flux $|\mathbf{q}|$ is the ratio of the dissipated heat rate to the plate area.

Convection heat transfer coefficient and pressure drop are evaluated for $\varepsilon = 0.92$, PPI = 10, $|\mathbf{u}| = 0.5$ m/s, $t = 2$ mm, $H = 20$ mm, and $D/W = 1$.

The convection heat transfer coefficient and pressure drop as a function of the number of fins, for $t = 2$ mm and 4 mm, are presented in Fig. 65. The figure

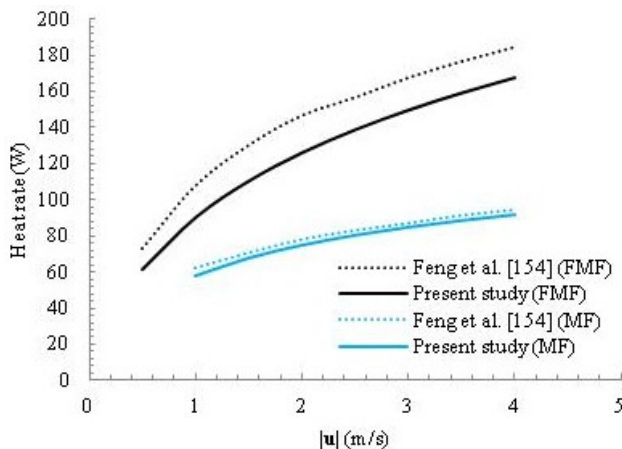


Fig. 64. Dissipated heat rate vs. the velocity, for the FMF and MF heat sinks.

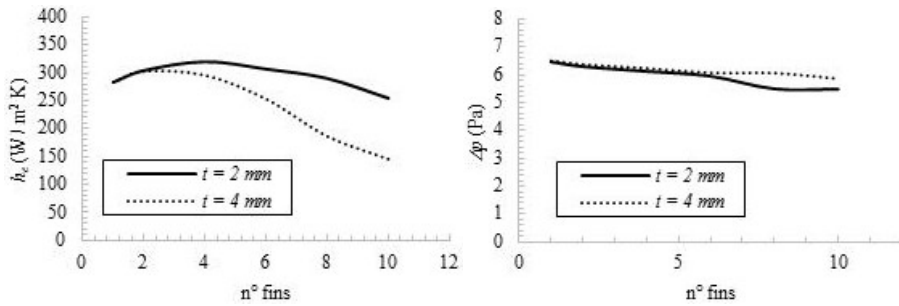


Fig.65. Convection heat transfer coefficient and pressure drop vs. number of fins, for $t = 2$ mm and 4 mm.

points out that, both for 2 and 4 fins, the heat transfer coefficient increases, attains a maximum and then decreases. This because there is a competition between two factors: the enhancement of number of fins, that promotes the dissipation, and the reduction of the foam inserts volume. In the first part of the curves, the enhancement of fins number improves heat sink performance, but when fins number increase, the reduction of foam volume causes a reduction in the dissipated heat. For the pressure drop, more fins means less foam volume, thus less pressure drop due to the reduction of foam inserts volume.

The convection heat transfer coefficient and pressure drop as a function of the sink height, for FMF and MF heat sinks with four fins, are reported in Fig.66. The heat transfer coefficient reduces with height because the impinging jet reaches the hot plate more difficultly, and also pressure drop reduces because a large fraction of the fluid exits the heat sink from the side walls of the foam immediately. Comparing the MF heat sink with the FMF heat sink, the latter exhibits a higher heat transfer coefficient but also a higher pressure drop.

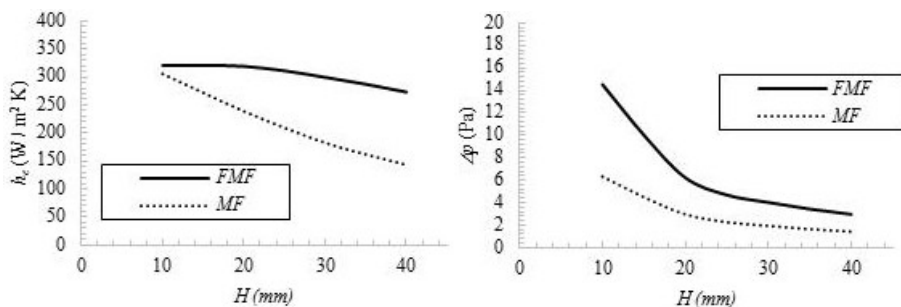


Fig.66. Convection heat transfer coefficient and pressure drop vs. height of the heat sink, for FMF and MF sinks with four fins.

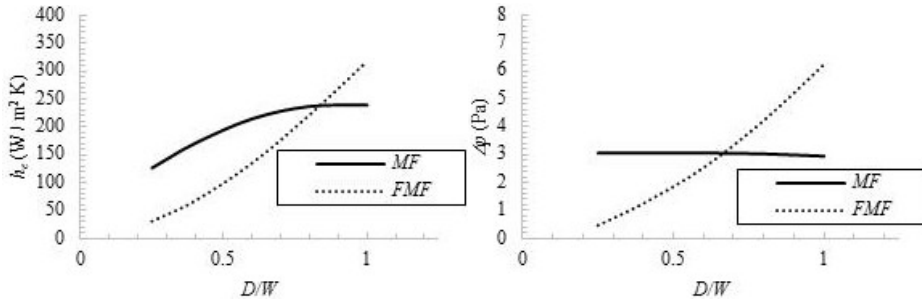


Fig.67. Convection heat transfer coefficient and pressure drop vs. D/W ratio, for FMF and MF sinks with four fins.

The convection heat transfer coefficient and pressure drop as a function of the ratio of the impinging jet diameter to the side length of the heated plate, for FMF and MF sinks with four fins, are reported in Fig.67. We notice that the larger the section, the higher the heat transfer coefficient, since increasing the plate size decreases the velocity of the fluid but allows the fluid to reach the plate in an easier way. The MF configuration performs better than the FMF one at low values of D/W because it is finned and has a smaller free area; thus the contribution of cold air is drastically reduced. Pressure drop in the MF configuration is unaffected by the size of the impinging section since the mass flow rate is unchanged, while pressure drop in FMF is affected by the size of impinging section because of the fins, that induce a concentrated pressure drop.

The convection heat transfer coefficient and pressure drop as a function of the porosity, for FMF and MF sinks with four fins, are reported in Fig.68. The figure shows that increasing the porosity reduces the volumetric heat transfer

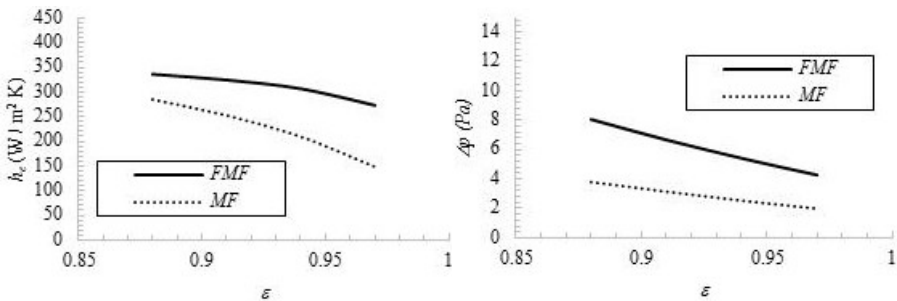


Fig. 68. Convection heat transfer coefficient and pressure drop vs. porosity, for FMF and MF sinks with four fins.

coefficient, because it is inversely proportional to the porosity, as well it reduces also the pressure drop, since the foam contains a decreasing fraction of solid.

The convection heat transfer coefficient and pressure drop as a function of PPI, for FMF and MF sinks with four fins, are reported in Fig.69. The figure exhibits a slight increase in heat transfer coefficient and a marked increase in pressure drop at increasing PPI. Heat transfer in MF configuration is almost independent of PPI, since at high values of the volumetric heat transfer coefficient a LTE condition is attained and enhancing PPI is useless.

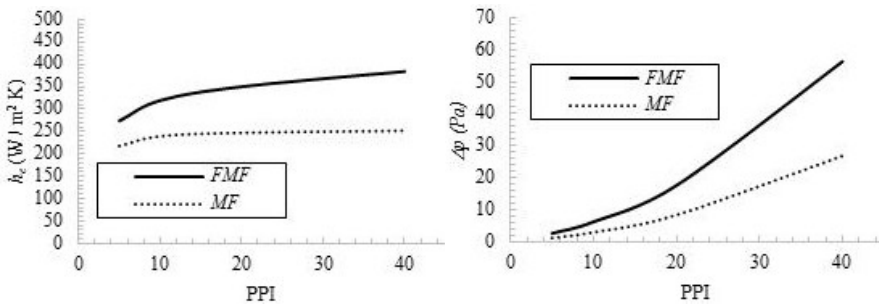


Fig. 69. Convection heat transfer coefficient and pressure drop vs. PPI, for FMF and MF sinks with four fins.

4.

BIOLOGICAL SYSTEMS

4. BIOLOGICAL SYSTEMS: A POROUS-MEDIA BASED APPROACH

As it was previously mentioned, porous media theories can be used to study transport phenomena in biological systems. The accumulation of Low-Density Lipoprotein (LDL) through the arterial wall is discussed in this section. The anatomy of an artery, together with the atherosclerotic plaque growth process, is presented. A multilayer model for the arterial wall is employed, in order to consider the wall heterogeneity. Analytical and numerical approaches are presented for a straight artery, a stenosed artery and the aorta-iliac bifurcation, analyzing LDL accumulation due to various effects, such as the non-Newtonian behavior of the fluid, the hypertension and the hyperthermia.

4.1. The cardiovascular system

4.1.1. General description

The cardiovascular system is the set of organs and vessels that ensures the blood circulation in a body [155]. Some of the most important contributors to its history are resumed in Fig. 70. One of the first witness on the study of this system is the Ebers Papyrus. It is dated in about 1550 B.C., about the Seventeenth Dynasty of ancient Egypt. It is a, 20 m x 20 cm, 110 page papyrus written in hieratic, with medical prescriptions. The heart is described as the main part of blood circulation, linked with the rest of the organism by vessels. In the classic antiquity, important contributions were given by Hippocrates, Aristotle, Erasistratus and Galen, while in the XIII century Ibn al-Nafis described the pulmonary circulation of the blood. William Harvey, in the XVII

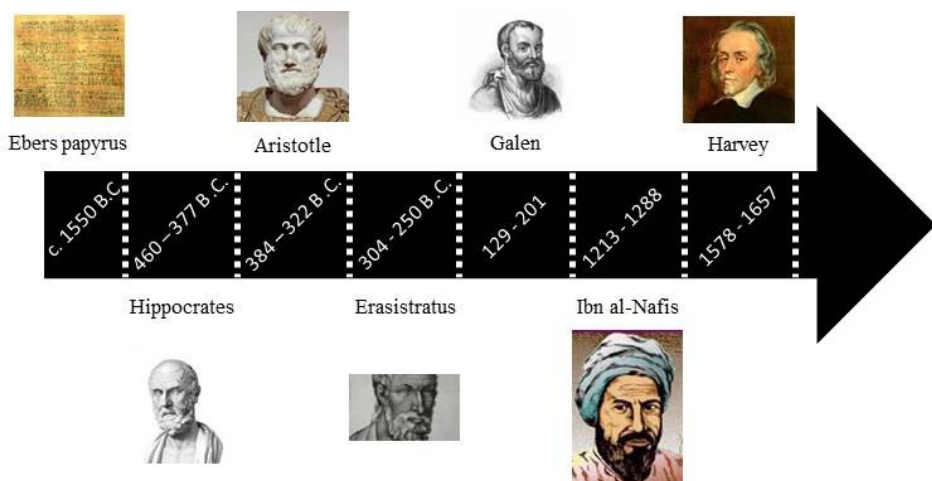


Fig. 70. Some contributors to the cardiovascular system knowledge.

century, was the first who described the systemic circulation and the properties of blood pumped through the body by the heart.

The human cardiovascular system is sketched in Fig. 71. In all the vertebrates, the heart (Fig. 71c) is the central part of the system. It acts as a pump that delivers blood to the body by arteries, veins and capillaries, able to generate a pressure that guarantees the blood circulation. The heart is mainly made up by striated muscle tissues; it is surrounded by a sack, named pericardium. Two cavities can be distinguished: on the left there is the arterious blood rich of oxygen, while on the right there is the venous blood. As to the higher and lower regions, in the upper we detect two thin walled compartments, named atria; in the lower we see two thick walled compartments, named ventricles. Each atrium is linked to the corresponding ventricle by the atrioventricular orifice. The left and right sides are separated by the interatrial septum, in the upper part, and by the interventricular septum, in the lower one. The blood poor in oxygen comes through the right atrium from the superior and inferior venae cavae, passing into the right ventricle by the tricuspid valve. Then, through the pulmonary artery, it enters the lungs, where it exchanges oxygen with carbon dioxide. The part of the cardiovascular system that has been described until now is called the small circulation. The oxygenated blood, through the left atrium, enters the left ventricle by the mitral valve, and then goes to the aorta, by which it is sent to the whole cardiovascular system. Together with the superior and inferior venae cavae, this part of the cardiovascular system is named the big circulation. After the aorta, the oxygenated blood passes through the arteries, and, after going through the capillaries, it goes back to the heart by the superior and inferior vena cavae.

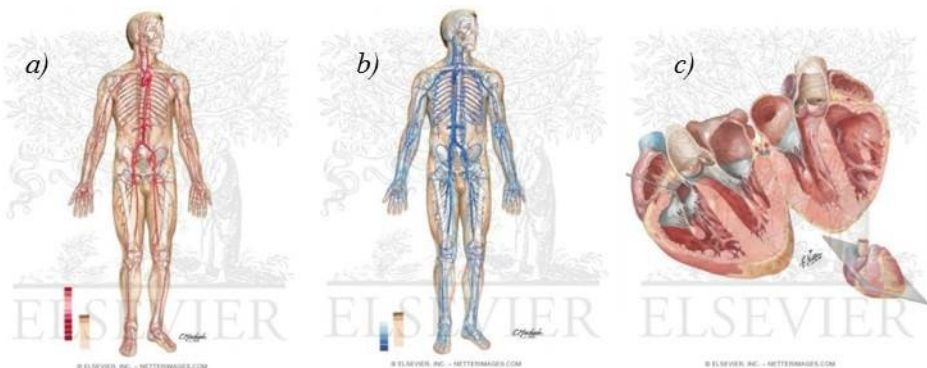


Fig. 71. Cardiovascular system [156]: a) major arteries, b) major veins; c) heart.

The arteries deliver oxygen and metabolites to cells and tissues, receiving from them carbon dioxide and catabolites. This causes the arterious blood to have a red color lighter than that of the venous blood.

Blood is a non-Newtonian fluid tissue that passes through the vessels. Its volume is made up by a 45% of cells embedded in a 55% of plasma. Cells are red (known as erythrocytes), white (known as leukocytes), platelets; red cells occupy the highest percentage in total volume. They are about 5 millions per mm^3 of blood. The role of red blood cells is to deliver oxygen from lungs to tissues, and their percentage in the blood volume is named hematocrit. In lungs, red blood cells exchange carbon dioxide with oxygen thanks to a protein named hemoglobin. White blood cells protect the body against infectious diseases and foreign invaders, while the platelets stop blood losses after an injury. The plasma is an aqueous solution with a 7.35 – 7.45 alkaline pH. It is composed of about 90% in volume of water (solvent), an 8% of proteins, and the rest are other substances, such as lipids. Plasma maintains the hematic volume, stabilizes the blood pH and the osmotic pressure with proteins, to deliver some substances, such as lipids. The nutrient substances are delivered from the vessels to the tissues, through the thin walls of the capillaries, that are vessels situated between an artery and a vein. A sketch of the capillary exchange is presented in Fig. 72. Along the capillary, mass exchange occurs through the semi-permeable walls, carrying some solutes, such as O_2 and CO_2 , via an interstitial fluid that is very similar to the plasma. Blood hydrostatic pressure and osmotic pressure are the main driving forces, and in the middle of the capillary they are equal, thus there is no solvent movement, Starling forces are zero. However, solutes are still passing due to the concentration gradient. Since

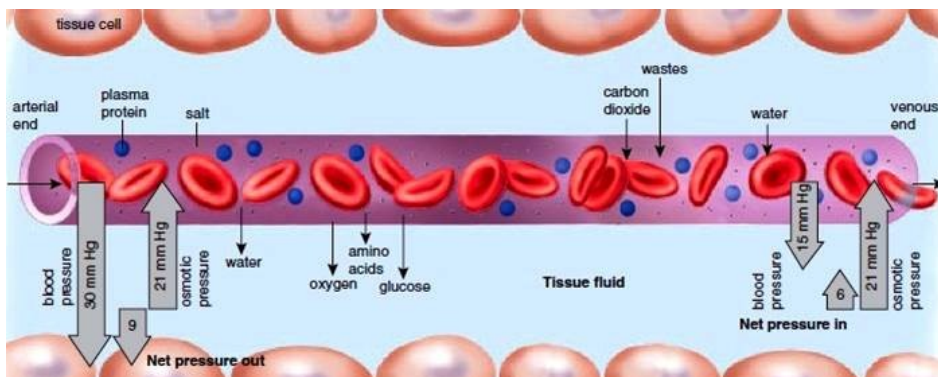


Fig. 72. Sketch of the capillary exchange [157].

not all the fluid leaving the artery goes into the venous end, the lymphatic system captures the remaining part of the fluid. In other words, it drains tissues from liquids and other exceeding substances, carrying them to the lymph. The lymph is a transparent fluid, with a composition similar to that of plasma, with some differences: for example, it has white blood cells and doesn't have plasma proteins.

4.1.2. Anatomy of an artery

With the exception of the pulmonary and the umbilical arteries, the oxygenated blood travels through the cardiovascular system by the arteries. They can be classified with reference to their dimensions. The biggest artery is the aorta, that exit the heart. It has a length of about 30-40 cm and a diameter of 2.5-3.5 cm (Fig. 73a) and can be divided into various sections. The first part is the ascending aorta, at which basis there are the left and the right coronary arteries, that circulate blood to the heart. Downstream of the ascending aorta, there is the aortic arch, whose upper part has three major branches: the brachiocephalic trunk, the left common carotid artery, and the left subclavian artery. The descending aorta is divided into the thoracic aorta and the abdominal aorta, that are limited by the passage through the diaphragm; in particular, in the lower border of the twelfth thoracic vertebra. From the first part, arteries such as

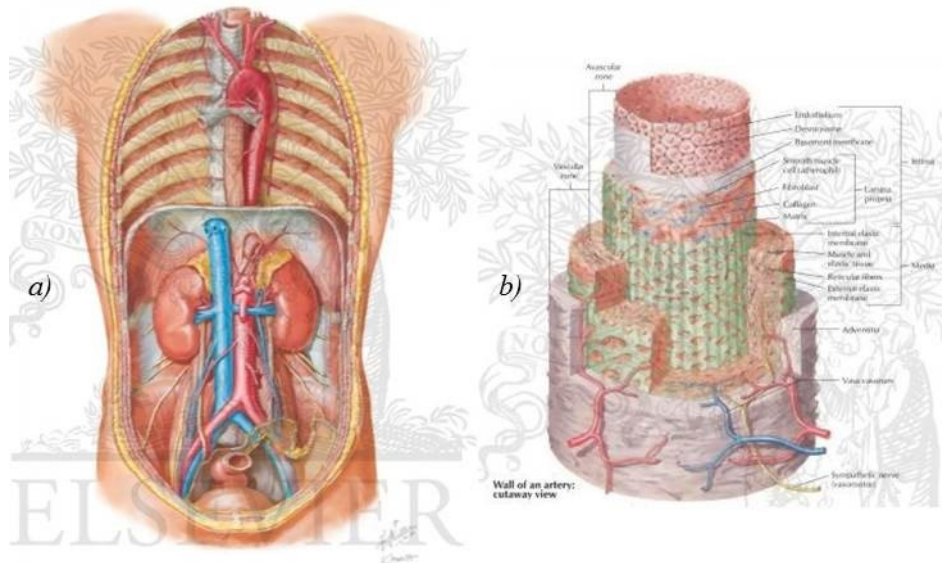


Fig. 73. Cardiovascular system [156]: a) aorta; b) artery wall.

the bronchial arteries start, while in the latter part other arteries, such as the celiac artery and the renal arteries, start. The end of the abdominal aorta bifurcates into the left and right common iliac arteries, where a smaller branch named the median sacral artery, is located. It is important to notice that, in a normal adult, aorta dimensions can vary from about 3 cm in the ascending aorta to 1.5 cm in the aorta-iliac bifurcation, that becomes 2 cm/m² and 1 cm/m² in the body surface area-adjusted version. Large arteries diameters span in the 7.0 – 30 mm range, while medium arteries diameters are in the 2.5 – 7.0 mm range. Diameters of small arteries are less than 2.5 mm. The arterioles, that forego the capillaries, have diameters less than 0.1 mm, while capillaries diameters are less than 10 μm. Capillaries are as small as to allow only one red blood cell to pass through it once a time. Such values are resumed in Table 6.

The microscopic anatomy of an artery is depicted in Fig. 73b. The lumen is the part which the blood flows through. Three parts, named tunica, can be distinguished through the wall: *tunica intima*, *tunica media* and *tunica adventitia*.

The tunica intima is the layer that faces the lumen; it is delimited by the endothelium and the Internal Elastic Lamina (IEL), also known as the internal elastic membrane. The part of the arterial wall in contact with the lumen is the endothelium. It is made up by squamous cells that form the epithelial tissue. It plays many roles, such as acting as a semi-selective barrier for solutes and white blood cells, or the control of blood pressure via vasoconstriction and vasodilation. A pathologic state that occurs when the endothelium loses its functions is the endothelial dysfunction. Endothelial cells are also covered by a glycoprotein-polysaccharide, named glycocalyx. The endothelium and the IEL are linked by a fine network of connective tissue, that is the main part of the tunica intima. The tunica intima is separated from the tunica media by the IEL. It is a membrane made of elastic tissue, thick and prominent in muscular arteries, while it is often incomplete and less prominent in arterioles.

The tunica media is made up by Smooth Muscle Cells (SMC) and elastic tissue. It is distinguishable from the tunica intima because of the different color, and of the fibers transverse arrangement. The amount of elastic tissue depends also on the dimensions; indeed, the aorta, that is the largest artery, has a very

Table 6. Typical arteries diameters.

	Aorta	large	medium	small	arterioles	capillaries
<i>d</i> (mm)	30 - 15	30 - 7	7 - 2.5	2.5 - 0.1	0.1 - 0.01	< 0.01

high amount of elastic tissue. A layer of elastic connective tissue, the External Elastic Lamina (EEL), separates the media tunica from the tunica adventitia.

The tunica adventitia is made up by collagen fibers, in order to anchor the vessel to nearby organs. It is absent in the capillaries. It is worth saying that also the vasa vasorum, that means “the vessels of the vessels”, is found in arteries. The vasa vasorum is a network of small blood vessels that supply the arterial walls, together with the nerva vasorum, that h control SMC of the tunica media.

4.1.3. Atherosclerotic plaque growth process

A Cardiovascular Disease (CVD) is a class of diseases that involves the cardiovascular system. In the 2012, CVD was the 47% of all deaths in the European Union (EU) [158]. It causes 4 millions of deaths in Europe per year, with 1.9 millions only in the EU [158]. It is the main cause of death of women in all Europe, and the main cause except for six countries for men [158]. CVD include coronary artery diseases (heart attack and angina pectoris), stroke, cerebral vascular disease, transient ischemic attacks, aorta aneurysms, and other phenomena. Despite many factors affect CVD, some, like coronary artery disease, stroke and peripheral artery disease, depend on atherosclerosis. Risk factors are smoking, diabetes, sedentary lifestyle and overweight. The atherosclerosis is a form of arteriosclerosis, for which a fibrofatty plaque through the wall of an artery makes it thicker.

The growth of an atherosclerotic plaque is sketched in Fig. 74 and described in the following. The blood flows through the lumen carrying many solutes,

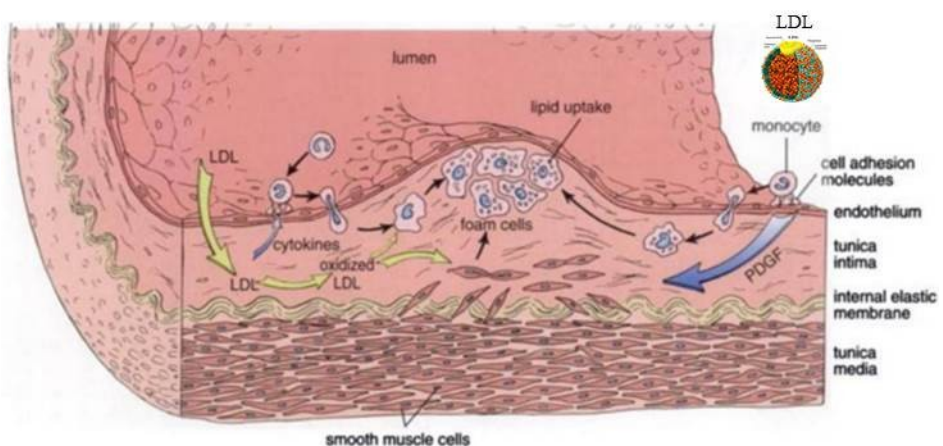


Fig. 74. Atherosclerotic plaque growth [159].

such as the Low-Density Lipoprotein (LDL) (Fig. (74)). LDL have a diameter in the 18 - 25 nm, range and a density spanning between 1006 and 1063 kg/m³. They are generated by the liver from the Intermediate-Density Lipoprotein (IDL), and they deliver triglycerides and esterified cholesterol to the peripheral tissues. When the LDL is in excess in the cardiovascular system, High-Density Lipoprotein (HDL) tends to remove it; when there is an excess of LDL, hypercholesterolemia occurs. The LDL tends to infiltrate through the arterial wall via the endothelium. This means that the integrity of this thin layer has a primary role into reflecting the LDL. When the LDL arrives to the tunica intima, it tends to oxidize, forming ox-LDL and causing an inflammation. This event recalls from the lumen the white blood cells, that tend to infiltrate the wall, especially when endothelium permeability is high. Since macrophages are now activated to absorb ox-LDL, foam cells are generated. Besides, foam cells have some chemiotactic factors that promote the infiltration of SMC from the tunica media, contributing to the formation of foam cells. This process causes the growth of an atherosclerotic plaque, that reduces the lumen section, hampering blood to flow normally. Besides, the above described process can generate, between the endothelium and the intima. a fibrous cap, made up by connective tissue. Depending on the consistency of this layer, the plaque can be either stable or unstable. In the first case, the fibrous cap is thick and solid, and the occlusion of the lumen can occur. This problem can be solved by a collateral circulation, since the plaque growth is relatively slow. In the second case, the plaque could break and form a thrombus. In such case, there is no collateral circulation that solves the problem. Stenosis severity can be classified depending on its area reduction, A [160], that expresses the percentage of area available for the flow. Assuming that the artery is cylindrical, it is possible to write:

$$A = 1 - \left(\frac{r}{r_{lumen}} \right)^2 \quad (58)$$

A stenosis with a 75 % of area reduction is considered as hemodynamically significant [160].

Although the best solution is the reduction of risk factors, many techniques can be used for the reduction of an atherosclerotic plaque. The most used one is the balloon angioplasty (Fig. 75a). An empty balloon is inserted in the diseased artery by means of a catheter, which is flattened when it reaches the occlusion.

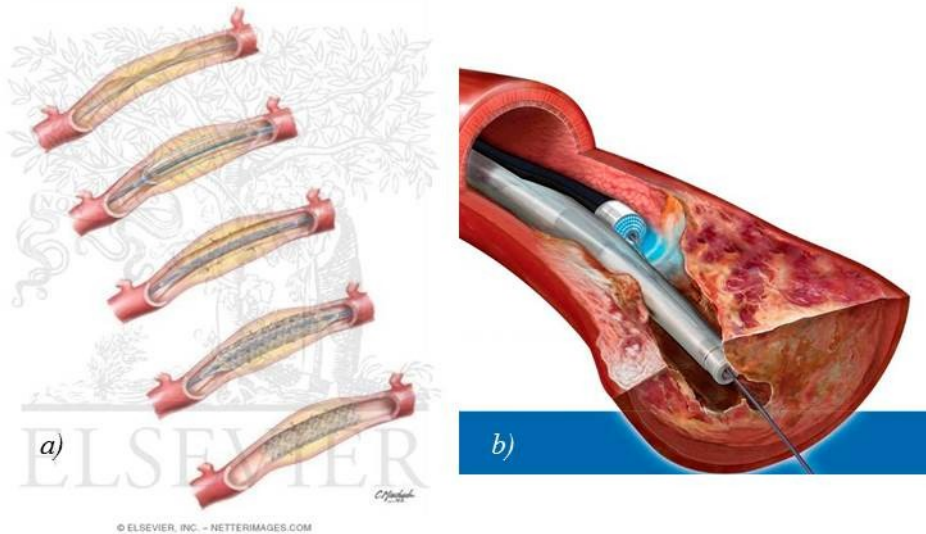


Fig. 75. a) Balloon angioplasty [156]; b) laser angioplasty.

This procedure is often completed by using a metallic wire, the stent, that may be covered or not by a drug. The surgery, in local anesthesia, lasts about 1 hour. After removing the balloon catheter, it is necessary to compress the place from which the catheter is inserted into the body. Often, the femoral artery is used to insert the catheter, but the radial artery can be also used because the mentioned compression can be performed by only using systems similar to bracelets.

Another technique that might be used for complicated stenosis is the laser angioplasty (Fig. 75b), approved by US Food and Drug Administration for coronary uses in 1992. It is based on a fiber-optic laser equipped on the tip of the catheter, that sends pulsating beams of light to vaporize the atherosclerotic plaque. Any fragments can be expelled by using a vacuum device. An excimer laser, together with a balloon, can be used to improve the accuracy. Many authors suggest that tip temperatures above 300 °C produce greater ablation than at lower temperatures, but transmural thermal damage can occur [161]. Barbeau et al. [162] concluded that, even if recanalization temperature had a wide range, for probe temperatures below 160 °C recanalization can occur, with powers between 5 and 10 W. It is important to remark that the main issue of this technique is the vessel damage; therefore different types of laser generators and probes have been investigated during the years [163]. Apart from the laser angioplasty, since temperature gradients affect the LDL transport due to the Ludwig-Soret effect (Eq. 9), it is interesting to realized how LDL transport

through the arterial wall is affected by temperature gradients. Besides, with reference to the hyperthermia treatments for cancers discussed in the introductory chapter, heat can be transferred from the surrounding tissues to the exterior part of an arterial wall during an hyperthermia treatment.

4.2. Modeling Low-Density Lipoprotein (LDL) transport: state-of-art

The role of LDL transport through an arterial wall is very crucial to understand the atherosclerotic plaque growth. However, experiments are very hard to be carried out, because of ethics and microscales. There are very few experimental results on LDL accumulation. Studies on the LDL and albumin uptake in the rabbit aortic wall were carried out by Meyer et al. [164]. Experiments on zebrafish embryos were carried out by Xie et al. [165] in studies on LDL concentration polarization. The concentration polarization consists of accumulation of solute on a membrane surface; it occurs in arteries because the endothelium selectively rejects the LDL.

Since experiments are difficult to carry out, modeling plays a primary role. Depending on the accuracy in the description of the arterial wall, it is possible to identify three classes of models [71]. The first class is the *wall-free* model, by which the arterial wall is modeled by means of a boundary condition. This class is the simpler one, since the model needs less parameters. However, these models are not able to predict concentration profiles across the wall. The second class is the *fluid-wall* model, and that is a little bit more complex than the first. It accounts for the arterial wall, that is treated as an equivalent homogeneous layer. Even if this class is able to catch concentration profiles across the wall, is not possible to exactly predict what occurs in each layer cannot be predicted. The most accurate and complex class is the *multi-layer* model, that accounts for the heterogeneity of the wall. Since several transport parameters are necessary to perform predictions in each artery layer, these models are the very difficult to develop, and they have had more attention only in the last years. However, using these models is very powerful in order to understand where the LDL tends to accumulate, with particular reference to the tunica intima, that is the layer in which the atherosclerotic plaque grows. An example of concentration profiles obtained with a wall-free model for the aorta and with a multi-layer model for a common carotid artery bifurcation is depicted in Fig. 76.

4.2.1. Wall-free and monolayer models

Wall-free models were the first to be proposed, due to their simplicity. They were proposed by Back et al. [168] for the oxygen transport. One of the first

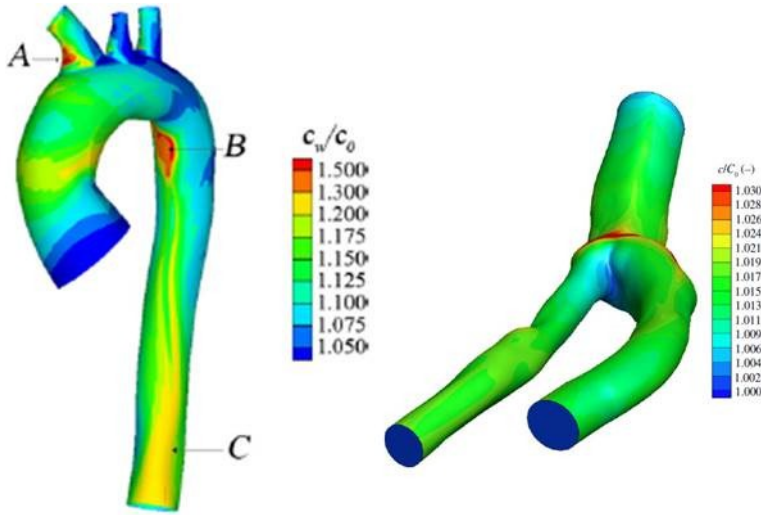


Fig. 76. Concentration profiles along the lumen wall of:
 a) aorta [166]; b) common carotid artery [167].

applications to LDL transport was made by Deng et al. [169]. The boundary conditions for the momentum equation and for the species equation are, respectively:

$$\begin{cases} \mathbf{u} \cdot \mathbf{n} = v \\ c_w v - D_{lumen} \left. \frac{\partial c}{\partial \mathbf{n}} \right|_w = \frac{D_{eff}}{L_{eff}} c_w = |\mathbf{j}| \end{cases} \quad (59)$$

where the subscript w refers to the lumen/arterial wall interface. The first condition describes a no-slip boundary condition, for the solvent coming through the arterial wall at the filtration velocity, that is the velocity of the solvent (plasma) through the wall. In axisymmetric models, the filtration velocity is the radial component of the flow field. Wada et al. [170] imposed a no-slip condition also for the filtration velocity, assuming its effects on the flow field to be negligible. The second boundary condition in Eq. (59) refers to the solute flux \mathbf{j} , and it takes into account the polarization effect on the lumen boundary wall. The term D_{eff} / L_{eff} represents the apparent permeability of the arterial wall, that can be modeled in several ways [171 – 173]. In some cases, the solute flux \mathbf{j} equation is further simplified. In particular, the solute flux through the wall can be assumed to be zero ($|\mathbf{j}| = 0$). This assumption is realistic

when a perfectly impervious artery is considered, and no LDL infiltrates through the wall [169, 174]. A further simplified form is exhibited when also convection is neglected, thus there is only a zero-gradient boundary condition on the wall [175].

Due to its simplicity, the wall-free model is the most widely used. It can be useful when complex conditions, such as particular geometries need to be simulated. Wall-free models were employed to model human aorta by Liu et al. [166] for the analysis of non-Newtonian and pulsatile flow effects on LDL accumulation, using MRI images. They concluded that, in most regions of the aorta, non-Newtonian effects on LDL concentrations are relatively insignificant. However, such effects are more important in areas with flow disturbance, for both steady state and pulsatile flow cases. LDL accumulation by means of a Large Eddy Simulation (LES) was analyzed by Lantz and Karlsson [176] for an aorta generated from MRI images. Stenosed carotid arteries were also modeled by using a wall-free model by Fazli et al. [177] and Nematollahi et al. [178].

The single-layer models are a compromise between the simplicity of the wall-free models and the accuracy of the multi-layer models. As it was previously discussed, the arterial wall is modeled as a unique homogeneous layer. The momentum equation is modeled by using Eq. (14b), while the mass transport equation is modeled by Eq. (26) or a similar form. Stangeby and Ross Ethier used a single-layer model for the momentum equation and a wall-free model for the LDL transport [179]. Single-layer models for both momentum and species equation were used by Olgac et al. [180] and by Sun et al. [181]. In both cases, the momentum equation is further simplified by using Darcy's law. Olgac et al. [180] analyzed LDL transport in a stenosed artery by considering the effects of WSS on endothelial cells and its pathways of volume and solute flux. They evaluated the volume and solute flux by using a three pore model that accounted for endothelial normal and leaky junctions and vesicular pathways. Sun et al. [181] studied pulsatile flow effects on LDL transport for a stenosed artery. The thermophysical properties for the arterial wall needed in their model were the solute lag coefficient, equal to $1 - \sigma_s$, the effective LDL wall diffusivity and the apparent permeability. Such properties were obtained by using an optimization technique based on experimental data.

4.2.2. Multilayer models

The most accurate predictive models for the LDL transport across the arterial wall are the multi-layer model. The the endothelium, the intima, the IEL and the media are considered, while the tunica adventitia is often replaced by a

boundary condition. These models are more complicated since they need several thermophysical parameters to close governing equations, and this estimation is quite challenging because of the scale of the problem and of the lack of experimental data. Models used for the determination of the above said parameters are often based on the fiber matrix models and on the pore theory [62]. In the fiber matrix models [182], the porous layer is assumed to be made up by fibers with certain radius and porosity. The permeability can be calculated from Carman-Kozeny equation. For the solute apparent permeability, it is possible to define a membrane solute diffusivity and a membrane partition coefficient. The membrane partition coefficient is a measure of the solubility of a substance, and it influences the permeation of a solute across a biological membrane. It measures how a substance dissolves in a membrane: if the concentration gradients between the boundaries of the membrane are higher, the rate of diffusion across the membrane is faster. Starting from these concepts, both the effective diffusion coefficient and the partition coefficient can be determined by using an exponential decay law that takes into account porosity, molecules radius and fiber radius and length, then considering hard spherical molecules through a random network of fibers. Thermophysical properties of the tunica intima were determined by using this technique by Chung and Vafai [183], and cholesterol lipid accumulation process can be considered by varying morphological parameters, such as porosity. Curry [62] showed that both Staverman coefficients can be expressed as the square of the complement to one of the partition coefficient. In the pore theory, it is assumed that the permeable channels of finite length are straight cylinders with a uniform diameter. The flow is assumed to be one-dimensional, and both solvent and solute share the same pathways. Permeability, effective diffusivity and reflection coefficients can be evaluated as a function of porosity, molecules and opening radius, and of partitioning coefficient. Often, a scale factor is used to match clinical data. The pore theorem was used by Chung and Vafai [184] to model endothelium thermophysical properties. Other techniques for the determination of these coefficients are based on in vitro and in vivo measurements [71, 73] and on optimization techniques [185].

As it was previously discussed, LDL transport through an arterial wall has been analyzed with multi-layer models only recently. Prosi et al. [71] proposed a new methodology for the transport closing coefficients, based on in vivo measurements. They analyzed in detail the effects of disturbed flow on LDL accumulation through the wall by analyzing an advanced stenosis. Effects of hypertension were analyzed by Yang and Vafai [186] by using a porous media

volume-averaged model. Ai and Vafai [73] developed a new technique for the closing coefficient, based on in vivo and in vitro measurements, and on a simplified analytical solution. LDL accumulation through a stenosed artery was also analyzed. Effects of transmural pressure and WSS on LDL accumulation were investigated by Sun et al. [185]. In order to obtain closing coefficients, they used an optimization approach based on matching one-dimensional simulations and experimental data. Comparing results from the multi-layer model with those from a single-layer model, they found that, even if solute flux through the wall and LDL distribution through the media are similar, the single-layer model could not provide a detailed description of the intima. Effects of gender-related geometries of aorta-iliac bifurcation on LDL transport were analyzed by Khakpour and Vafai [187]. A comprehensive analytical solution using the method of matched asymptotic expansions was presented by Khakpour and Vafai [188], while a simplified analytical solution was presented by Yang and Vafai [189]. Non-Newtonian aspects through the arterial wall were analyzed by Hong et al. [190] by using a one-dimensional four-layer model based on a power-law modified Darcy law. Comparisons with predictions based on a Newtonian fluid with a 1.39 mPa s viscosity showed that non-Newtonian effects through the wall had to be taken into account because differences on filtration velocities were remarkable. Fluid-Structure Interactions (FSI) effects and atherosclerotic plaque growth effects on LDL deposition were investigated by Chung and Vafai [183, 184], while hyperthermia effects coupled with FSI were analyzed by Chung and Vafai [191]. Hyperthermia effects on a stenosed artery were analyzed by Iasiello et al. [192]. Analytical solutions for an artery in presence of a stent and for a curved artery were developed by Wang and Vafai [193, 194], while coupled hyperthermia and hypertension effects were analytically studied by Iasiello et al. [195]. A realistic carotid artery bifurcation was analyzed with a multilayer model by Kenjeres and de Loor [167]. The geometry was reconstructed by using CT scans, adding inlet and outlet flow extensions to facilitate computations. Combined effects of non-Newtonian blood behavior and FSI were analyzed by Deyranlou et al. [196], who concluded that a Newtonian assumption was accurate for large vessels, even if it seemed to underestimate concentration through the wall. The non-Newtonian effects of artery sizes and aorta-iliac bifurcation on LDL deposition were investigated by Iasiello et al. [197].

4.3. Straight artery

4.3.1. Mathematical model

A straight artery, together with boundary conditions of the present study, is sketched in Fig.77. The multi-layer model is made up by four layers. Glycocalyx effects on mass transport are neglected due to the negligible thickness [198]. However, it has been found that Glycocalyx health can play a role [199]. The length of the artery is set as 124 mm [186], with a lumen radius of 3.1 mm [186], that is typical of a medium-sized artery. In order to analyze transport for different artery sizes, also radius equal to 6.1 mm and 9.1 mm have been investigated. The arterial wall thickness is set as 214 μm , where the endothelium's is 2 μm , the intima's is 10 μm , the IEL's is 2 μm and the media's is 200 μm [186]. The tunica adventitia is replaced by a boundary condition on the media/adventitia interface.

Non-Newtonian, hypertension and hyperthermia effects are here analyzed. For the sake of readability, the volume averaging symbols $\langle \rangle$ will be dropped in the following. The flow is assumed as steady-state and incompressible, since pulsation effects can be neglected [186]; osmosis pressure effects are also negligible compared to hydraulic pressure effects [186]. An LTE model is used for the energy equation through the arterial wall [200, 201].

For the free blood stationary flow through the lumen, governing equations for mass, momentum and species are Eqs. (3c), (4a) and (8), respectively, with \mathbf{f}

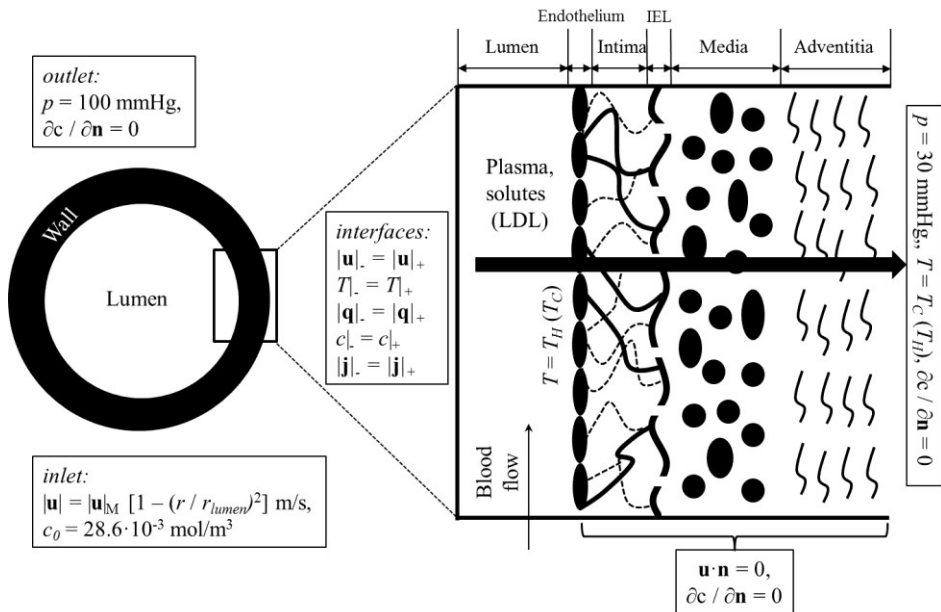


Fig. 77. Sketch of an arterial wall with boundary conditions.

and r equal to 0. Governing equations for mass, momentum, energy and species through the arterial wall are Eqs. (12c), (13), (24) and (27), respectively. Equation (13) is taken in its stationary form, and the integral relative to Eq. (13) is replaced by the two last terms on the right side of Eq. (14), where the Forchheimer term is negligible, due to very low Reynolds numbers. A 2-D axisymmetric model is used in the computations.

In order to solve governing equations, boundary conditions are needed for both lumen and arterial wall. They are reported in Fig. 77. The flow is assumed to be fully developed at the inlet, with a maximum velocity $|\mathbf{u}|_M = 0.338$ m/s [186]. This value gives a $Re \approx 1000$, that is typical of a medium artery. At the outlet of the lumen, a 100 mmHg pressure is set up, with no viscous stresses. Hypertension effects are analyzed by increasing the pressure up to 150 mmHg and 190 mmHg. A $28.6 \cdot 10^{-3}$ mol/m³ LDL inlet concentration and an outflow condition with a zero-gradient concentration at the lumen outlet are assumed. At the lumen/wall boundary, and at boundaries between wall layers, the continuity of velocity, concentration, temperature, mass flux and energy is applied, while a jump condition is applied for the shear stresses. The continuity of mass flux $|\mathbf{j}|$ described for the i -layer boundary is:

$$|\mathbf{j}| = |\mathbf{j}^a| + |\mathbf{j}^D| + |\mathbf{j}^T| = (1 - \sigma_s)vc - D_{eff} \nabla c - \frac{k_T \rho_f D_{eff}}{M_f T} \nabla T \quad (60)$$

$$|\mathbf{j}| = \left[|\mathbf{j}^a| + |\mathbf{j}^D| + |\mathbf{j}^T| \right]_- = \left[|\mathbf{j}^a| + |\mathbf{j}^D| + |\mathbf{j}^T| \right]_+ \quad (61)$$

where the subscripts a , D and T stays for advective, diffusive and thermal, respectively. The filtration velocity, v , is the radial component of the velocity. For the energy equation and for the same boundary we also write the continuity of the heat flux $|\mathbf{q}|$:

$$|\mathbf{q}| = |\mathbf{q}^a| + |\mathbf{q}^D| = \rho C_p v (T - T_{ref}) - k_{eff} \nabla T \quad (62)$$

$$|\mathbf{q}| = \left[|\mathbf{q}^a| + |\mathbf{q}^D| \right]_- = \left[|\mathbf{q}^a| + |\mathbf{q}^D| \right]_+ \quad (63)$$

At the lumen/endothelium interface, a Dirichlet condition is imposed for the temperature. Two cases are analysed. In the first, named internal heating, heat is applied from the interior part of the artery, while in the second, named external

heating, heat is applied from outside. Considering 310 K as the isothermal arterial wall temperature, a temperature of 330 K or 350 K is set up for the interior wall when heat is applied from the lumen side. The highest temperature in the computational domain is referred as T_H and the lowest as T_C . A slip condition is applied at the extremities of each porous domain, in order to simulate the symmetry of the walls. For the species and energy equations, a zero-gradient condition is imposed for both concentration and temperature, respectively. At media/adventitia interface, a 30 mmHg hydraulic pressure is set up, causing a $\Delta p = 70$ mmHg transmural pressure in healthy conditions; it increases when hypertension is considered by changing the lumen outlet pressure value. A zero-gradient condition is imposed for the concentration field. Effects of this boundary condition have been discussed by Prosi et al. [71] and by Yang and Vafai [186]. When heat enters the interior side of the arteria, a 330 or 350 K on the lumen/endothelium interface and 310 K on the media/adventitia interface Dirichlet condition is imposed; when heat enters the exterior side of the artery a 310 K boundary condition is imposed on the media/adventitia interface and a 330 or 350 K on the lumen/endothelium interface boundary condition is imposed. Therefore, in the following reference will be made to 20 K or 40 K differences in the temperature of the artery walls.

Thermophysical properties and closing coefficients are further needed for the governing equations. Thermophysical properties are those of the blood, for the lumen, and of the plasma, for the arterial wall. Since non-Newtonian effects are analysed in the present paper, different rheological models are used. For the lumen they are four. The first is the Newtonian model, in which $\mu = 3.7$ mPa s. In the Newtonian case, it is possible to write $\nabla \cdot \mathbf{T} = \nabla^2 \mathbf{u}$. The other rheological models that are employed are:

- a Power-law fluid model, where $\mu = \mu^* (\gamma)^{n-1}$, with μ^* the fluid consistency index, γ the shear rate and n the power-law index. In this study, $\mu^* = 9.267$ mPa sⁿ and $n = 0.828$ [202].
- a Carreau fluid model, where $\mu = \mu_\infty + (\mu_z - \mu_\infty) \left[1 + (\lambda \gamma)^2 \right]^{\frac{n-1}{2}}$, with μ_∞ and μ_z the fluid dynamic viscosities at infinite and zero shear rate, respectively, and λ the relaxation time. In this study, $\mu_\infty = 3.45$ mPa s, $\mu_z = 56$ mPa s, $\lambda = 3.313$ s and $n = 0.3568$ [203, 204].

- a Carreau-Yasuda fluid model, where $\mu = \mu_\infty + (\mu_z - \mu_\infty) \left[1 + (\lambda\gamma)^q \right]^{\frac{n-1}{q}}$, with q a coefficient relative to the Carreau-Yasuda fluid model herein used. In this study, $\mu_\infty = 3.45$ mPa s, $\mu_z = 56$ mPa s, $\lambda = 1.902$ s, $q = 1.25$ and $n = 0.22$ [203].

The fluid viscosity as a function of the shear rate, for different rheological methods, is reported in Fig:78.

For the arterial wall, in order to consider non-Newtonian effects, the following non-Newtonian momentum equation is considered:

$$\frac{\rho}{\varepsilon^2} \nabla \cdot (\langle \mathbf{u} \rangle \langle \mathbf{u} \rangle) = \langle \mathbf{f} \rangle - \nabla \langle p \rangle + \frac{\mu^*}{\varepsilon^n} \nabla \cdot \left\{ \left[\sqrt{\frac{1}{2} (\langle \dot{\gamma} \rangle \cdot \langle \dot{\gamma} \rangle)} \right]^{n-1} \langle \dot{\gamma} \rangle \right\} - \left(\frac{\mu^* |\langle \mathbf{u} \rangle|^{n-1}}{K^*} + \frac{C\rho \langle \mathbf{u} \rangle}{\sqrt{K}} \right) \langle \mathbf{u} \rangle \quad (64)$$

Inertial forces, buoyancy, viscous effects and microscopically inertial effects are assumed negligible and Eq. (64) is simplified to a power-law Darcy equation [186, 188, 189, 193]:

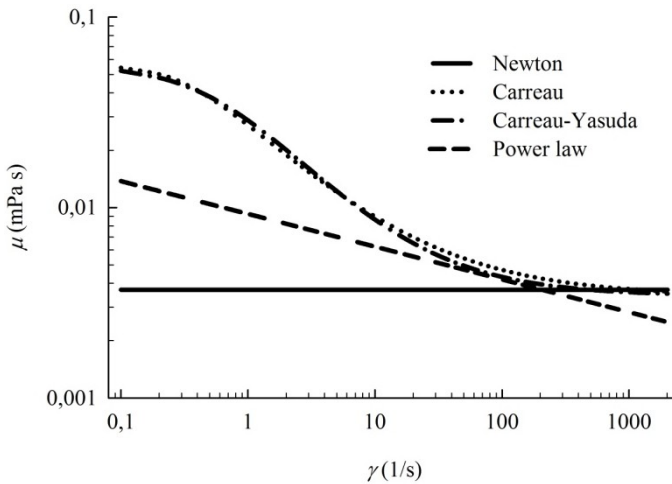


Fig. 78. Rheological models used in this study.

$$\nabla \langle p \rangle = - \left(\frac{\mu^* |\langle \mathbf{u} \rangle|^{n-1}}{K^*} \right) \langle \mathbf{u} \rangle \quad (65)$$

where the consistency index is $\mu^* = \mu / \gamma^{n-1}$. The power law permeability is [205]:

$$K^* = \frac{1}{2\tau} \left(\frac{n\varepsilon}{3n+1} \right)^n \left(\frac{50K}{3\varepsilon} \right)^{\frac{(n+1)}{2}} \quad (66)$$

where the tortuosity, τ , is set equal to 25/12 [206].

In order to correlate viscosity and shear stresses, experimental data from Graf and Barras [207] are used to obtain the consistency index, μ^* , and the power law fluid index, n . By performing a regression analysis on Graf and Barras's data, a power-law function is found, that, with $\mu^* = 3.16 \text{ mPa s}^n$ and $n = 0.81$, fits experimental data. When the Newtonian model is employed for the arterial wall, $\mu = 0.72 \text{ mPa s}$ is used [71].

Closing coefficients for the porous media equations are taken after Chung and Vafai [191] and resumed in Table 7, together with geometrical features and thermophysical properties, which are considered as Newtonian for simplicity in the table. The hydraulic permeability, K^{end} , the effective diffusivity, D^{end} , the Staverman reflection coefficient, σ_s^{end} , are taken from Chung and Vafai [184] (2012). They are obtained, obtained by using the pore theory, considering a leaky junction fraction of $5 \cdot 10^{-4}$, a radius of the endothelial cells of $15 \mu\text{m}$, with a 14.343 nm half width of leaky junctions. The porosity is taken from Lin et al. [208]. The intima properties are taken from studies carried out on fiber matrix model, for both permeability and diffusivity, by Huang et al. [209]. The reflection coefficient is taken from Prosi et al. [71], who obtained it by assuming that the mass flux is only advective through the intima. The porosity is taken from Huang et al. [209]. In the IEL, hydraulic permeability and effective diffusivity obtained from the pore theory are taken from Prosi et al. [71]; the reflection coefficient is obtained from mass fluxes through the various layer [71]. The porosity is taken from Song et al. [210]. Hydraulic permeability and effective diffusivity for the media are taken from Huang et al. [209]. Both reflection coefficient and first-order reaction coefficient are taken from Prosi et al. [71], who solved a non-linear system of two equations in two unknowns, obtained from an electrical analogy and from the mass conservation principle.

Table 7. Thermophysical properties and closing coefficients [191].

Property	Lumen	Endothelium	Intima	IEL	Media
Thickness r (μm)	3100	2	10	2	200
Density ρ (kg/m^3)	$1.07 \cdot 10^3$	$1.057 \cdot 10^3$	$1.057 \cdot 10^3$	$1.057 \cdot 10^3$	$1.057 \cdot 10^3$
Viscosity μ ($\text{kg}/\text{m s}$)	$3.7 \cdot 10^{-3}$	$0.72 \cdot 10^{-3}$	$0.72 \cdot 10^{-3}$	$0.72 \cdot 10^{-3}$	$0.72 \cdot 10^{-3}$
Porosity ε	-	0.0005	0.983	0.002	0.258
Permeability K (m^2)	-	$3.22 \cdot 10^{-21}$	$2 \cdot 10^{-16}$	$4.392 \cdot 10^{-19}$	$2 \cdot 10^{-18}$
Diffusivity D_{eff} (m^2/s)	$2.87 \cdot 10^{-11}$	$5.7 \cdot 10^{-18}$	$5.4 \cdot 10^{-12}$	$3.18 \cdot 10^{-15}$	$5 \cdot 10^{-14}$
Reflection coefficient σ_s	-	0.9888	0.8272	0.9827	0.8836
Reaction k (1/s)	-	0	0	0	$-3.197 \cdot 10^{-4}$
Thermal diffusivity α_{eff} (m^2/s)	-	$1.42 \cdot 10^{-7}$	$1.42 \cdot 10^{-7}$	$1.42 \cdot 10^{-7}$	$1.42 \cdot 10^{-7}$

The porosity is taken from Huang and Tarbell [211]. The effective thermal diffusivity, α_{eff} , of each layer is taken from Duck [212]. There is a lack of data of the thermo-diffusion coefficient, k_T , in the literature. Its value is about 0.01 [38, 39], but it is expected to be lower because LDL is a heavy molecule. Therefore, herein a sensitivity analysis has been carried out, by varying, k_T .

Governing equations are solved with either numerical or analytical approaches. Numerical approaches for non-Newtonian studies and analytical approaches for hypertension coupled with hyperthermia are used. The latter approach will be discussed in detail in the next paragraph. When numerical approaches are employed, a Galerkin-based finite element scheme is used from the commercial code COMSOL Multiphysics. It is important to remark that the conservative form of the species equation is used instead of the non-conservative one. Since geometries are regular, a mapped quadrilateral mesh is used, with about 500,000 elements. Grid independence and RMS relative tolerance have been checked by comparing the LDL concentration profiles along the lumen/endothelium interface with different number of elements and relative tolerances.

4.3.2. Numerical approaches

4.3.2.1. Non-Newtonian effects

Blood is often assumed as a Newtonian fluid when flowing through large arteries [203, 204, 213, 214, 215] and, sometimes, when flowing through medium arteries [214], because of the typical shear rates depending on the vessel dimensions. The importance of non-Newtonian effects on blood was highlighted by Johnston et al. [204], and the analysis was further extended to stenosed arteries by Razavi et al. [216]. The assumption of Newtonian fluid loses its accuracy especially when shear stresses at the wall are lower, as in complicate geometries, such as stenoses, bends or bifurcation. Further, there are only few studies on non-Newtonian effects on LDL transport in an artery [166, 190, 196]. Non-Newtonian effects on LDL transport are presented in the following, in order to evaluate the accuracy of the Newtonian assumption for different arteries.

Non-Newtonian effects for a medium straight artery are analyzed under hypertension conditions and for different artery sizes. Hyperthermia effects are neglected. First of all, non-Newtonian effects are analyzed for a medium size artery with $r_{lumen} = 3.1$ mm. The filtration velocity for different transmural pressures, $\Delta p = 70$ mmHg, 120 mmHg and 160 mmHg, can be obtained either from simulations or from a hydraulic analogy. From Eq. (6), assuming that the flow is one-dimensional, one can write [190]:

$$v = \left(\frac{\Delta p}{\sum_{i=1}^4 R^i} \right)^{1/n} = \left(\frac{\Delta p}{R^{end} + R^{int} + R^{IEL} + R^{med}} \right)^{1/n} \quad (67)$$

where the hydraulic resistance, R^i , of the i -layer is:

$$R^i = \frac{\mu^* L^{i,*}}{K^{i,*}} \quad (68)$$

Results from the numerical model and from the hydraulic analogy are essentially the same. The filtration velocity, for different rheological models and transmural pressure, as a function of the axial coordinate and the pressure drop

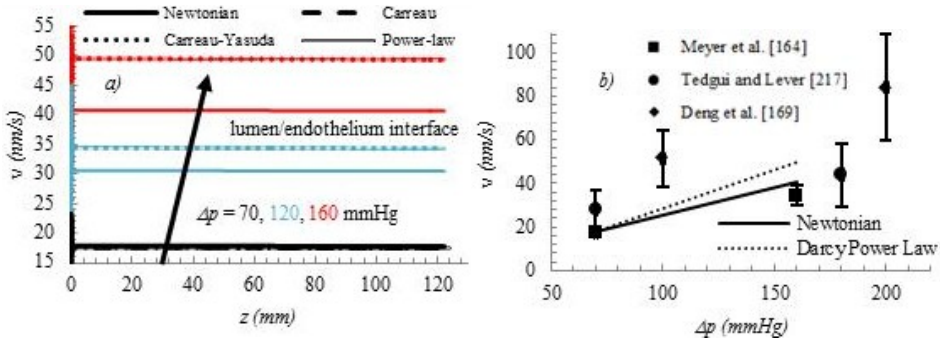


Fig. 79. Filtration velocity, for different rheological models and transmural pressure, vs. a) the axial coordinate; b) the pressure drop.

are reported in Fig. 79a) and 79b), respectively. For the sake of comparison, experimental data from the literature are also reported in Fig 79b). Figure 79b shows that the filtration velocity increases with transmural pressure, due to the increase of the driving force. One can also notice that, for low pressure drop, nearly common values are predicted by both Newtonian and Darcy Power-law fluid, while the Newtonian model underestimates, up to 15%, the filtration velocity at larger Δp . The comparison of predicted values with experimental data shows a better agreement of results obtained with the model proposed in the present work.

Defining the wall shear stresses (WSS) as the product of the dynamic viscosity and the shear rate, the shear rate and the wall shear stresses as a function of the axial coordinate, for different rheological models, are reported in Fig.80a) and 80b), respectively. The figures exhibit small differences between the predictions of the different models; the maximum differences in the WSS values are those between Newtonian and Carreau fluid models.

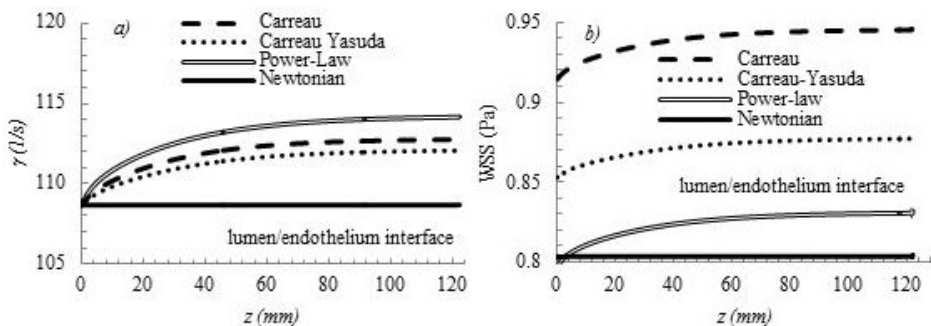


Fig. 80. Shear rate and wall shear stresses vs. the axial coordinate, for different rheological models.

Reference is made in the following to the LDL concentration polarization, defined as the concentration scaled with the inlet concentration value $c_0 = 28.6 \cdot 10^{-3} \text{ mol/m}^3$. The concentration polarization as a function of the axial coordinate, for different rheological models and intramural pressure, is presented in Fig. 81. Figures point out an increasing in the concentration both with the axial coordinate, because of to the polarization, and with the transmural pressure, because of the enhancement of the solvent driving force through the wall. Comparing predictions of non-Newtonian models, we notice that the Power-Law model predicts both the highest shear rate and concentrations.

Differences in LDL concentrations predicted by non-Newtonian models for various transmural pressure are negligible, less than 1%. Finally, the comparison between predictions by non-Newtonian models and Newtonian models shows negligible differences too, less than 2%.

LDL concentration polarization as a function of the radius in the arterial wall, for different rheological models and transmural pressure, is presented in Fig. 82. The concentration polarization is almost uniform in the intima, while it rapidly decreases in the IEL. This is explained mainly by the change in diffusivity, as reported in Table 7. The concentration polarization is rapidly consumed in the media by the chemical reaction term, that describes the solute

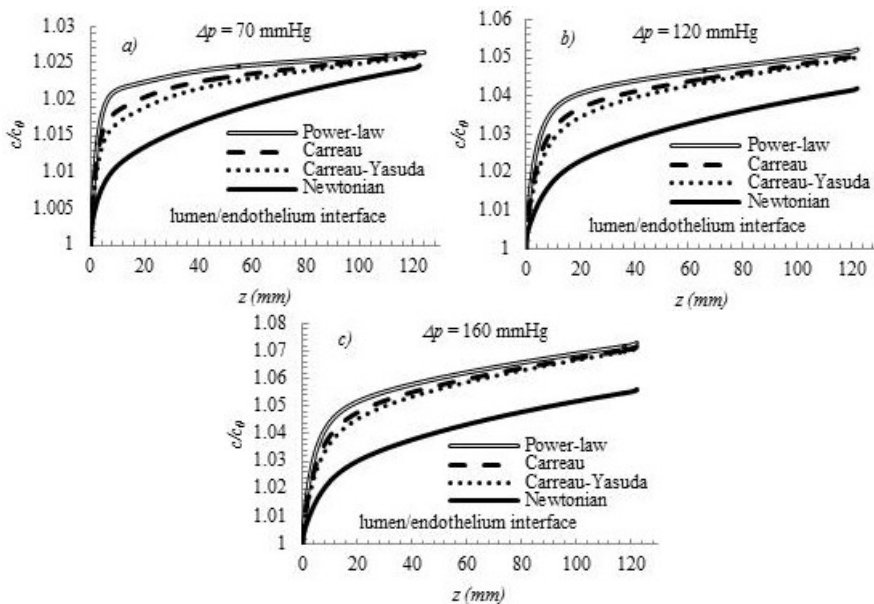


Fig. 81. LDL concentration polarization vs. the axial coordinate, for different rheological models and transmural pressures.

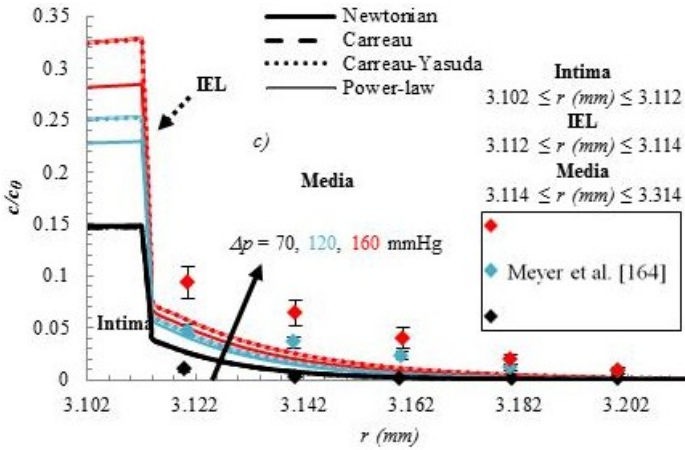


Fig. 82. LDL concentration polarization vs. the radius in the arterial wall, for different rheological models and transmural pressures.

uptake made by the SMC. Because of the increasing filtration velocity with transmural pressure, the concentration polarization increases with transmural pressure. The comparison between Newtonian and non-Newtonian models highlights higher values predicted by non-Newtonian models, because of their higher filtration velocity. Differences are negligible at normal transmural pressure, while they are slightly less than 15 % at the highest investigated transmural pressure. The comparison with experimental results from Meyer et al. [164] shows a good agreement, especially at the normal transmural pressure, referred to a healthy cases. However, differences increase with transmural pressure, attaining an almost 30% value.

Wall shear stresses as a function of the axial coordinate, for different models and lumen radius is presented in Fig.83. Non-Newtonian models predict an increase in the wall shear stresses as the artery radius becomes smaller. Differences between predictions of rheological models, for different artery sizes, are found, as it occurred for medium arteries.

LDL concentration polarization as a function of the axial coordinate at the lumen/endothelium interface, for different models and artery sizes, is reported in Fig.84. Figures show that the larger the artery the larger the concentration since more solvent is driven through the arterial wall from shear rates. Differences between Newtonian and non-Newtonian models slightly increase with the lumen radius; they are no larger than 3%. Also in this case a correlation is noticed between shear rates and concentrations.

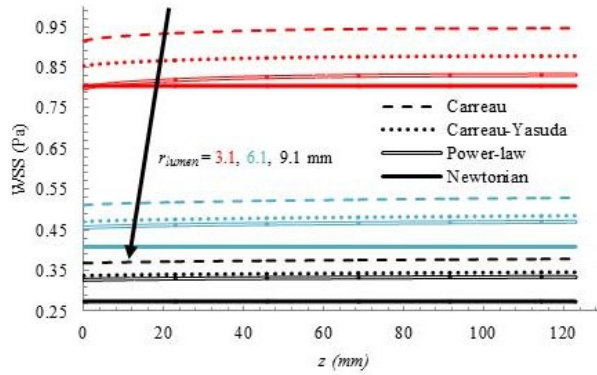


Fig. 83. Wall shear stresses vs. the axial coordinate, for different models and lumen radius.

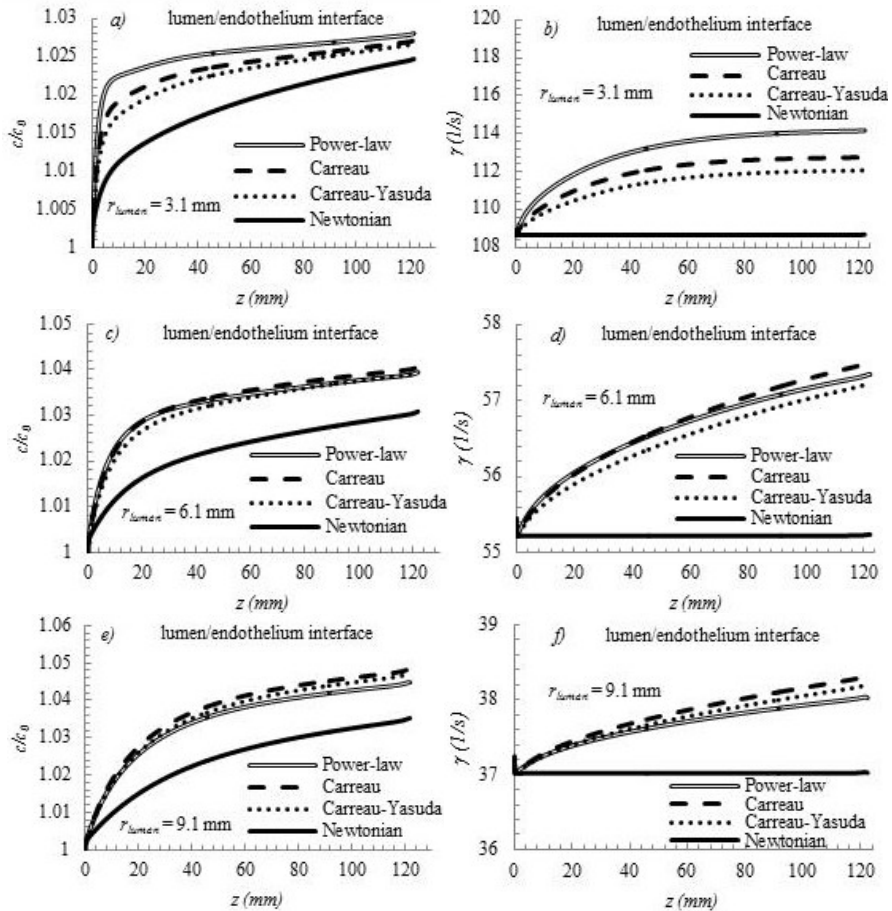


Fig. 84. LDL concentration polarization vs. the axial coordinate at the lumen/endothelium interface, for different models and artery sizes.

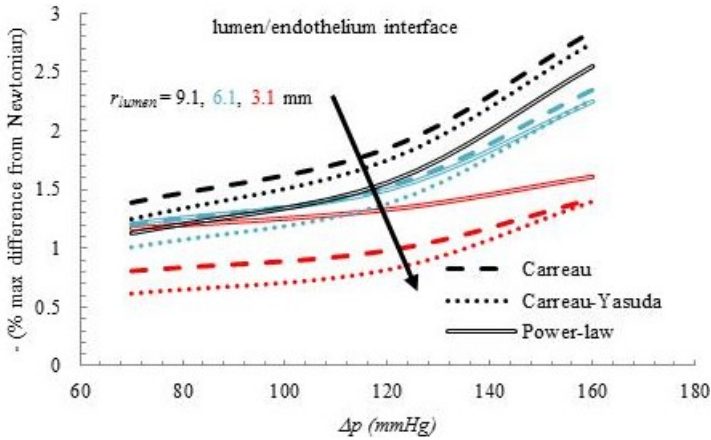


Fig. 85. Percent difference in concentrations among models vs. the pressure drop at the lumen/endothelium interface, for different artery sizes.

Finally, percent differences in LDL concentrations among models as a function of the transmural pressure at the lumen/endothelium interface, for different artery sizes are reported in Fig.85. Differences among concentrations predicted by the Newtonian and non-Newtonian models slightly increase both with the lumen radius and the transmural pressure, the maximum value being less than 3%.

On the basis of the above presented results, we can conclude that Newtonian models can be usefully used in predicting LDL transport in medium and large straight arteries.

4.3.3. Analytical approaches

4.3.3.1. Deriving a simplified analytical solution

An analytical solution is presented for coupled hyperthermia and hypertension effects on LDL transport. Since PDE that describe the LDL transport are difficult to solve analytically, well-established results from previous works are employed to obtain a simplified solution. First of all, only the arterial wall is modeled, and the lumen domain is replaced with a boundary condition on the lumen/endothelium interface. Governing equations for the arterial wall previously described in the mathematical model sub-section are further simplified. The fluid is assumed to be Newtonian. The macroscopic inertial term can be neglected, and the Brinkman viscous term too. Besides, the problem is further reduced to a one-dimensional problem. Filtration velocity in the radial direction is much higher than it is in the axial direction, and the heat

transfer is independent of the axial direction (Chung and Vafai [191] and Iasiello et al. [192]). Since the arterial wall thickness is much smaller than the overall artery diameter, the effect of curvature is negligible [194]. Finally, with reference to the thermodiffusion (Ludwig-Soret) term that appears in Eqs. (27) and (60), the temperature at the denominator is supposed to be uniform in each layer and reference is made to its mean value. With reference to a one-dimensional coordinate, y^* , governing equations for each layer are scaled in a dimensionless form, obtaining the following equations for mass, momentum, energy and species:

$$\frac{dv^*}{dy^*} = 0 \quad (69)$$

$$\frac{dp^*}{dy^*} = -\frac{1}{\text{ReDa}} v^* \quad (70)$$

$$v^* \frac{dT^*}{dy^*} = \frac{1}{\text{Pe}^T} \frac{d^2 T^*}{dy^{*2}} \quad (71)$$

$$(1 - \sigma_s) v^* \frac{dc^*}{dy^*} = \frac{1}{\text{Pe}} \frac{d^2 c^*}{dy^{*2}} + \frac{k_T \Delta T}{\text{Pe} T_M} \frac{\rho_f}{M_f c_0} \frac{d^2 T^*}{dy^{*2}} - \frac{k L_0}{v_0} c^* \quad (72)$$

with the following dimensionless parameters:

$$v^* = \frac{v}{v_0}; \quad c^* = \frac{c}{c_0}; \quad p^* = \frac{p}{\rho_f v_0^2}; \quad y^* = \frac{y}{L_0}; \quad \text{Re} = \frac{\rho_f v_0 L_0}{\mu_f}; \quad \text{Da} = \frac{K}{L_0^2};$$

$$\text{Pe}^T = \frac{v_0 L_0}{\alpha_{eff}}; \quad T^* = \frac{T - T_C}{T_H - T_C}; \quad \text{Pe} = \frac{v_0 L_0}{D_{eff}}$$

where Da is the Darcy number; Pe^T is the thermal Peclet number; Pe is the mass Peclet number; T_M is the mean temperature; v_0 is the reference filtration velocity, equal to $2.31 \cdot 10^{-8}$ m/s [164]; c_0 is the reference concentration value at the lumen inlet section, namely $28.6 \cdot 10^{-3}$ mol/m³; L_0 is the reference length of the arterial wall, in the radial direction, that represents its thickness; T_H is the temperature at the hot surface; T_C is the temperature at the cold surface.

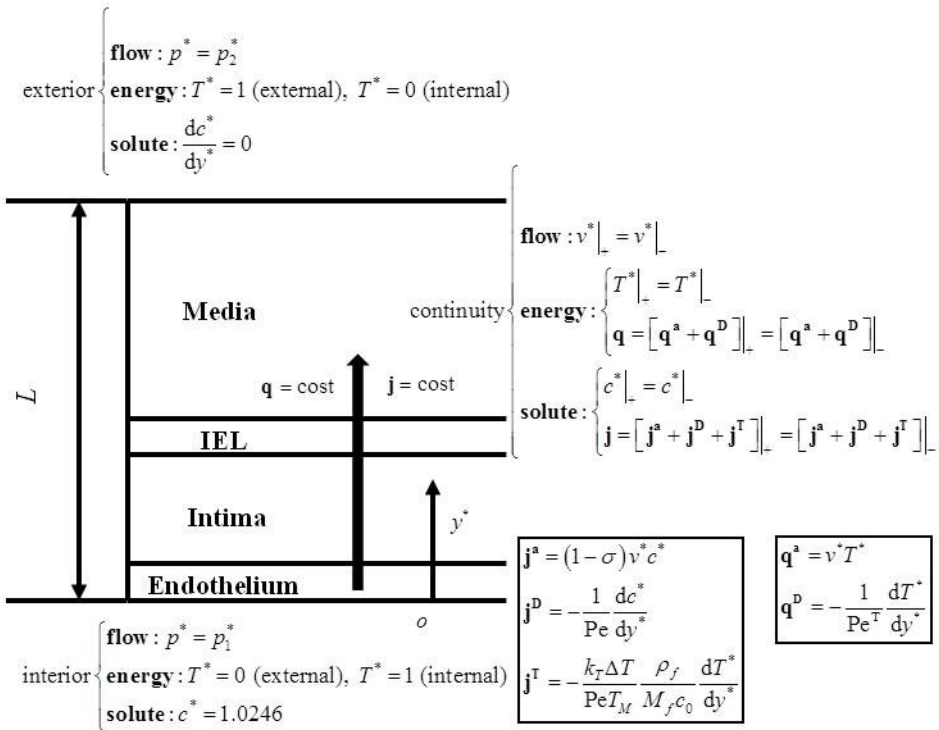


Fig. 86. Boundary conditions for the analytical problem.

Boundary conditions are reported in Fig. 86. They are, in a dimensionless form, essentially the same as those described in the mathematical model subsection. At the lumen/endothelium boundary, it is assumed that $p_1 = 100$ mmHg and $c^* = 1.0246$. The pressure is the same as that at the outlet flow section in the lumen, for a normal transmural pressure, while the dimensionless concentration is the LDL concentration at the wall in the midsection of the vessel [186]. At the media/adventitia interface, a pressure $p_2 = 30$ mmHg is set.

Equation (70) is solved by means of an electrical analogy, as it was previously did for non-Newtonian fluids (Eqs.67, 68). Equation (67) is now assumed with $n = 1$, since the flow is Newtonian; the pressure difference Δp is $\Delta p = p_1^* - p_2^*$; the hydraulic resistance of the i -layer is $R^i = L^i \text{Re Da}$.

The filtration velocity as a function of the axial coordinate along the lumen/endothelium interface, under normal pressure and under hypertension, is reported in Fig.87, respectively. Prediction are in very good agreement with data from the literature.

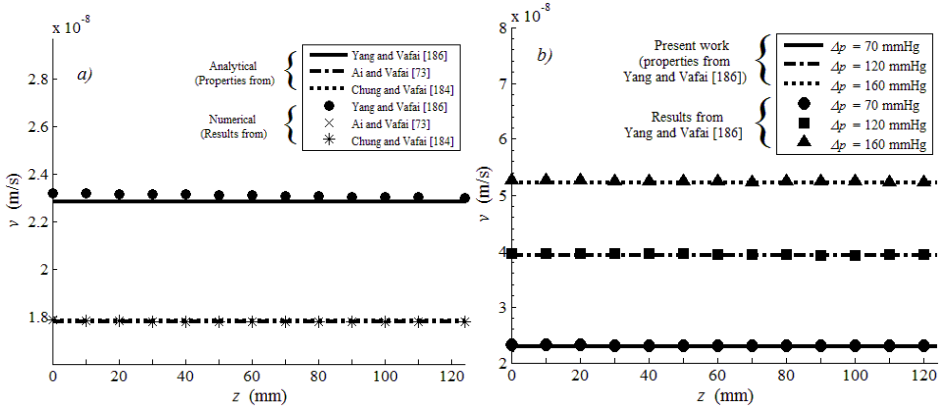


Fig. 87. Filtration velocity vs. the axial coordinate along the lumen/endothelium interface: a) under normal pressure; b) under hypertension.

The energy equation, Eq. (71), is solved and used in the LDL equation to account for Ludwig-Soret effect. The temperature distribution in each layers is

$$T^*(y^*) = c_1^T e^{\lambda_1^T y^*} + c_2^T \quad (73)$$

With reference to Table 7, thermal diffusivities are the same in each layer; therefore Pe^T is equal everywhere. This means that a two equations linear system is to be solved to obtain the temperature profiles. The ODE constants are:

$$\begin{cases} c_1^T = \frac{1}{1 - e^{\lambda_1^T}} \\ c_2^T = -\frac{e^{\lambda_1^T}}{1 - e^{\lambda_1^T}} \end{cases} \Rightarrow \begin{cases} c_1^T = -3.73 \cdot 10^4 \\ c_2^T = 3.73 \cdot 10^4 \end{cases} \quad (74)$$

for the internal heating, and:

$$\begin{cases} c_1^T = -\frac{1}{1 - e^{\lambda_1^T}} \\ c_2^T = \frac{1}{1 - e^{\lambda_1^T}} \end{cases} \Rightarrow \begin{cases} c_1^T = 3.73 \cdot 10^4 \\ c_2^T = -3.73 \cdot 10^4 \end{cases} \quad (75)$$

for the external heating.

The solutions to Eqs.74 are presented in Figs.88.

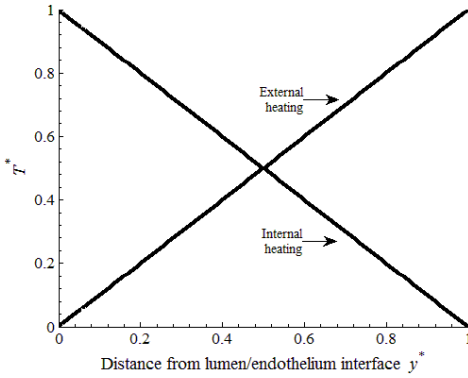


Fig. 88a. Dimensionless temperature vs. the distance from lumen/endothelium interface

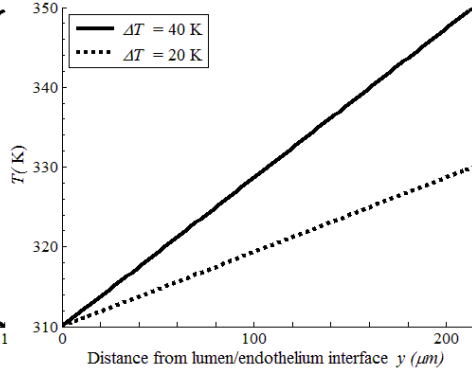


Fig. 88b. Temperature vs. the distance from lumen/endothelium interface

The solution to the solute Eq. (13) is obtained by solving it in each layer, with continuity boundary conditions at the interfaces. Equation (72) is rearranged in the form:

$$\frac{1}{Pe} \frac{d^2 c^*}{dy^{*2}} - (1 - \sigma_S) v^* \frac{dc^*}{dy^*} - \frac{kL_0}{v_0} c^* = -\frac{k_T \Delta T}{Pe T_M} \frac{\rho_f}{M_f c_0} \frac{d^2 T^*}{dy^{*2}} \quad (76)$$

Substituting the term on the right side of this equation with the second derivative of Eq. (73), we obtain:

$$\frac{1}{Pe} \frac{d^2 c^*}{dy^{*2}} - (1 - \sigma_S) v^* \frac{dc^*}{dy^*} - \frac{kL_0}{v_0} c^* = -\frac{k_T \Delta T}{Pe T_M} \frac{\rho_f}{M_f c_0} c_1^T v^{*2} Pe^{T^2} e^{v^* Pe^T y^*} \quad (77)$$

Equation (77) is a second order ODE. Its solution has the following general form:

$$c^*(y^*) = c_1^i e^{\lambda_1 y^*} + c_2^i e^{\lambda_2 y^*} + A^i e^{\lambda_1^T y^*} \quad (78)$$

where i refers to the i^{th} -layer. Eigenvalues λ_1 and λ_2 are:

$$\lambda_{1,2} = \frac{\text{Pe}(1-\sigma_S)v^* \pm \sqrt{\left[\text{Pe}(1-\sigma_S)v^*\right]^2 + 4\frac{k\text{Pe}L_0}{v_0}}}{2} \quad (79)$$

By setting $k = 0$, eigenvalues for endothelium, IEL and intima are obtained, then, in the three layers, $\lambda_2 = 0$. A^i is given by

$$A^i = -\left[\frac{k_T\Delta T}{T_M} \frac{\rho_f}{M_f c_0} c_1^T\right] \cdot \frac{1}{1 - \text{Le}(1-\sigma_S) - \frac{kL_0\text{Le}}{v_0 v^{*2} \text{Pe}^T}} \quad (80)$$

where the Lewis number, Le , is defined as $\text{Le} = \text{Pe}/\text{Pe}^T$. Continuity between layers is guaranteed by boundary conditions reported in Fig. 1b. Constants c_1^i and c_2^i are obtained, for each i^{th} -layer, by applying boundary conditions to Eq. (77). The following equations system is derived:

$$c_1^{\text{end}} + c_2^{\text{end}} + A^{\text{end}} = 1.0246 \quad (81a)$$

$$c_1^{\text{end}} e^{\lambda_1^{\text{end}} y^{*,\text{end}}} + c_2^{\text{end}} + A^{\text{end}} e^{v^* \text{Pe}^T y^{*,\text{end}}} = c_1^{\text{int}} e^{\lambda_1^{\text{int}} y^{*,\text{end}}} + c_2^{\text{end}} + A^{\text{end}} e^{v^* \text{Pe}^T y^{*,\text{end}}} \quad (81b)$$

$$\begin{aligned} & \left[(1-\sigma_S^{\text{end}}) \right] v^* \left(c_1^{\text{end}} e^{\lambda_1^{\text{end}} y^{*,\text{end}}} + c_2^{\text{end}} + A^{\text{end}} e^{v^* \text{Pe}^T y^{*,\text{end}}} \right) - \\ & - \frac{1}{\text{Pe}^{\text{end}}} \left(\lambda_1^{\text{end}} c_1^{\text{end}} e^{\lambda_1^{\text{end}} y^{*,\text{end}}} + A^{\text{end}} v^* \text{Pe}^T e^{v^* \text{Pe}^T y^{*,\text{end}}} \right) - \\ & - \frac{k_T\Delta T}{\text{Pe}^{\text{end}} T_M^{\text{end}}} \frac{\rho_f}{M_f c_0} v^* \text{Pe}^T c_1^T e^{v^* \text{Pe}^T y^{*,\text{end}}} = \\ & = \left[(1-\sigma_S^{\text{int}}) \right] v^* \left(c_1^{\text{int}} e^{\lambda_1^{\text{int}} y^{*,\text{end}}} + c_2^{\text{int}} + A^{\text{int}} e^{v^* \text{Pe}^T y^{*,\text{end}}} \right) - \\ & - \frac{1}{\text{Pe}^{\text{int}}} \left(\lambda_1^{\text{int}} c_1^{\text{int}} e^{\lambda_1^{\text{int}} y^{*,\text{end}}} + A^{\text{int}} v^* \text{Pe}^T e^{v^* \text{Pe}^T y^{*,\text{end}}} \right) - \\ & - \frac{k_T\Delta T}{\text{Pe}^{\text{int}} T_M^{\text{int}}} \frac{\rho_f}{M_f c_0} v^* \text{Pe}^T c_1^T e^{v^* \text{Pe}^T y^{*,\text{end}}} \end{aligned} \quad (81c)$$

$$c_1^{\text{int}} e^{\lambda_1^{\text{int}} y^{*,\text{int}}} + c_2^{\text{int}} + A^{\text{int}} e^{v^* \text{Pe}^T y^{*,\text{int}}} = c_1^{\text{IEL}} e^{\lambda_1^{\text{IEL}} y^{*,\text{int}}} + c_2^{\text{IEL}} + A^{\text{IEL}} e^{v^* \text{Pe}^T y^{*,\text{int}}} \quad (81d)$$

Biological systems

$$\begin{aligned}
 & \left[(1 - \sigma_S^{int}) \right] v^* \left(c_1^{int} e^{\lambda_1^{int} y^{*,int}} + c_2^{int} + A^{int} e^{v^* \text{Pe}^T y^{*,int}} \right) - \\
 & - \frac{1}{\text{Pe}^{int}} \left(\lambda_1^{int} c_1^{int} e^{\lambda_1^{int} y^{*,int}} + A^{int} v^* \text{Pe}^T e^{v^* \text{Pe}^T y^{*,int}} \right) - \\
 & - \frac{k_T \Delta T}{\text{Pe}^{int} T_M^{int}} \frac{\rho_f}{M_f c_0} v^* \text{Pe}^T c_1^T e^{v^* \text{Pe}^T y^{*,int}} = \\
 & = \left[(1 - \sigma_S^{IEL}) \right] v^* \left(c_1^{IEL} e^{\lambda_1^{IEL} y^{*,int}} + c_2^{IEL} + A^{IEL} e^{v^* \text{Pe}^T y^{*,int}} \right) - \\
 & - \frac{1}{\text{Pe}^{IEL}} \left(\lambda_1^{IEL} c_1^{IEL} e^{\lambda_1^{IEL} y^{*,int}} + A^{IEL} v^* \text{Pe}^T e^{v^* \text{Pe}^T y^{*,int}} \right) - \\
 & - \frac{k_T \Delta T}{\text{Pe}^{IEL} T_M^{IEL}} \frac{\rho_f}{M_f c_0} v^* \text{Pe}^T c_1^T e^{v^* \text{Pe}^T y^{*,int}}
 \end{aligned} \tag{81e}$$

$$c_1^{IEL} e^{\lambda_1^{IEL} y^{*,IEL}} + c_2^{IEL} + A^{IEL} e^{v^* \text{Pe}^T y^{*,IEL}} = c_1^{med} e^{\lambda_1^{med} y^{*,IEL}} + c_2^{med} + A^{med} e^{v^* \text{Pe}^T y^{*,IEL}} \tag{81f}$$

$$\begin{aligned}
 & \left[(1 - \sigma_S^{IEL}) \right] v^* \left(c_1^{IEL} e^{\lambda_1^{IEL} y^{*,IEL}} + c_2^{IEL} + A^{IEL} e^{v^* \text{Pe}^T y^{*,IEL}} \right) - \\
 & - \frac{1}{\text{Pe}^{IEL}} \left(\lambda_1^{IEL} c_1^{IEL} e^{\lambda_1^{IEL} y^{*,IEL}} + A^{IEL} v^* \text{Pe}^T e^{v^* \text{Pe}^T y^{*,IEL}} \right) - \\
 & - \frac{k_T \Delta T}{\text{Pe}^{IEL} T_M^{IEL}} \frac{\rho_f}{M_f c_0} v^* \text{Pe}^T c_1^T e^{v^* \text{Pe}^T y^{*,IEL}} = \\
 & = \left[(1 - \sigma_S^{med}) \right] v^* \left(c_1^{med} e^{\lambda_1^{med} y^{*,IEL}} + c_2^{med} + A^{med} e^{v^* \text{Pe}^T y^{*,IEL}} \right) - \\
 & - \frac{1}{\text{Pe}^{med}} \left(\lambda_1^{med} c_1^{med} e^{\lambda_1^{med} y^{*,IEL}} + \lambda_2^{med} c_2^{med} e^{\lambda_2^{med} y^{*,IEL}} + A^{med} v^* \text{Pe}^T e^{v^* \text{Pe}^T y^{*,IEL}} \right) - \\
 & - \frac{k_T \Delta T}{\text{Pe}^{med} T_M^{med}} \frac{\rho_f}{M_f c_0} v^* \text{Pe}^T c_1^T e^{v^* \text{Pe}^T y^{*,IEL}}
 \end{aligned} \tag{81g}$$

$$\lambda_1^{med} c_1^{med} e^{\lambda_1^{med} y^{*,IEL}} + \lambda_2^{med} c_2^{med} e^{\lambda_2^{med} y^{*,IEL}} + A^{med} v^* \text{Pe}^T e^{v^* \text{Pe}^T y^{*,IEL}} = 0 \tag{81h}$$

where $y^{*,i}$ is the dimensionless coordinate y^* , with reference to the location of each i^{th} -layer. Equations 81 are rearranged in a matrix form:

$$\mathbf{B} = \begin{bmatrix} 1 & 1 & 0 & 0 & 0 & 0 & 0 & 0 \\ B_{2,1} & 1 & B_{2,3} & -1 & 0 & 0 & 0 & 0 \\ B_{3,1} & B_{3,2} & B_{3,3} & B_{3,4} & 0 & 0 & 0 & 0 \\ 0 & 0 & B_{4,3} & 1 & B_{4,5} & -1 & 0 & 0 \\ 0 & 0 & B_{5,3} & -B_{3,4} & B_{5,5} & B_{5,6} & 0 & 0 \\ 0 & 0 & 0 & 0 & B_{6,5} & 1 & B_{6,7} & B_{6,8} \\ 0 & 0 & 0 & 0 & B_{7,5} & -B_{5,6} & B_{7,7} & B_{7,8} \\ 0 & 0 & 0 & 0 & 0 & 0 & B_{8,7} & B_{8,8} \end{bmatrix} \mathbf{g} = \begin{bmatrix} c_1^{end} \\ c_2^{end} \\ c_1^{int} \\ c_2^{int} \\ c_1^{IEL} \\ c_2^{IEL} \\ c_1^{med} \\ c_2^{med} \end{bmatrix}$$

$$\mathbf{e} = \begin{bmatrix} 1.0246 - A^{end} \\ (A^{int} - A^{end}) e^{v^* \text{Pe}^T y^{*,end}} \\ E_{3,1} e^{v^* \text{Pe}^T y^{*,end}} \\ (A^{IEL} - A^{int}) e^{v^* \text{Pe}^T y^{*,int}} \\ E_{5,1} e^{v^* \text{Pe}^T y^{*,int}} \\ (A^{med} - A^{IEL}) e^{v^* \text{Pe}^T y^{*,IEL}} \\ E_{7,1} e^{v^* \text{Pe}^T y^{*,IEL}} \\ E_{8,1} e^{v^* \text{Pe}^T y^{*,IEL}} \end{bmatrix} \quad (82)$$

where the terms in the matrix \mathbf{B} are:

$$\begin{aligned}
 B_{2,1} &= e^{\lambda_1^{end} y^{*,end}}, & B_{2,3} &= -e^{\lambda_1^{int} y^{*,end}}, & B_{3,1} &= \left[(1 - \sigma_S^{end}) v^* - \frac{1}{\text{Pe}^{end}} \lambda_1^{end} \right] e^{\lambda_1^{end} y^{*,end}}, \\
 B_{3,2} &= (1 - \sigma_S^{end}) v^*, & B_{3,3} &= -\left[(1 - \sigma_S^{int}) v^* - \frac{1}{\text{Pe}^{int}} \lambda_1^{int} \right] e^{\lambda_1^{int} y^{*,end}}, \\
 B_{3,4} &= -(1 - \sigma_S^{int}) v^*, & B_{4,3} &= e^{\lambda_1^{int} y^{*,int}}, & B_{4,5} &= -e^{\lambda_1^{IEL} y^{*,int}}, \\
 B_{5,3} &= \left[(1 - \sigma_S^{int}) v^* - \frac{1}{\text{Pe}^{int}} \lambda_1^{int} \right] e^{\lambda_1^{int} y^{*,int}}, & B_{5,5} &= -\left[(1 - \sigma_S^{IEL}) v^* - \frac{1}{\text{Pe}^{iel}} \lambda_1^{IEL} \right] e^{\lambda_1^{IEL} y^{*,int}}, \\
 B_{5,6} &= -(1 - \sigma_S^{IEL}) v^*, & B_{6,5} &= e^{\lambda_1^{IEL} y^{*,IEL}}, & B_{6,7} &= -e^{\lambda_1^{med} y^{*,IEL}}, & B_{6,8} &= -e^{\lambda_2^{med} y^{*,IEL}}, \\
 B_{7,5} &= \left[(1 - \sigma_S^{IEL}) v^* - \frac{1}{\text{Pe}^{IEL}} \lambda_1^{IEL} \right] e^{\lambda_1^{IEL} y^{*,IEL}},
 \end{aligned}$$

Biological systems

$$B_{7,7} = - \left[(1 - \sigma_S^{med}) v^* - \frac{1}{Pe^{med}} \lambda_1^{med} \right] e^{\lambda_1^{med} y^{*,IEEL}},$$

$$B_{7,8} = - \left[(1 - \sigma_S^{med}) v^* - \frac{1}{Pe^{med}} \lambda_2^{med} \right] e^{\lambda_2^{med} y^{*,IEEL}}, B_{8,7} = \lambda_1^{med} e^{\lambda_1^{med} y^{*,med}},$$

$$B_{8,8} = \lambda_2^{med} e^{\lambda_2^{med} y^{*,med}},$$

while the terms in the vector \mathbf{e} are:

$$E_{3,1} = e^{v^* Pe^T y^{*,end}} \left[(1 - \sigma_S^{int}) v^* A^{int} - \frac{A^{int}}{Pe^{int}} v^* Pe^T - \frac{k_T \Delta T}{Pe^{int} T_M^{int}} \frac{\rho_f}{M_f c_0} v^* Pe^T c_1^T - \right. \\ \left. - (1 - \sigma_S^{end}) v^* A^{end} - \frac{A^{end}}{Pe^{end}} v^* Pe^T - \frac{k_T \Delta T}{Pe^{end} T_M^{end}} \frac{\rho_f}{M_f c_0} v^* Pe^T c_1^T \right] \quad (83a)$$

$$E_{5,1} = e^{v^* Pe^T y^{*,int}} \left[(1 - \sigma_S^{IEEL}) v^* A^{IEEL} - \frac{A^{IEEL}}{Pe^{IEEL}} v^* Pe^T - \right. \\ \left. - (1 - \sigma_S^{int}) v^* A^{int} - \frac{A^{int}}{Pe^{int}} v^* Pe^T - \right. \\ \left. - \frac{k_T \Delta T}{Pe^{IEEL} T_M^{IEEL}} \frac{\rho_f}{M_f c_0} v^* Pe^T c_1^T \right] \quad (83b)$$

$$E_{7,1} = e^{v^* Pe^T y^{*,IEEL}} \left[(1 - \sigma_S^{med}) v^* A^{med} - \frac{A^{med}}{Pe^{med}} v^* Pe^T - \right. \\ \left. - \frac{k_T \Delta T}{Pe^{med} T_M^{med}} \frac{\rho_f}{M_f c_0} v^* Pe^T c_1^T - (1 - \sigma_S^{IEEL}) v^* A^{IEEL} - \right. \\ \left. - \frac{A^{IEEL}}{Pe^{IEEL}} v^* Pe^T - \frac{k_T \Delta T}{Pe^{IEEL} T_M^{IEEL}} \frac{\rho_f}{M_f c_0} v^* Pe^T c_1^T \right] \quad (83c)$$

$$E_{8,1} = -A^{med} v^* Pe^T e^{v^* Pe^T y^{*,med}} \quad (83d)$$

The vectorial form of the coefficients \mathbf{g} is obtained using the following matrix format:

$$\mathbf{g} = \mathbf{B}^{-1} \cdot \mathbf{e} \quad (84)$$

that is the compact form of the analytical solution to Eq. (72).

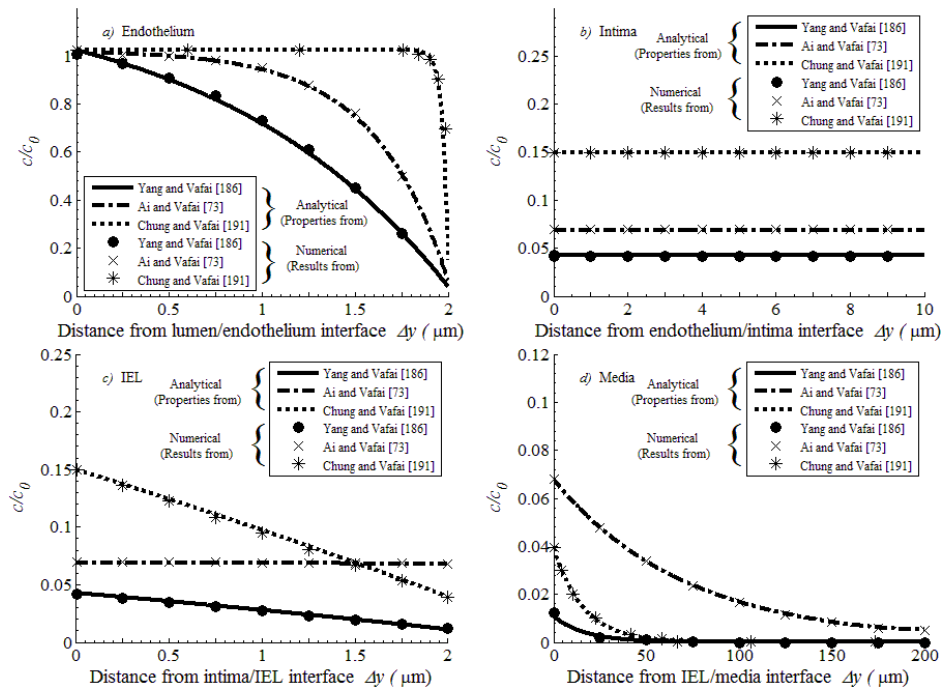


Fig. 89. LDL concentration vs. the distance from interfaces in isothermal conditions, for different models.

The LDL concentration as a function of the distance from interfaces in isothermal conditions, for different model, obtained by the analytical solution of the above presented equations, is reported in Fig.89. Figures point out that concentration is strongly affected by the set of thermophysical properties and closing coefficients. Indeed, in the endothelium layer, differences in slopes are due to different values of mass Peclet number. The Peclet number obtained with properties from the present work, the same as that of Chung and Vafai [191], is the highest one, thus indicating that advection is dominating on diffusion.

A comparison with isothermal analytical solutions from literature is reported in Fig. 90, also considering different transmural pressures and endothelium diffusivities. Again, a very good agreement has been found.

Comparisons with numerical results from Chung and Vafai [191] for LDL transport under hyperthermia conditions are reported in Figs. 91 and 92, with different values of ΔT and k_T . It is noticed that the external heating mode increases the LDL concentration, especially in the intima layer, whereas the

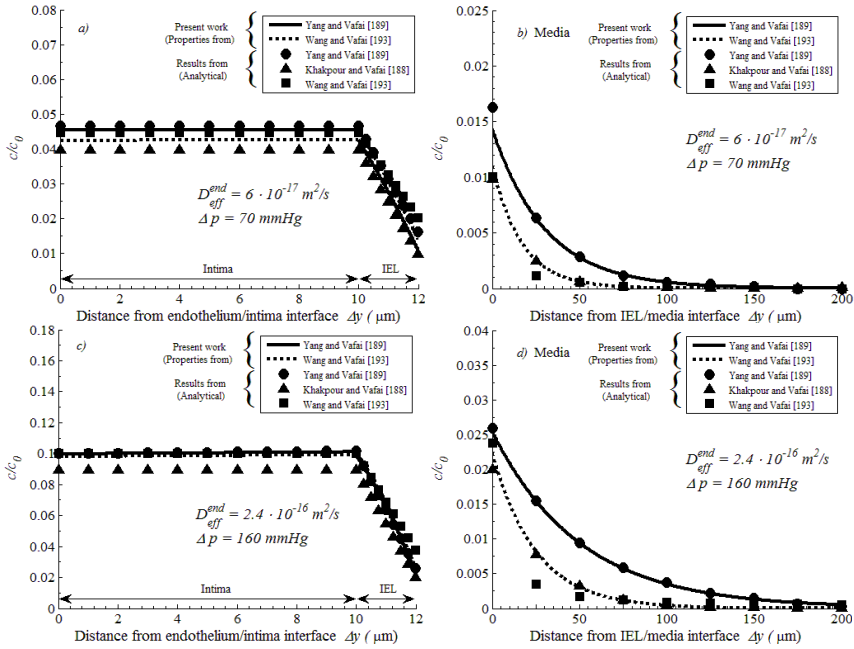


Fig. 90. LDL concentration vs the distance from interfaces in isothermal conditions, for different models.

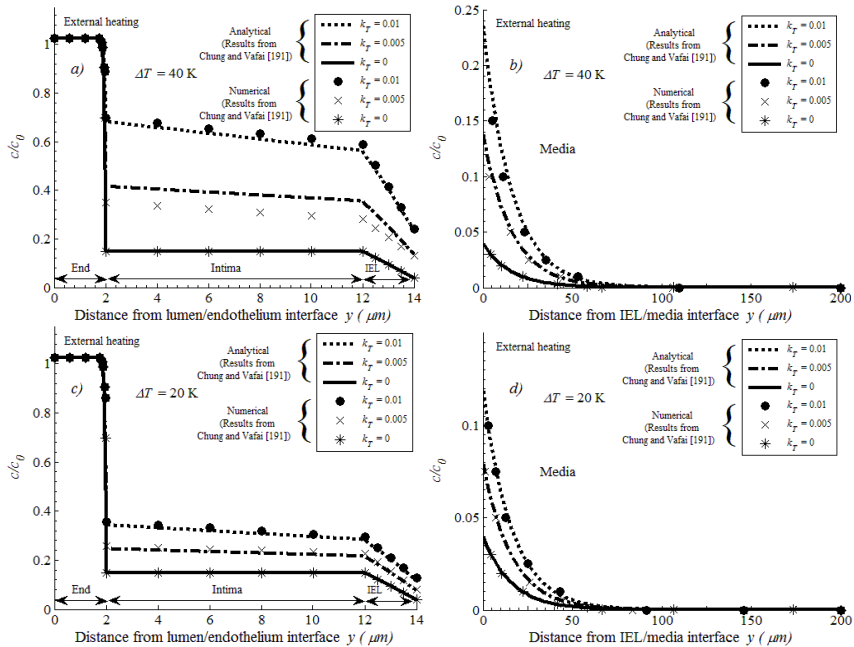


Fig. 91. LDL concentration vs the distance from lumen/endothelium interface, for external heating and different models and thermodiffusion coefficients.

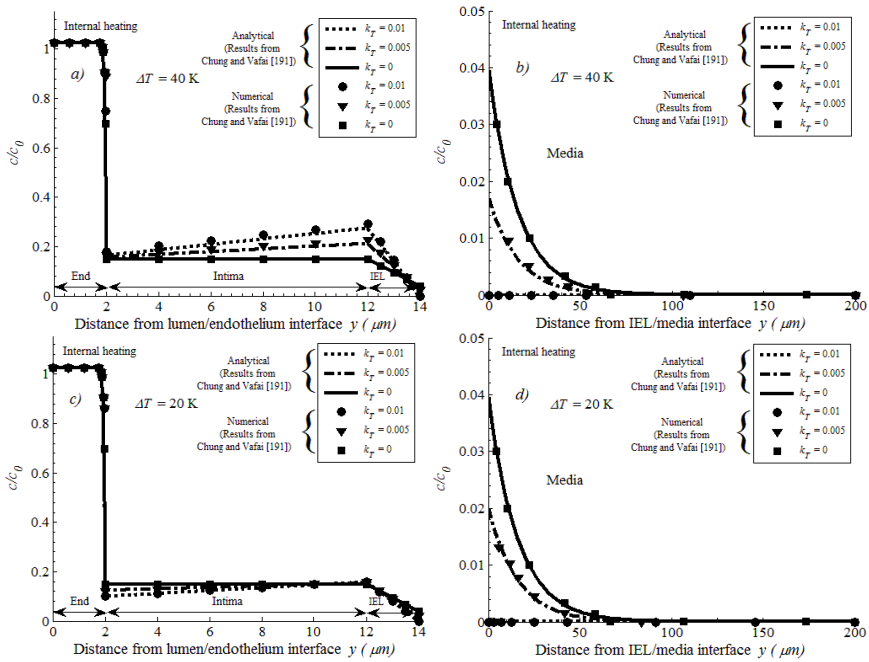


Fig. 92. Concentration vs the distance from interfaces, for different models or internal heating for models and thermodiffusion coefficients.

internal heating causes a slight reduction only for low thermal loads. In the external heating the particles migrate from the hot to the cold zone, while the opposite occurs for the internal heating. This is very stressed in the intima layer. In the intima, LDL concentration gradients are higher with external heating than with the internal heating. This occurs because, with reference to Eq. (27), the thermal diffusion term has an absolute temperature term at denominator, that enhances the mass flux due to thermodiffusion. Temperatures in the intima layer are lower for external heating than for internal heating and, therefore LDL concentration is higher. Comparing the present analytical solution with numerical data from Chung and Vafai [191], a very good agreement is remarked.

4.3.3.2 Hypertension and hyperthermia effects

Combined effects of hypertension and hyperthermia on LDL transport are analyzed by using the analytical solution derived in the previous sub-section. Results are reported in Figs. 93 and 94, where LDL concentration as a function of the distance from lumen/endothelium interface, for different transmural

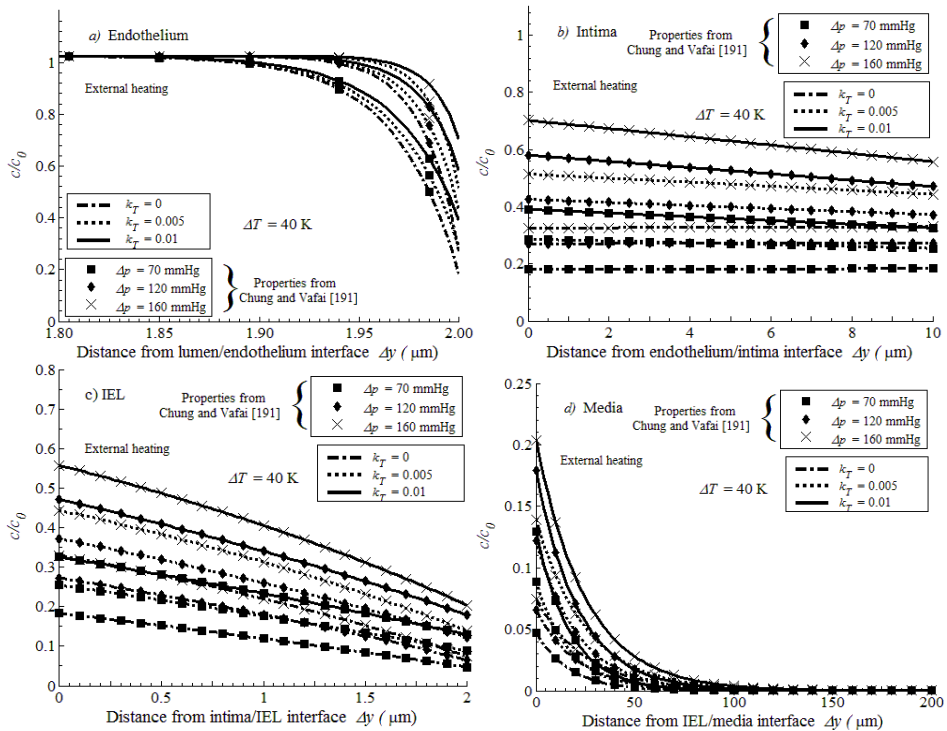


Fig. 93. LDL concentration vs the distance from lumen/endothelium interface, for external heating, different transmural pressures and thermodiffusion coefficients.

pressures and thermodiffusion coefficients, as well as for external and internal heating are reported.

As it was noticed for non-Newtonian effects, hypertension increases LDL accumulation across the wall. The highest LDL concentrations are obtained when transmural pressure, thermo-diffusion coefficient and temperature difference are the highest, for both external and internal hyperthermia cases. With reference to internal heating case (Fig. 94), for all the transmural pressures the larger the thermodiffusion coefficient the lower the LDL concentration at the endothelium/intima interface. However, the opposite occurs at the intima/IEL interface, since concentration increases along the intima, more remarkably with increasing thermodiffusion. In the IEL, the situation changes again, since at the IEL/media interface the lowest values of concentration are reached when $k_T = 0.01$.

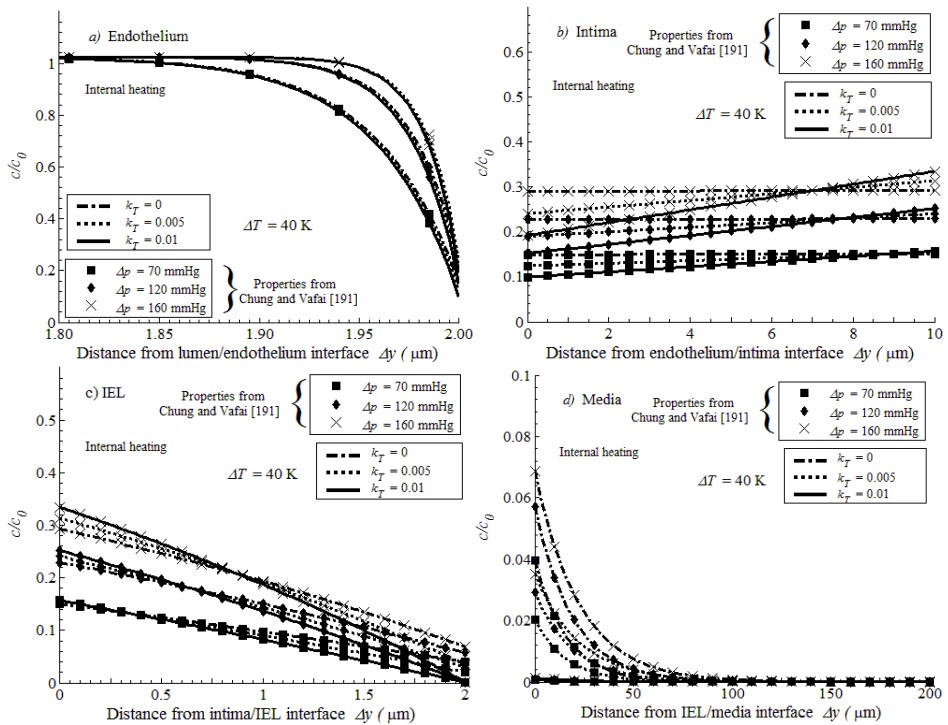


Fig. 94. LDL concentration vs the distance from lumen/endothelium interface, for internal heating, different transmural pressures and thermodiffusion coefficients.

In conclusion, the coupled effect of hypertension and hyperthermia dramatically increases LDL concentrations across the arterial wall, especially when the heat enters its exterior boundary.

4.4. Stenosed artery

When an artery with a stenosis is modeled, geometrical modeling plays the main role. Many different geometrical models were proposed. A trapezoidal shape of the stenosis was proposed by Jung et al. [218]. Dash et al. [219] used a sinusoidal function, while a bell-shaped Gaussian function was used by Liao et al. [220]. Longa et al. [221] used two integrated Gaussian functions at a certain distance, with a straight segment between them in order to have a smooth stenosis. Another function was based on a cosinusoid [222]. Differences among various stenosis geometries are resumed in Fig. 95. Different stenosis models have been applied for the same case. Even if there are some little differences,

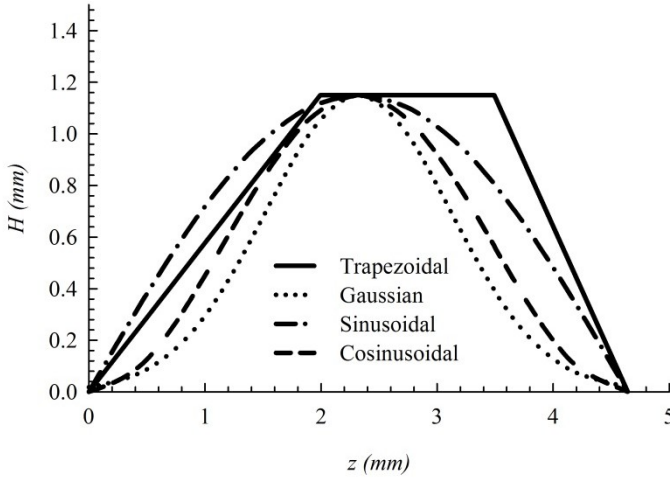


Fig. 95. Some geometrical models of the stenosis shape.

the stenosis shapes are almost the same. In this study, a cosinusoidal stenosis shape is used, that will be described in the following sub-section.

4.4.1. Mathematical model

The geometrical model used in the following is similar to the one described in the previous section. The length of the artery is assumed to be equal to 22.32 cm [73]. An axisymmetric stenosis is modeled with the following cosinusoidal function [222]:

$$\frac{r}{r_{lumen}} = 1 - \frac{\delta}{2r_{lumen}} \left[1 + \cos \frac{\pi(z - z_{st})}{z_{st}} \right] \quad (85)$$

that is valid for $-z_0 \leq (z - z_{st}) \leq z_0$. The dimensionless parameter δ that takes into account the severity of the stenosis. The subscripts 0 and st refer to the axial coordinate on the centerline of the stenosis, that is also the minimum lumen cross section, and to the distance between the center of the stenosis and its beginning, respectively. The stenosis severity parameter is correlated to the stenosis area reduction (Eq. (58)) with the following equation:

$$A = 1 - \left[\frac{r(z_{st})}{r_{lumen}} \right]^2 = 1 - (1 - \delta)^2 \quad (86)$$

In this study, two values, $\delta = 1/2$ and $\delta = 1/4$, are investigated, in order to analyze the effects of a mild stenosis (43%) and of a severe stenosis (75%). The fibrous cap formed during the atherosclerosis process is also accounted for in the geometrical model, because of its primary role. Its thickness is assumed to be $65 \mu\text{m}$, above which the fibrous cap is considered as thin [223], and its effective diffusivity is $4.5 \cdot 10^{-13} \text{ m}^2/\text{s}$ [223].

Governing equations are essentially the same as those of the mathematical model in the previous section. A Newtonian model is referred to. Thermodiffusion effects are considered, since the aim of this study is to analyze hyperthermia effects on a stenosed artery. Equations (3c), (4d) and (8) are employed for the mass, momentum and species transport through the lumen, respectively. Equation (8) is taken in its stationary form, with $r = 0$. For the arterial wall, Eqs. (12c), (14b), (24) and (27) are employed for mass, momentum, energy and solute, respectively. Equations (14b), (24) and (27) are taken in their stationary form. Forchheimer term and body forces are neglected in the momentum equation. Thermophysical properties and closing coefficients are resumed in Table 7. Boundary conditions, the same as those of the mathematical model, are resumed, together with the geometrical model, in Fig. 96.

Because of the complex geometry, a triangular mesh is used to solve numerically the governing equations.

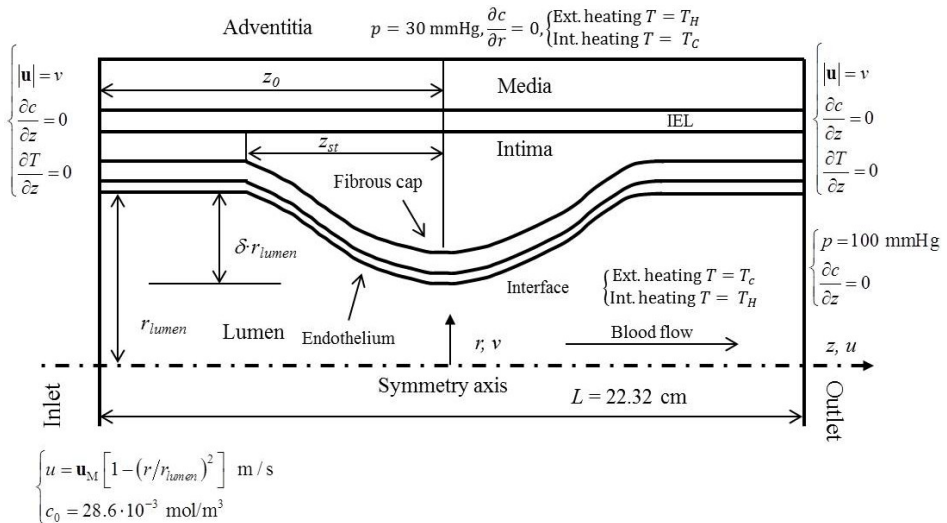


Fig. 96. Boundary conditions for the stenosis problem.

4.4.2. Hyperthermia effects

The present model has been validated comparing predicted temperature profiles in the straight part of artery with the analytical solution from Mahjoob and Vafai [224] and with numerical results from Chung and Vafai [191]. Predictions for the stenosed part of an artery have been compared with results by Chung and Vafai [183]. The above said comparisons are presented in Fig. 97, that shows a good agreement among data.

Temperature across the arterial wall as a function of the radius, for different stenosis severity and stenosis locations, is shown in Figs. 98a and 98b, respectively. Figs.98a exhibits a strong dependence of the temperature, on the stenosis thickness, that is consistent with differences in thermal Peclet number, whose order is $O(10^{-5})$ in regions where there is no stenosis and $O(10^{-4})$ in the region with a stenosis. This means that the increasing advective contribution makes the temperature profile non linear, as that it in mere conduction is. Similar considerations can be made on the effect of the stenosis location in Fig.98b.

Hyperthermia effects on LDL transport are highlighted in Figs. 99 and 100, where the LDL concentration as a function of the radius, for different stenosis severities and thermodiffusion coefficients as well as for both external and internal heating, is reported in Fig.99. Increasing the thermodiffusion effect increases the concentration, especially in the intima layer. Comparing external and internal heating modes shows that effects on internal heating are lower, as it was found for a straight artery in the previous section.

LDL concentration as a function of the radius, for different stenosis severity and thermal load as well as for both external and internal heating, respectively, is reported in Fig.100. One can notice that the axial location of the stenosis has

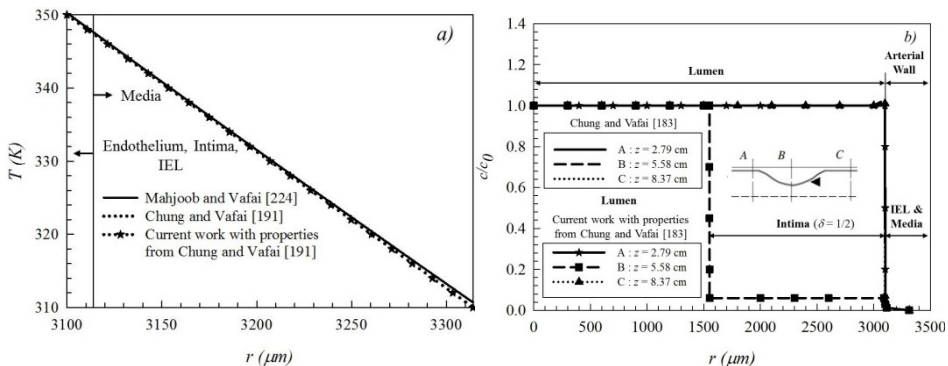


Fig. 97. Comparisons with literature data: a) temperature profiles; b) LDL concentration profiles across the stenosis.

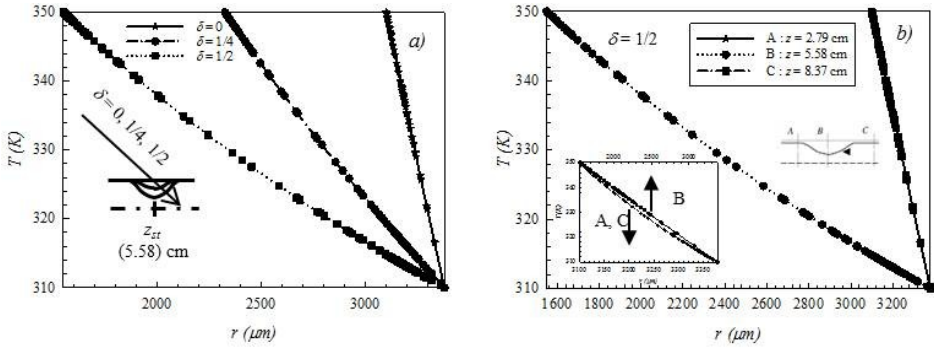


Fig. 98. Temperature across the arterial wall vs. the radius, for various: a) stenosis severities; b) stenosis locations.

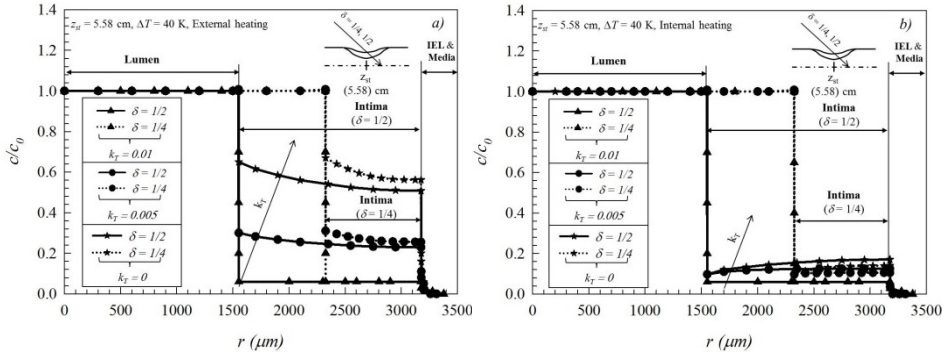


Fig. 99. LDL concentration vs. the radius, for different stenosis severities and thermodiffusion coefficients: a) external heating; b) internal heating.

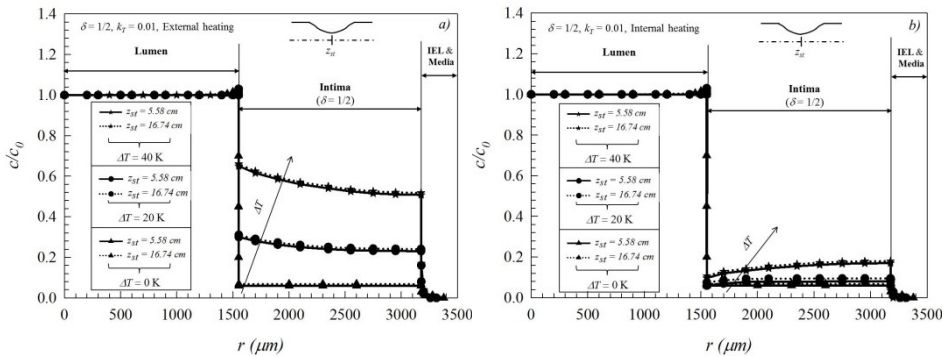


Fig. 100. LDL concentration vs. the radius, for different stenosis severity and thermal load: a) external heating; b) internal heating.

a negligible effect on mass transport. The thermal load increases the LDL concentration in the intima layer; the increase in the external heating is larger than that in internal heating.

Definitely, LDL concentration is increased under hyperthermia loads also in a stenosed artery.

4.5. Aorta-iliac bifurcation

The geometry of the aorta-iliac bifurcation is complicated, because of the bifurcation. Both for males and females it was exhaustively described by Shah et al. [225]. They found that the abdominal aorta has an asymmetrical left lateral orientation, which implies a longer right common iliac, a smaller left take-off angle, and a smaller right radius of curvature at the bifurcation. Measurements on eleven Asian people were performed by Ganananda Nanayakkara et al. [226]. Studies on the bifurcation exact position and its local geometry were recently carried out by Deswal et al. [227]. They remarked that the geometry of the aorta-iliac is influenced by many parameters, that depend on sex and other factors. The gender-related aorta-iliac effects on macromolecule transport were investigated by Khakpour and Vafai [187].

4.5.1. Mathematical model

The aorta-iliac bifurcation geometry, which this study refers to, is represented in Fig. 101. Its geometrical features are obtained with the following procedure, also used by Khakpour and Vafai [187]. Making reference to the anatomical data from Shah et al. [225], the mean values of the geometrical parameters reported for the male cases are considered. The lumen diameter of the aorta is 2.1 cm; the length is 5.0 cm. The lumen diameter of the right common iliac is 1.28 cm; its length is 6.1 cm. The lumen diameter of the left common iliac is 1.24 cm; its length is 5.8 cm. Both the right and the left take-off angles are 40°. Numbers #1 and #2 refer to the right and left iliac arteries, respectively.

Governing equations, thermophysical properties, closing coefficients and boundary conditions are the same as those of the mathematical model, used in the non-Newtonian analysis of the straight artery. A 2-D model is used in the present analysis. Thermophysical properties and closing coefficients are taken from Table 7. Governing equations are solved with the finite element method, and a triangular mesh was chosen with a larger number of elements than for the straight artery, since the geometry is more complicated and flow recirculation may occur. Grid independence and relative tolerance have been checked on the concentration polarization along the lumen/endothelium interface.

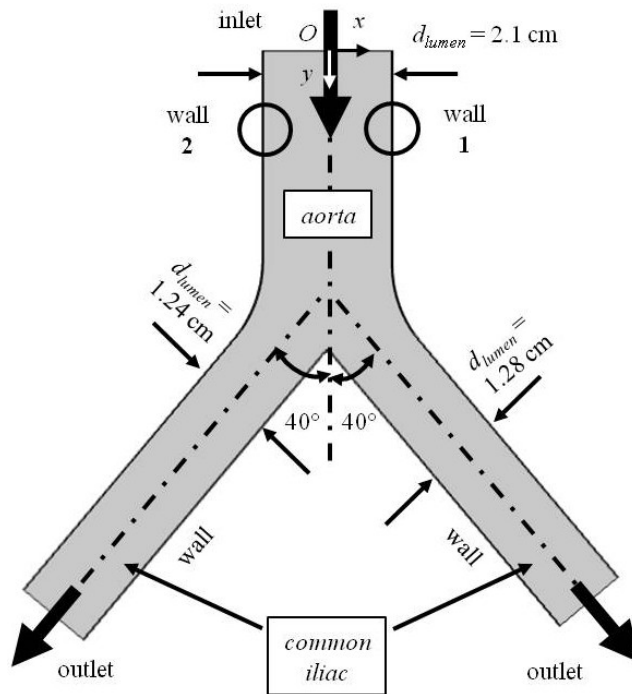


Fig. 101. Geometry of the aorta-iliac bifurcation.

4.5.2. Non-Newtonian effects

Dimensionless velocity as a function of the radius, at various axial coordinates is reported in Fig.102. We can remark that the less the distance from

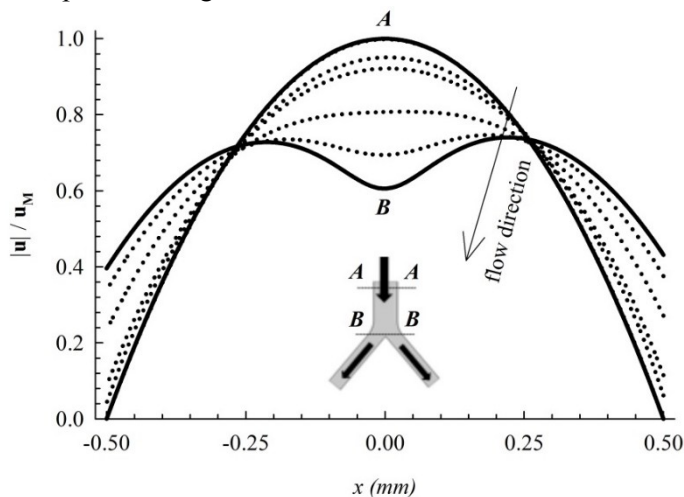


Fig. 102. Dimensionless velocity vs. the radius, at various axial coordinates.

the bifurcation the larger the flatness of velocity distribution in the cross section of the artery. The slight asymmetry on the right side depends on the larger blood flow rate entering the right common iliac.

Wall shear stress and LDL concentration along the lumen/endothelium interface, for the Newtonian model and various Reynolds numbers, are presented in Fig.103. The Reynolds number is $Re = 2 \rho u_m r_{lumen}/\mu$. The figure shows that wall shear stresses increase with increasing Reynolds number. As to the right iliac, they slightly increase upstream of the curve, attaining a maximum at the point A, where the bifurcation begins. WWS decrease in the curved region and act in the opposite direction for higher Reynolds numbers. This causes flow recirculation, exhibited in Fig. 104, where velocity vector and LDL concentration in the right bifurcation region are reported. No recirculation occurs in the region of the left iliac, because of the smaller variation of the artery geometry. The concentration polarization decreases at increasing Reynolds numbers. Upstream of the bifurcation, the concentration increases due to the polarization effect; then it slightly decreases in the bent, because of the flow deceleration; finally, it increases again. The LDL concentration attains a maximum where recirculation occurs, due to the change in the sign of the WSS, that causes a solute stagnation. A similar behavior for stenosis was found by

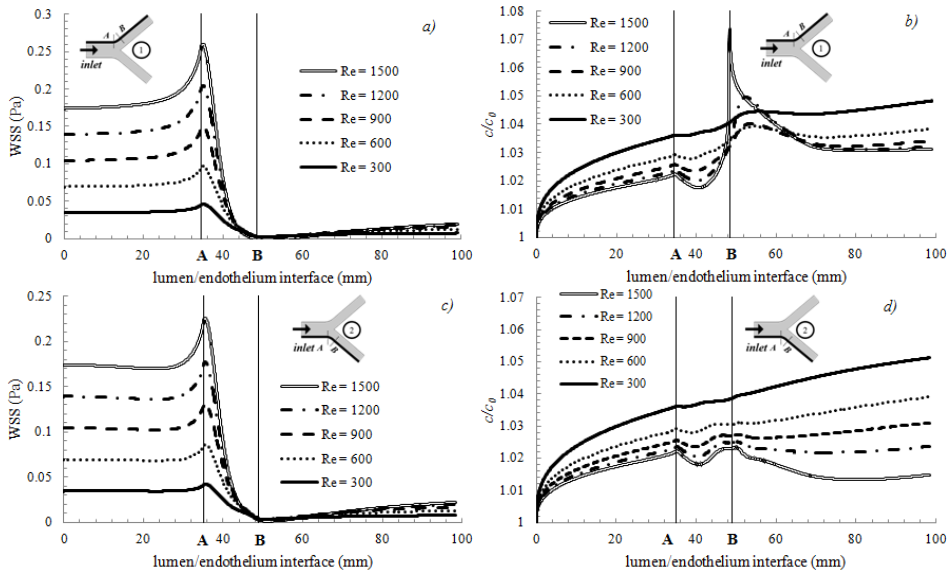


Fig. 103. Wall shear stress and LDL concentration along the lumen/endothelium interface, for the Newtonian model and various Reynolds numbers.

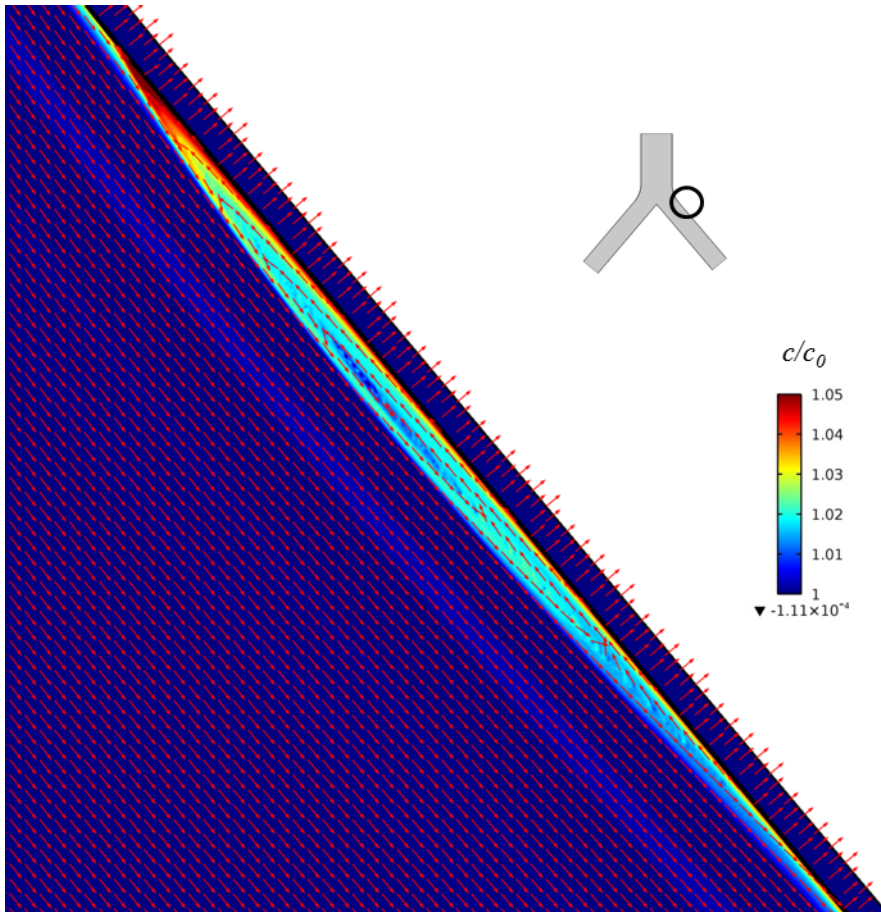


Fig. 104. Velocity vector and LDL concentration in the right bifurcation region.

Nematollahi et al. [228]. Finally, Figs. 103a and 103b, as well as Figs.103c and 103d) show that, for Newtonian fluids, there is an inverse relationship between WSS and concentration profiles.

Wall shear stress and LDL concentration along the lumen/endothelium interface, for various rheological models, Reynolds numbers and for the right and left iliac arteries are reported in Figs.105 - 108. Figures 105 and 106 show that, apart from the aorta region, wall shear stresses, at each value of the Reynolds number, both in the right and left iliac arteries, are independent of the rheological model. Different viscosities are the reason why in the aorta region wall shear stresses depend on models. Figure 105 show that recirculation flow in the right iliac artery occurs in Newtonian fluid for $Re = 1200$ and $Re=1500$ as well as Power-law and Carreau-Yasuda non-Newtonian models for $Re=1500$.

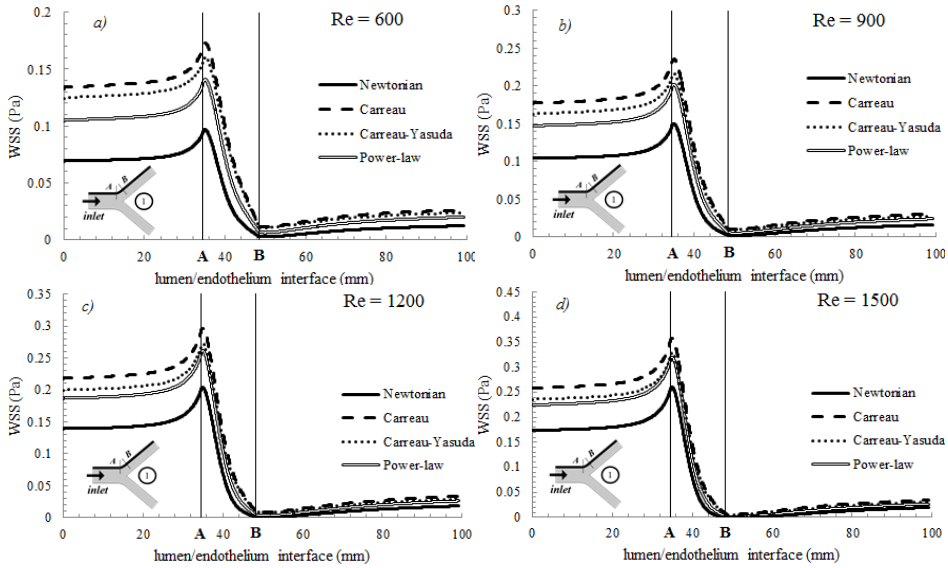


Fig. 105. Wall shear stresses along the lumen/endothelium interface of the right iliac artery, for various rheological models and Reynolds numbers.

LDL concentrations predicted by all rheological models are similar, apart from the cases at $Re = 900, 1200, 1500$ in the right iliac artery, where

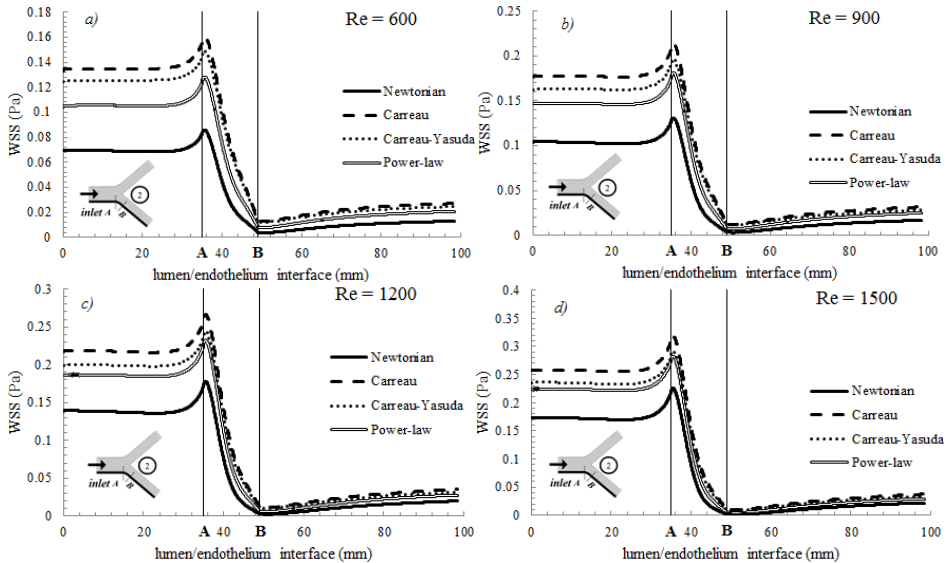


Fig. 106. Wall shear stresses along the lumen/endothelium interface of the left iliac artery, for various rheological models and Reynolds numbers.

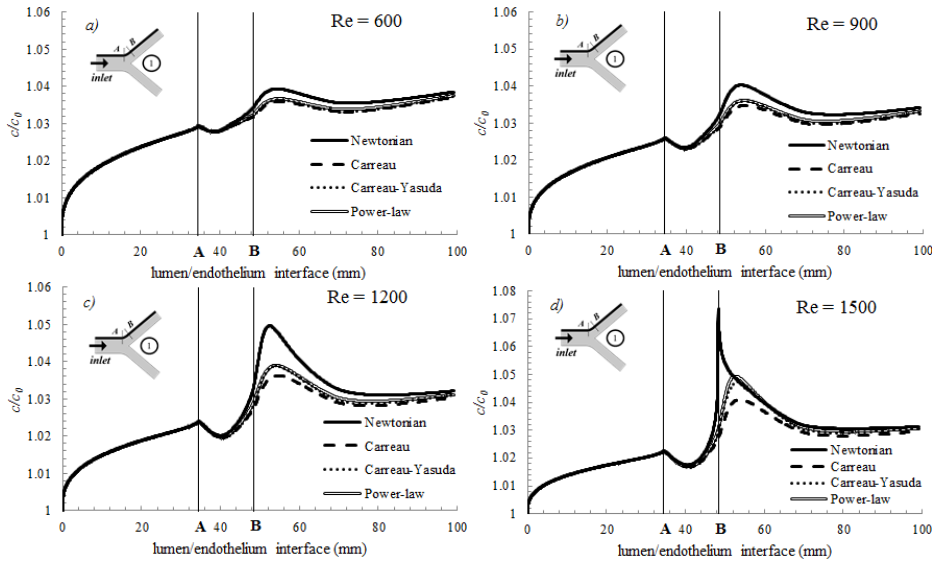


Fig. 107. LDL concentration along the lumen/endothelium interface of the right iliac artery, for various rheological models and Reynolds numbers.

recirculation occurs. This means that predictions are less accurate when a Newtonian model is used for low shear stress regions, like bifurcations or other particular geometries.

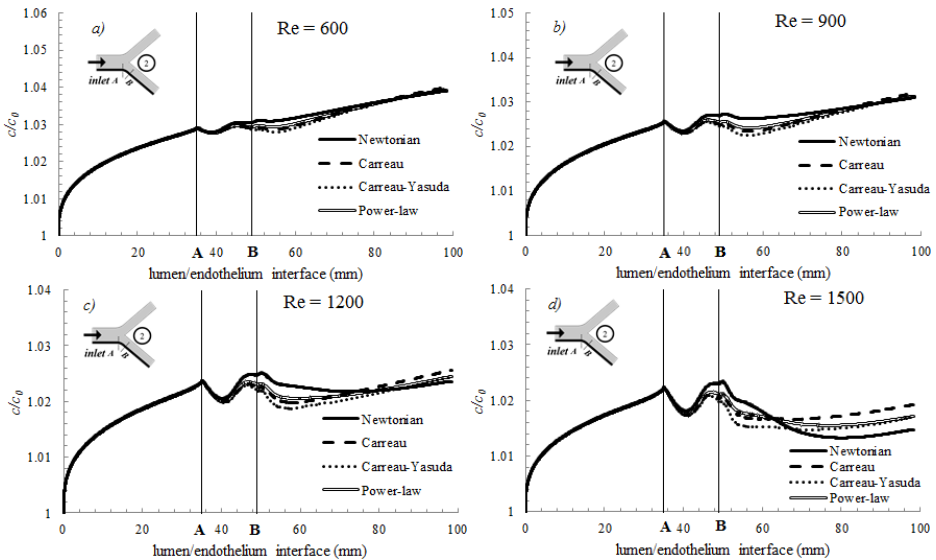


Fig. 108. LDL concentration along the lumen/endothelium interface of the left iliac artery, for various rheological models and Reynolds numbers.

Biological systems

In conclusions, Newtonian models may not predict accurately LDL accumulation when particular geometries with low WSS are analyzed.

CONCLUSIONS

Transport in porous media has been analyzed in the present thesis. Two classes of porous media have been chosen for this study: open-cell foams and biological systems, with reference to the low density lipoprotein (LDL) transport through the arterial wall. Heat transfer and pressure drop in open-cell foams have been investigated both on micro and macro scales. Experiments and numerical simulations on real and ideal foams have been carried out to solve the problem at microscale; numerical simulations have been developed for foam-based volumetric solar receivers and heat sinks at macroscale. LDL transport has been analyzed by using a multi-layer model, that studies the arterial wall layers with the volume-averaged porous media governing equations. Many aspects like non-Newtonian, hypertension and hyperthermia effects have been analyzed by using either an numerical or an analytical approach.

In the open-cell foams microscale analysis, experiments have been carried out on aluminum open-cell foam samples to analyze pressure drop and convection heat transfer. Porosity and PPI effects on pressure drop and its closing coefficients have been studied. Results showed that the PPI effect is much higher than the porosity one. In particular, pressure drop increases with PPI, while it slightly increases with porosity. Preliminary transient experiments on volumetric heat transfer coefficients have been also presented, for different velocities of the fluid. They showed that the higher the velocity the higher the decrease of the transfer coefficient with the time. Numerical approaches for pressure drop and convection heat transfer have been used for both real and ideal foams samples. Three real foams samples, with equal PPI and different porosities, have been investigated. Their geometry has been reconstructed by using x-ray Computed Tomography (xCT). After a comprehensive study on their morphology, pressure drop and volumetric heat transfer coefficients have been evaluated for a Representative Volume Element (RVE) of the scanned sample by using a finite-element scheme. Ideal foam samples have been reconstructed with reference to the tetrakaidechadric Kelvin's foam model. The specific surface area has been correlated to the porosity and cell diameter. Thermally developing effects have been analyzed by simulating an array of Kelvin's cells. Three different regions along the flow direction were distinguished: an impinging region where the heat transfer coefficient increases, a thermally developing region where the heat transfer coefficient decreases, and a thermally developed region where the heat transfer coefficient is uniform. The extension of the first two regions increases at larger Reynolds numbers and lower porosities. A correlation for the thermally developed Nusselt number has

Conclusions

been obtained. The pore-scale analysis of Nusselt number in a single thermally developed cell showed that the convection heat transfer becomes periodic at very low scales. The effects of strut shape on convection heat transfer and pressure drop have been evaluated for a single cell, by changing the strut shape with a MATLAB-based in-house code. It was found that the more accurate the strut shape the closer the ideal model results to the real model ones.

The thermo-fluid-dynamic of open-cell foams engineering applications, such as volumetric receivers and foam-based heat sinks, has also been analyzed by using a macroscopic porous media approach. Various foam morphologies of the volumetric receivers have been analyzed. Results showed that higher porosities and lower cell sizes increase the so-called volumetric effect and, consequently, the efficiency of the receivers. The fluid outlet temperature was almost independent of the morphological parameters of the investigated foams. Two configurations of the foam-based heat sinks have been investigated. In the first, inserts of foam are placed between fins; in the second the sink is made up only by the open-cell foam. The finned metal foam heat sink enhances heat transfer more than the metal foam heat sink. Parametric analysis for various geometries and foam morphologies has been accomplished, in order to find the best configuration for both heat transfer and pressure drop.

As far as the LDL transport through an arterial wall is concerned, different geometries have been analyzed: a straight artery, a stenosed artery and the aorta-iliac bifurcation. The accumulation through the arterial wall of a straight artery has been analyzed either numerically or analytically. Non-Newtonian fluid effects on mass transport have been investigated numerically under hypertension conditions, for both medium and large arteries. Differences on LDL concentration polarization along the lumen/wall interface between Newtonian and non-Newtonian models were always less than about 3%; therefore, a Newtonian model may be an acceptable approximation in modeling LDL transport. Differences among depositions through the arterial wall were less than 1% for a healthy case, reaching a value mainly less than the 10% for the highest transmural pressure value, that can still be considered negligible. Analytical approaches have been performed to solve the mass transport through the wall under both hypertension and hyperthermia effects. Hyperthermia effects on mass transport were included by considering the Ludwig-Soret effect. Both hypertension and hyperthermia increased mass transport. However, it was also noticed that hyperthermia can sometimes reduce the concentration when the heating load is applied from the interior of the wall, in particular for low heat loads.

The stenosed artery has been studied by using a cosinusoidal function to model its geometry; different stenosis severities have been considered. A numerical approach based on a finite-element scheme has been chosen. The study of hyperthermia effects on mass deposition showed that hyperthermia increases LDL accumulation. The aorta-iliac bifurcation has been investigated numerically. Various rheological models, for different Reynolds numbers, have been compared. Differences among the various rheological models were negligible when no flow recirculation occurred. One can conclude that a non-Newtonian fluid model must be preferred when geometries are complicated and wall shear stresses are low.

REFERENCES

- [1] “Definition of Pore,” Treccani, accessed February 06, 2016, <http://www.treccani.it/vocabolario/poro>.
- [2] Kaviany, M., 1995, *Principles of Heat Transfer in Porous Media: Second Edition*, Springer, New York (NY), USA.
- [3] Whitaker, S., 1986, “Flow in porous media I: A theoretical derivation of Darcy's law,” *Transport Porous Med.*, 1(1), pp. 3-25.
- [4] Kaviany, M., 1991, *Principles of Heat Transfer in Porous Media*, Springer, New York (NY), USA.
- [5] Nield, D. A., and Bejan, A., 2013, *Convection in porous media: Fourth edition*, Springer, New York (NY), USA.
- [6] Vafai, K., 2015, *Handbook of porous media: Third edition*, CRC Press, Boca Raton (FL), USA.
- [7] Bear, J., 1972, *Dynamics of Fluids in Porous Media*, American Elsevier Publishing Company, New York (NY), USA.
- [8] Vafai, K., 2010, *Porous Media: Applications in Biological Systems and Biotechnology*, CRC Press, Boca Raton (FL), USA.
- [9] Plateau, J., 1873, *Statique expérimentale et théorique des liquides soumis aux seules forces moléculaires: Tome Second*, Gauthier-Villars, Paris, France.
- [10] Cantat, I., Cohen-Addad, S., Elias, F., Graner, F., Höhler, R., Flatman, R., Pitois, O., Rouyer, F., and Saint-Jalmes, A., 2013, *Foams: Structure and Dynamics*, Oxford University Press, New York (NY), USA.
- [11] IG Farbenindustrie AG. 1942. Verfahren zur Herstellung von Polyurethanen bzw. Polyharnstoffen. German Patent 728,981, filed

References

- November 13, 1937 and issued December 7, 1942.
- [12] Seymour, R. B., and Kauffman, G. B., 1992, "Polyurethanes: A class of modern versatile materials," *J. Chem. Educ.*, 69(11), pp. 909-910.
- [13] Volz, Robert A.. 1965. Reticulated polyurethane foams and process for their production. U.S. Patent 3,171,820, filed February 17, 1964 and issued March 2, 1965.
- [14] Banhart, J., 2013, "Light-Metal Foams—History of Innovation and Technological Challenges," *Adv. Eng. Mater.*, 15(3), pp. 82-111.
- [15] de Meller, Alexander. 1926. Produit métallique pour l'obtention d'objets laminés, moulés ou autres, et procédés pour sa fabrication. French Patent 615,147, filed September 12, 1925 and issued December 30, 1926.
- [16] Elliott, John C.. 1956. Method of producing metal foam. U. S. Patent 2,751,289, filed October 8, 1951 and issued June 19, 1956.
- [17] Ashby, M. F., Evans, A. G., Fleck, N. A., Gibson, L. J., Hutchinson, J. W., and Wadley, H. N. G., 2000, *Metal Foams: A Design Guide*, Butterworth-Heinemann, Waltham (MA), USA.
- [18] Binner, J., 2005, "Ceramic Foams," *Cellular Ceramics: Structure, Manufacturing, Properties and Applications*. M. Scheffler, and P. Colombo, eds., Wiley-VCH Verlag GmbH & Co. KGaA, Weinheim, Germany, pp. 31-224.
- [19] Schwartzwaldner, Karl, and Arthur V. Somers. 1963. Method of making porous ceramic articles. U. S. Patent 3,090,094, filed February 21, 1961 and issued May 21, 1963.
- [20] Ortona, A., D'Angelo, C., Gianella, S., and Gaia, D., 2012, "Cellular ceramics produced by rapid prototyping and replication," *Mater. Lett.*, 80, pp. 95-98.

- [21] Gibson, L.J., and Ashby, M. F., 1999, *Cellular solids: Structure and properties – second edition*, Cambridge University Press, Cambridge, UK.
- [22] Dukhan, N., 2013, *Metal Foams: Fundamentals and Applications*, DEStech Publications Inc., Lancaster (PA), USA.
- [23] “Duocel[®] Foam Application Guide,” ERG Materials & Aerospace Corporation, accessed February 6, 2016, <http://www.ergaerospace.com>.
- [24] Mancin, S., Diani, A., Doretto, L., Hooman, K., and Rossetto, L., 2015, “Experimental analysis of phase change phenomenon of paraffin waxes embedded in copper foams,” *Int. J. Therm. Sci.*, 90, pp. 79-89
- [25] Khalili, A., Liu, B., Javadi, K., Morad, M. R., Kindler, K., Matyka, M., Kindler, K., Stocker, R., and Koza, Z., 2010, “Application of porous media theories in marine biological modeling,” *Porous Media: Applications in Biological Systems and Biotechnology*. K. Vafai ed., CRC Press, Boca Raton (FL), USA, pp. 365–398.
- [26] Khaled, A. –R. A., and Vafai, K., 2003, “The role of porous media in modeling flow and heat transfer in biological tissues,” *Int. J. Heat Mass Tran.*, 46(26), pp. 4989–5003.
- [27] Khanafer, K., and Vafai, K., 2006, “The role of porous media in biomedical engineering as related to magnetic resonance imaging and drug delivery,” *Heat Mass Transfer*, 42, pp. 939-953.
- [28] “Basi Scientifiche per Linee Guida: Terapie mini-invasive delle lesioni epatiche,” Istituto Superiore di Sanità, accessed February 6, 2016, <http://www.iss.it/lgac/docu/cont.php?id=212&tipo=32>.
- [29] Nakayama, A., and Kuwahara, F., 2008, “A general bioheat transfer model based on the theory of porous media,” *Int. J. Heat Mass Tran.*, 51 (11-12), pp. 3190-3199.

References

- [30] “Magnetic Resonance Imaging (MRI),” Naperville Imaging Center, accessed February 25, 2016, <http://www.napervillemri.com/mri-naperville-imaging-center-chicago-il.html>.
- [31] Dufour, L., 1872, Arch. Sci. Phys. Nat. (II series), 45, pp. 9-12.
- [32] Aouachria, Z., Rouichi, F., and Haddad, D., 2012, “Double diffusion effects on convection in flow on vertical plate imbedded in a porous media,” *Frontiers in Heat and Mass Transfer*, 3(2), art. no. 023004.
- [33] Uwanta, I. J., and Usman, H., 2014, ”On the Influence of Soret and Dufour Effects on MHD Free Convection Heat and Mass Transfer Flow over a Vertical Channel with Constant Suction and Viscous Dissipation,” *Int. Sch. Res. Notices*, 2014, art. no. 639159.
- [34] De Groot, S. R., and Mazur, P., 1984, *Non-Equilibrium Thermodynamics*, Dover Publications, New York (NY), USA.
- [35] Bird, R. B., Stewart, W. E., Lightfoot, E. N., 2002, *Transport Phenomena: Second Edition*, John Wiley & Sons, New York (NY), USA.
- [36] Ludwig, C., 1856, “Diffusion zwischen ungleich erwärmten Orten gleich zusammengesetzter Lösungen,“, *Sitzungsbericht. Kaiser. Akad. Wiss. (Mathem.-Naturwiss. Cl.)*, 65, pp. 539.
- [37] Soret, C., 1879, “Sur l'état d'équilibre que prend, du point de vue de sa concentration, une dissolution saline primitivement homogène, dont deux parties sont portées à des températures différentes,“ *Arch. Sci. Phys. Nat. (III series)*, 2, pp. 48-61.
- [38] Chapman, S., and Cowling, T. G., 1970, *The mathematical theory of non uniform gases: An Account of the Kinetic Theory of Viscosity, Thermal Conduction, and Diffusion in Gases (III edition)*, Cambridge University Press, Cambridge, UK.
- [39] Wakeham, W. A., Nagashima, A., and Sengers, J. V., 1991,

Experimental Thermodynamics (Vol. III): Measurement of the transport properties of fluids, Blackwell Scientific Publications, Oxford, UK.

- [40] Platten, J. K., 2005, "The Soret Effect: A Review of Recent Experimental Results," *J. Appl. Mech.*, 73(1), pp. 5-15.
- [41] Rahman, M. A., and Saghir, M. Z., 2014, "Thermodiffusion or Soret effect: Historical review," *Int. J. Heat Mass Tran.*, 73, pp. 693-705.
- [42] Whitaker, S., 1967, "Diffusion and dispersion in porous media," *AIChE J.*, 13(3), pp. 420-427.
- [43] Marle, C. M., 1967, "Ecoulements monophasiques en milieu poreux," *Rev. Inst. Franç. Pétrol.*, 22(10), pp. 1471-1509.
- [44] Slattery, J. C., 1967, "Flow of viscoelastic fluids through porous media," *AIChE J.* 13(6) pp. 1066-1071.
- [45] Anderson, T. B., and Jackson, R., 1967, "Fluid Mechanical Description of Fluidized Beds: Equations of Motion," *Ind. Eng. Chem. Fundamen.*, 6(4), pp. 527-539.
- [46] Whitaker, S., 1969, "Advances in theory of fluid motion in porous media," *Ind. Eng. Chem.*, 61(12), pp. 14-28.
- [47] Whitaker, S., 1999, *The Method of Volume Averaging*, Kluwer Academic Publishers, Norwell (MA), USA.
- [48] Gray, W. G., and O'Neill, K., "On the general equations for flow in porous media and their reduction to Darcy's law," *Water Resour. Res.*, 12(2), pp. 148-154.
- [49] Quintard, M., and Whitaker, S., 1993, "One and two equation models for transient diffusion processes in two-phase systems," *Adv. Heat Transfer*, 23, pp. 369-464.
- [50] Whitaker S., 1996, "The Forchheimer equation: a theoretical

References

- development,” *Transport Porous Med.*, 25(1), pp. 27-61.
- [51] Nakayama, A., and Kuwahara, F., 2008, “A general bioheat transfer model based on the theory of porous media,” *Int. J. Heat Mass Tran.*, 55(11), pp. 3190-3199.
- [52] Vafai, K., and Tien, C. L., 1981, “Boundary and inertia effects on flow and heat transfer in porous media,” *Int. J. Heat Mass Tran.*, 24(2), pp. 195-302.
- [53] Nield, D. A., and Bejan, A., 2006, *Convection in porous media: Third edition*, Springer, New York (NY), USA.
- [54] Brinkman, H. C., 1947, “A Calculation of the Viscous Force Exerted by a Flowing Fluid on a Dense Swarm of Particles,” *Appl. Sci. Res.*, 1(1), pp. 27–34.
- [55] Darcy, H., 1856, *Les fontaines publiques de la ville de Dijon : exposition et application des principes à suivre et des formules à employer dans les questions de distribution d'eau*, Victor Dalmont, Paris, France.
- [56] Forchheimer, P., 1901, “Wasserbewegung durch Boden,” *Z. Ver. Deutsch. Ing.*, 45, pp. 1781-1788.
- [57] Neuman, S. P., 1977, “Theoretical Derivation of Darcy’s Law,” *Acta Mech.*, 25(3), pp. 153-170.
- [58] Kedem, O., and Katchalsky, A., 1958, “Thermodynamic analysis of the permeability of biological membranes to non-electrolytes,” *Biochim. Biophys. Acta*, 27, pp. 229-246.
- [59] Staverman, A. J., 1951, “The theory of measurement of osmotic pressure,” *Recl. Trav. Chim. Pay. B.*, 7(4), pp. 344-352.
- [60] Kamiuto, K., 2008, “Modeling of composite heat transfer in open-cellular porous materials at high temperatures”. *Cellular and Porous Materials: Thermal Properties Simulation and Prediction*. A. Öchsner,

- G. E. Murch, and M. J. S. de Lemos, eds., Wiley-VCH Verlag GmbH & Co. KGaA, Weinheim, Germany, pp. 165-198.
- [61] Modest, M., 2003, *Radiative Heat Transfer: Second edition*, Academic Press, Burlington (MA) USA.
- [62] F.E. Curry, 1984, "Mechanics and thermodynamics of transcappillary exchange". *Handbook of Physiology: The Cardiovascular system*. E. M., Renkin, and C. C. Michel, eds., American Physiological Society, Bethesda (MD), USA, pp. 309-374.
- [63] Carman, P. C., 1937, "Fluid flow through granular beds," *T. I. Chem. Eng-Lond.*, 15, pp. 150–166.
- [64] Ergun, S., and Orning, A.A., 1952, "Fluid Flow Through Packed Columns," *Chem. Eng. Progr.*, 48, pp 89-94.
- [65] Akgiray, Ö., and Saatçi, A. M. , 2001, "A New Look at Filter Backwash Hydraulics ," *Wa. Sci. Technol.*, 1(2), pp. 65–72.
- [66] Boomsma, K., and Poulikakos, D., 2001, "On the effective thermal conductivity of a three-dimensionally structured fluid-saturated metal foam," *Int. J. Heat Mass Tran.*, 44(4), pp. 827-836.
- [67] Vafai, K., 2005, *Handbook of porous media: Second edition*, CRC Press, Boca Raton (FL), USA.
- [68] Zukauskas, A., 1972, "Heat transfer from Tubes in Cross Flow". *Advances in Heat Transfer: Volume 8*. Hartnett, J. P., and F. T. Irvine, eds., Academic Press, New York (NY), USA, pp. 93-160.
- [69] Kuwahara, F., Shirota, M., and Nakayama, A., 2001, "A numerical study of interfacial convection heat transfer coefficient in two-energy equation model for convection in porous media," *Int. J. Heat Mass Tran.*, 44(6), pp. 1153-1159.
- [70] Saito, M. B., and de Lemos, M. J. S., 2005, "A Correlation for

References

- Interfacial Heat Transfer Coefficient for Turbulent Flow Over an Array of Square Rods,” ASME J. Heat Trans., 128(5), pp. 444-452.
- [71] Prosi, M., Zunino, P., Perktold, K., and Quarteroni, A., 2005, “Mathematical and numerical models for transfer of low-density lipoproteins through the arterial walls: a new methodology for the model set up with applications to the study of disturbed luminal flow,” J. Biomech., 38(4), pp. 903-917.
- [72] Karner, G., Perktold, K., and Zehentner, 2001, “Computational modeling of macromolecule transport in the arterial wall,” Comput. Meth. Biomech. Biomed. Eng., 4(6), pp. 491-504.
- [73] Ai, L., and Vafai, K., 2006, “A coupling model for macromolecule transport in a stenosed arterial wall,” Int. J. Heat Mass Tran., 49(9), pp. 1568-1591.
- [74] “Definition of Cell,” Treccani, accessed February 27, 2016, <http://www.treccani.it/vocabolario/cellula>.
- [75] Mills, N., 2007, *Polymer Foams Handbook: Engineering and Biomechanics Applications and Design Guide*, Butterworth-Heinemann, Waltham (MA), USA.
- [76] “Alvéotec metallic foam”, Alvéotec, accessed February 27, 2016, <http://www.alveotec.fr/fr/innovation.html>.
- [77] Inayat, A., Freund, H., Zeiser, T., and Schwieger, W., 2011, “Determining the specific surface area of ceramic foams: The tetrakaidehedra model revisited,” Chem. Eng. Sci., 66(6), pp. 1179-1188.
- [78] Grosse, J., Dietrich, B., Martin, H., Kind, M., Vicente, J., and Hardy, E. H., 2008, “Volume image analysis of ceramic sponges,” Chem. Eng. Technol., 31(2), 307-314.
- [79] Iasiello, M., Cunsolo, S., Oliviero, M., Harris, W. M., Bianco, N.,

- Chiu, W. K., and Naso, V., 2014, "Numerical Analysis of Heat Transfer and Pressure Drop in Metal Foams for Different Morphological Models," *ASME J. Heat. Trans.*, 136(11), art. no. 112601.
- [80] Berryman, J., and Blair, S., 1986, "Use of Digital Image Analysis to Estimate Fluid Permeability of Porous Material: Application of Two-Point Correlation Functions," *J. Appl. Phys.*, 60(6), pp. 1930-1938.
- [81] Blair, S. C., Berge, P. A., and Berryman, J. G., 1996, "Using two-point correlation functions to characterize microgeometry and estimate permeabilities of sandstones and porous glass," *J. Geophys. Res-Sol. Ea* 101(B9), pp. 20359-20375.
- [82] Doube, M., Kłosowski, M. M., Arganda-Carreras, I., Cordelières, F. P., Dougherty, R. P., Jackson, J. S., Schmid, B., Hutchinson, J. R., and Shefelbine, S. J., 2010, "BoneJ: free and extensible bone image analysis in ImageJ." *Bone*, 47(6), pp. 1076-1079.
- [83] Richardson, J. T., Peng, Y., and Remue, D., 2000, "Properties of ceramic foam catalyst supports: pressure drop," *Appl. Catal. A-Gen.*, 204(1), pp. 19-32.
- [84] Grosse, J., Dietrich, B., Incera Garrido, G., Habisreuther, P., Zarzalis, N., Martin, H., Kind, M., and Kraushaar-Czarnetzki, B., 2009, "Morphological characterization of ceramic sponges for applications in chemical engineering," *Ind. Eng. Chem. Res.* 48 (23), pp. 10395–10401.
- [85] Howell, J. R., Hall, M. J., and Ellzey, J. L., 1996, "Combustion of hydrocarbon fuels within porous inert media," *Prog. Energ. Combust.*, 22(2), pp. 121-145.
- [86] Jongerius, A., Schoonderbeek, D., and Jager, A., 1972, "The application of the Quantimet 720 in soil micromorphometry, *The Microscope*, 20, pp. 243-254.

References

- [87] Petrasch, J., Meier, F., Friess, H., and Steinfeld, A., 2008, "Tomography based determination of permeability, Dupuit–Forchheimer coefficient, and interfacial heat transfer coefficient in reticulate porous ceramics", *Int. J. Heat Fluid Fl.*, 29(1), pp. 315-326.
- [88] Vogel, H.J., and Roth, K., 2001, "Quantitative morphology and network representation of soil pore structure". *Adv. Water Resour.*, 24(3-4), pp. 233–242.
- [89] Inayat, A., 2013, "Open-cell Foams as Catalyst Support: A Description of Morphology, Fluid Dynamics and Catalytic Performance," Ph.D. dissertation, Friedrich-Alexander-Universität Erlangen-Nürnberg, Erlangen-Nürnberg, Germany.
- [90] Maire, E., Colombo, P., Adrien, J., Babout, L., and Biasetto, L., 2007, "Characterization of the morphology of cellular ceramics by 3D image processing of X-ray tomography," *J. Eur. Ceram. Soc.*, 27(4), pp. 1973-1981.
- [91] Kopanidis, A., Theodorakakos, A., Gavaises, E., and Bouris, D., 2010, "3D numerical simulation of flow and conjugate heat transfer through a pore scale model of high porosity open cell metal foam," *Int. J. Heat Mass Tran.*, 53(11), pp. 2539-2550.
- [92] Kumar, P., "Investigation of Kelvin-like solid foams for potential engineering applications: an attractive set of geometrical and thermo-hydraulic properties," Ph.D. dissertation, Aix-Marseille Université, Marseille, France.
- [93] Perrot, C., Panneton, R., and Olny, X., 2007, "Periodic unit cell reconstruction of porous media: Application to open-cell aluminum foams," *J. Appl. Phys.*, 101(11), art. no. 113538.
- [94] Rabi, I.I., Zacharias, J.R., Millman, S., and Kusch, P., 1938, "A New Method of Measuring Nuclear Magnetic Moment," *Phys. Rev.*, 53(4), pp. 318-327.

- [95] Hardy, E. H., 2006, "Magnetic resonance imaging in chemical engineering: basics and practical aspects," *Chem. Eng. Technol.* 29(7), pp. 785-795.
- [96] Smith, N. B., and Webb, A., 2010, *Introduction to Medical Imaging: Physics, Engineering and Clinical Applications*, Cambridge University Press, Cambridge, UK.
- [97] Ridler, T. W., and Calvard, S., 1978, "Picture thresholding using an iterative selection method," *IEEE T. Syst. Man Cyb., Man and Cybernetics*, 8(8) pp. 630-632.
- [98] Otsu, N., 1979, "A threshold selection method from gray-level histograms," *IEEE T. Syst. Man Cyb., Man and Cybernetics*, 9(1) pp. 62-66.
- [99] Weaire, D., 1997, *The Kelvin Problem*, CRC Press, Boca Raton (FL), USA.
- [100] Lord Kelvin (Sir William Thomson), 1887, "On the Division of Space with Minimum Partitional Area," *Acta Math.-Djursholm*, 11(1-4), pp. 121-134.
- [101] Weaire, D., and Phelan, R., 1994, "A counter-example to Kelvin's conjecture on minimal surfaces," *Phil. Mag. Lett.*, 69(2), pp. 107-110.
- [102] Brakke, K., 1992, "The Surface Evolver," *Exp. Math.*, 1(2), pp. 141-165.
- [103] Buciuman, F. C., and Kraushaar-Czarnetzki, B., 2003, "Ceramic foam monoliths as catalyst carriers. 1. Adjustment and description of the morphology," *Ind. Eng. Chem. Res.*, 42(9), pp. 1863-1869.
- [104] Wu, Z., Caliot, C., Bai, F., Flamant, G., Wang, Z., Zhang, J., and Tian, C., 2010, "Experimental and numerical studies of the pressure drop in ceramic foams for volumetric solar receiver applications," *Appl. Energ.*, 87(2), pp. 504-513

References

- [105] Antohe, B. V., Lage, J. L., Price, D. C., and Weber, R. M., 1997, “Experimental determination of permeability and inertia coefficients of mechanically compressed aluminum porous matrices,” *ASME J. Fluid. Eng.*, 119(2), pp. 404-412.
- [106] Bhattacharya, A., Calmidi, V. V., and Mahajan, R. L., 2002, “Thermophysical properties of high porosity metal foams,” *Int. J. Heat Mass Tran.*, 45(5), pp. 1017-1031.
- [107] Boomsma, K., and Poulikakos, D., 2002, “The effects of compression and pore size variations on the liquid flow characteristics in metal foams,” *ASME J. Fluid. Eng.*, 124(1), pp. 263-272.
- [108] Liu, Z. B., He, Y. L., Qu, Z. G., and Tao, W. Q., 2015, “Experimental study of heat transfer and pressure drop of supercritical CO₂ cooled in metal foam tubes,” *Int. J. Heat Mass Tran.*, 85, pp. 679-693.
- [109] Diani, A., Mancin, S., Doretto, L., and Rossetto, L., 2015, “Low-GWP refrigerants flow boiling heat transfer in a 5 PPI copper foam,” *Int. J. Multiphas. Flow*, 76, pp. 111-121.
- [110] Mancin, S., Zilio, C., Cavallini, A., and Rossetto, L., 2010, “Pressure drop during air flow in aluminum foams,” *Int. J. Heat Mass Tran.*, 53(15), pp. 3121-3130.
- [111] Liu, J. F., Wu, W. T., Chiu, W. C., and Hsieh, W. H., 2006, “Measurement and correlation of friction characteristic of flow through foam matrixes,” *Exp. Therm. Fluid Sci.*, 30(4), pp. 329-336.
- [112] Hwang, J. J., Hwang, G. J., Yeh, R. H., and Chao, C. H., 2002, “Measurement of interstitial convective heat transfer and frictional drag for flow across metal foams,” *ASME J. Heat Trans.*, 124(1), pp. 120-129.
- [113] Dietrich, B., Schabel, W., Kind, M., and Martin, H., 2009, “Pressure drop measurements of ceramic sponges - determining the hydraulic diameter,” *Chem. Eng. Sci.*, 64(16), pp. 3633-3640.

- [114] Dukhan, N., 2006, "Correlations for the pressure drop for flow through metal foam," *Exp. Fluids.*, 41(4), pp. 665-672.
- [115] Boomsma, K., Poulikakos, D., and Ventikos, Y., 2003, "Simulations of flow through open cell metal foams using an idealized periodic cell structure," *Int. J. Heat Fluid Fl.*, 24(6), pp. 825-834.
- [116] Haussener, S., Coray, P., Lipiński, W., Wyss, P., and Steinfeld, A., 2010, "Tomography-based heat and mass transfer characterization of reticulate porous ceramics for high-temperature processing," *ASME J. Heat Trans.*, 132(2), art. no. 023305.
- [117] Ranut, P., Nobile, E., and Mancini, L., 2014, "High resolution microtomography-based CFD simulation of flow and heat transfer in aluminum metal foams," *Appl. Therm. Eng.* 69(1), pp. 230-240.
- [118] Diani, A., Bodla, K. K., Rossetto, L., and Garimella, S. V., 2015, "Numerical investigation of pressure drop and heat transfer through reconstructed metal foams and comparison against experiments," *Int. J. Heat Mass Tran.*, 88, pp. 508-515.
- [119] Du Plessis, J. P., and Masliyah, J. H., 1988, "Mathematical modelling of flow through consolidated isotropic porous media," *Transport Porous Med.*, 3(2), pp. 145-161.
- [120] Du Plessis, P., Montillet, A., Comiti, J., and Legrand, J., 1994, "Pressure drop prediction for flow through high porosity metallic foams," *Chem. Eng. Sci.*, 49(21), pp. 3545-3553.
- [121] Fourie, J. G., and Du Plessis, J. P., 2002, "Pressure drop modelling in cellular metallic foams," *Chem. Eng. Sci.*, 57(14), pp. 2781-2789.
- [122] Lu, T. J., Stone, H. A., and Ashby, M. F., 1998, "Heat transfer in open-cell metal foams," *Acta Mater.*, 46(10), pp. 3619-3635.
- [123] Lacroix, M., Nguyen, P., Schweich, D., Huu, C. P., Savin-Poncet, S., and Edouard, D., 2007, "Pressure drop measurements and modeling on SiC foams," *Chem. Eng. Sci.*, 62(12), pp. 3259-3267.

References

- [124] Huu, T. T., Lacroix, M., Huu, C. P., Schweich, D., and Edouard, D., 2009, "Towards a more realistic modeling of solid foam: use of the pentagonal dodecahedron geometry," *Chem. Eng. Sci.*, 64(24), pp. 5131-5142.
- [125] Cunsolo, S., Iasiello, M., Oliviero, M., Bianco, N., Chiu, W. K., and Naso, V., 2016, "Lord Kelvin and Weaire–Phelan Foam Models: Heat Transfer and Pressure Drop," *ASME J. Heat Trans.*, 138(2), art. no. 022601.
- [126] Suleiman, A. S., and Dukhan, N., 2014, "Long-domain simulation of flow in open-cell mesoporous metal foam and direct comparison to experiment," *Micropor. Mesopor. Mat.*, 196, pp. 104-114.
- [127] Bai, M., and Chung, J. N., 2011, "Analytical and numerical prediction of heat transfer and pressure drop in open-cell metal foams," *Int. J. Therm. Sci.*, 50(6), pp. 869-880.
- [128] Fuller, A. J., Kim, T., Hodson, H. P., and Lu, T. J., 2005, "Measurement and interpretation of the heat transfer coefficients of metal foams," *P. I. Mech. Eng. C-J. Mec.*, 219(2), pp. 183-191.
- [129] Dukhan, N., Bağcı, Ö., and Özdemir, M., 2015, "Thermal development in open-cell metal foam: An experiment with constant wall heat flux," *Int. J. Heat Mass Tran.*, 85, pp. 852-859.
- [130] Ghosh, I., 2008, "Heat-transfer analysis of high porosity open-cell metal foam," *ASME J. Heat Trans.*, 130(3), art. no. 034501.
- [131] Mancin, S., Zilio, C., Diani, A., and Rossetto, L., 2013, "Air forced convection through metal foams: Experimental results and modeling," *Int. J. Heat Mass Tran.*, 62, pp. 112-123.
- [132] Younis, L. B., and Viskanta, R., 1993, "Experimental determination of the volumetric heat transfer coefficient between stream of air and ceramic foam," *Int. J. Heat Mass Tran.*, 36(6), pp. 1425-1434.

- [133] Vijay, D., Goetze, P., Wulf, R., and Gross, U., 2015, "Forced convection through open cell foams based on homogenization approach: Transient analysis," *Int. J. Therm. Sci.*, 98, pp. 395-408.
- [134] Schlegel, A., Benz, P., and Buser, S., 1993, "Wärmeübertragung und Druckabfall in keramischen Schaumstrukturen bei erzwungener Strömung," *Warme Stoffübertrag.*, 28(5), pp. 259-266.
- [135] Fu, X., Viskanta, R., and Gore, J. P., 1998, "Measurement and correlation of volumetric heat transfer coefficients of cellular ceramics," *Exp. Therm. Fluid Sci.*, 17(4), pp. 285-293.
- [136] Dietrich, B., 2013, "Heat transfer coefficients for solid ceramic sponges - Experimental results and correlation," *Int. J. Heat Mass Tran.*, 61, pp. 627-637,
- [137] Pusterla, S., Barbato, M., Ortona, A., and D'Angelo, C., 2012, "Numerical study of cell morphology effects on convective heat transfer in reticulated ceramics," *Int. J. Heat Mass Tran.*, 55(25), pp. 7902-7910.
- [138] Ambrosio, G., Bianco, N., Chiu, W. K. S., Iasiello, M., Naso, V., and Oliviero, M., 2015, "The effect of open-cell metal foams strut shape on convective heat transfer and pressure drop," *Proceedings of ASME-ATI-UIT 2015 Conference on Thermal Energy Systems: Production, Storage, Utilization and the Environment, Naples, Italy, May 17-20, 2015*, and submitted in a revised form on *Applied Thermal Engineering*.
- [139] Wu, Z., Caliot, C., Flamant, G., and Wang, Z., 2011, "Numerical simulation of convective heat transfer between air flow and ceramic foams to optimise volumetric solar air receiver performances," *Int. J. Heat Mass Tran.*, 54(7), pp. 1527-1537.
- [140] Wu, Z., Caliot, C., Flamant, G., and Wang, Z., 2011, "Coupled radiation and flow modeling in ceramic foam volumetric solar air receivers," *Sol. Energy*, 85(9), pp. 2374-2385.

References

- [141] ISO 5167-1:2003 Measurement of fluid flow by means of pressure differential devices inserted in circular cross-section conduits running full -- Part 1: General principles and requirements.
- [142] Dybbs, A., and Edwards, R. V., 1984, "A new look at porous media fluid mechanics - Darcy to turbulent," *Fundamentals of transport phenomena in porous media*. J. Bear, and M. Y. Corapcioglu, eds., Springer Netherlands, Dordrecht, Netherlands, pp. 199-256.
- [143] Hall, M. J., and Hiatt, J. P., 1996, "Measurements of pore scale flows within and exiting ceramic foams," *Exp. Fluids*, 20(6), pp. 433-440.
- [144] Della Torre, A., Montenegro, G., Tabor, G. R., and Wears, M. L., 2014, "CFD characterization of flow regimes inside open cell foam substrates," *Int. J. Heat Fluid Fl.*, 50, pp. 72-82.
- [145] Contento, G., 2013, "Modeling of the morphology and of the heat transfer in open-cell foams," Ph.D. dissertation, Università degli Studi di Napoli Federico II, Naples, Italy.
- [146] Noman, R., and Kalam, M. Z., 1990, "Transition from laminar to non-darcy flow of gases in porous media," *Advances in core evaluation – Accuracy and precision in reserves estimation*. P. F. Worthington ed., Gordon and Breach Science Publishers, Amsterdam, Netherlands, pp. 447-462.
- [147] Dukhan, N., and Patel, P., 2008, "Equivalent particle diameter and length scale for pressure drop in porous metals," *Exp. Therm. Fluid Sci.*, 32(5), pp. 1059-1067.
- [148] Avila-Marin, A. L., 2011, "Volumetric receivers in solar thermal power plants with central receiver system technology: a review," *Sol. energy*, 85(5), pp. 891-910.
- [149] Fricker, H.W., 1983, "Proposal for a novel type of solar gas receiver," *Proceedings of the International Seminar on Solar Thermal Heat Production and Solar Fuels and Chemicals*, Stuttgart, Germany, October 13-14, 1983, art. no. 11.

- [150] “SOLGATE Project”, European Commission, accessed March 3, 2016, https://ec.europa.eu/research/energy/pdf/solgate_en.pdf.
- [151] Hennecke, K., Schwarzbözl, P., Koll, G., Beuter, M., Hoffschmidt, B., Göttsche, J., and Hartz, T., 2007, “The Solar Power Tower Jülich — A Solar Thermal Power Plant for Test and Demonstration of Air Receiver Technology,” *Proceedings of ISES World Congress 2007 (Vol. I–Vol. V)*. D. Y. Goswami, and Y. Zhao, eds., Springer Berlin Heidelberg, Heidelberg, Germany, pp. 1749-1753.
- [152] Bhattacharya, A., and Mahajan, R. L., 2002, “Finned metal foam heat sinks for electronics cooling in forced convection,” *J. Electron. Packaging*, 124(3), pp. 155-163.
- [153] Shih, W. H., Chou, F. C., and Hsieh, W. H., 2007, “Experimental investigation of the Heat Transfer Characteristics of Aluminum-Foam Heat Sinks with Restricted Flow Outlet,” *ASME J. Heat Trans.*, 129(11), pp. 1554-1563.
- [154] Feng, S. S., Kuang, J. J., Wen, T., Lu, T. J., and Ichimiya, K., 2014, “An experimental and numerical study of finned metal foam heat sinks under impinging air jet cooling,” *Int. J. Heat Mass Tran.*, 77, pp. 1063-1074.
- [155] “Cardiovascular system,” Treccani, accessed March 13, 2016, <http://www.treccani.it/enciclopedia/sistema-cardiovascolare/>.
- [156] “Medical illustration libraries,” Netter Images, accessed March 13, 2016, <https://www.netterimages.com/>.
- [157] “Capillary Exchange,” www.encyclopedia.lubopitko-bg.com, accessed March 13, 2016, http://encyclopedia.lubopitko-bg.com/Capillary_Exchange.html.
- [158] “European Cardiovascular Disease Statistics: 2012 edition,” European Society of Cardiology, accessed March 13, 2016, http://www.escardio.org/static_file/Escardio/Press-media/press-

References

- releases/2013/EU-cardiovascular-disease-statistics-2012.pdf.
- [159] Ross, M. H., and Pawlina, W., 2006, *Histology: A Text and Atlas*, Lippincott Williams & Wilkins, Baltimore (MD), USA.
- [160] AbuRahma, A. F., and Bergan, J. J., 2007, *Noninvasive Vascular Diagnosis: A Practical Guide to Therapy, Second Edition*, Springer, London, UK.
- [161] Vincent, G. M., Fox, J., Johnson, M. D., Strickland, R., Garry, S. L., and Hammond, E., 1990, "Thermal laser probe angioplasty: Influence of constant tip temperature, plaque composition, and probe/vessei diameter ratio," *Laser. Surg. Med.*, 10(5), pp. 420-426.
- [162] Barbeau, G. R., Abela, G. S., Friedl, S. E., Tomaru, T., Giacomino, P. P., and Seeger, J. M., 1990, "Temperature monitoring during peripheral thermo-optical laser recanalization in humans," *Clin. Cardiol.*, 13(10), pp. 690-697.
- [163] Karsch, K. R., and Haase, K. K., 2013, *Coronary laser angioplasty: an update*, Springer Berlin Heidelberg, Heidelberg, Germany.
- [164] Meyer, G., and Tedgui, A., 1996, "Effects of pressure-induced stretch and convection on low-density lipoprotein and albumin uptake in the rabbit aortic wall," *Circ. Res.*, 79(3), pp. 532-540.
- [165] Xie, X., Tan, J., Wei, D., Lei, D., Yin, T., Huang, J., Zhang, X., Qiu, J., Tang, C., and Wang, G., 2013, "In vitro and in vivo investigations on the effects of low-density lipoprotein concentration polarization and haemodynamics on atherosclerotic localization in rabbit and zebrafish," *J. R. Soc. Interface*, 10(82), art. no. 20121053.
- [166] Liu, X., Fan, Y., Deng, X., and Zhan, F., 2011, "Effect of non-Newtonian and pulsatile blood flow on mass transport in the human aorta," *J. Biomech*, 44(6), pp. 1123-1131.
- [167] Kenjereš, S., and de Loo, A., 2014, "Modelling and simulation of

- low-density lipoprotein transport through multi-layered wall of an anatomically realistic carotid artery bifurcation,” *J. R. Soc. Interface*, 11(91), art. no. 20130941
- [168] Back, L. H., Radbill, J. R., and Crawford, D. W., 1977, “Analysis of oxygen transport from pulsatile, viscous blood flow to diseased coronary arteries of man,” *J. Biomech*, 10(11), pp. 763-774.
- [169] Deng, X., Marois, Y., How, T., Merhi, Y., King, M., and Guidoin, R., 1995, “Luminal surface concentration of lipoprotein (LDL) and its effect on the wall uptake of cholesterol by canine carotid arteries,” *J. Vasc. Surg*, 21(1), pp. 135-145.
- [170] Wada, S., Koujiya, M., and Karino, T., 2002, “Theoretical study of the effect of local flow disturbances on the concentration of low-density lipoproteins at the luminal surface of end-to-end anastomosed vessels,” *Med. Biol. Eng. Comput*, 40(5), pp. 576-587.
- [171] Truskey, G. A., Roberts, W. L., Herrmann, R. A., and Malinauskas, R. A., 1992, “Measurement of endothelial permeability to 125I-low density lipoproteins in rabbit arteries by use of en face preparations,” *Circ. Res*, 71(4), pp. 883-897.
- [172] Rappitsch, G., and Perktold, K., 1996, “Computer simulation of convective diffusion processes in large arteries,” *J. Biomech*, 29(2), pp. 207-215.
- [173] Lei, M., Kleinstreuer, C., and Truskey, G. A., 1996, “A focal stress gradient-dependent mass transfer mechanism for atherogenesis in branching arteries,” *Med. Eng. Phys*, 18(4), pp. 326-332.
- [174] Fatouraee, N., Deng, X., Champlain, A., and Guidoin, R., 1998, “Concentration polarization of low density lipoproteins (LDL) in the arterial system,” *Ann. Ny. Acad. Sci*, 858(1), pp. 137-146.
- [175] Hong, J., Wei, L., Fu, C., and Tan, W., 2008, “Blood flow and macromolecular transport in complex blood vessels,” *Clin. Biomech*, 23(1), S125-S129.

References

- [176] Lantz, J., and Karlsson, M., 2012, "Large eddy simulation of LDL surface concentration in a subject specific human aorta," *J. Biomech*, 45(3), pp. 537-542.
- [177] Fazli, S., Shirani, E., and Sadeghi, M. R., 2011, "Numerical simulation of LDL mass transfer in a common carotid artery under pulsatile flows," *J. Biomech*, 44(1), pp. 68-76.
- [178] Nematollahi, A., Shirani, E., Sadeghi, M. R., and Mirzaee, I., 2015, "Effects of shear-dependent transport properties on lumen surface concentration of LDL particles in stenosed carotid artery," *Meccanica*, 50(7), pp. 1733-1746.
- [179] Stangeby, D. K., and Ethier, C. R., 2002, "Computational analysis of coupled blood-wall arterial LDL transport," *ASME J. Biomech. Eng*, 124(1), pp. 1-8.
- [180] Olgac, U., Kurtcuoglu, V., and Poulidakos, D., 2008, "Computational modeling of coupled blood-wall mass transport of LDL: effects of local wall shear stress," *Am. J. Physiol.-Heart C.*, 294(2), pp. H909-H919.
- [181] Sun, N., Wood, N. B., Hughes, A. D., Thom, S. A., and Xu, X. Y., 2007, "Influence of pulsatile flow on LDL transport in the arterial wall," *Ann. Biomed. Eng.*, 35(10), pp. 1782-1790.
- [182] Ogston, A. G., 1958, "The spaces in a uniform random suspension of fibres," *T. Faraday Soc.*, 54, 1754-1757.
- [183] Chung, S., and Vafai, K., 2013, "Low-density lipoprotein transport within a multi-layered arterial wall—Effect of the atherosclerotic plaque/stenosis," *J. Biomech*, 46(3), pp. 574-585.
- [184] Chung, S., and Vafai, K., 2012, "Effect of the fluid–structure interactions on low-density lipoprotein transport within a multi-layered arterial wall," *J. Biomech*, 45(2), pp. 371-381.

- [185] Sun, N., Wood, N. B., Hughes, A. D., Thom, S. A., and Xu, X. Y., 2007, “Effects of transmural pressure and wall shear stress on LDL accumulation in the arterial wall: a numerical study using a multilayered model,” *Am. J. Physiol.-Heart C.*, 292(6), pp. H3148-H3157.
- [186] Yang, N., and Vafai, K., 2006, “Modeling of low-density lipoprotein (LDL) transport in the artery—effects of hypertension,” *Int. J. Heat Mass Tran.*, 49(5), pp. 850-867.
- [187] Khakpour, M., and Vafai, K., 2008, “Effects of gender-related geometrical characteristics of aorta–iliac bifurcation on hemodynamics and macromolecule concentration distribution,” *Int. J. Heat Mass Tran.*, 51(23), pp. 5542-5551.
- [188] Khakpour, M., and Vafai, K., 2008, “A comprehensive analytical solution of macromolecular transport within an artery,” *Int. J. Heat Mass Tran.*, 51(11), pp. 2905-2913.
- [189] Yang, N., and Vafai, K., 2008, “Low-density lipoprotein (LDL) transport in an artery—A simplified analytical solution,” *Int. J. Heat Mass Tran.*, 51(3), pp. 497-505.
- [190] Hong, J., Fu, C., Lin, H., and Tan, W., 2012, “Non-Newtonian effects on low-density lipoprotein transport in the arterial wall,” *J. Non-Newton. Fluid.*, 189, pp. 1-7.
- [191] Chung, S., and Vafai, K., 2014, “Mechanobiology of low-density lipoprotein transport within an arterial wall—impact of hyperthermia and coupling effects,” *J. Biomech.*, 47(1), pp. 137-147.
- [192] Iasiello, M., Vafai, K., Andreozzi, A., Bianco, N., and Tavakkoli, F., 2015, “Effects of external and internal hyperthermia on LDL transport and accumulation within an arterial wall in the presence of a stenosis,” *Ann. Biomed. Eng.*, 43(7), pp. 1585-1599.
- [193] Wang, S., and Vafai, K., 2013, “Analysis of the effect of stent emplacement on LDL transport within an artery,” *Int. J. Heat Mass*

References

- Tran.,64, pp. 1031-1040.
- [194] Wang, S., and Vafai, K., 2015, "Analysis of low density lipoprotein (LDL) transport within a curved artery," *Ann. Biomed. Eng.*, 43(7), pp. 1571-1584.
- [195] Iasiello, M., Vafai, K., Andreozzi, A., and Bianco, N., 2016, "Low-density lipoprotein transport through an arterial wall under hyperthermia and hypertension conditions—An analytical solution," *J. Biomech.*, 49(2), pp. 193-204.
- [196] Deyranlou, A., Niazmand, H., and Sadeghi, M. R., 2015, "Low-density lipoprotein accumulation within a carotid artery with multilayer elastic porous wall: fluid–structure interaction and non-Newtonian considerations," *J. Biomech.*, 48(12), pp. 2948-2959.
- [197] Iasiello, M., Vafai, K., Andreozzi, A., and Bianco, N., 2016, "Analysis of Non-Newtonian Effects on Low-Density Lipoprotein Accumulation in an Artery," *J. Biomech.*, accepted for publication.
- [198] Tarbell, J. M., 2003, "Mass transport in arteries and the localization of atherosclerosis," *Annu. Rev. Biomed. Eng.*, 5(1), pp. 79-118.
- [199] Liu, X., Fan, Y., and Deng, X., 2011, "Effect of the endothelial glycocalyx layer on arterial LDL transport under normal and high pressure," *J. Theor. Biol.*, 283(1), pp. 71-81.
- [200] Alazmi, B., and Vafai, K., 2001, "Analysis of fluid flow and heat transfer interfacial conditions between a porous medium and a fluid layer," *Int. J. Heat Mass Tran.*, 44(9), pp. 1735-1749.
- [201] Amiri, A., and Vafai, K., 1994, "Analysis of dispersion effects and non-thermal equilibrium, non-Darcian, variable porosity incompressible flow through porous media," *Int. J. Heat Mass Tran.*, 37(6), pp. 939-954.
- [202] Kim, S., Cho, Y. I., Jeon, A. H., Hogenauer, B., and Kensey, K. R., 2000, "A new method for blood viscosity measurement," *J. Non-*

- Newton. Fluid, 94(1), pp. 47-56.
- [203] Cho, Y. I., and Kensey, K. R., 1991, "Effects of the non-Newtonian viscosity of blood on flows in a diseased arterial vessel. Part 1: Steady flows," *Biorheology*, 28(3-4), pp. 241-262.
- [204] Johnston, B. M., Johnston, P. R., Corney, S., and Kilpatrick, D., 2004, "Non-Newtonian blood flow in human right coronary arteries: steady state simulations," *J. Biomech.*, 37(5), pp. 709-720.
- [205] Hayes, R. E., Afacan, A., Boulanger, B., and Shenoy, A. V., 1996, "Modelling the flow of power law fluids in a packed bed using a volume-averaged equation of motion," *Transport Porous Med.*, 23(2), pp. 175-196.
- [206] Christopher, R. H., and Middleman, S., 1965, "Power-law flow through a packed tube," *Ind. Eng. Chem. Fund.*, 4(4), pp. 422-426.
- [207] Graf, C., and Barras, J. P., 1979, "Rheological properties of human blood plasma—a comparison of measurements with three different viscometers," *Experientia*, 35(2), pp. 224-225.
- [208] Lin, S. J., Jan, K. M., Schuessler, G., Weinbaum, S., and Chien, S., 1988, "Enhanced macromolecular permeability of aortic endothelial cells in association with mitosis," *Atherosclerosis*, 73(2), pp. 223-232.
- [209] Huang, Y., Rumschitzki, D., Chien, S., and Weinbaum, S., 1994, "A fiber matrix model for the growth of macromolecular leakage spots in the arterial intima," *ASME J. Biomech. Eng.*, 116(4), pp. 430-445.
- [210] Song, S. H., and Roach, M. R., 1983, "Quantitative changes in the size of fenestrations of the elastic laminae of sheep thoracic aorta studied with SEM," *J. Vasc. Res.*, 20(3), pp. 145-153.
- [211] Huang, Z. J., and Tarbell, J. M., 1997, "Numerical simulation of mass transfer in porous media of blood vessel walls," *Am. J. Physiol.-Heart C.*, 273(1), pp. H464-H477.

References

- [212] Duck, F. A., 1990, *Physical Properties of Tissues: A Comprehensive Reference Book*, Academic Press, San Diego (CA), USA.
- [213] Johnston, B. M., Johnston, P. R., Corney, S., and Kilpatrick, D., 2006, "Non-Newtonian blood flow in human right coronary arteries: transient simulations," *J. Biomech.*, 39(6), pp. 1116-1128.
- [214] Ross Ethier, C., and Simmons, C. A., 2007, *Introductory Biomechanics: From Cells to Organisms*, Cambridge University Press, New York City (NY), USA.
- [215] Yilmaz, F., and Gundogdu, M. Y., 2008, "A critical review on blood flow in large arteries; relevance to blood rheology, viscosity models, and physiologic conditions," *Korea-Aust. Rheol. J.*, 20(4), pp. 197-211.
- [216] Razavi, A., Shirani, E., and Sadeghi, M. R., 2011, "Numerical simulation of blood pulsatile flow in a stenosed carotid artery using different rheological models," *J. Biomech.*, 44(11), pp. 2021-2030.
- [217] Tedgui, A., and Lever, M. J., 1984, "Filtration through damaged and undamaged rabbit thoracic aorta," *Am. J. Physiol.-Heart C.*, 247(5), pp. H784-H791.
- [218] Jung, H., Choi, J. W., and Park, C. G., 2004, "Asymmetric flows of non-Newtonian fluids in symmetric stenosed artery," *Korea-Aust. Rheol. J.*, 16(2), pp. 101-108.
- [219] Dash, R. K., Jayaraman, G., and Mehta, K. N., 1999, "Flow in a catheterized curved artery with stenosis," *J. Biomech.*, 32(1), pp. 49-61.
- [220] Liao, W., Lee, T. S., and Low, H. T., 2004, "Numerical studies of physiological pulsatile flow through constricted tube," *Int. J. Numer. Method. H.*, 14(5), pp. 689-713.
- [221] Long, Q., Xu, X. Y., Ramnarine, K. V., and Hoskins, P., 2001, "Numerical investigation of physiologically realistic pulsatile flow

- through arterial stenosis,” *J. Biomech.*, 34(10), pp. 1229-1242.
- [222] Young, D. F., and Tsai, F. Y., 1973, “Flow characteristics in models of arterial stenoses—I. Steady flow. *Journal of biomechanics*,” 6(4), pp. 395, IN3, 403-402-410.
- [223] Hossain, S. S., Hossainy, S. F., Bazilevs, Y., Calo, V. M., and Hughes, T. J., 2012, “Mathematical modeling of coupled drug and drug-encapsulated nanoparticle transport in patient-specific coronary artery walls,” *Comput. Mech.*, 49(2), pp. 213-242.
- [224] Mahjoob, S., and Vafai, K., 2009, “Analytical characterization of heat transport through biological media incorporating hyperthermia treatment,” *Int. J. Heat Mass Tran.*, 52(5), pp. 1608-1618.
- [225] Shah, P. M., Scarton, H. A., and Tsapogas, M. J., 1978, “Geometric anatomy of the aortic--common iliac bifurcation,” *J. Anat.*, 126(3), pp. 451-458.
- [226] Nanayakkara, B., Gunarathne, C. K., Sanjeewa, A. D. S. S., Gajaweera, K. A. R., Dahanayake, A. S., Sandaruwan, U. H. C., and De Silva, U. A. M. D., 2009, “Geometric anatomy of the aortic-common iliac bifurcation,” *Galle Medical Journal*, 12(1), pp. 8-12.
- [227] Deswal, A., Tamang, B. K., and Bala, A., 2014, “Study of aortic-common iliac bifurcation and its clinical significance,” *J. Clin. Diagn. Res.*, 8(7), pp. AC06-AC08.
- [228] Nematollahi, A., Shirani, E., Mirzaee, I., and Sadeghi, M. R., 2012, “Numerical simulation of LDL particles mass transport in human carotid artery under steady state conditions,” *Sci. Iran.*, 19(3), pp. 519-524.